Gems & Gemology

Fall 2019
VOLUME LV

The Quarterly Journal of the Gemological Institute of America

Gem Art of the Taj Mahal and the Mughal Era

Characteristics of Fancy White and Black Diamonds

Vanadium-Rich Emerald from Malipo, China

Inclusions in Corundum from Bo Welu, Thailand

GEMS & GEMOLOGY®
Fall 2019
VOLUME 55, No. 3


p. 309


p. 321


p. 338


p. 372


p. 437

Editorial

Feature Articles

Notes and New Techniques

Regular Features

GEMS & GEMOLOGY®

gia.edu/gems-gemology

Subscriptions
Copies of the current issue may be purchased for $29.95 plus shipping. Subscriptions are $79.99 for one year (4 issues) in the U.S. and $99.99 elsewhere. Canadian subscribers should add GST. Discounts are available for renewals, group subscriptions, GIA alumni, and current GIA students. To purchase print subscriptions, visit store.gia.edu or contact Customer Service. For institutional rates, contact Customer Service.

Database Coverage
Gems & Gemology's impact factor is 1.844, according to the 2017 Thomson Reuters Journal Citation Reports (issued July 2018). *G&G* is abstracted in Thomson Reuters products (Current Contents: Physical, Chemical & Earth Sciences and Science Citation Index—Expanded, including the Web of Knowledge) and other databases. For a complete list of sources abstracting *G&G*, go to gia.edu/gems-gemology, and click on "Publication Information."

Manuscript Submissions
Gems & Gemology, a peer-reviewed journal, welcomes the submission of articles on all aspects of the field. Please see the Author Guidelines at gia.edu/gems-gemology or contact the Managing Editor. Letters on articles published in *G&G* are also welcome. Please note that Field Reports, Lab Notes, Gem News International, Micro-World, and Charts are not peer-reviewed sections but do undergo technical and editorial review.

Gems & Gemology is published quarterly by the Gemological Institute of America, a nonprofit educational organization for the gem and jewelry industry.

Postmaster: Return undeliverable copies of *Gems & Gemology* to GIA, The Robert Mouawad Campus, 5345 Armada Drive, Carlsbad, CA 92008.

Our Canadian goods and service registration number is 126142892RT.

About the Cover

This issue features an examination of the gem art of the Taj Mahal, an iconic architectural treasure erected at the pinnacle of the Mughal dynasty. The seventeenth-century necklace on the cover features seven spinels from Tajikistan, pearls, and a pear-shaped emerald cabochon drop. The spinels are inscribed with the names of various Mughal emperors. The necklace was sold by Christie's New York in June 2019 for more than $3 million. Photo courtesy of Christie's.

Printing is by L+L Printers, Carlsbad, CA.
GIA World Headquarters The Robert Mouawad Campus 5345 Armada Drive Carlsbad, CA 92008 USA

ISSN 0016-626X

Gem Art of the Taj Mahal, Fancy White and Black Diamonds, and Unique Inclusions in Thai Corundum

Welcome to the Fall 2019 issue of *G&G*! Inside you'll find eight articles on a variety of gemological topics, plus dozens of brief reports and discoveries from contributors around the world.

Our lead article delves into the gem art of the iconic Taj Mahal. Dona Dirlam and co-authors examine the intricate gem inlay that graces this architectural treasure, as well as the gem connoisseurship of the Mughal dynasty and how it influenced global gem commerce in the seventeenth century.

In the second article, Sally Eaton-Magaña and Christopher M. Breeding continue their series of colored diamond characterization studies with an in-depth look at Fancy white and Fancy black diamonds. Their systematic study, based on GIA's data for approximately 500 Fancy white and 1,200 Fancy black diamonds, is the first of its kind for these uncommon diamonds.

"A systematic study, based on GIA's data for approximately 500 Fancy white and 1,200 Fancy black diamonds, is the first of its kind for these uncommon diamonds."

Next, Yang Hu and Ren Lu offer a gemological, spectroscopic, and chemical analysis of emeralds from Malipo County in Yunnan Province of southwestern China. Among notable deposits worldwide, Malipo emerald has a unique chemical composition: a combination of high vanadium, low chromium, and moderate iron, as well as high lithium and cesium concentrations.

Supparat Promwongnan and Chakkaphan Sutthirat use Raman spectroscopy and electron probe micro-analysis to identify mineral inclusions in alluvial corundum from the Bo Welu gem deposit in Thailand's Chanthaburi Province. Several of the inclusions they identify are reported for the first time in Thai corundum.

Next are a pair of studies on organic gem materials. Yamei Wang and co-authors explore hydrothermally treated "beeswax" amber, offering a series of comprehensive tests to identify this product and separate it from untreated material. Kannika Kanjanachatree and co-authors follow the operations at a pearl farm in Phuket, Thailand, to determine the effects of mollusk size on growth and color of half-cultured pearls from *Pteria penguin*.

The issue rounds out with two brief but informative studies. Wenqing Huang and co-authors investigate a hydrogen-rich faceted green diamond color-treated by a complex multi-step process that has not previously been reported in the gemological literature. Last, Hanyue Xu and Xiaoyan Yu analyze a new rhodochrosite imitation composed of pressed gibbsite and calcite powder with a granular structure.

Highlights from the Lab Notes section include a faceted diamond with a star-shaped cloud inclusion, new resin imitations of ivory, and cobalt-coated sapphire. Micro-World once again offers up a variety of beautiful and unusual scenes from the inner world of gemstones. Among the many Gem News International reports are a new source of Nigerian aquamarine, black non-nacreous pearl imitations made of beads cut from shell, and the new mineral johnkoivulaite. This member of the beryl family is named in recognition of distinguished researcher and longtime *G&G* contributor John Koivula. Congratulations to John for this exceptional honor—well deserved!

Duncan Pay | Editor-in-Chief | dpay@gia.edu

GEMSTONES IN THE ERA OF THE TAJ MAHAL AND THE MUGHALS

Dona Mary Dirlam, Chris L. Rogers, and Robert Weldon

The Taj Mahal evokes an image of a monumental building and reflecting pool—its classic view. But the Taj Mahal complex is much more than that. It is actually a series of beautiful buildings and gardens in Agra, India, built in the seventeenth century in loving memory of Mumtaz Mahal. This name, given by the Mughal emperor Shah Jahan to one of his brides, means "Chosen One of the Palace." Famed for its architectural magnificence, the landmark holds additional significance for the gemologist. Upon closer investigation, one is impressed with the intricacies of the inlay of numerous gems to create thousands of designs throughout the buildings on the grounds. This article sheds light on the gems used in decorating the Taj Mahal and in the extraordinary jewelry collected by Shah Jahan and other Mughals. These gems often took intricate trade routes to Agra, which are also discussed, along with the craft used to create the inlays and the efforts undertaken to preserve this Wonder of the World.

The magnificent Taj Mahal is a large complex of buildings and gardens in the city of Agra, located in the northern Indian state of Uttar Pradesh (figure 1). The Yamuna (or Jumna) River flows in a wide arc around the rear of the majestic site (figure 2). Recognized as one of the most beautiful structural compositions in the world, it was designated as a UNESCO World Heritage site in 1983. Visitors are amazed by its breathtaking beauty. Its exquisite domed white marble mausoleum, situated within four gardens with raised walkways and reflecting pools, is one of the most astonishing architectural marvels.

Viewed from the south, it is startling to realize that the Taj Mahal is not set in the serene countryside, as photos suggest, but rather in a largely impoverished city with a population of nearly two million (figure 3). The city of Agra has expanded around the complex. Walking around the grounds and taking a closer look at the buildings, one marvels at the elaborate decorative inlay that includes ornamental gem materials as well as fine gems. This stonework is generally referred to as *pietra dura* ("hard stone" in Italian) and known as *parchin kari* in India.

Emperor Shah Jahan (1592–1666), who ruled from 1628 to 1658, built the Taj Mahal for one of his wives, Mumtaz Mahal. Construction began shortly after her death. It eventually took more than 1,000 elephants and 20,000 craftsmen from all over Asia to build (Nath, 1985). Begun in 1632, the entire complex was not completed until 1653 (Sarkar, 1920; "The Taj Mahal," n.d.). In 2007, it was chosen as one of the New Seven Wonders of the World.

In this article, we will examine the story behind the detailed features of the gem inlay work as well as the history and architecture of the Taj Mahal,

In Brief

- The Mughal era, from the early sixteenth to mid-nineteenth century, ushered in a time of unparalleled patronage of the arts, gem collecting, and architecture in India.
- The inspiration for the Taj Mahal, which took more than two decades to complete, was love.
- Trade during the Mughal era spread ideas, products, and culture across land and sea on a global scale.
- A signature design element of the Taj Mahal is the exquisite *parchin kari* hard stone inlay that incorporated gem materials from various sources.

See end of article for About the Authors and Acknowledgments.
GEMS & GEMOLOGY, Vol. 55, No. 3, pp. 294–319,
http://dx.doi.org/10.5741/GEMS.55.3.294

Figure 1. The grandeur of the Taj Mahal and its intricate stone inlays immediately greets the visitor upon entering the complex in Agra, India. Photo by Robert Weldon/GIA.

which represents the artistic height of the Mughal dynasty. Through famous portraits, we will get a glimpse of the types of jewels and gems acquired by Shah Jahan. We will also see gems and jewels that illustrate gem connoisseurship of the Mughal era at its pinnacle (Jaffer, 2013).

Figure 2. The Taj Mahal complex is best viewed from a distance, in this case from the Yamuna River. Photo by Robert Weldon/GIA.

Figure 3. The city of Agra has grown along the edges of the Taj Mahal, which presents challenges to the integrity and long-term survival of the architectural marvel. Photo by Robert Weldon/GIA.

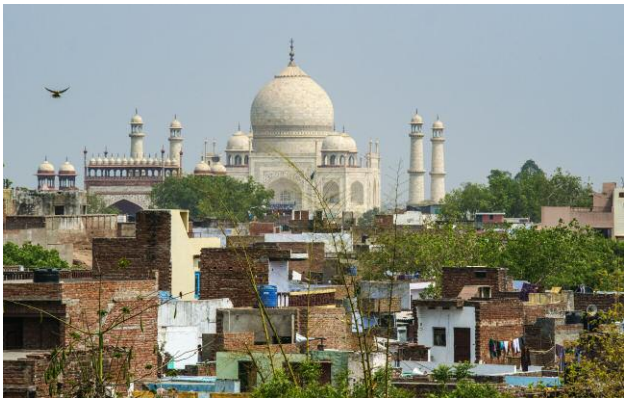

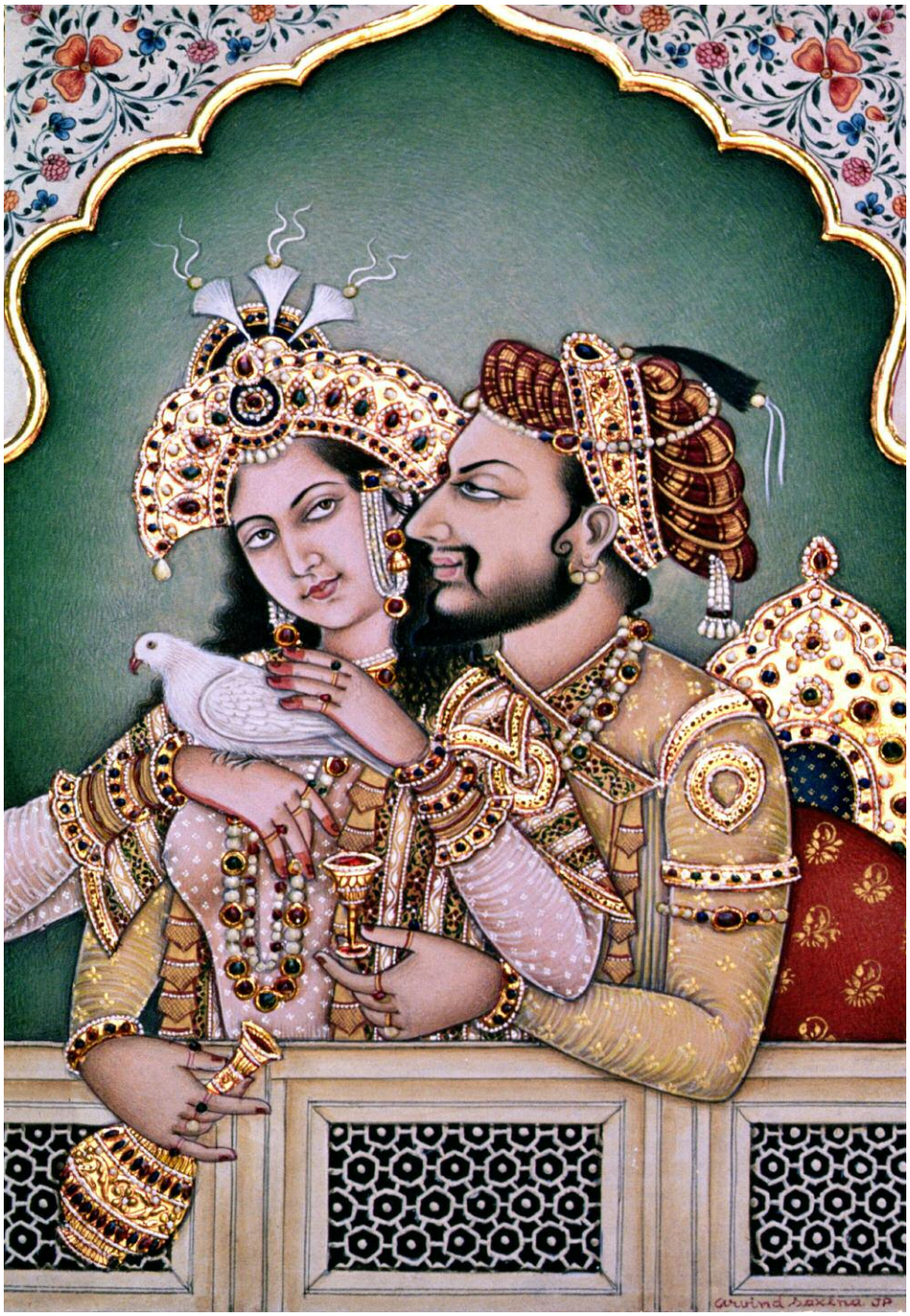

Figure 4. Shah Jahan (1592–1666) and his wife Arjumand Banu Begum, who became known as Mumtaz Mahal, appear in this painting from the Indian School. From a private collection, courtesy of Dinodia/Bridgeman Images.

INSPIRATION FOR THE TAJ MAHAL

Called "a teardrop on the cheek of time" by Indian poet Rabindranath Tagore (Nath, 1985), the marvel of architecture and art known as the Taj Mahal was inspired by love—specifically, the devotion for one woman, Arjumand Banu Begum. Shah Jahan, a son of Jahangir, met her in 1607 when she was just 15 years old. He asked to marry her the next day, but romantic marriages were unheard of, even for a prince; they were traditionally arranged. It would be another five years before they could marry.

After they married, Arjumand Banu Begum became known as Mumtaz Mahal, or "Chosen One of the Palace." Shah Jahan's two other marriages were secured for political reasons. Although he bore one child each with his other wives, they were no com-

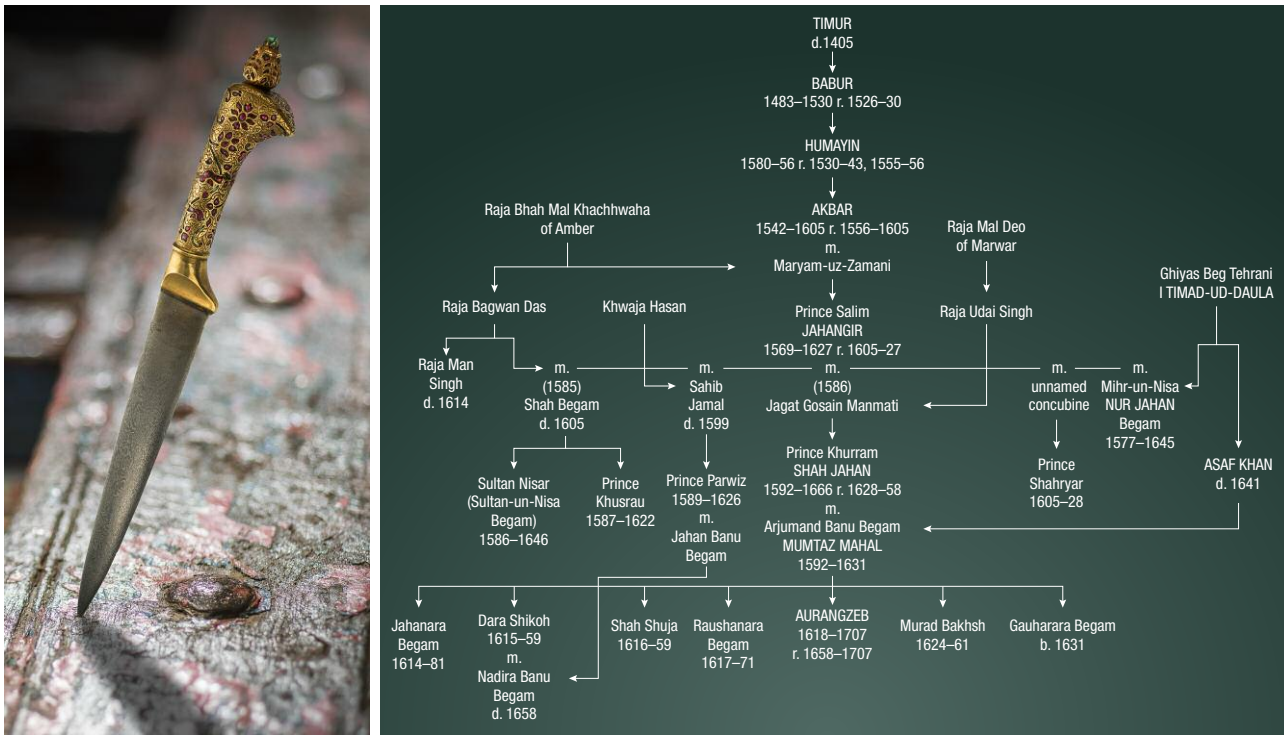

Figure 5. Left: This seventeenth-century ceremonial knife from Hyderabad contains emerald, ruby (including some recently replaced treated ruby), and Damascus steel with a 23K engraved gold handle. Photo by Robert Weldon/GIA. Right: Genealogy of the Mughal dynasty, reproduced with permission of Ebba Koch.

petition for his affections (figure 4). Mumtaz gave birth to fourteen children from their marriage, though only seven survived.

Mumtaz's reign as queen was short-lived. Three years later, she died moments after the birth of their fourteenth child. Early accounts say that she whispered two final requests. One was that he not remarry. The second was to build a monument to resemble paradise on earth, just as she had dreamed of the night before her death (Nath, 1985).

Mumtaz was temporarily buried in the garden of Zainabad. Almost immediately, Shah Jahan began work on what would emerge as one of the greatest memorials ever constructed. He took inspiration from a verse from the imperial goldsmith and poet Bibadal Khan: "May the abode of Mumtaz Mahal be Paradise" (Koch, 2006). He chose a site on the banks of the Yamuna River at Agra. Shah Jahan called the mausoleum a "monument of sorrow" (Nath, 1985).

Shah Jahan's Place in the Mughal Lineage. Babur (1483–1530), a Central Asian prince who went to India in search of wealth and conquest, became the founder of the Mughal Empire in 1526 (see the genealogy chart in figure 5). Babur distributed the spoils from his wars among the nobles whose soldiers fought, following the tradition of Timur or Tamerlane (r. 1370–1405) of the Central Asian Dynasty. Babur and his Mughal successors embraced their Timurid ancestry through subjugation to legitimize and solidify their rule. This is apparent in the succession leading to Shah Jahan's rule. In 1628, Shah Jahan succeeded his father. His eldest brother failed to take the throne, and his other brother died under mysterious circumstances. Shah Jahan had other potential successors killed (Delmerick, 1883). He became the new emperor through this process of elimination, earning him the title "King of the World" (Koch, 2006). Shah Jahan would encounter similar familial struggles for power in his later years. After a serious illness, he was deposed and imprisoned by his own son, Aurangzeb, in 1658. Nonetheless, the rulers saw the importance of documenting their rule, which they did by having the names of their ancestors (and the current ruler) inscribed on the most treasured of the gems they obtained through trade.

As Jaffer (2013) points out, "India was a land of fabled wealth that had lured both conquerors and merchants from around the globe since antiquity." The Indian subcontinent was known for its gems and jewelry, a place where aspirations for owning them became a part of daily life for people of all classes and religions.

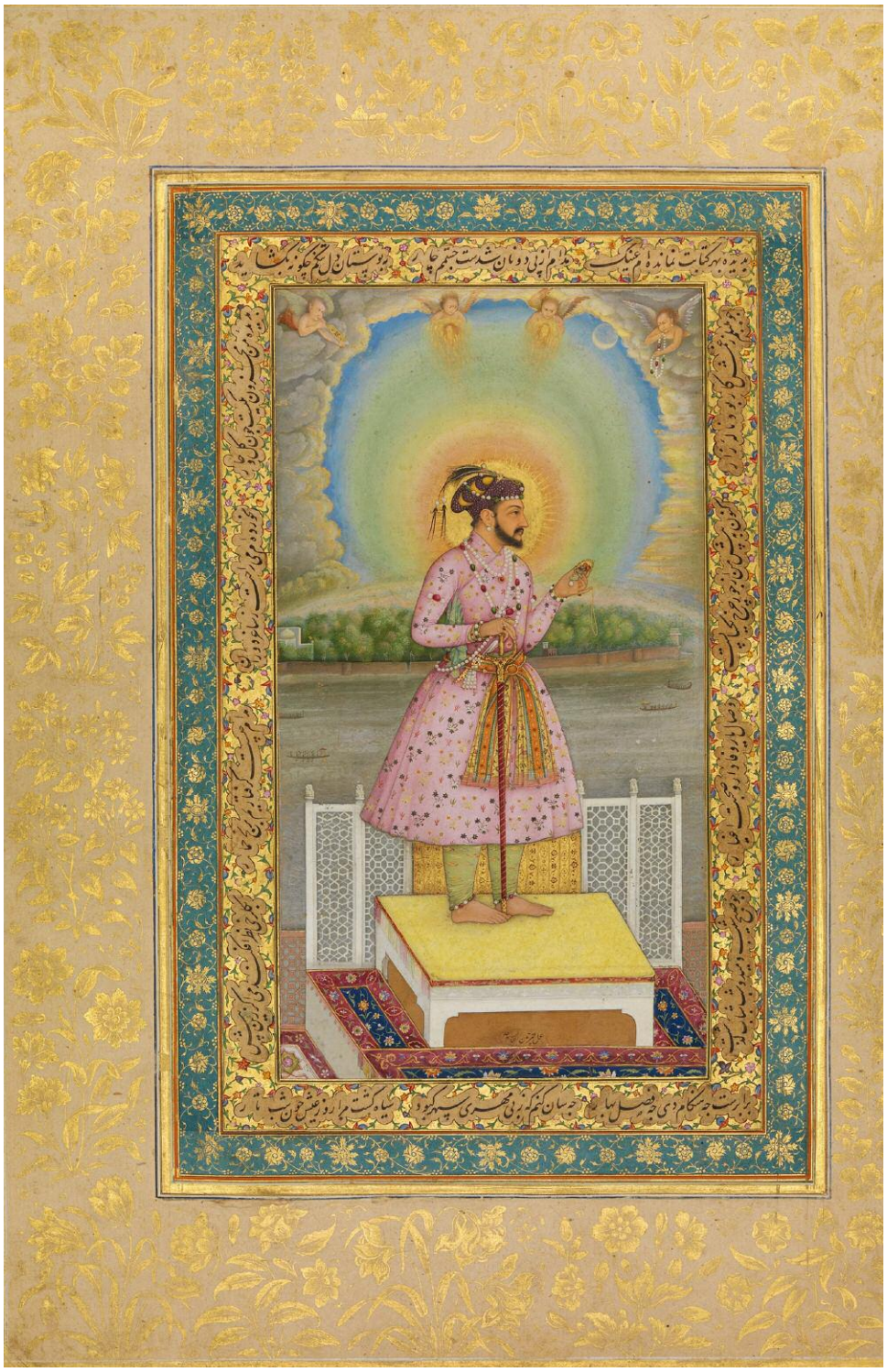

Figure 6. This portrait by Chitarman, his earliest dated painting, shows Shah Jahan exquisitely dressed and richly adorned with jewels. His imperial halo and the hovering angels are borrowed from European art. Courtesy of the Metropolitan Museum of Art, public domain.

To the Mughals, gems, jewelry, and jeweled objects were more than just beautiful treasures: They were symbols of power. Mughal expansion was an effort to acquire more territory and more of these treasures. The Mughals had competition in their expansion from two other great regional Muslim empires, the Ottomans and the Persian Safavids.

It is remarkable that we have such detailed information and resources about this period. Some of the information comes from court records, inventories by

jewelry and gem curators, writings by the Mughal rulers themselves, and foreign travelers such as Sir Thomas Roe and Jean-Baptiste Tavernier. Court paintings also provide intricate detail about the style and variety of gems treasured by the Mughal leaders.

The Mughals' Support for the Arts. With the ascension to the throne of Jahangir, Shah Jahan's father, the Mughals' patronage of artisans began to flourish, especially when he married a supporter of the arts, Nur Jahan (Latif, 1982). Jahangir was known to wear gemstones and pearls with extravagance. In 1619, Flemish diamond dealer and noted chronicler Jacques de Coutre described the emperor as "looking like an idol on account of the quantities of jewels he wore, with many precious stones around his neck as well as spinels, emeralds and pearls on his arms, and diamonds hanging from his turban" (Jaffer, 2013) (figure 6). This is confirmed by later portraits of the emperor that show him draped in pearls, gemstones, and rings.

Early in the Mughal era, jewels were used as gifts on rare occasions, but only for the most special of royal guests. They were bestowed at feasts and celebrations. But starting with Jahangir and following with Shah Jahan, gift giving became an important political and cultural practice, layered with many intricacies. These two leaders also embraced European and Asian craftsmen, which is evident in the types of gems and jewelry they collected and later in the style of the architectural gem inlay work they adopted. In 1615, at the "Feast of the Water Aspersion," an array of gemstones and jeweled utensils was offered (Melikian-Chirvani, 2004).

Gifts were also given to commemorate the transfer of power, as when Shah Jahan became governor of Bengal and received a jeweled sword belt. A jeweled dagger belt was given to the great grandson of the founder of the Safavid dynasty (Shah Ismail I of Iran) by the governor of Zamindawar on a similar occasion in 1593. During the rule of Shah Jahan, gold decanters enameled and encrusted with gems were given at the annual Rosewater Celebration (Melikian-Chirvani, 2004).

Islamic law (see figure 7) prohibited men from wearing gold jewelry, but this was generally not enforced during the Mughal period in India except under the reign of Shah Jahan's son Aurangzeb, from 1658 to 1707. Mughal rulers were influenced more by the Hindu tradition of adorning themselves with gold jewelry than by Persian traditions. Jahangir was known for wearing strung jewels such as pearls and strands of gemstones, as well as jeweled turban ornaments, as evidenced by writings and paintings of the era. Shah Jahan's own devotion to jewelry started well before his reign. In a portrait from 1617, he is wearing pearls and bracelets and holding a jeweled turban ornament. In portraits as emperor, he is draped in gemstones and gold, and in some paintings depicted on bejeweled thrones, including the famous Peacock Throne (Jaffer, 2013).

Figure 7. This seventeenth-century miniature painting on ivory depicts Shah Jahan in his durbar *(court) and the* al-Mizaan *(Islamic scales of justice). Photo by Robert Weldon/GIA.*

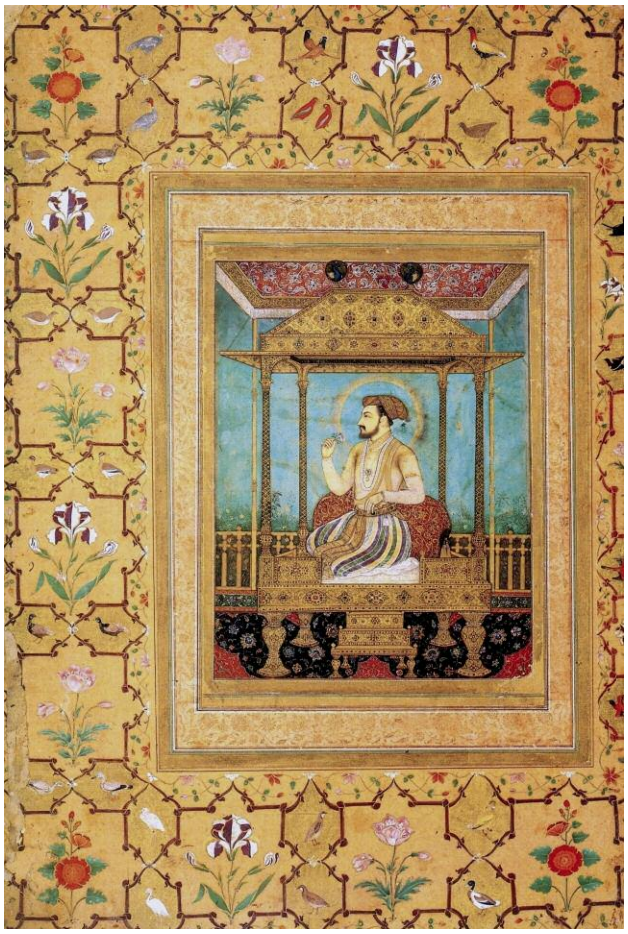

Figure 8. A painting of Shah Jahan on the Peacock Throne. The painting is attributed to the noted Mughal painter Govardhan, circa 1635.

From 1707 to 1739, following the reign of Aurangzeb, Mughal laws gave the emperor and certain noblemen exclusive ownership of gemstones over 5 carats, as well as jewelry. Earrings and lengthy strands of pearls and gemstones, turban ornaments, amulets, finger rings, archer's rings, belts, and jeweled weapons were part of that wealth and power (Jaffer, 2013). They also had the exclusive right to bestow jewel-encrusted weapons and turban ornaments, of which the latter were especially popular gifts.

Some of these extravagant jewels were distributed to the needy in a Hindu tradition that began during the reign of Akbar and ended with Aurangzeb. At the emperor's biannual birthday weighing ceremony, which happened on his lunar and solar birthdays, his weight (and the weight of royal princes) was measured against expensive fabrics and gemstones. The monetary equivalent of this weight was given to the poor. With Aurangzeb's reign, the lavish ceremonies and patronage of the arts that took place under previous emperors were drastically reduced.

According to the writings of French traveler and gem merchant Jean-Baptiste Tavernier (1605–1689), who made six voyages to Turkey, Persia, and India in search of gems and treasures, there was a particular protocol in gift giving. Aurangzeb would have merchants sell gemstones and jewelry from the imperial treasury to nobles, and these items would then be gifted back to the emperor (Tavernier, 1678). The political nature of these gifts endowed the giver and the receiver with symbolic gestures, while ensuring that the Mughal rulers retained their valuable treasures.

Pearls, too, were highly valued. The Mughal emperors preferred round pearls, whereas baroque pearls were popular in Europe at the time. The appreciation for pearls is evidenced by their ubiquity in paintings and sculptures (Bala Krishnan and Sushil Kumar, 2001). Despite their passion for pearls, emperors such as Shah Jahan treasured richly colored emeralds even more. Emeralds from South American deposits, which had been discovered by Europeans in the late 1500s, made their way to India. These were often carved with floral motifs and Islamic inscriptions. Such items were given as gifts by the emperor and the royal court (Lane, 2010).

This all came to an end when the Persian ruler Nadir Shah (r. 1736–1747) sacked Delhi in 1739. Much of the Mughal wealth, including the fabled Peacock Throne (figure 8), was taken to Persia and added to what would become the Crown Jewels of Iran. This was the first of several times the Mughal capital fell and its riches were taken away. With the collapse of the central authority, the declining Mughal Empire splintered into autonomous states and finally dissolved in 1857 (Jaffer, 2013).

Enameling in the Mughal World. Although enameling dates back to the Egyptians and Sumerians prior to 2500 BCE (Sharma and Varadarajan, 2004), it reached new heights under the Mughal rulers. It was during this period that the most outstanding pieces were produced. The first reference to enameling in India was under Akbar's reign during the sixteenth century, in Mubarak's account *Ain-i-Akbari* (1894), which mentions the enameling of "cups, flagons, rings and other articles with gold and silver." The art of enameling spread throughout India, including among Hindus, beginning in Multan (in modern-day Pakistan) and Lahore, extending from workshop to workshop, circulating to Jaipur and other cities.

Figure 9. This seventeenth-century hand of Vishnu with exquisite enameling from Maharashtra contains Colombian emeralds and Indian diamonds set in 22K enameled gold, illustrating a popular enameling style. The hand measures 14 × 8 × 1.5 cm. The inscription on the back, in Sanskrit, quotes devotional verses from the Bhagavad Gita. Photos by Robert Weldon/GIA. Courtesy of private collectors.

According to Sharma (2004), "the style during [the Mughal] period, and used by Hindus as well, was to decorate the frontal side of the ornaments on an enameled background with precious gems while the reverse was adorned with enameled patterns…. This effortless blending of Muslim and Hindu decorative art in the realm of jewellery made these pieces stylistically unique." The back was often as beautiful or more beautiful than the front (figure 9).

The style of Mughal-era enameling, most likely adapted from the South Indian Deccan enamelers, shares common themes with the decor of the Taj Mahal, which features red poppies and floral patterns on a white background. This style is a hallmark of Jaipuri enamelwork. Jaipur was the center of Indian enameling during the eighteenth and nineteenth centuries. The advancement of Jaipur as an important enameling capital was a result of close ties with the Rajasthani Rajputs and the Mughals (Sharma, 2004).

It was under Shah Jahan's reign that enameling began to flourish. Jahan was truly a connoisseur of all things artistic. Through enameling he could combine his appreciation for gemstones, art, and architecture. He used enameling to embellish some of the finest thrones, such as the Peacock Throne, as well as magnificent decorative objects and weaponry (Sharma, 2004).

With the Taj Mahal, Shah Jahan displayed the enameling of the Mughal period most consummately and passionately. While the Taj Mahal was still under construction, he had a golden screen created. It contained enameled inscriptions and cupolas that were to be placed around Mumtaz Mahal's tomb on the second anniversary of her death (Bala Krishan, 2001).

Shah Jahan, the Gem Connoisseur. The incredible gem wealth available to Shah Jahan made it possible for him to decorate the Taj Mahal with his vast collection of gems, jewels, and jeweled objects. Some highlights from Shah Jahan's collection were inscribed gems. Early on, Indian gem cutters mastered the technique of drilling gems with diamond points and inscribing them to mark ownership by the Mughal elites (S.H. Ball, 1931). The inscriptions follow an imperial regal style and include important dates (Jaffer, 2013). One famous diamond, known as the Shah diamond, has three separate inscriptions reading "Burhan Nizam Shah, 1591"; "Shah Jahan, 1641"; and "Fath Ali Shah, 1824" (Haidar and Stewart, 2014). This 88.71 ct table cut was later presented to Czar Nicholas I in 1829 by an Iranian prince. The Shah diamond is now part of the State Diamond Fund, housed in the Kremlin Museum in Moscow.

Another favorite gem to inscribe was spinel. Necklaces of inscribed spinels were painstakingly assembled by the Mughals. A 54 ct spinel auctioned by Sotheby's in London in April 2017 contained the names of Jahangir, Prince Khurram, and Aurangzeb and was dated 1615 and 1659. While the estimate was $77,000–$103,000, the realized price was more than $330,000. Sotheby's catalog described the spinel as a "pinkish stone…pierced through the centre and set with a later gold chain and hanging seed-pearl and metal-thread pendant."

A remarkable inscribed spinel necklace appeared in the June 2019 Christie's New York auction "Maharajas & Mughal Magnificence," featuring gems and jeweled objects from the Al Thani Collection. The seven spinels are dated by Persian inscriptions ranging from 1607 to 1608 and 1754 to 1755 (figure 10). These inscriptions include *la'l-I jalali* ("glorious spinel") and name Akbar, Jahangir, and Shah Jahan, among other emperors. With a reserve of $1,000,000–$2,000,000, the necklace fetched a final price of $3,015,000. Spinels were held in the highest esteem, equal to that of rubies and emeralds, and were chosen by the Mughals to bear imperial names.

The timelessness of Mughal splendor is seen today in the enthusiasm for this auction. The 400 lots generated $109,271,000, the highest total for any auction of Indian and Mughal objects, and the second highest for any private collection. In 2020, nearly 6,000 pieces from the Al Thani Collection, assembled by Sheikh Hamad bin Abdullah Al Thani of the Qatari royal family, will go on exhibit at the Hôtel de la Marine in Paris as a permanent museum collection and education facility.

Figure 10. This seventeenth-century necklace containing seven spinels, pearls, and a pear-shaped cabochon emerald drop, set in gold, is inscribed in Persian with Mughal emperors' names. It was sold by Christie's New York in June 2019 for $3,015,000. Courtesy of Christie's.

TRADE ROUTES FOR GEM MATERIALS

To understand how such gem wealth, gold, and silver were available to the Mughals, one needs to review the regional powers of Asia in the fifteenth and sixteenth centuries. Gem traders came from around the world, driven by their passion for acquiring what India produced, as well as the goods that flowed through Indian trade centers. Indian trade followed ancient land and sea routes. The routes became more complex as brave travelers ventured into new locations with a more sophisticated understanding of trade winds and navigation. New trading centers arose as others declined. Shah Jahan acquired his vast collection of jewels for the Taj Mahal largely because of the key role India played in the global gem trade.

Some of the key trade routes are shown in the world trade route map on pp. 304–305.

The ancient trade routes included the Silk Road, which had been used for thousands of years. UNESCO has identified 12 sites in India along the Silk Road. Rivers throughout India also provided an inexpensive means to move people and goods. It is no accident that Agra and the Taj Mahal are situated next to the Yamuna River, an important route. Other factors also contributed, such as

> globalized international trade that brought such wealth to the Mughal ruler that he was able to contemplate this extraordinary gesture to his beloved spouse. [Shah Jahan's] ability to complete [the Taj Mahal] stemmed from the profound shifts in the world's axis of power, for Europe and India's glory came at the expense of the Americas.…Gold and silver taken from the Americas, and from Africa, found their way to Asia through trade: it was this redistribution of wealth that enabled the Taj Mahal to be built (Frankopan, 2017).

The influx of South American emeralds, and the expanding European trade in these goods, coincided with Mughal appreciation for the gem. This was underscored by the Prophet Muhammad's favoring of the color green. Finer emeralds had never been seen, and the sheer volume of them provided Jahangir and Shah Jahan with exceptional trading possibilities. Emeralds from Egypt had been mined up until medieval times. According to Lane (2010), emeralds from what is now Pakistan and Afghanistan provided occasional supplies through trade along the Silk Road. But nothing compared with the quality and quantity of South American emeralds.

One of the most fascinating trade routes at this time brought emeralds from the present-day Colombian mining areas of Chivor and Muzo, mined since pre-Columbian times, to India and the Mughals (Weldon et al., 2016) (figure 11). Lane (2010) describes how these emeralds traveled across the Atlantic and Indian Oceans through new Christian, Jewish, and Sephardic family networks to Seville, Antwerp, and Lisbon. Later, Jewish Ashkenazi families became active in this commerce, and gems were transported by land and by sea from Mediterranean and European cities. Traded along with the emeralds were pearls from the New World, Baltic amber, Mediterranean coral, and Mexican pearls and silver from Potosí (modern-day Bolivia). These were exchanged for spices, silk, and porcelain, as well as diamonds, rubies, sapphires, and other gem materials. Armenian merchants were particularly successful with the ruby trade from the city of Pegu (in modern-day Myanmar), then under Persian Safavid protection. The great demand for silver established another route from Mexico to Manila. Tavernier also describes the trade of emeralds from Peru (mined from Muzo and Chivor). Gold, silver, and rough emeralds were traded through Manila (Tavernier, 1678). Modern gem testing has confirmed the origin in many such examples (Weldon et al., 2016).

Figure 11. The centerpiece of this Mughal horn pendant is a 125 ct Colombian emerald engraved in Arabic with salutations of peace based on a verse from the Koran. It dates back to the eighteenth century. The pendant also contains ruby, diamond, and pearls set in 22K gold and measures 6 × 8.5 × 2 cm. Photo by Robert Weldon/GIA. Courtesy of private collectors.

The port city of Goa, located in Panaji State on the Indian Ocean, is 1,667 km (1,036 miles) from Agra. As Emilio Rui Vilar relates in the introduction to *Goa and the Great Mughal*:

> Following the arrival of the Portuguese in India (1498), the newcomers were forced into a complex web of strategic moves and political alliances that guaranteed

World Trade Routes of the Mughal Era


Moscow
Karakorum
Venice
Genoa
Black Sea
Caspian Sea
Kashgar
Beijing
1.
Badakhshan
Tunis
Mediterranean Sea
2.
Kabul
Suzhou
Basra
1.
3.
Agra
Cambay
Surat
Akyab
Macao
Red Sea
Golconda
Goa
Bay of Bengal
South China Sea
Manila
Arabian Sea
Gulf of Mannar
Malindi
Mombasa
Luanda
Nacala
Beira
N
W
E
S
Silk Road
Water Routes
Across North Africa
1. Ottoman Empire
2. Safavid Empire
3. Mughal Empire

> that they could sail, trade, and carry out missionary work in safety and ensured the security of their settlements and trading posts….not only stimulating trade, diplomatic contacts and missionary work, but also mutual associations and influences in the fields of culture and the arts (Vassallo e Silva and Flores, 2004).

With the emergence of Goa as a trading center, the emphasis shifted there (Vassallo e Silva and Flores, 2004). The capital of the Portuguese state of India, Goa had become a major trading center for importing goods and exporting decorative arts by the late 1500s. Gemstones and jewelry were leading items in the luxury trade. Interestingly, it was the relative freedom for foreign merchants, a favorable tax status, and other trade concessions that gave rise to the growth of Goa. Tavernier, the jeweler merchant to Louis XIV of France, wrote of its significance:

> Goa was formerly the place where there was the largest trade in all Asia in diamonds, rubies, sapphire, topaz and other stones. All the miners and merchants were there to see the best which they had obtained at the mines, because they had their full liberty to sell, whereas in their own country, … they were compelled to sell at whatever price was fixed (V. Ball, 1977b).

Just as a variety of gems entered Goa from global sources, this port also became the principal center for gemstones heading west, especially diamonds (Bala Krishnan, 2001).

Figure 12. A recent scene at a camel fair in Pushkar, Rajasthan, India, shows that the trading of camels has changed little since the Mughal time. Photo by Robert Weldon/GIA.

As Tavernier describes, value-added businesses began to emerge in the thriving port, employing a multicultural and diverse contingent of craftspeople. It became famous for its Portuguese lapidary operations. The street called Rua Direita was the center for many workshops and stalls of jewelers, silversmiths, and lapidaries (V. Ball, 1977b).

The Importance of Gem Trade from Goa to Agra. Because of the Mughals' insatiable desire for gems, precious metals, and decorative arts, the trade route from Goa to Agra became well established. An equally insatiable appetite for diamonds from the Golconda mines drove explorers and merchants to India, helping establish trade. There was no other place on earth to acquire diamonds of significant size and quantity. The success of the Portuguese in bringing all manner of precious goods to Goa made this possible. According to the Flemish merchant Jacques de Coutre, "It is very true that from all parts of the World, they send pearls, emeralds, rubies, and jewels of great value to Eastern India, and we all know full well that they came to the Mughal" (Vassallo e Silva and Flores, 2004). During de Coutre's 32-year career in India, he and his brother dealt in precious stones and jewels. He knew that the important gems ended up in the Mughal treasury. According to the early seventeenth-century Italian explorer Francesco Carletti:

> The Great Mughal purchased all the spinel rubies from all over the world, as these gems brought high profits when sent on for sale in India. The consumption and aesthetic demands of the Mughal Empire required a constant flow of goods, jewels, and countless rarities that only a port such as Goa could properly supply (Vassallo e Silva and Flores, 2004).

Just as early scholars wrote about the port of Goa, modern archaeologists and other scholars have documented the growth and decline of other regional trading centers (see trade route map on pp. 304–305). Intricate maps and chronicles of these sites paint a picture of the goods and products traded (Thoresen, 2017). Gold, ivory, and rock crystal—as well as slaves—came from Africa. Silks, spices, gems, silver, and gold were traded between Asia and the Americas, while furs and gems came from Russia.

In addition to spinels, emeralds, pearls, rubies, and other gems, Tavernier described the large diamonds recovered from India. He visited four diamond mines around Golconda: Rammalakota (Roalconda), Kollur (Coulour or Gani), Soumelpour in the kingdom of Bengal, and Kistna (between Rammalakota and Kollur). This information is found in Ball's Volume II of

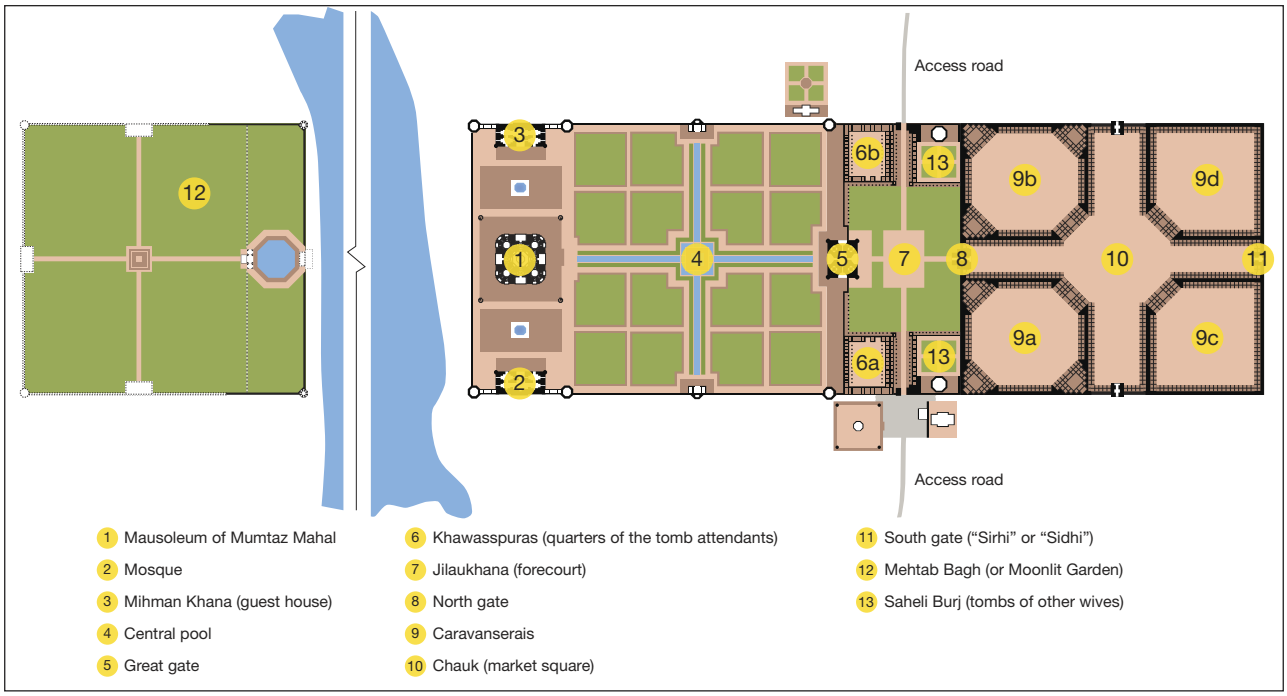

Figure 13. This diagram shows the symmetry of the architecture, reflecting pools, and gardens of the Taj Mahal. Courtesy of I. Mcginnly, Wikipedia Commons.

Travels in India by Jean-Baptiste Tavernier (based on Tavernier's 1676 French edition). Ball (1977a) pointed out the challenges of following the names of the diamond mines given by Tavernier. Ball included an appendix with a list of Indian diamond mines, with latitudes and longitudes. He reproduced Tavernier's famous plate that shows the 20 diamonds he sold to the French king upon his return. This includes the rough now believed to be the French Blue, which was eventually cut into the Hope Diamond. There are also Tavernier's depictions of the Great Mogul, the Golconda, the Grand Duke of Tuscany, and the Bazu.

Travel was by camel caravan. The number of camels in a caravan could vary from several hundred to several thousand (figure 12). Two species were popular along the Silk Road. The Bactrian camel was used for the eastern trade roads and their cold climates in Central Asia and Mongolia. Arabian camels were used for warmer climates on the western routes. Camels were the ideal pack animal, able to carry more weight than horses or donkeys. They carried more than 300 pounds each and required much less water. Without water, a loaded camel could travel for nearly 15 days. Sometimes breeders would crossbreed the two camel species for even greater endurance.

This confluence of international trade, art, and building techniques contributed to the uniquely complex and iconic structure that the Taj Mahal remains today, 366 years since its completion. In the next section, we analyze the architecture of this Wonder of the World and the gem materials that were used to adorn her.

ARCHITECTURE AND GEM MATERIALS OF THE TAJ MAHAL

The mausoleum is the iconic part of the Taj Mahal, but it makes up only a portion of the complex. The entire complex occupies 66.62 acres (0.27 square km), while the preserved complex takes up just under 42 acres (169 square km). The names of the architects are not known with certainty, but several architects are believed to have worked on the project. Of those, Ustad Ahmad Lahauri and Mir Abdul Karim are the two most often mentioned (Koch, 2006) (figure 13).

The grounds of the Taj Mahal are accessed through the forecourt (Koch, 2006), a large courtyard with the east and west gates. It was used for ceremonial purposes, such as marking the anniversary of the death of Mumtaz Mahal. The tops of the gates slope up in the center to a rectangular structure called a *pishtaq*. Within this shape sits an archway through which the complex is entered. While the inner facade of the archway is quite embellished, the outer face is simpler, with some floral ornamentation on the spandrels (the two triangular spaces between the top of the arch

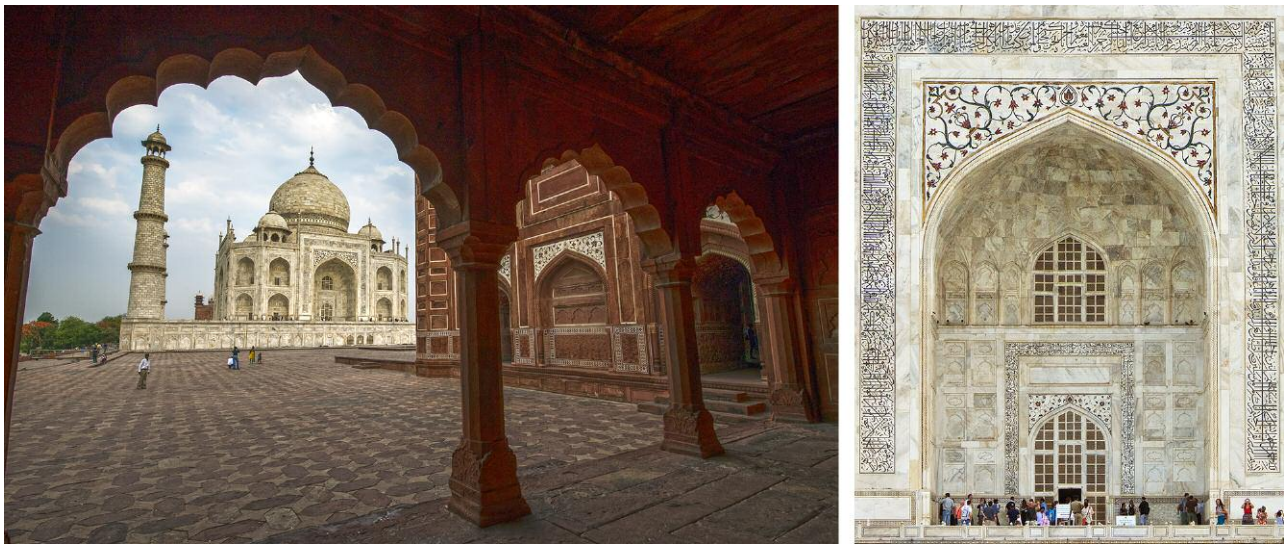

Figure 14. Left: A view of the Taj Mahal from the Mihman Khana, or guest pavilion. Right: A view of the inscribed entryway, called a pishtaq*, with floral embellishment on the spandrels. Photos by Robert Weldon/GIA.*

and the rectangular frame) (figure 14). Unlike the detailed inner facades of the east and west gates, both the inner and outer facades of the south gate are simple in ornamentation (Koch, 2006).

The Great Gate is the centerpiece of the forecourt, located on the southern wall within the funerary garden, a symmetrical garden divided into quarters. The garden once contained fruit-bearing trees (symbolic of life) and herbs. Abundant roses (symbols of love) were mentioned by Shah Jahan's poet, Qudsi, but there were many more unnamed blooms throughout. The reflecting pools are lined with cypress trees, symbolizing death.

The mausoleum sits on a raised square platform standing seven meters high. The dome of the mausoleum is 73 meters high and nearly 18 meters in diameter. Four minarets, towers with domed pavilions, surround the mausoleum.

Two additional tomb buildings, called Saheli Burj, lie along the south end of the complex. They hold the bodies of Shah Jahan's lesser wives. According to the Taj Mahal Museum, Akbarabadi Mahal lies in the western tomb, and Sirhindi Mahal lies in the eastern tomb. Akbarabadi Mahal was a favorite consort in the last reigning days of Shah Jahan and the wife that he spoke highly of to his daughter, Jahanara, in his final moments (Koch, 2006). One of the four tombs contains a marble cenotaph embellished with parchin kari (this technique was only used in the tombs of the emperor's family at the time the Taj Mahal was built), but vandals have stolen many of the more valuable inlaid stones.

Water is a very important part of the garden (figure 15). According to Begley (1979) and the official Taj Mahal website, the garden features four water channels symbolic of the Rivers of Paradise mentioned in the Koran: the rivers of water, milk, wine, and honey. The Archaeological Survey of India is charged with maintaining the trees and flowers of the Taj Mahal. They have done their best to reconstruct the original planting based on the discovery of old plans. However, some of this work amounts to educated speculation.

Significance of the Gems Used. Gems were chosen not only for their color but also for the spiritual properties attributed to them at that time. Of the many different types of gems used in the parchin kari of the Taj Mahal, the most significant in Islamic culture is carnelian (figure 16). The Prophet Muhammad is said to have worn a silver ring set with carnelian on the little finger of his right hand, using it as a seal. Jafar, one of the most well-known of the imams, proclaimed that any man who wore carnelian would have his desires fulfilled (Kunz, 1938).

Jade and chlorite were likely used because green was the Prophet Muhammad's favorite color (Brill, 1993). Some ancient cultures also believed that jade was a healing stone, particularly for the kidneys (Tagore, 1881). Lapis lazuli is another gem that was chosen; the Sumerians believed that anyone who car-

Figure 15. The tranquil reflecting pools add to the symmetry of the Taj Mahal. Photo by Robert Weldon/GIA.

ried an amulet made of this material was in the company of a god (Budge, 2011). It was cherished throughout the ancient worlds of India, Mesopotamia, and Iran, as well as Egypt, where it was used in talismans, particularly of the eye and heart (Thomas and Pavitt, 1993).

Figure 16. A close-up of the parchin kari *consisting of multicolor chalcedony and other materials set in marble showing a typical floral pattern that decorates the interior and exterior of the Taj Mahal. Photo by Robert Weldon/GIA.*

In Mesopotamian culture, jasper was associated with the heavens (Horowitz, 1998), as well as driving away evil spirits (Kunz, 1938). Agate and jasper (both chalcedonies) were used as protection against the evil eye (Budge, 1968). Chalcedony was believed to render enemies terror-stricken while also having the power to promote peacefulness (Budge, 1968) and happiness (Tagore, 1881) and dispel sadness (Jones, 1968). Bloodstone was said to have the power to bring rain, a benefit to Shah Jahan's beautiful gardens (Kunz, 1938). It might have been for protection against enchantments and spells that sard was used in the parchin kari. Sard was also believed to bring happiness (Kunz, 1938). Other materials used that might have been chosen for purely aesthetic reasons include green plasma jasper, yellow limestone, variegated limestone, yellow marble, striped marble, and clay slate (Koch, 2006).

TABLE 1. Types of gem materials used in the Taj Mahal.

Farsi	English	Hindi	Early name(s) of the source(s)
Yaqut-e-Gulabi	Rose or pink sapphire	Gulabi	Ceylon
Hajr-ul-Dum	Bloodstone	Pitunia	India
Rukham	Alabaster	Sangmarmar	Makrana, India
Yaqoot	Amethyst	Kathela	Moldova, India
Nilgoo'n billor	Aquamarine	Beruj	Bihar, India and Ceylon
Marmar-e-Seeya	Black marble	Kala sangmarmar	Jhari
Aqiq-e-Jegari	Carnelian	Aqiq	Baghdad or Yemen
Sang-e-Yemani	Chalcedony	—	India
Zaituni Zabarjad	Chrysolite	Laksunia	Nile River
Sadaf Halazoni	Conch shell	Sankh	Persian Gulf and Gulf of Mannar
Marjan-e-Sorkh	Coral, red	Moonga	Indian Ocean
Boloor	Crystal quartz	Billoor	Hyderabad, India
Almas	Diamond	Hira	Golconda region
Zomorrod	Emerald	Panna	South America and Egypt
La'l	Garnet	Tamra	Ganges River
Sang-e-Tálai	Golden stone	Sunela	Unknown
Daarchini yaqoot	Hessonite garnet	Gomed	Ceylon
Yashm	Jasper	Margaj	Cambay, India
Lajvard	Lapis lazuli	Lajward	Afghanistan
Ahan Roba	Lodestone	Maqnatis	Gwalior, India
Malaqeet	Malachite	Dhana-i-farang	Russia
Marmar	Marble	Sangmarmar	Jaipur
Sadaf Morvaridi	Mother-of-pearl	Sip	Persian Gulf and Gulf of Mannar
Nafreit	Nephrite	Yashav	Chinese Turkestan
Aqiq Suleimani	Onyx	Suleimani	Deccan Plateau, India
Morvarid/Dor	Pearl	Mukta/Moti	Persian Gulf and Gulf of Mannar
Sang-e-Sorkh	Redstone	Surkh	Gwalior, India
Yaqut	Ruby	Manak	Pegu (Myanmar) and Badakhshan (Afghanistan)
Sang-e-Maaseh	Sandstone	Bansi	India
Yaqut-e-Kabud	Sapphire	Neelam	Pegu (Myanmar) and Ceylon
Aqiq-e-Qermez	Sard	Gomedak	India
Sang-e-Looh	Slate	Siliyat	Monghir and the ruins of Gaur
—	Sodalite	Sodaliti	Afghanistan
Laal	Spinel	Naram	Badakhshan, Afghanistan
Chasm-e-Babri	Tiger's-eye	Dariyai lahsunia	India
Zebarjad-e-Hendi	Topaz	Pukhraj	Ceylon
Firoozeh	Turquoise	Firoza	Persia and Tibet

Localities named in Voysey (1825). Descriptions also from Markel (2004). Additional information from Moin-Ud-Din (1905) and Dayalan (2006).
Farsi translations by A. Sinchawla and Hindi translations from B. Mookim (pers. comms., 2019).

Types of Gem Materials Used by the Artisans and Collected by the Emperors. Along with the large diamonds it produced, India was a source of rock crystal and agates recovered from the Deccan Traps. Related industries emerged, such as the shaping, processing, and inscribing of diamonds. Spinels were believed to have come from Badakhshan in present-day Afghanistan and Tajikistan, along the Mughal trade routes. Lapis lazuli was mined in Afghanistan. Turquoise originated from Persia, and Iran remains an important source of the gem to this day. Rubies, sapphire, and rock crystal quartz were shipped in from Ceylon (Sri Lanka) and Pegu. Pearls came from the Americas, the Persian Gulf, and from trade at Basra, a crossroads between the East and West. Nephrite was imported from China along with a variety of green opaque stones such as green jasper. Jadeite did not arrive from Burma until later in the nineteenth century. As Markel (2004) points out, nephrite was imported from Khotan and Kashgar in Chinese Turkestan in Central Asia. He also explains that jadeite was not yet used in South Asia and that there were dozens of nephrite jade simulants in use.

Voysey (1825) offered the first detailed description of the inlaid stones used in the parchin kari of the Taj Mahal. Over 40 different gem materials used for inlay have been referenced in the literature. Moin-Ud-Din, a general superintendent in Agra in 1905, expanded greatly on Voysey's list with his 120-page study of materials used at the Taj Mahal, which included an itemized table. More recent authors such as Dayalan (2006) have added to the list (see table 1).

A fascinating area of potential study would be to apply modern gemological techniques and advanced instrumentation to known examples of Mughal gemstones and jewelry. Trained gemologists would be able to contrast them with gems from modern sources. Comparative inclusion studies, advanced chemistry, and other techniques that aid in origin determinations would add greatly to our understanding of gems from this era.

Source of the Building Stones and Construction Materials. The Taj Mahal was built on a marble platform over a sandstone foundation. The buildings are brick overlaid with a veneer of marble that was brought in from the Makrana quarries in Rajasthan in western India, nearly 400 km from Agra. These quarries are famous for their milky white marble. Stretching more than 22 km, they were open-pit mines using traditional labor-intensive methods of excavation. The stones were cut into blocks and transported by oxcart to Agra. Voysey (1825) wrote that the red sandstone came from Fatehpur Sikri, 35 km west of Agra. Red sandstone was used to create the mosque and guest pavilion. Balasubramaniam (2009), in his study about the architects of the Taj Mahal, expands on Voysey's observations to include the nearby Rupbas and Tantpur quarries as sources.

Expertise of the Craftsmen. The craftsmen working with minerals and gem materials on the Taj Mahal fell into several groups. First there were the bricklayers and stonecutters, called *raj* and *sangtarash*, respectively. According to Ebba Koch, an architectural historian and author of a seminal work on the Taj Mahal, the stonecutters were paid for each linear yard of stone they cut. They left symbols and sometimes Hindu or Arabic names on the bricks. Next came the stone carvers or *munabbatkar*, who carved the moldings in the rooms and created the exquisite renderings of plants and flowers in sandstone and marble. At the time, Indian artisans were often guided by European experts. Balasubramaniam (2009) writes:

> While the supervision and superintendence may have been of people of foreign origin, the current study proves that the actual engineering of the complex was the accomplishment of the genius of local Indian talent… [This proves] that the ultimate realization of the wonderfully engineered construction of Taj was possible due to the engineering abilities and skill of native architects and artisans, as confirmed by their adherence to the traditional measurement units of the subcontinent.

Such traditions have continued to the present day. Koch (2006) illustrates one man, Hajii Nizamuddin Naqshbandi, who did stone restoration at the Taj Mahal for more than 40 years until his death in 2005. He was a follower of the Naqshbandi Sufis and continued the long tradition of Sufi craftsmanship in the building arts (figure 17).

Next came the craftsmen who did the stone inlay. This simple form of intarsia has been used for decorative objects and decor for centuries. It is based on inlaying colorful minerals into a recess to create a mosaic-like pattern. In India the term *parchin kari* is used both for the simple form of inlay as well as the intricate examples found throughout the Taj Mahal. A master artist known as the *parchinkar* would first draw the pattern in henna dye on the marble's surface. Then the artist would carve out a space in the marble and fill it with thin polished pieces of gem materials, affixing them with organic glue. The stones were grooved so they would fit together, making the contact between them almost invisible. The technique is still used to this day (figure 18).

Figure 17. Hajii Nizamuddin Naqshbandi, with other stone carvers, using hammer and point chisel. He worked at the Taj Mahal for more than 40 years and was still employed there when he died in 2005. Reproduced with permission of Ebba Koch, 2006.

In advanced inlays, slivers of different gem materials were artfully placed in the space with a view toward creating colors and shapes of the desired geometric patterns or floral designs. A bow saw coated with abrasives was used to fashion the slivers (figure 19). The technique was mastered by Shah Jahan's lapidaries, and one art historian notes that the "complexity, subtlety and elegance of their work far surpasses that of the Italian artists" (Koch, 2006). Most historians credit the Italians with creating this technique in Florence, where it was called *commesso di pietre dure* ("composition of hard stones") and often abbreviated to *pietra dura* (see box A). European artists brought the technique with them to

Figure 18. Modern inlay workers creating parchin kari objects for tourists in Agra near the Taj Mahal. Photos by Robert Weldon/GIA.

Box A: History of Pietra Dura

The Mughals were very interested in European art. European paintings and prints were the subject of exhibitions and many discussions (Koch, 2001). One style of stone inlay emerged in ancient Greece as early as the fifth century BCE (Dunbabin, 2006). This evolved into the use of small slices of opaque and semitransparent gems such as carnelian and other agates, lapis lazuli, and jasper that were cut and set into a base material such as marble to create the effect of a painting. Florence became a center for this style of art, and in 1588 the Grand Duke Ferdinand established the first state factory in the Uffizi Galleries, the Opificio delle Pietre Dure, which operated well into the nineteenth century. The facility is now a museum (Giusti, 2006).

Nature themes were often the focus of the pietra dura style. Flowers, landscapes, and birds and other animals were executed with such an exuberance of colors and style that they immediately became popular throughout Europe. Large vases, ewers, and bowls were later fashioned with pietra dura and set in elaborate mounts of gold and enamel. Even statuettes and life-size busts were made of inlaid marble, but these were very rare and reserved only for royalty.

Similar workshops were established throughout Europe. In Prague, Rudolf II employed the Miseroni family from Milan and the Castruccis from Florence to create new and elaborate forms of pietra dura for the palaces of the Habsburg rulers. In France, pietra dura was produced in Louis XIV's ateliers and incorporated in ornamented furniture. There was a reaction against this style during the Rococo period, which was marked by scrolling curved forms and gilded opulence. Many pieces were dismantled, only to enjoy a triumphant revival in furniture of the Louis XVI period. Workshops flourished in Germany, Italy, and Spain, where Carlos of Bourbon's artisans specialized in superb consoles and inlays of landscapes, figures, and trompe l'oeil. A seventeenth-century cabinet designed by Robert Adam and housed in the Victoria and Albert Museum is inset with pietra dura panels signed by Baccio Cappelli, one of the Uffizi workmen.

During the Victorian era, which spanned most of the nineteenth century, pietra dura was used for small pieces such as desk blotters, inkstands, postal scales, and lamp bases. These accessories are not as scarce or costly as the furniture from two centuries earlier, and as a consequence they can be unearthed at antique shows and shops.

India to work on the Taj Mahal. The Mughals had received gifts from Italy of decorative objects with inlay and had acquired an appreciation for the art.

History of the Families that Performed the Inlay. The pietra dura inlay technique was handed down from generation to generation, beginning with fam-

Figure 19. Slivers of carnelian, malachite, turquoise, and lapis lazuli are cut and assembled for inlay in modern parchin kari decorative pieces. Photos by Robert Weldon/GIA.

Figure 20. Minarets at the Taj Mahal frame its four corners. At sunset, sunlight peeks through the minarets, adding to their mystical enchantment. From this view, the superb inlay and craftsmanship of the mausoleum are visible. Photo by Robert Weldon/GIA.

ilies in Europe and then moving east into Russia. From there, the technique was passed from fathers to sons in northern Afghanistan. It was in Afghanistan that the art of calligraphy in stone began (Kazim, 2014).

The tradition of fine stone inlay, or parchin kari, developed independently in India and began to be incorporated into the monuments of the Mughal empire during the sixteenth century. Because of the close relationship between the development of pietra dura in Renaissance Italy and parchin kari at the Mughal court, the terms are often used interchangeably (L. Thoresen, pers. comm., 2019). Parchin kari is still used in India today on tables, plaques, tiles, and other decorative items (figure 20). Records indicate that the parchin kari craftsmen were mostly from Kannauj and were not Muslim but Hindus (Havell, 2003). A lesser-known literary work, *The History of the Taj and the Buildings in Its Vicinity* by Moin-Ud-Din (1905), lists the names of men who worked on various aspects of the Taj Mahal.

Symbolic Significance of the Designs. The floral pattern inlaid in the marble throughout the Taj Mahal is not random. Persian culture strongly influenced the Mughals. Floral imagery abounds in Persian poetry (Wescoat et al., 1996), which describes flowers as "springing forth from the waters of Paradise" (Janin, 2004), and this symbolism was no doubt the intention for Mumtaz's final resting place ("Taj Mahal," 2007). In the case of the Taj Mahal's floral motif, the choice of red and yellow as prevailing colors was most likely deliberate. Red blossoms represent death and blood in Persian poetry, while yellow denotes rebirth and dispels grief. Although some of the flowers of the Taj Mahal are creations sprung from the minds of the craftsmen, others are depictions of real flowers such as lilies (similar to martagon lilies), tulips, poppy blossoms, buds, and calyxes (Koch, 2006) (figure 21).

The red flowers are a symbol of sorrow, anguish, and death—poppies specifically are associated with the dead in Islamic thought (Koch, 2006). The Persian poet Hafiz claimed in the fourteenth century that

Figure 21. This large panel of carved marble with floral motifs at the Taj Mahal contains a border of parchin kari. Photo by Robert Weldon/GIA.

tulips are tokens of great love (Hafiz, 1905; Connolly, 2004). Poppies and red flowers similar to lilies embellish the upper cenotaphs of Mumtaz Mahal and Shah Jahan. Their graceful leaves and blooms rain down in sorrow, and the blood red stands in contrast against the stark white of the marble.

Both cenotaphs feature inscriptions of black onyx inlay. The Arabic inscription that runs around the sides and along the top of Mumtaz Mahal's cenotaph are verses from the Koran, meant to put her soul at ease. The cenotaph of Shah Jahan features an ornate epitaph in Nastaʿlīq calligraphy (containing a pronounced rounded script) that reads:

> This is the sacred grave of His Most Exalted Majesty, Dweller in Paradise, Second Lord of the Auspicious Conjunction, Shah Jahan, Padshah; may it ever be fragrant! The year 1076 [AD 1666] (Koch, 2006).

While the cenotaphs on the main level are meant for public view, and are aligned to the north, the actual tombs of Shah Jahan and Mumtaz lie in a chamber just below, facing west, toward Mecca. In keeping with Islamic tradition, these actual tombs are much simpler in design.

Islamic Inscriptions. Words from the Koran are similarly inlaid throughout the complex using black onyx. The inscription process itself was ambitious, as more than two dozen Koranic quotations are displayed on the Great Gate, mausoleum, and mosque. In a sense, this work is even more intricate because the onyx had to be carved to fit the script of the letters. The passage from the Koran on the Great Gate calls the charitable and the faithful to enter Paradise (figure 22). The artist responsible for these inscriptions, Abd al-Haqq Shirazi, is the only artist whose

Figure 22. The eastern facade of the Taj Mahal is framed by parchin kari and an inscription from the Koran. Photo by Robert Weldon/GIA.

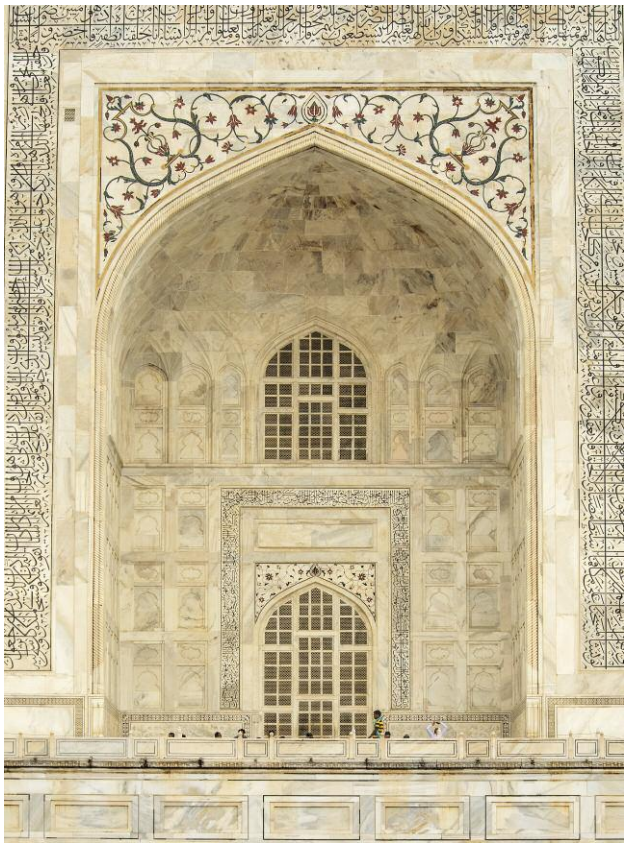

name was allowed on the Taj Mahal for posterity. This further demonstrated Shah Jahan's high regard for the inscriptions and the artist. As Al-Haqq Shirazi had designed the inscriptions for the tomb of Akbar, Shah Jahan's grandfather, he was the logical choice (Begley, 1978/1979). One of the three dated epigraphs inscribed at the Taj Mahal reads "Finished with His help" and was written by Amanat Khan al-Sjorazo in the year corresponding to the twelfth year of Shah Jahan's reign, somewhere between October 1638 and April 1639. The larger words are in Arabic and the smaller ones in Persian (Begley, 1978/1979).

The Taj Mahal Today and Its Conservation. On April 11, 2018, severe storm winds caused two minarets at the Taj Mahal to collapse. Fortunately, the taller ones remained standing. While one of the destroyed minarets was located at the southern gate, the other was at the royal gate, where one gets a first glimpse of the Taj Mahal. This world wonder also faces deterioration from exposure to air pollution and wear from its eight million visitors every year. The result is a general yellowing of the buildings. As the custodians of this monument, the Archaeological Survey of India reported in January 2018 that the Taj Mahal was in danger of losing its attractive marble gloss due to air pollution in Agra ("India Taj Mahal minarets damaged…," 2018).

For a time up until the restoration by British Viceroy Lord Curzon was completed in 1908, security was not stringent, so some of the stones in the pietra dura as well as other decor were stolen ("Theft in Taj Mahal myth," n.d.). The Archaeological Survey of India stated that it would take until 2018 to clean the buildings, replace the missing stones, and take protective measures to minimize further damage by visitors (Devi, 2015). Most of the work has been accomplished, though some questions remain as to the safest method of cleaning the Taj Mahal's main dome, which was scheduled for late 2019.

To remove the yellow stains, a clay pack known as *multani mitti* (or fuller's earth), known since the late 1800s, was applied for decades with positive results on the building exteriors. This facial treatment consisting of lime, cereal, soil, and milk was slathered onto the buildings, left to sit for 24 hours, and then washed with warm water ("Multani mitti is being used…," 2002) (figure 23).

Governmental protection began in 1996, when the Supreme Court of India enacted the Taj Trapezium Zone, a 10,400 square km area surrounding the Taj Mahal complex. This trapezoid-shaped zone, meant to protect the Taj from environmental pollution damage, bans the burning of coal within the area. It also requires some industries to switch to natural gas or even relocate outside of the zone ("Why is the Taj…," 2008). Another measure to control pollution has been to ban the burning of cow dung, used for kindling in wood fires, within Agra ("Fuel guzzling vehicles…," 2015). Fuel-powered vehicles are banned within 500 meters of the Taj Mahal (Lusted, 2013). Visitors arrive by foot or electric shuttle. Upon arrival, they can either go barefoot or wear covers over their shoes. Most recently, it was reported that the Archaeological Survey of India was considering the use of spectrography to measure incremental differences in the Taj Mahal's exterior color. The first step was cleaning the surface of the marble using

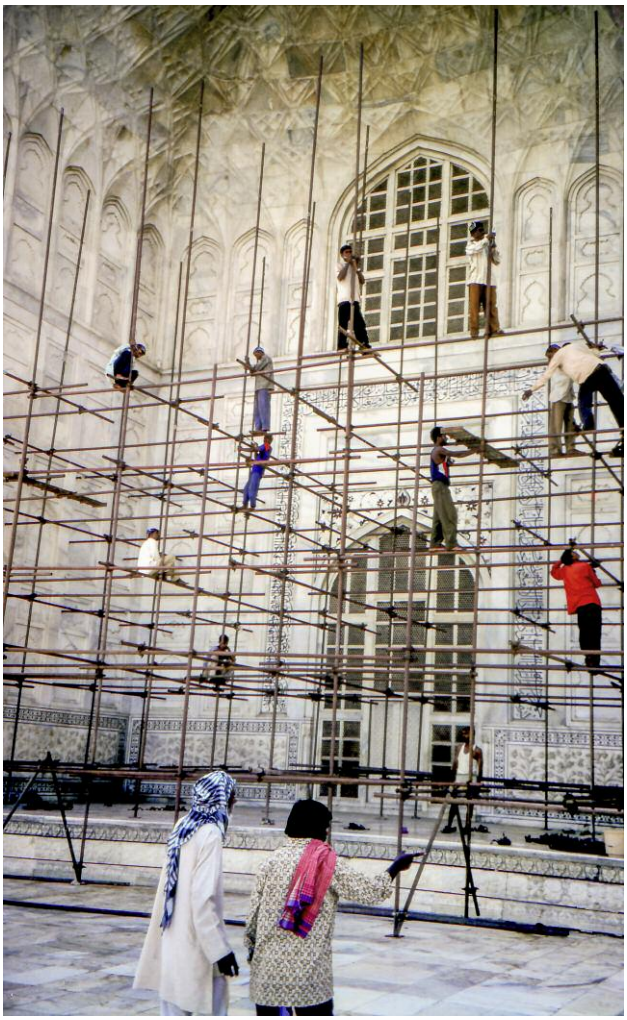

Figure 23. Scaffolding was erected for chemical cleaning of the northern pishtaq of the mausoleum in September 2002. Reproduced with permission of Ebba Koch, 2006.

multani mitti, as discussed earlier. From now on, the changes will be recorded over time and reported to the Supreme Court of India (Qureshi, 2019).

Some of the restoration planning and execution is culturally fraught. But despite cultural differences and debate over financial allocations, the Supreme Court instructed the Indian government to take immediate action: "Even if you have the expertise, you are not utilizing it. Or perhaps you don't care. We need to save it," the court urged (Meixler, 2018).

CONCLUSIONS

The Taj Mahal is a monument to an everlasting love. The indefatigable Mughal emperor Shah Jahan had it built 366 years ago for his wife Mumtaz's final resting place. Much like his father, Jahangir, Shah Jahan was one of the most prolific gem collectors and connoisseurs of his day (figure 24). The sources of the 40 or more gem materials (Dayalan, 2006) that are incorporated into the Taj Mahal's facade tell a compelling story of global trade and commerce. This culturally rich era brought about an exchange of gems and knowledge, fostering craftsmanship and cultural adaptations from Europe and Asia. Raw materials were also the catalysts for attracting the world's most talented lapidaries, architects, stonemasons, and workers, who made possible an unsurpassed creation.

India itself has been a major source of gems since antiquity, including its fabled diamonds from the Golconda region and agates from the Deccan Traps.

Figure 24. The finest parchin kari work was reserved for Mumtaz's cenotaph, in the interior of the mausoleum. Photo by Jean-Louis Nou, courtesy of AKG Images.

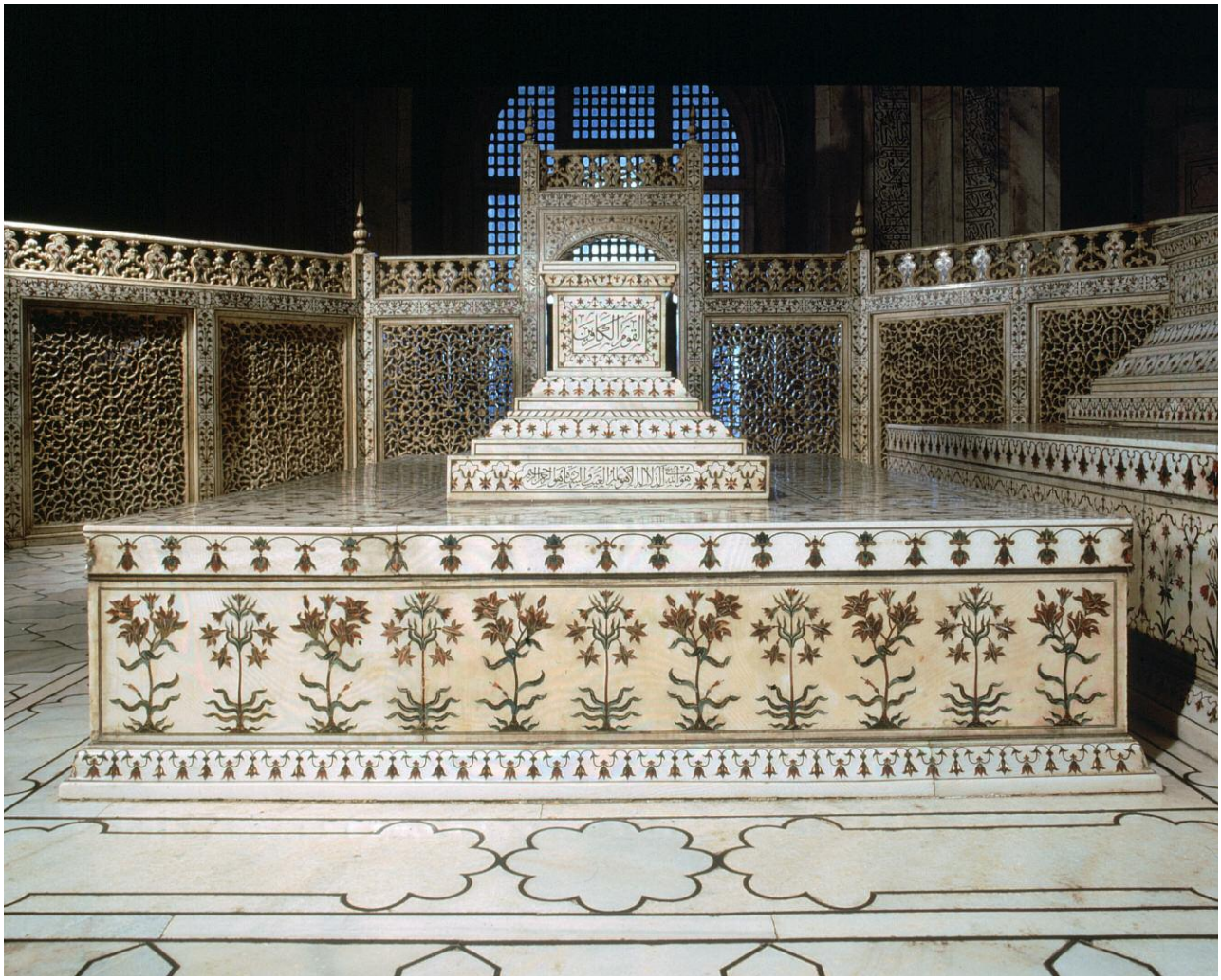

Figure 25. The Taj Mahal is visible in the distance from Agra Fort, where Shah Jahan was imprisoned by his son Aurangzeb in 1658. He would have had a futile daily view of the Taj Mahal at sunrise, positioned on the bank of the glimmering Yamuna River. Photo by Robert Weldon/GIA.

Although much of the Mughals' exquisite jewelry has been melted down to make new ornaments (Sharma and Varadarajan, 2004), we can still enjoy the beauty of the era through the artistry of the Taj Mahal, which has stood the test of time. As millions continue to visit each year, conservation will be essential to preserve its beauty for generations to follow (figure 25).

ABOUT THE AUTHORS

Ms. Dirlam is librarian emeritus, Ms. Rogers is a research librarian, and Mr. Weldon is director, of GIA's Richard T. Liddicoat Gemological Library and Information Center in Carlsbad, California.

ACKNOWLEDGMENTS

The authors would like to thank the following for their assistance: Tarun Adlakha, Faizah Bhatti, Si and Ann Frazier, Dr. Ebba Koch, Tsajon von Lixfeld, Lisbet Thoresen, Bhupendra Mookim, Ashoo Sinchawla, and the staff of the Richard T. Liddicoat Gemological Library and Information Center.

REFERENCES

Bala Krishnan U.R., Sushil Kumar M. (2001) *Indian Jewellery: Dance of the Peacock*. India Book House Ltd., Mumbai, pp. 20–53, 110–135.

Balasubramaniam R. (2009) New insights on artisans of Taj. *Indian Journal of History of Science*, Vol. 44, No. 4, pp. 521–550.

Ball S.H. (1931) Historical notes on gem mining. *Economic Geology*, Vol. 26, No. 7, pp. 681–738.

Ball V. (1977a) *Travels in India by Jean-Baptiste Tavernier*, Vol. 1, 2nd ed. Oriental Books Reprint Corporation, New Delhi, 335 pp.

Ball V. (1977b) *Travels in India by Jean-Baptiste Tavernier*, Vol. 2, 2nd ed. Oriental Books Reprint Corporation, New Delhi, 399 pp.
Begley W. (1978/1979) Amanat Khan and the calligraphy on the Taj Mahal. *Kunst des Orients*, Vol. 12, No. 1/2, pp. 5–60. http://www.jstor.org/stable/20752477
Begley W. (1979) The myth of the Taj Mahal and a new theory of its symbolic meaning. *The Art Bulletin*, Vol. 61, No. 1, pp. 7–37. http://www.collegeart.org/pdf/artbulletin/Art%20Bulletin%20Vol%2061%20No%201%20Begley.pdf
Brill E. (1993) *E.J. Brill's First Encyclopaedia of Islam, 1913–1936*. Brill Academic Publishing, Boston, pp. 886–887.
Budge E.A.W. (1968) *Amulets and Talismans*. University Books, New Hyde Park, p. 311.
Budge E.A.W. (2011) *Amulets and Superstitions*. Dover Publications, New York, p. 317.
Connolly S. (2004) *The Secret Language of Flowers*. Rizzoli International Publications, New York, p. 86.
Dayalan D. (2006) *Use of Remote Sensing and GIS in the Management and Conservation of Heritage Properties at Agra*. Archaeological Survey of India, New Delhi.
Delmerick J.G. (1883) On a silver coin of Dáwar Bakhsh. *In Proceedings of the Asiatic Society of Bengal: 1883-34*. Asiatic Society, Calcutta, p. 60.
Devi A. (2015) ASI backtracks, says Taj restoration will take only 3 yrs. *The Times of India*, Sept. 30, http://timesofindia.indiatimes.com/city/agra/ASI-backtracks-says-Taj-restoration-will-take-only-3-yrs/articleshow/49180538.cms
Dunbabin K. (2006) *Mosaics of the Greek and Roman World*. Cambridge University Press, Cambridge, p. 5.
Frankopan P. (2017) *The Silk Roads*. Penguin Random House, New York, p. 231.
Fuel guzzling vehicles to go off Taj Trapezium Zone (2015) *The Hindu*, Jan. 31, http://www.thehindu.com/todays-paper/tp-in-school/fuel-guzzling-vehicles-to-go-off-taj-trapezium-zone/article6840248.ece
Giusti A. (2006) *Pietre Dure: The Art of Semiprecious Stonework*. Getty Publications, Los Angeles, p. 47
Hafiz (1905) *Odes from the Divan of Hafiz*. Duckworth, London. p. 169.
Haidar N., Stewart C.A. (2014) *Treasures from India: Jewels from the Al-Thani Collection*. Yale University Press, New York, p. 23.
Havell E. (2003) *Handbook to Agra and the Taj – Sikandra, Fatehpur – Sikri*. Asian Education Services, New Delhi, p. 141.
Horowitz W. (1998) *Mesopotamian Cosmic Geography*. Eisenbrauns, Warsaw, p. 14.
India Taj Mahal minarets damaged in storm (2018) *BBC News*, April 12, http://www.bbc.com/news/world-asia-india-43735757
Jaffer A., Ed. (2013) *Beyond Extravagance: A Royal Collection of Gems and Jewels*. Assouline Publishing, New York. p. 26–56.
Janin H. (2004) *The Pursuit of Learning in the Islamic World, 610-2003*. McFarland & Company, Jefferson, North Carolina, p. 125.
Jones W. (1968) *History and Mystery of Precious Stones*. Singing Tree Press, Detroit, p. 31.
Kazim S. (2014) Pietra dura—an art form passed down through centuries. *Dawn*, Apr. 30. http://www.dawn.com/news/1103225
Koch E. (2001) *Mughal Art and Imperial Ideology*. Oxford University Press, New Delhi, p. 63.
Koch E. (2006) *The Complete Taj Mahal*. Thames & Hudson, Ltd., London.
Kunz G.F. (1938) *The Curious Lore of Precious Stones*. Halcyon House, New York.
Lane K. (2010) *Colour of Paradise: The Emerald in the Age of Gunpowder Empires*. Yale University Press, New Haven, Connecticut, 280 pp.
Latif M. (1982) *Mughal Jewels*. F. Poot, Brussels, p. 21.
Lusted M.A. (2013) Taj Mahal: how long will it last? *Faces*, Vol. 30, No. 3, p. 24.
Markel S. (2004) Non-imperial Mughal sources for jades and jade simulants in South Asia. In *Jewelled Arts of Mughal India: Papers of the Conference Held Jointly by the British Museum and the Society of Jewellery Historians at The British Museum, London in 2001*. Society of Jewellery Historians, London, pp. 68–75.
Meixler E. (2018) The Taj Mahal is changing color. That has India's highest court concerned. https://time.com/5262395/taj-mahal-india-change-color-supreme-court/
Melikian-Chirvani A. (2004) The jewelled objects of Hindustan. *Jewellery Studies*, Vol. 10, pp. 9–32.
Moin-Ud-Din M. (1905) *The History of the Taj and the Buildings in Its Vicinity*. Moon Press, Agra, p. 27.
Mubarak A. (1894) *The Ain I Akbari*. The Asiatic Society of Bengal, Calcutta, p. 315.
Multani mitti is being used to beautify Taj Mahal: Report (2002) *The Times of India*, December 8, http://timesofindia.indiatimes.com/topic/Multani-Mitti-Is-Being-Used-To-Beautify-Taj-Mahal:-Report
Nath R. (1985) *The Taj Mahal & Its Incarnation: Original Persian Data on Its Builders, Material, Costs, Measurements, etc*. The Historical Research Documentation Programme, Jaipur, p. 13.
Qureshi S. (2019) ASI looking for scientific methods to protect Taj Mahal from pollution. *India Today*, March 11, https://www.indiatoday.in/india/story/asi-looking-for-scientific-methods-to-protect-taj-mahal-from-pollution-1474984-2019-03-11
Sarkar J. (1920) *Studies in Mughal India*. Longmans, London.
Sharma R.D., Varadarajan M. (2004) *Handcrafted Indian Enamel Jewellery*. Roli Books, New Delhi, 144 pp.
Tagore S. (1881) *Mani-Málá, or a Treatise on Gems*. I.C. Bose & Company, Calcutta.
The Taj Mahal (n.d.) http://thetajmahal.co.in/art-and-architecture/engineering-team-taj-and-costs/
Taj Mahal (2007) *Lost Worlds*. The History Channel, aired November 28.
Tavernier J.-B. (1678) *The Six Voyages of John Baptista Tavernier, a Noble Man of France Now Living, Through Turky* [sic] *into Persia and the East-Indies, Finished in the Year 1670*. Printed for R.L. and M.P., London, p. 58–83.
Theft in Taj Mahal myth (n.d.) Retrieved from https://www.tajmahal.org.uk/legends/theft-in-taj.html
Thomas W., Pavitt K. (1993) *The Book of Talismans: Amulets and Zodiacal Gems*. Bracken Books, London, p. 222.
Thoresen L. (2017) Archaeogemmology and ancient literary sources on gems and their origins. In A. Hilgner et al., Eds., *Gemstones in the First Millennium AD: Mines, Trade, Workshops and Symbolism: International Conference*, October 20–22, 2015. Verlag des Römisch-Germanischen Zentralmuseums, Mainz, Germany, pp. 155–217.
Vassallo e Silva N., Flores J., Eds. (2004) *Goa and the Great Mughal*. Scala Publishers Ltd, London, pp. 240
Voysey H. (1825) On the building stones and mosaic of Akberabad or Agra. *Asiatic Researches, or Transactions of the Society*, Vol. 15. Asiatic Society, Calcutta, pp. 429–435.
Weldon R., Ortiz J.G., Ottaway T. (2016) In Rainier's footsteps: Journey to the Chivor emerald mine. *G&G*, Vol. 52, No. 2, pp. 168–187, http://dx.doi.org/10.5741/GEMS.52.2.168
Wescoat J., Wolschke-Bulmahn J., Oaks D. (1996) *Mughal Gardens: Sources, Places, Representations, and Prospects*. Dumbarton Oaks Research Library and Collection, Washington D.C., p. 233.
Why is the Taj Trapezium Zone and why is it called so? (2008) *The Times of India*, May 4, http://timesofindia.indiatimes.com/home/sunday-times/Why-is-the-Taj-Trapezium-Zone-and-why-is-it-called-so/articleshow/3008537.cms

Natural-Color Fancy White and Fancy Black Diamonds: Where Color and Clarity Converge

Sally Eaton-Magaña, Troy Ardon, Christopher M. Breeding, and James E. Shigley

Natural Fancy white and Fancy black diamonds are not routinely submitted to GIA for grading (fewer than 2,000 since 2008). These fancy-color diamonds are distinctive since the causes of color generally are not atomic-scale defects, but nanometer- to micrometer-sized inclusions that reduce the diamond's transparency by scattering or absorbing light (some exceptions exist among Fancy black diamonds). To clarify, Fancy white diamonds are those rare stones colored by inclusions that give a "whitish" appearance, and are distinct from "colorless" diamonds on the D-to-Z scale.

These two colors, often thought of as opposites in the color world, are grouped here as outliers within the colored diamond world. Both can be colored by inclusions so numerous the stone would fall below the I_3 grade on the clarity scale, demonstrating that inclusions, often perceived as a negative quality factor, can create a distinctive appearance. Among the Fancy white diamonds examined for this study, the vast majority (82%) were type IaB, making them a rare subset of a rare diamond type. Based on prior geological research, these are surmised to be mostly sublithospheric in origin (i.e., forming more than 250 km below the earth's surface). The Fancy white diamonds generally have a different chemistry from D-to-Z type IaB diamonds, with greater quantities of several hydrogen- and nickel-related defects. Among Fancy black diamonds, the major causes of color are either micrometer-sized dark crystal inclusions, nanometer-sized inclusions clustered into clouds, or a combination of the two. For these two colors of diamond, we summarize their gemological properties along with the absorption and luminescence spectra of a representative subset of diamonds from each color, examining how they deviate from the standard grading methodology. Because of their rarity, there has been very little systematic study of either of these color categories, and never a sample set of this quantity, which includes data for ~500 Fancy white and ~1,200 Fancy black diamonds.

When discussing the cause of color in diamond, we typically discuss atomic-level defects rather than inclusions—relying more on our spectrometers than our microscopes. Seldom are the diamonds distinguished not by color saturation, but by tone (neutral lightness and darkness) and transparency. Nevertheless, Fancy white and Fancy black diamonds break these rules and exist within their own special category, distinct from the other fancy-color diamonds described previously in our article series (Breeding et al., 2018; Eaton-Magaña et al., 2018a, 2018b).

Fancy white diamonds, due to their scarcity as faceted stones, comparatively small size, and the lack of notable historical examples, are not well known. They are largely procured by connoisseurs. Probably the most famous of Fancy black diamonds is the Black Orlov (figure 1), a 67.50 ct cushion with a provenance dating back two centuries and, like the Hope diamond, rumored to be "cursed" (Balfour, 2009).

Other famous Fancy black diamonds include the 312.24 ct Mogul-cut Spirit of de Grisogono, one of the world's largest black diamonds, which originated from the Central African Republic. The Gruosi diamond is a 115.34 ct heart shape reportedly discovered in India, and the Korloff Noir is an 88 ct round brilliant.

See end of article for About the Authors and Acknowledgments.
Gems & Gemology, Vol. 55, No. 3, pp. 320–337,
http://dx.doi.org/10.5741/GEMS.55.3.320

Figure 1. The famous Black Orlov, a 67.50 ct Fancy black diamond, is flanked by two Fancy white diamonds (2.26 ct and 30.87 ct). Photos are not to scale. The Fancy white diamond photos are by GIA staff (left) and Jessica Arditi (right).

The appearance of Fancy black and Fancy white diamonds varies more because of differences in transparency than because of variations in saturations or modifying hues (figure 2). They can range from

Figure 2. These examples of Fancy white and Fancy black diamonds do not show major variations in hue or color saturation, but they do vary by transparency. Photos by GIA staff.

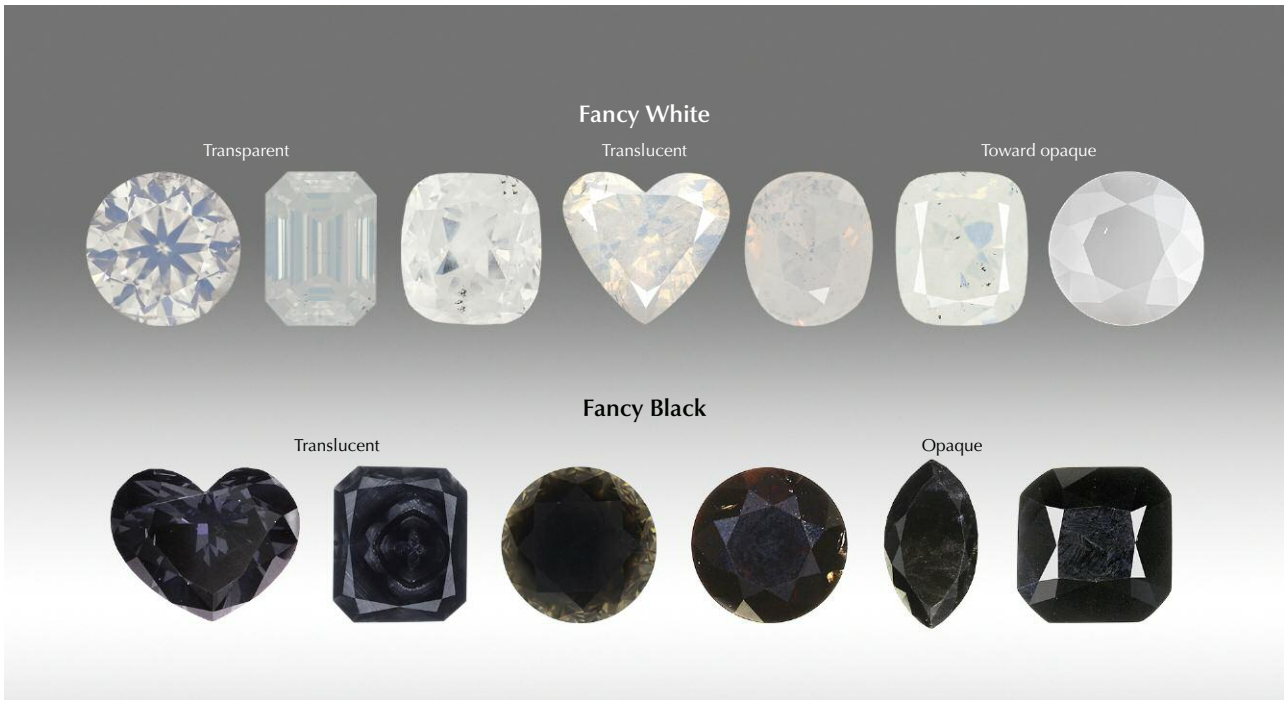

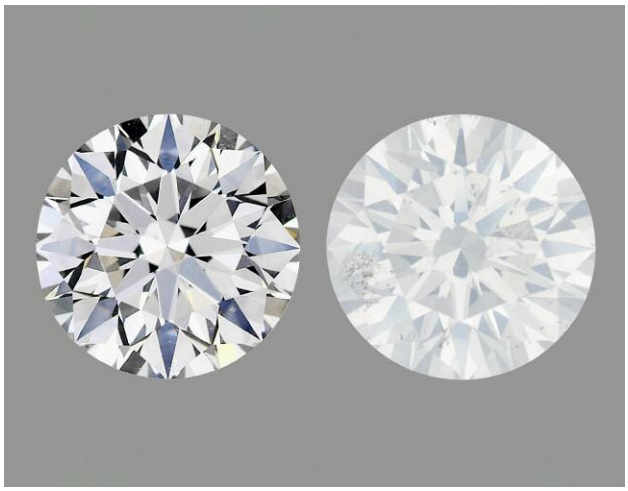

Figure 3. A colorless D-color diamond (left) is often described as "white" in the trade and by consumers. However, such terminology should not be confused with Fancy white diamonds. The E-color diamond with I_2 clarity and whitish internal graining on the right is one of the color master stones in GIA's Carlsbad lab. It represents the boundary between the D-to-Z color scale and those deemed Fancy white. Photos by Robison McMurtry.

transparent to translucent to opaque, but they generally are not transparent. Other natural forms of carbon such as bort, ballas, and carbonado are not submitted to GIA in large quantities and will only be discussed briefly. Additionally, Fancy white diamonds should not be confused with colorless diamonds (those generally graded as D to F), which are often termed "white" within the trade and by consumers (figure 3).

CAUSES OF COLOR

Fancy White. Fancy white diamonds are sometimes referred to as having an "opalescent" appearance due to the unusual way that light is scattered inside the stone. Gemologists, however, often describe them as "hazy," "milky," or "cloudy" when observing them through a microscope (figure 4). Recent studies on both hazy and cloudy diamonds show that these observations (e.g., Rudloff-Grund et al., 2016; Kagi et al., 2016; Gu et al., 2019) are due to two distinct phenomena: nano-inclusions and dislocation loops, both described below. These studies have shed light on the nature of these features, which can appear nondescript even at high magnifications with an optical microscope. These features are best imaged and identified using more advanced forms of microscopy such as transmission electron microscopy (Rudloff-Grund et al., 2016; Gu et al., 2019). In TEM, a beam of electrons is transmitted through the sample to form an image. This tool is capable of much higher resolution than an optical microscope. It is also a destructive test method that requires "foils" made of extremely thin films, generally less than 100 nm, of the diamond (more information on this technique may be found in Titkov et al., 2003).

Rudloff-Grund et al. (2016) showed by TEM the presence of both nano-inclusions and dislocation loops in these milky white diamonds. The nano-inclusions were observed in two distinct size ranges—the majority were 20–30 nm, and some were 150–200 nm. In comparison, inclusions that are large enough to be classified as crystals are generally larger than ~50 µm (500 times larger). The nano-inclusions appeared as octahedrons or elongated trapezoids, and were found to contain nitrogen; other researchers have confirmed the presence of nitrogen, but there is still no consensus on the exact configuration of the nitrogen (Kagi et al., 2016; Rudloff-Grund et al., 2016; Navon et al., 2017; Gu et al., 2019). Rudloff-Grund et al. also found that areas of the diamond with these nano-inclusions correlated with detection of higher nitrogen and hydrogen by IR absorption mapping. Other researchers (Kagi et al., 2016) additionally found several transition metals (such as Ni) within these nano-inclusions.

Gu et al. (2019) continued this study by creating TEM foils with diamond that they deemed as only "hazy" or only "cloudy" based on their microscopic differences. They wished to see if distinguishing phenomena could be observed between the "hazy" and "cloudy" descriptions. They found that "hazy" diamonds did not show distinct pinpoints by optical microscopy even when viewed at high magnifications. In contrast, diamonds termed "cloudy" did display distinct pinpoints at high magnifications.

In Brief

- Fancy white diamonds are predominantly type IaB, and their "milky" color originates from nano-inclusions and structural imperfections.
- Fancy black diamonds have a variety of causes of color but are due largely to inclusions (either appearing as clouds of dark nano-inclusions, micron-sized crystal inclusions, or a combination of both).
- As cause of color is generally due to inclusions, these diamonds pose distinct grading challenges.

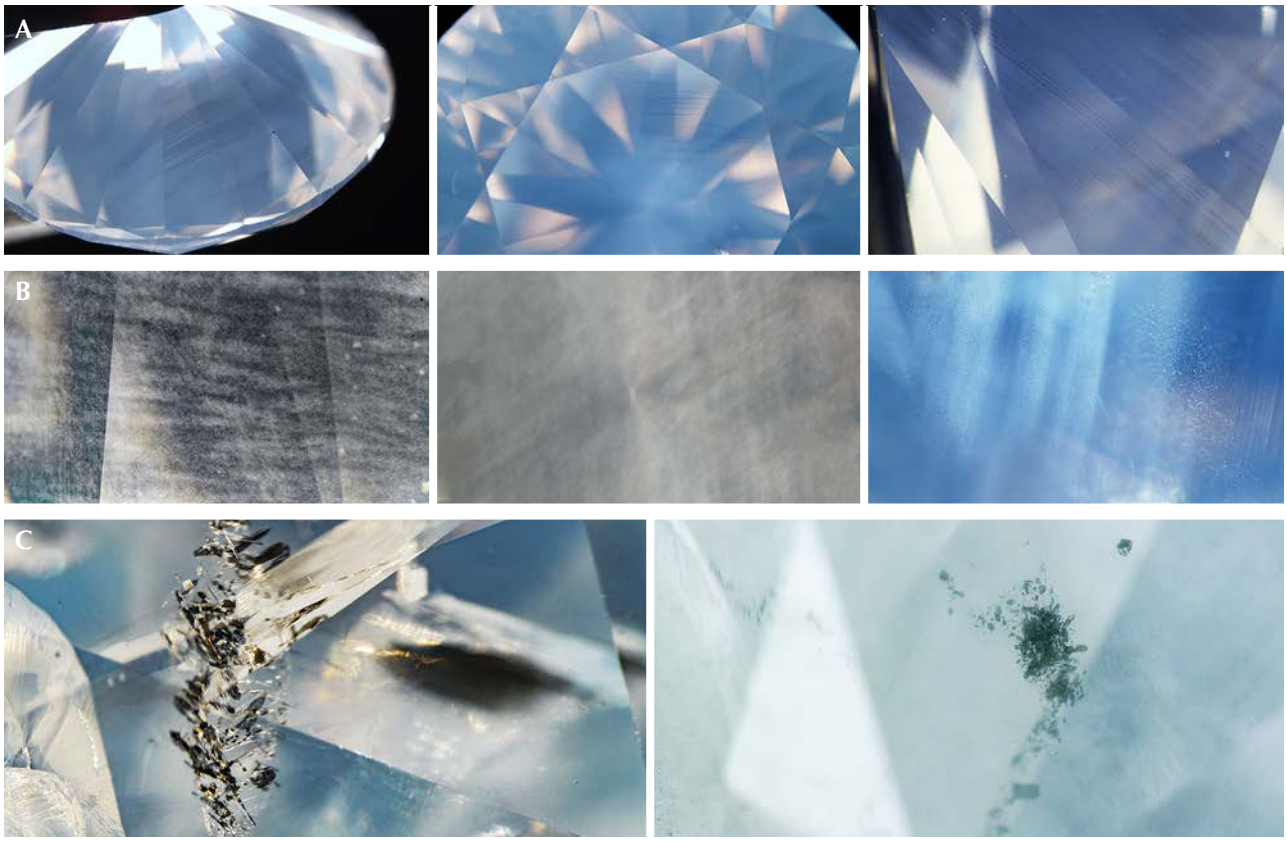

Figure 4. This photomicrograph array shows the variety of observations possible in Fancy white diamonds. The responsible defects can be seen as linear bands (A), crisscrossing bands, or isolated pinpoints (B), and these can be described as "hazy" or "cloudy." Due to the nature of these nano-inclusions, the features can be difficult to photograph. Often present in Fancy white diamonds (e.g., figures 1 and 2) are dark, obvious inclusions (C), generally due to graphitized inclusions or graphitized stress fractures (Jang-Green, 2006). Fields of view: A1: 8.9 mm; A2: 8.0 mm; A3: 2.9 mm; B1: 2.9 mm; B2: 3.6 mm; B3: 1.9 mm; C1: 2.3 mm; C2: 2.5 mm.

TEM showed more differences. In "hazy" diamonds, the TEM results indicated only the presence of dislocation loops. Dislocation loops are created from a disarrangement of the atoms that are disruptions in the crystal lattice (Stukowski et al., 2012). These lattice defects form into a dislocation loop of distorted atoms since the loop exists at a more favorable lower-energy state than the isolated lattice defects themselves. This doughnut-shaped feature of disordered atoms exists within the normal crystal structure. Dislocation loops in diamonds have been experimentally shown to form from platelet defects in type IaB diamonds when heated to very high temperatures (2400–2700°C; Evans et al., 1995). Platelets are extended defects thought to form when A aggregates transition into B aggregates; they involve carbon interstitials (i.e., clusters of carbon atoms not in normal positions in the lattice) and nitrogen in thin layers (Humble, 1982; Speich et al., 2017). In these diamonds, dislocation loops are impossible to discern directly with an optical microscope, unlike a foreign inclusion with distinct boundaries; however, the effects of these dislocation loops appear to scatter light.

In contrast with the observations of "hazy" diamonds, in the diamonds that appeared "cloudy" instead, Gu et al. (2019) detected nano-inclusions (described as negative crystals) containing solid nitrogen. As with prior researchers, they confirmed the size ranges of these features as ~20 to 200 nm.

Fancy Black. There are several different causes of color for natural black diamonds: internal inclusions (such as graphite, non-carbon crystal inclusions, and

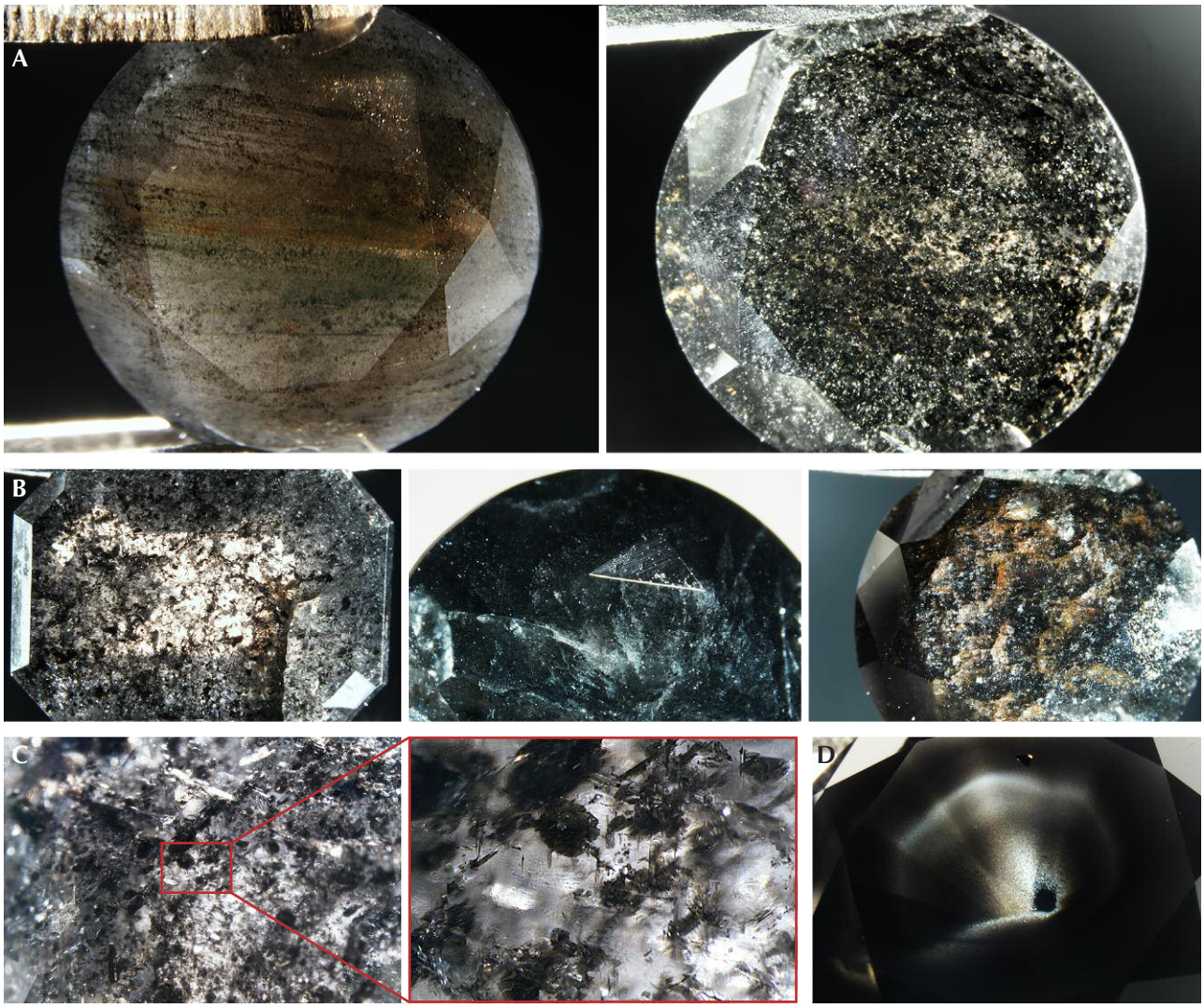

Figure 5. This photomicrograph array shows the variety of observations possible in Fancy black diamonds. Fancy black diamonds are generally very heavily included. Based on the size of the inclusions, they are termed crystals or clouds of pinpoints. All photomicrographs were collected in transmitted light by GIA staff. A: Diamonds can show irregular or linear banding of inclusions. B: Diamonds with masses of dark inclusions; the one on the right also shows iron oxide staining. C: The graphitic inclusions in a Fancy black diamond and a higher-resolution photomicrograph of one area. Image widths of 4.8 and 1.26 mm, respectively. D: Diamond with cloud inclusions. Field of view: A1: 6.7 mm; A2: 9.5 mm; B1: 7.8 mm; B2: 7.5 mm; B3: 8.7 mm; C1: 4.8 mm; C2: 1.3 mm; D: 6.9 mm.

clouds; figure 5), high-density radiation stains along surfaces or fractures (usually contributing to a darker appearance), and in rare cases very high absorption across much of the visible spectrum that results from atomic or extended lattice defects.

Crystals. Kammerling et al. (1990) described a set of black diamond jewelry and used microscopic observation to identify the inclusions as graphite. Titkov et al. (2003) later studied a suite of black diamonds they had sourced from Siberia in Russia (principally from the Mir kimberlite pipe). In their samples from that locality, graphite inclusions were rare and instead the inclusions they found were mostly magnetite (Fe_3O_4), hematite (Fe_2O_3), and native iron. These inclusions were determined by individually studying their chemical compositions using energy-dispersive X-ray spectroscopy (EDX). More recently, Smit et al. (2018)

studied an extensive suite of faceted black diamonds sourced from the Marange alluvial deposits in Zimbabwe, and many of these showed graphite inclusions that generally appeared as needles.

Clouds. Here, clouds are distinguished from the inclusions described above by their size. Clouds are generally described as a cluster of tiny pinpoint inclusions. They can vary in density (and therefore transparency), and some examples show a distinct outline while others are spread through the diamond. At 10× magnification, the morphology of individual pinpoints that make up a "cloud" cannot be distinguished. The Marange black diamond suite (Smit et al., 2018) also showed a few examples (4 of 40) in which dark clouds previously identified as graphite (Smit et al., 2016; Eaton-Magaña et al., 2017) were the source of the Fancy black coloration. These clouds are often associated with high quantities of hydrogen in IR spectra (Johnson, 2008).

Radiation Stains. Radiation stains on diamond surfaces, created from physical contact with a radiation source (typically a radioactive mineral grain or fluid; Breeding et al., 2018) can appear as either green or brown depending on subsequent temperature exposure, as green radiation stains generally become brown at temperatures of ~550°C (Nasdala et al., 2013). Although not always found in black diamonds, and generally observed in conjunction with inclusions and clouds described previously, abundant brown radiation stains in highly fractured diamonds are occasionally seen (particularly from Marange). When enough stain-filled fractures are present in a stone, it has a very dark overall appearance. However, shining a bright light from behind the diamond (i.e., transmitted light) reveals the green or brown appearance due to the radiation stains.

Absorption Defects. Although this cause of color is more common among treated diamonds (described below), pronounced absorption across much of the visible spectrum due to high concentration of atomic or extended defects can lead to a Fancy black color. When the stone is viewed through the pavilion, depending on the defect, it can often appear violet (Breeding and Rockwell, 2009; Johnson, 2011) or green, though the face-up color is Fancy black. If the absorbing defect had a lower concentration or the stone had a smaller size, the diamond may have received the corresponding color description instead of Fancy black.

Polycrystalline Diamond. Carbonado is a naturally occurring polycrystalline diamond material composed of randomly oriented cuboidal microcrystals (about ~5–20 µm in size; Haggerty, 2017). The cumulative effect of these microcrystals along with the incorporation of non-diamond carbon material is that the carbonado appears opaque and generally black, gray, or brown. Carbonados have occasionally been faceted as gems (De Corte et al., 2004; Wang et al., 2009), but their polycrystalline structure and variation in polishing directions makes it difficult to achieve a flat, reflective polished facet surface.

OCCURRENCE AND FORMATION

Fancy White. Fancy white diamonds are predominantly type IaB (i.e., showing only B-form nitrogen aggregates in their IR spectra; see Breeding and Shigley, 2009 for more on diamond types). The B aggregate has been identified as four nitrogen atoms surrounding a vacancy (Boyd et al., 1995), and it is generally considered the end product of the nitrogen aggregation process; geologically young diamonds show nitrogen as single isolated atoms that coalesce over geologic time into pairs (A aggregates). This pairing of nitrogen atoms (and the subsequent steps of aggregation) involves internal diffusion at relatively high temperature and/or long geologic residence times during which the nitrogen atoms can move through the lattice. During the next stage of aggregation, the A centers form B aggregates, and there is a minor side reaction (Woods, 1986) that produces N3 centers (three nitrogen atoms with a vacancy). Generally, if all A aggregates have converted to B aggregates in a diamond to form a type IaB diamond, we can conclude that it is geologically quite old or was subjected to higher than normal temperatures that encouraged aggregation, or we can assume a combination of both time and temperature. Since the vast majority of Fancy white diamonds are type IaB, this review of nitrogen aggregation is a good starting point to recount what is known about the elusive cause of color in these diamonds.

Several researchers have studied "milky" diamonds and concluded, based on mineral inclusions, that these type IaB diamonds have an origin from the transition zone or the lower mantle (400–670 km depth; Rudloff-Grund et al., 2016; Kagi et al., 2016; Gu and Wang, 2017; Gu et al., 2019). Most diamonds shown to have a superdeep origin are type II diamonds (Smith et al., 2016, 2018). Meanwhile, the vast majority of nitrogen-containing diamond (D-to-Z color

type Ia and yellow type Ib) form in the continental lithosphere (depths of ~140–200 km; Shirey and Shigley, 2013). Those studied diamonds ("milky," type IaB) were subjected to unusual conditions for nitrogen-containing diamonds, such as higher pressures and temperatures corresponding to their deeper origin. These conditions could have instigated the complete aggregation of B centers, and the high temperature could promote some of the other unique characteristics that were observed, such as the destruction of platelets and the formation of dislocation loops.

Gu and Wang (2017) tested 50 milky type IaB diamonds with inclusions that could be identified by Raman spectroscopy. A majority of them contained mineral inclusions from the sublithospheric mantle, such as walstromite, Ca-perovskite, and ferropericlase, which they considered fragments of phases in the transition zone or lower mantle (>400 km; Shirey and Shigley, 2013).

To our knowledge, there are no reliable geographical sources for Fancy white diamonds. However, a few examined by GIA have come from the Panna mine in India (Koivula et al., 1992), and there have been some scientific reports on "milky" sub-lithospheric type IaB diamonds sourced from the Juina mine in Brazil (Rudloff-Grund et al., 2016; Kagi et al., 2016).

Fancy Black. The geographic sources of most Fancy black diamonds are uncertain, and these are likely quite rare at most mines. If colored by mineral inclusions, there are several possible origins. Many black diamonds that contain radiation stains may be sourced from mines known for naturally irradiated material like Marange in Zimbabwe.

Graphite Crystal Inclusions and Clouds. As with Fancy white diamonds, there is evidence that Fancy black diamonds colored by graphite (either as crystals or as clouds) are also influenced by rapid growth. Smit et al. (2018) showed that all of the diamonds in a suite from Marange contained evidence of nickel (926 nm PL peak using 830 nm excitation) and high amounts of hydrogen (such as a 3107 cm^{-1} peak in IR spectra), while a good percentage contained evidence of methane (CH_4, as a 3050 cm^{-1} peak in IR spectra; Smit et al., 2018 and references therein). This combination of spectral features coincides with those seen in the cuboid sectors of mixed-habit growth—natural diamonds that contain simultaneously grown cuboid and octahedral sectors where each sector has very distinct chemistry and inclusions. These cuboid sectors grow faster than octahedral sectors, and this rapid growth allows them to incorporate micron-sized cavities (Klein-BenDavid et al., 2007) along with a greater variety and concentration of impurities and inclusions than the octahedral regions (Lang, 1974). Therefore, these cuboid sectors have higher concentrations of non-diamond carbon (such as graphite and methane) and other impurity elements such as nickel and hydrogen. There is likely some similarity in the formation of these black diamonds, as with the cuboid sectors of mixed-habit diamonds. The Marange alluvial deposits have been a steady source of graphite-bearing diamonds for several years, although it is likely not the only source of graphite-included black diamonds, as some gemological reports (e.g., Kammerling et al., 1990) predate the Marange discovery. Additionally, Marange is unique as a source of diamonds exposed to high levels of radiation (Smit et al., 2018), with many containing abundant brown radiation stains in fractures that contribute to their Fancy black coloration.

Non-Carbon Inclusions. Although several reports have chronicled Fancy black diamonds with color due to non-carbon inclusions (e.g., Win and Lu, 2009), to our knowledge the only analyzed samples with a known locality were those reported by Titkov et al. (2003). These contained magnetite (Fe_3O_4), hematite (Fe_2O_3), and native iron and were sourced from the Mir kimberlite field in Siberia, which is also a known source for pink to purple diamonds (Titkov et al., 2008).

Carbonado. According to previous reports, carbonado has only been found in Brazil and the Central African Republic (Haggerty, 2017), and its method of formation remains unknown. Several theories regarding how the material originated have been proposed, such as sintering in the earth's crust and a potentially extraterrestrial origin.

LABORATORY GRADING

Grading of Fancy white and Fancy black diamonds poses unique challenges, as their limited transparency makes some observations difficult. At GIA, these stones' transparency is evaluated to determine if a Colored Diamond Grading (CDG) report may be issued. In an opaque stone, for example, a grader cannot look through the table to the pavilion facets and properly judge symmetry as one would in a transparent stone. Therefore, most Fancy white and almost

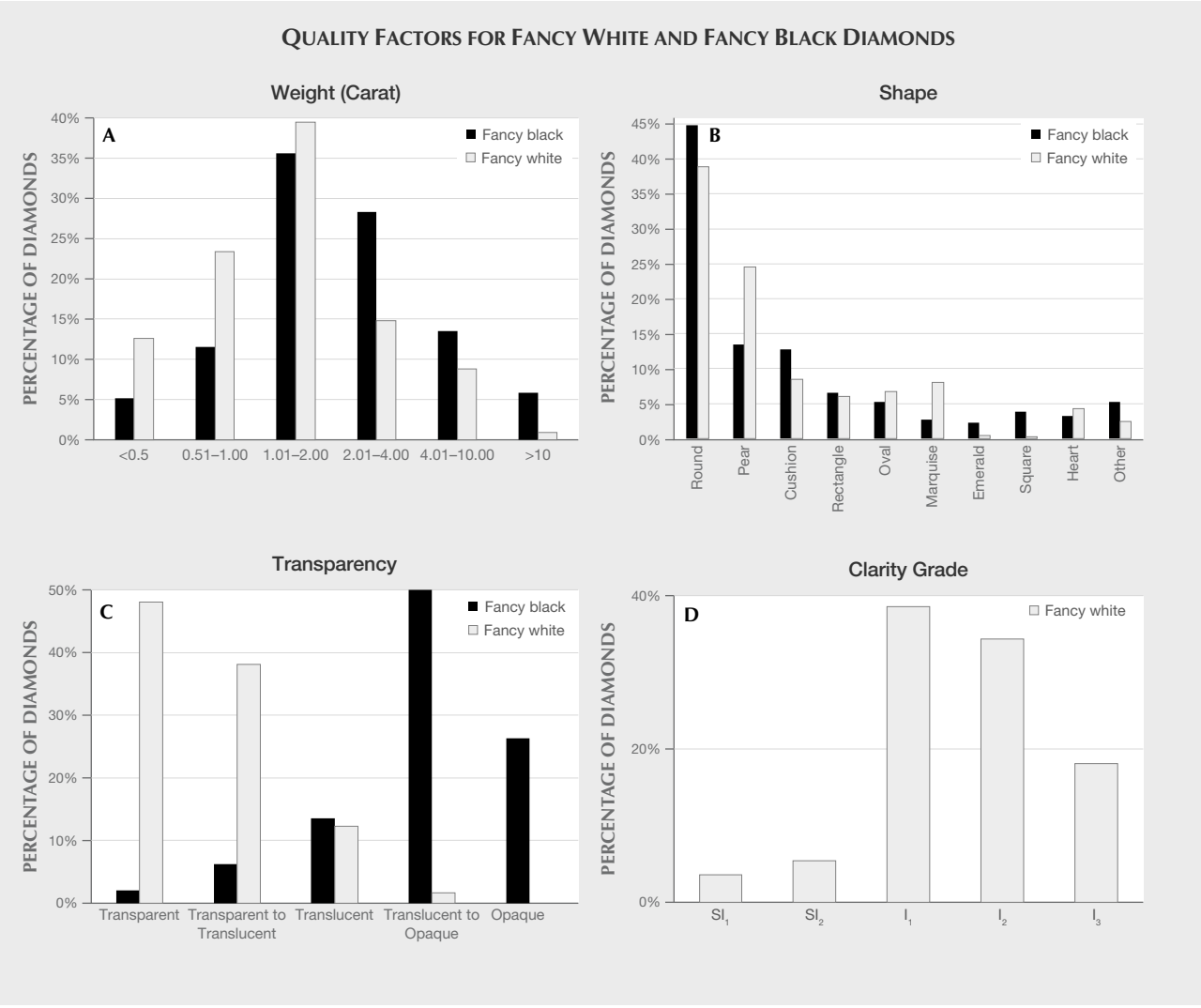

Figure 6. Quality factors for Fancy white and Fancy black diamonds analyzed by GIA, 2008–2016: weight (A), shape (B), transparency (C), and clarity grade (D). Transparency observations and clarity grades were not recorded for all submitted diamonds.

all Fancy black stones submitted have received a Colored Diamond Identification and Origin report. (The CDIOR determines origin of color and certifies if a diamond is natural, treated, or synthetic; it should not be confused with a Diamond Origin report, which states country of origin.) Of the Fancy white diamonds submitted in the last ten years, about 30% were issued CDG reports and the balance received CDIOR reports. The clarity grades shown in figure 6 are taken from this small subset.

Figure 6 shows the distribution of Fancy white and Fancy black diamonds according to several quality factors and observations. In figure 6A, the weight distribution for Fancy white and Fancy black diamonds indicates that Fancy white diamonds skew toward smaller sizes with ~75% having weights of less than 2 carats. The shape distribution in figure 6B reveals that a plurality of both colors have a round shape. Figure 6C provides the transparency distribution—a comparison not often made for other diamonds. This plot shows the distribution among those for which a transparency was recorded based on the judgment of the GIA gemologist. According to the plot, the majority of Fancy white diamonds skew toward a transparent observation. Figure 6D shows the clarity grade distribution among those Fancy white diamonds for which a clarity grade could be assigned, and almost all are in the Included range. The majority of Fancy white and nearly all Fancy black diamonds did not satisfy the criteria for

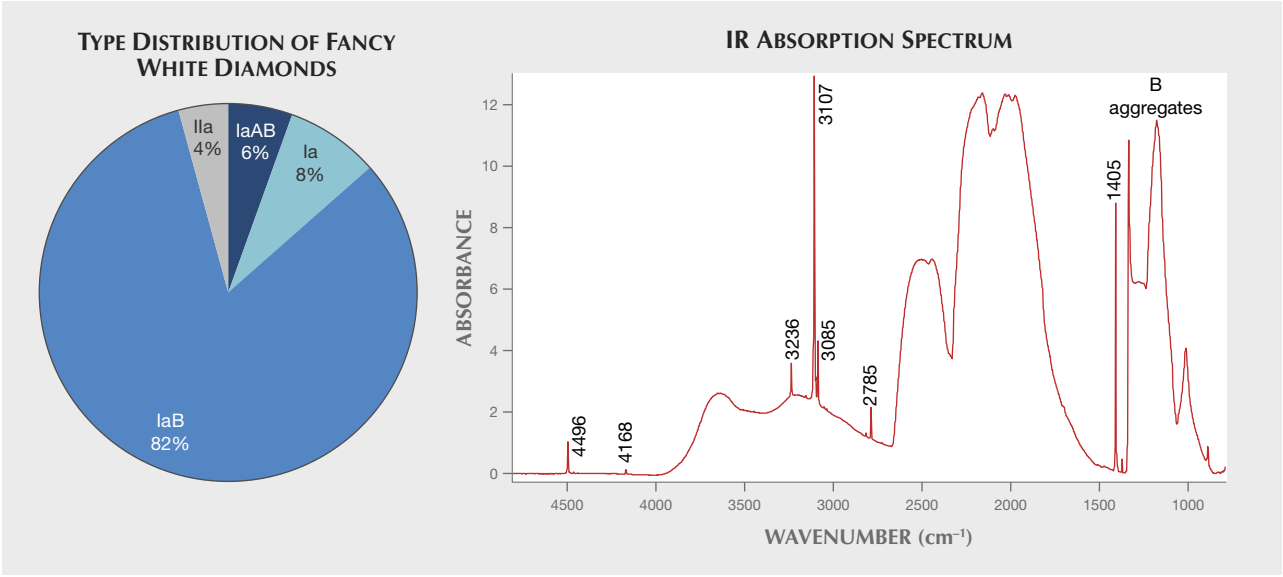

Figure 7. The vast majority of Fancy white diamonds are type IaB. The diamond types were determined for a survey of 400 randomly selected Fancy white diamonds in which 82% were type IaB (left). Another 8% were type Ia, meaning the aggregated nitrogen absorption was so strong that it saturated the detector and the A/B aggregate ratio could not be determined. The remaining diamonds were either type IIa or type IaAB. At right, a representative absorption spectrum is shown for a 1.06 ct type IaB Fancy white diamond. Also shown are several hydrogen-related peaks (Fritsch et al., 2007).

a CDG report (instead of a CDIOR) and are not represented in this plot; if plotted, they would skew toward lower clarity grades.

SPECTROSCOPY

Standard testing conditions and instrumentation are applied to all diamonds submitted to GIA. These methods have been detailed in other publications (e.g., Smit et al., 2018) and summarized for this series of articles in Breeding et al. (2018).

Fancy White. *Infrared Absorption.* As mentioned earlier, the vast majority of Fancy white diamonds have been shown to be type IaB. We quantify it here by randomly selecting a subset of 400 Fancy white diamonds and examining their infrared absorption spectra (figure 7) and long-wave fluorescence (discussed below). Of these 400 Fancy white diamonds, 32 (8%) had saturated type Ia infrared spectra—namely, there was so much nitrogen in the diamond that we could only determine its presence but not its concentration or A/B ratio because the corresponding spectral features exceeded the absorption range of the instrument detector. An additional 22 (6%) were type IaAB and 17 (4%) were type IIa. The remaining 329 diamonds (82%) were able to be classified as type IaB. Since the percentage of type IaB diamonds among all diamonds submitted to GIA is ~0.1–0.2% (internal GIA statistics), the conditions to produce type IaB diamonds are very rare and those necessary to produce Fancy white diamonds even more so.

Comparison to Other Type IaB Diamonds. To try to discern any additional spectroscopic information that distinguishes Fancy white diamonds, we compared three groups of type IaB diamonds:

1. A randomly selected population of 100 type IaB *without* a cloudy/hazy/milky appearance, and with high clarity grades (VVS or higher) and good color (majority D–F).
2. A randomly selected population of 100 type IaB diamonds *with* a cloudy/hazy/milky appearance, as evidenced by low clarity grades (generally SI to I), that must contain clarity characteristics such as clouds and pinpoints, and potentially a "hazy" comment on the worksheet by the grader. However, the diamond was still on the D-to-Z scale (majority D–F).
3. A randomly selected population of 100 type IaB diamonds that were color graded as Fancy white (selected from the 329 type IaB diamonds mentioned above).

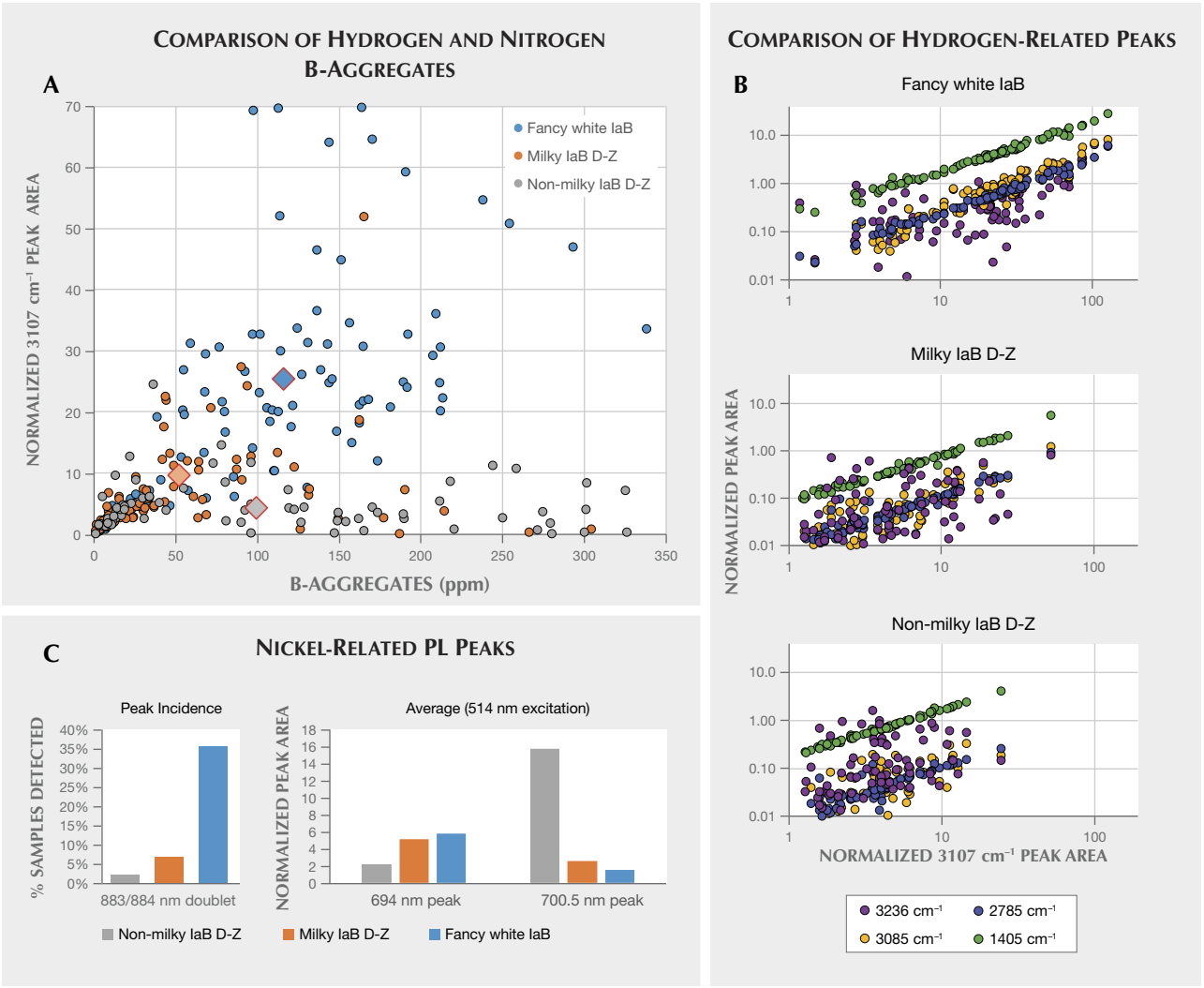

Figure 8. To better understand the optical properties that distinguish Fancy white type IaB diamonds from those on the D-to-Z scale, we compared three groupings of type IaB diamonds. Comparing the B aggregate concentration (ppm) and the normalized 3107 cm^{-1} peak area, the Fancy white diamonds have high concentrations of both nitrogen and hydrogen (A). The diamond-shaped markers in (A) indicate the average values for each grouping. The 3107 cm^{-1} peak area shows a positive trend with a few other hydrogen-related peaks (B), and the Fancy white diamonds have the highest intensities of hydrogen. Fancy white diamonds also show the highest incidence (C) of the 883/884 nickel doublet and the highest occurrence of the 694 nm PL peak (identified as a Ni-N complex).

We wished to see if there was any progression in IR absorption and PL spectroscopic features among these three groups. Gu and Wang (2018) had previously looked at the optical features in "milky" type IaB diamonds but grouped categories 2 and 3 together. The most interesting results from comparing these three categories are presented in figure 8.

Figure 8A shows the distribution of B aggregates (or total nitrogen, as these are type IaB diamonds) versus the 3107 cm^{-1} normalized peak area.[1] The 3107 cm^{-1} peak has been identified as the N_3VH center; this may be visualized as an N3 center (ZPL at 415.2 nm; often responsible for blue fluorescence in diamond) with a hydrogen atom located within the vacancy (Goss et al., 2014). For the 100 diamonds in each of the

[1]It is generally accepted that the absorption coefficient of diamond is constant in the two- and three-phonon regions. For example, at 2000 cm^{-1} the absorption coefficient is 12.3 cm^{-1} (Tang et al., 2005; Breeding and Shigley, 2009) and each diamond IR spectrum, regardless of the thickness or path length, can be compared by applying this normalization. Because the two-phonon region was often saturated in these spectra, however, we normalized each IR spectrum using the third-phonon region. The area of each hydrogen-related peak (the area above the baseline) was then determined from the normalized spectra.

three groups described above, the data for nitrogen and hydrogen were determined from each sample's IR spectrum and the averages were calculated and plotted. Figure 8A shows that Fancy white diamonds have both high amounts of hydrogen (as the 3107 cm^{-1} peak) and high B aggregates. The non-milky, high-clarity D-to-Z diamonds also contain high amounts of B aggregates but comparatively low concentrations of hydrogen. In between these two groups are the milky D-to-Z diamonds that show lower nitrogen than both the non-milky and Fancy white diamonds; however, they contain higher amounts of hydrogen than the non-milky D-to-Z diamonds. From these results, it appears that hydrogen-related defects contribute to the milky appearance. It also appears that higher amounts of nitrogen and hydrogen help distinguish between a milky D-to-Z diamond and one with a Fancy white color grade. Finally, figure 8A shows that for all three groups, when B aggregates (lower left corner of graph) are low in concentration, there appears to be a trend between the nitrogen concentration and 3107 cm^{-1} peak area; however, the data begin to scatter for nitrogen concentrations greater than 30 ppm.

The corresponding intensity between nitrogen concentration and the 3107 cm^{-1} peak in the Fancy white diamonds seems to indicate that nitrogen concentration is the limiting factor, and that hydrogen is available in excess and probably exists in the diamond in other configurations that may not be IR active (i.e., producing no spectral features due to hydrogen in the infrared spectrum). In contrast, the non-milky, high-clarity type IaB diamonds have comparatively low 3107 cm^{-1} intensities even with high nitrogen concentrations; this likely indicates that hydrogen is the limiting factor for those diamonds in forming the 3107 cm^{-1} center.

Figure 8B shows the linear relationship between the most prominent hydrogen-related peak at 3107 cm^{-1} (again, see figure 7B) and other IR peaks associated with hydrogen. Several peaks are part of the 3107 cm^{-1} system (e.g., 1405, 2785, 4168, and 4496 cm^{-1}; Fritsch et al., 2007). This linear relationship holds between all three groups, though, as mentioned above, the Fancy white diamonds have the highest hydrogen concentration. Also shown are the intensities of the 3085 and 3236 cm^{-1} peaks that are also ascribed to hydrogen-related peaks, but not part of the 3107 cm^{-1} system (Fritsch et al., 2007). Although these peaks show more scatter in figure 8B, they do maintain a positive trend, with increasing 3107 cm^{-1} peak intensity. Therefore, if these other hydrogen-related peaks are more often seen in Fancy white diamonds than in other type IaB diamonds (e.g., Gu and Wang, 2018), it is likely ascribed to a higher overall amount of hydrogen in those diamonds.

Additionally, detection of the platelet peak was seen to decrease within the milky diamonds. In the non-milky D-to-Z type IaB diamonds, 22 of the 100 showed a platelet peak, generally positioned at ~1360 cm^{-1}. Among the milky D-to-Z IaB diamonds, only four displayed a platelet peak, all positioned at ~1360 cm^{-1}. Among the Fancy white IaB diamonds, none had a platelet peak. The lack of platelet peaks in these Fancy white diamonds is consistent with the prior observation that dislocation loops—features seen in milky and Fancy white diamonds—can form from the destruction of platelets at high temperatures. This observation is also consistent with the supposition that these have a superdeep origin.

Figure 8C shows the trends seen for some nickel-related peaks when measured by PL spectroscopy. The milky D-to-Z and especially the Fancy white IaB diamonds show a pronounced difference in peak intensity (or incidence) of nickel-related peaks. The 883/884 nm doublet is quite rare in the non-milky type IaB diamonds (found in only 2%), whereas it is detected in more than one-third of Fancy white diamonds. This nickel-related doublet is commonly detected in HPHT synthetics and some low-nitrogen natural diamonds (Collins et al., 1998), and is ascribed to an interstitial Ni^{+} ion along the <111> direction. The 694 and 700.5 nm PL peaks are both ascribed to NiN_x complexes. For the non-milky D-to-Z diamonds, we see the 700.5 nm PL peak as dominant, whereas for the Fancy whites the 694 nm PL peak is greater. Although the exact compositions of these two nickel-related peaks are unknown, the 700.5 nm PL peak is dominant in other natural diamonds such as chameleons (Hainschwang et al., 2005). In the highly included, high-hydrogen cuboid sectors of mixed-habit diamonds, however, the 694 nm peak is dominant (Eaton-Magaña et al., 2017), as with the Fancy white diamonds documented here. As shown in figure 9, the peak area intensity of the 694 nm peak is significantly greater within the cloudy portion of a Fancy white diamond.

Fancy Black. For the vast majority of Fancy black diamonds, Vis-NIR absorption spectra are not helpful for determining the cause of color. Their color is due to inclusions and not lattice defects, and microscopy is far more diagnostic for inclusions than spectroscopy. Among a randomly selected subset of 1,000 Fancy black diamonds, 536 had IR absorption spectra

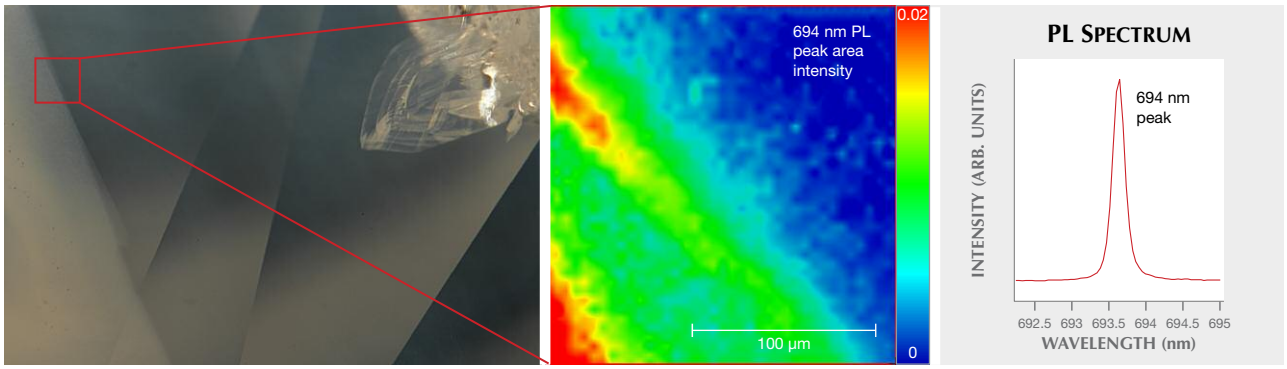

Figure 9. A 3.04 ct Fancy white diamond (left) was used to produce a PL map (center) using 532 nm excitation at the boundary between the clouded area and unclouded area; the false-color map corresponds to the intensity of the 694 nm peak (peak area normalized using the diamond Raman area). The whitish cloud in the left portion of the image (indicated by the red square in the photomicrograph) and in the PL map corresponds with a much higher intensity of the 694 nm peak (right)—a nickel-related peak often seen in Fancy white diamonds and, as shown here, within the clouds themselves. Photomicrograph by Garrett McElhenny; field of view 2.34 mm.

available for examination. Due to the opacity of most Fancy black diamonds, meaningful spectra could not be collected on many of them. Of those 536 with useful spectra available, most (436, or 81%) were saturated type Ia with high nitrogen concentrations, and many also showed very high intensities of hydrogen-related peaks (figure 10). Diamonds with high hydrogen concentrations would be expected in diamonds containing cloud inclusions. Additionally, many of the diamonds with graphite inclusions had high quantities of hydrogen detected in them as well.

As with Fancy white diamonds, Fancy black diamonds show a positive trend between various hydrogen-related peaks, although there is significantly more scatter. In contrast with the Fancy white diamonds (figure 8B), the 3085 cm^{-1} peak has very low intensity in Fancy black diamonds (if detected) and is not shown in figure 10. Also, it was mentioned in the previous section that Fancy white diamonds had high quantities of hydrogen; when compared to the non-milky D-to-Z diamonds, the intensities of the 3107 cm^{-1} peak are up to one order of magnitude greater. The hydrogen concentrations (as shown in the IR absorption spectrum in figure 10) are even greater still, with values another order of magnitude greater than those seen in the Fancy white diamonds.

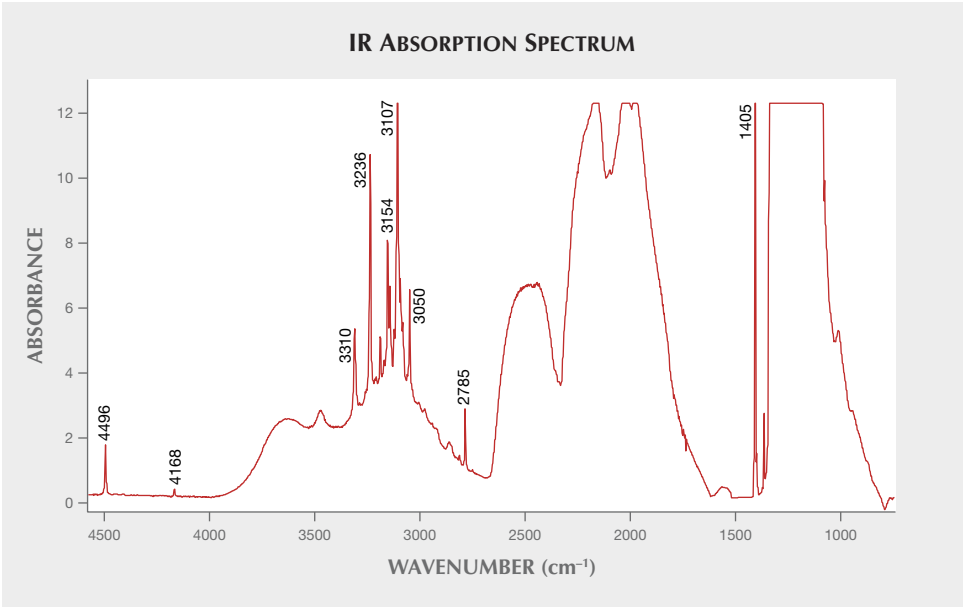

Figure 10. Many Fancy black diamonds have very high intensities of the hydrogen-related peaks—even compared with the "high-hydrogen" Fancy white diamonds (e.g., figures 7 and 8). A typical IR absorption spectrum includes saturated nitrogen aggregates and several hydrogen-related peaks, such as a methane-related peak at 3050 cm^{-1}.

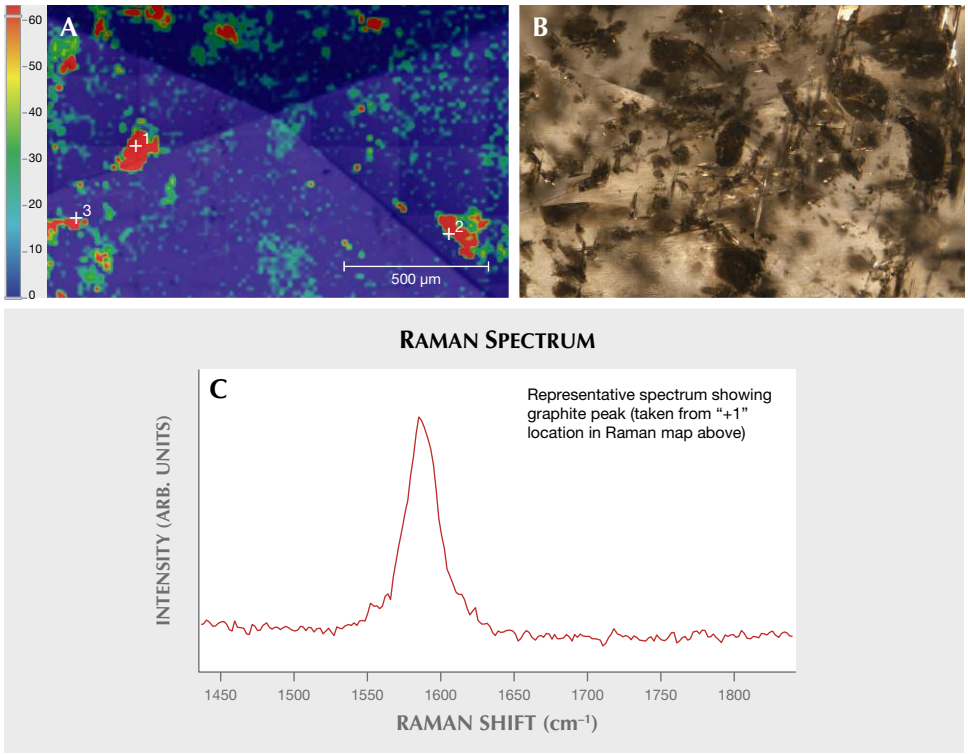

Figure 11. A Raman map (A) was collected on the pavilion side of a 5.27 ct Fancy black diamond (B). The false-color map shows the peak area intensity of the graphite peak with a representative peak shown in the Raman spectrum (C). While the Raman map indicates where graphite was detected, a chromite inclusion was detected at "+2" and a forsterite inclusion was detected at "+3." The pixel size was 15 µm, and the map is composed from 8,136 spectra collected over five hours.

Although several other publications have identified the crystal inclusions found in Fancy black diamonds (e.g., Titkov et al., 2003; Win and Lu, 2009; Smit et al., 2016, 2018), we provide here for illustrative purposes a Raman map of a typical Fancy black diamond colored by crystal inclusions. Most of the inclusions in this sample proved to be graphite, but a few were identified as other minerals (figure 11). This map, along with the corresponding image, shows that the majority of the crystal inclusions in this particular diamond are graphite.

GEMOLOGICAL OBSERVATIONS

Fancy White. The microscopic observations reported by GIA gemologists generally mentioned the presence of whitish clouds and a hazy appearance, which is to be expected for diamonds in this color range.

Blue fluorescence is the most common color to be observed with long-wave UV excitation (figure 12, left). Among the 329 type IaB diamonds identified from the 400-stone subset, a majority (254 of the 262 with reported fluorescence reaction) showed blue fluorescence due to the N3 defect, most of them with medium-strength intensity. Only seven showed a weak yellow fluorescence, and one displayed no fluorescence.

Among the other diamond types, IaAB diamonds all showed medium to strong blue fluorescence. Saturated type Ia diamonds similarly exhibited medium to strong blue fluorescence, though 8 of the 32 showed a weak yellow and one had no fluorescence. Among the 17 type IIa diamonds, 10 showed a weak blue fluorescence, 2 a weak yellow, and the others no observable reaction.

Some diamonds have a very strong blue fluorescence, and terms such as "hazy" or "milky" are used to describe these (Moses et al., 1997). The 127 ct Portuguese diamond at the Smithsonian Institution is a famous example of an "overblue"—that is, a diamond with a reportedly hazy appearance due to strong blue fluorescence. Nevertheless, the "hazy" appearance due to very strong fluorescence and the "hazy" observation in Fancy white diamonds appear to be unrelated phenomena. Figure 12 (bottom) shows a similar distribution of fluorescence intensities among the transparent type IaB diamonds and the Fancy white type IaB stones. While Fancy white diamonds show a higher incidence of faint and medium fluorescence, only a small percentage in each grouping show strong fluorescence and none showed very strong fluorescence. There is no pronounced shifting to strong or very strong fluorescence among the milky or Fancy white diamonds, which might be expected if the haziness observed in "overblue" diamonds coincided with the nano-inclusions creating the Fancy white color.

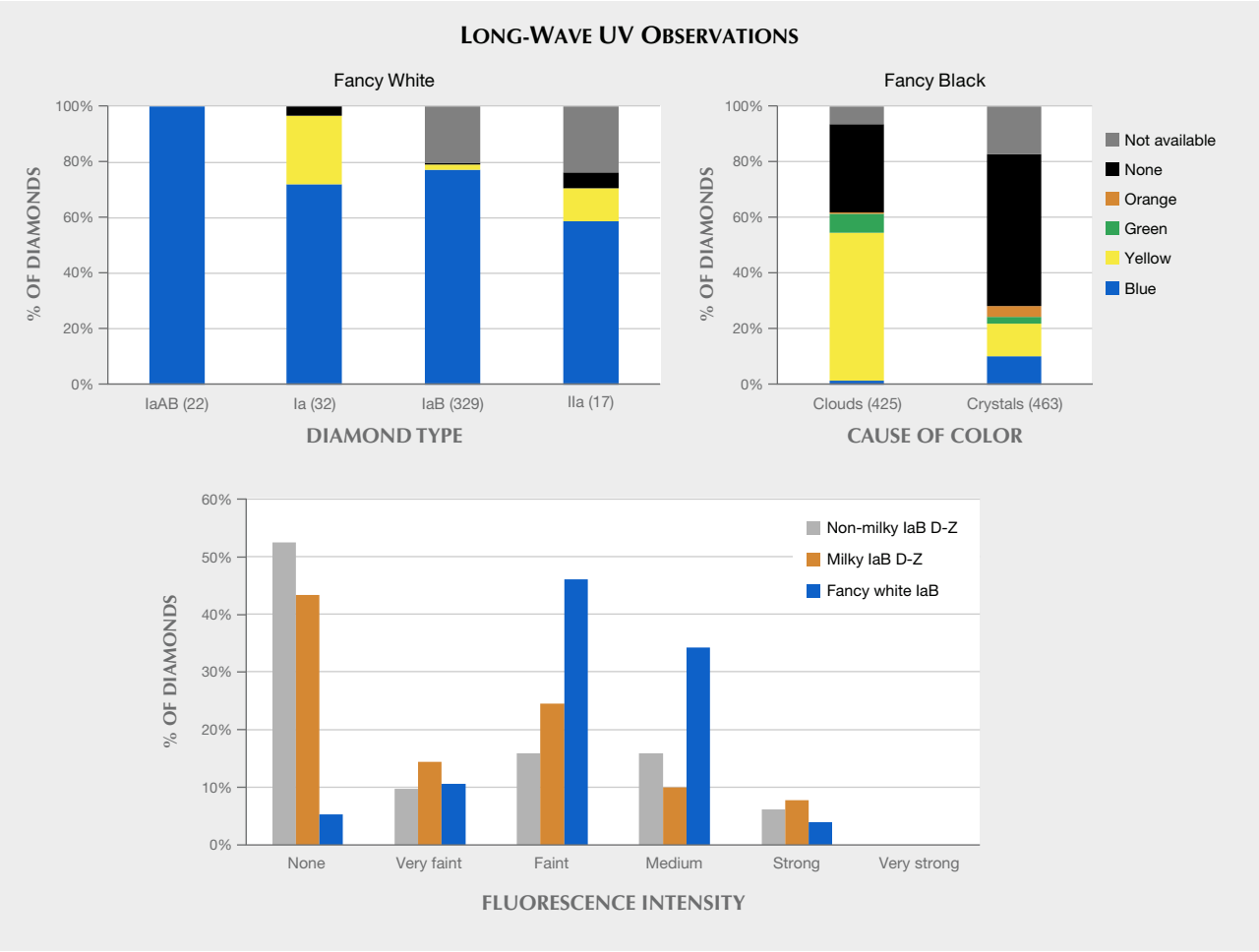

Figure 12. The long-wave UV (365 nm) observations are shown for Fancy white as distinguished by diamond type (left) and Fancy black as distinguished by inclusion type (right). Most Fancy white diamonds showed blue fluorescence due to the N3 defect, while most Fancy black diamonds displayed a weak yellow or no response. Those diamonds identified as having either clouds or crystals as the cause of color are plotted. Those Fancy black diamonds with color due to absorption or polycrystalline diamond are not plotted, and they showed no fluorescence. Bottom: A comparison of the three different groups of type IaB diamonds described earlier and also plotted in figure 8. The fluorescence intensities do not vary much between the different groupings or shift significantly toward strong or very strong fluorescence. These observations were made by laboratory staff following normal grading procedures.

Fancy Black. *Microscopic Observations*. While examining Fancy black diamonds, GIA gemologists note their observations of the cause of color, such as dark crystal inclusions or clouds, along with other features that generally do not contribute to the diamond color. We catalogued gemologist observations for 1,000 Fancy black diamonds and grouped them based on whether the cause of color was:

- Crystal inclusions—either as graphite, such as those seen in Smit et al. (2018), or as foreign minerals, such as those seen by Titkov et al. (2003).
- Clouds of nano-inclusions (generally assumed as graphite and verified in some cases); see Smit et al. (2016, 2018) and Eaton-Magaña et al. (2017).
- A high concentration of absorption defects, polycrystalline diamond, or radiation stains (usually as a contributing factor; Smit et al., 2018).

Figure 13 shows the compilation of these gemological observations for 1,000 Fancy black diamonds. Crystal inclusions were reported in 46% of the diamonds, some of which also contained radiation stains; 43% of the observations noted clouds, and a significant percentage of those also contained radiation stains. An additional 10% of the observations noted the presence of both crystals and clouds. Only

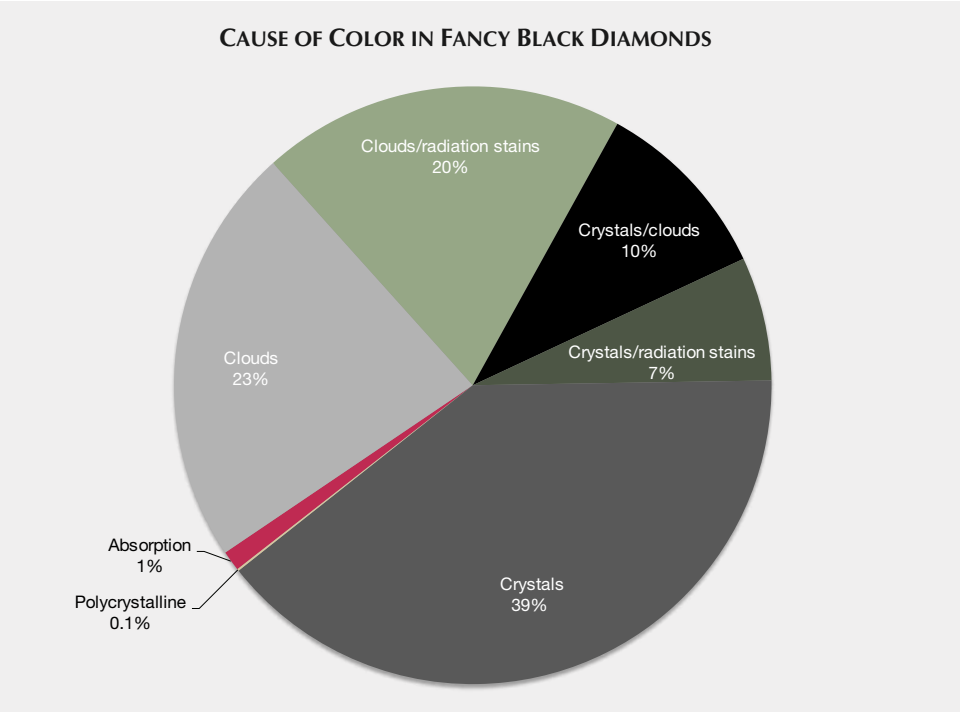

Figure 13. Observations noted by the gemologist for 1,000 randomly selected Fancy black diamonds were chronicled to determine the major causes of color documented in each. A roughly equal distribution was seen for "clouds" (either with or without radiation stains) and for "crystals" (either with or without radiation stains). In another 10%, both features were mentioned. A very small percentage of diamonds were Fancy black due to absorbing defects or polycrystalline diamond growth.

1% of the stones had strong absorption; generally these had a deep violet to purple color observed through the pavilion, consistent with previously published Lab Notes entries (e.g., Breeding and Rockwell, 2009) and absorption spectra consistent with violet-related hydrogen bands (e.g., Eaton-Magaña et al., 2018a).

The radiation stains were generally described as brown rather than green, consistent with Smit et al. (2018) and an indication that these diamonds likely had been heated above 550°C. In 116 of the 1,000 diamonds, the gemologist noted the presence of iron oxide stains, although such stains are generally not sufficient to affect the color.

Additionally, because so many of these diamonds are heavily included, many such inclusions break the facet surface, which can lead to a textured surface and noticeable polish lines (figure 14). Differential hardness due to inclusions in black diamond is known to create serious challenges in polishing these stones.

Long-Wave UV Fluorescence. Figure 12 (right) shows the color distribution of long-wave UV fluorescence for diamonds characterized by either crystal inclusions or clouds. Almost all that showed fluorescence had weak intensity, regardless of the observed color. Most of those colored by clouds had either weak yellow or no fluorescence, while most colored by crystal inclusions exhibited no fluorescence.

IDENTIFICATION CONCERNS

Fancy White. For Fancy white diamonds, there is no known method of treatment to mimic the cloudy and hazy appearance formed by the nano-inclusions in natural diamonds in this color range. To date, GIA has not observed a treated or laboratory-grown Fancy white diamond.

However, since the IR peak at 3085 cm^{-1} that has been associated with milky diamonds (Gu et al., 2018) can be generated by annealing (Kupriyanov et al., 2006), some have speculated that it might be possible to obtain a hazy diamond from a hydrogen- and B center nitrogen-enriched diamond by HPHT treatment. However, we have never encountered a diamond known to be treated in this way.

Fancy Black. In contrast, there are several methods to create Fancy black color in diamonds by treatment. Over one-third of the black diamonds examined by the laboratory have been treated, so it is important to understand that all Fancy black diamonds have the potential to be treated or synthetic and should be sent to a gemological laboratory for confirmation. Today, the most common method for creating this black color is heating a diamond to high temperatures under vacuum to allow pervasive graphitization of preexisting fractures or inclusions (Overton and Shigley, 2008). This is done on heavily fractured diamonds or on diamonds that contain abundant clouds of micro-inclu-

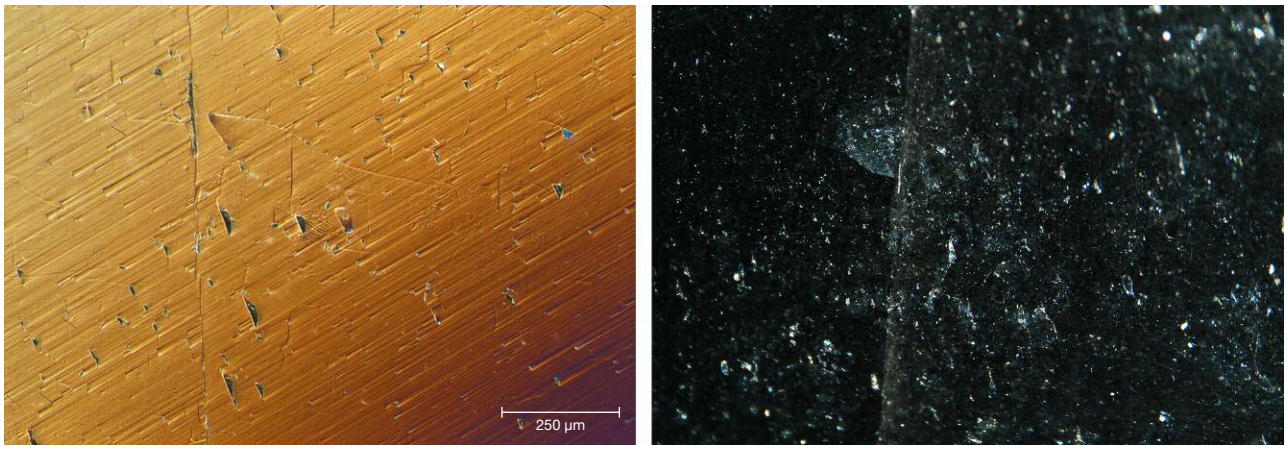

Figure 14. The table facet of a 1.78 ct Fancy black pear is shown under differential interference contrast lighting (see Renfro, 2015) that enhances the surface topography (left) and in reflected light (right). The differential interference contrast image shows features interrupting the facet surface and visible polish lines. Such an image collected on a typical colorless diamond would appear featureless.

sions and often initially have a grayish appearance (Eaton-Magaña et al., 2017).

Early treatments to produce black color involved introduction of very high concentrations of defects by heavy irradiation treatment. At lower doses, this irradiation would typically give the diamond a fancy blue or green color, but extremely high irradiation doses produce so many light-absorbing defects that the stone has a very dark appearance. Some of these historically treated diamonds have been found to emit measurable radioactivity (Overton and Shigley, 2008). Diamonds that have been heavily irradiated (Hainschwang et al., 2009) often show a dark greenish appearance when examined through the pavilion with fiber-optic light yet appear Fancy black when viewed face-up. They have a dark brown appearance if annealed after the irradiation treatment.

Additionally, some CVD-grown diamonds have been manufactured with such a high concentration of nitrogen-vacancy (NV) centers that they appear Fancy black, while appearing reddish in intense transmitted light. All Fancy black diamonds—whether their color derives from micro-inclusions, graphitization, or a high quantity of defects—should have their color origin confirmed by a gemological laboratory.

CONCLUSIONS

Although Fancy white and Fancy black diamonds do not occur in large numbers, they create an interesting niche in the fancy-color diamond world. The ingredients creating color in most natural diamonds are atomic-scale defects. Here, Fancy white and Fancy black diamonds (figure 15) typically receive their color from nano-inclusions (generally described as clouds of pinpoints) to micro-sized crystal inclusions.

Figure 15. This snake ring with black and colorless diamonds, from the Malafemmina collection by Dada Arrigoni, contains 3.60 carats of black diamonds. Photo © Dada Arrigoni.

In Fancy white diamonds, the vast majority (82%) are type IaB, and recent research (e.g., Gu and Wang, 2017; Gu et al., 2019) has shown these to have a sublithospheric origin in either the transition zone or the lower mantle, which has helped diagnose the cause of color in these enigmatic gems. When diamond is formed under superdeep conditions, they are exposed to higher pressures and temperatures than the vast majority of diamonds that form within the lithosphere. The effect of higher temperatures likely contributes to the complete aggregation of the nitrogen (from single nitrogen to A aggregates to B aggregates) and other high-temperature effects such as destruction of the platelets that potentially aid in forming the dislocation loops or the nitrogen-bearing nano-inclusions that lead to the "milky" appearance of Fancy white diamonds. Additionally, nickel- and hydrogen-related defects were seen in much greater numbers in Fancy white type IaB diamonds than in their transparent counterparts. The normalized intensity of the 3107 cm^{-1} peak in FTIR was about one order of magnitude higher in Fancy white diamonds than in high-clarity D-to-Z type IaB diamonds.

The last few years have proven interesting for both of these classes of colored diamonds. The Marange deposit has become a reliable source for natural Fancy black diamonds in which the black color is caused principally through graphitic inclusions or clouds and the presence of radiation stains contributing to the dark color. This comparatively recent source has inclusions that are distinctly different from other documented mines such as the Mir kimberlite pipe, in which non-graphitic mineral inclusions are the major cause of color.

The ability to examine such a large number of colored diamonds and perform systematic data collection provides a unique opportunity to document gemological and spectroscopic trends in these diamonds that would likely not be possible otherwise.

ABOUT THE AUTHORS

Dr. Eaton-Magaña and Dr. Breeding are senior research scientists, Mr. Ardon is a research associate, and Dr. Shigley is a distinguished research fellow, at GIA in Carlsbad, California.

ACKNOWLEDGMENTS

The authors thank Dr. Tingting Gu, Dr. Chloe Peaker, and the peer reviewers for their suggestions on this article. We also thank GIA's Garrett McElhenny and Alex Balter for their assistance with data compilation.

REFERENCES

Balfour I. (2009) *Famous Diamonds*. Antique Collector's Club, Woodbridge, England.

Boyd S.R., Kiflawi I., Woods G.S. (1995) Infrared absorption by the B nitrogen aggregate in diamond. *Philosophical Magazine B*, Vol. 72, No. 3, pp. 351–361, http://dx.doi.org/10.1080/13642819508239089

Breeding C.M., Shigley J.E. (2009) The "type" classification system of diamonds and its importance in gemology. *G&G*, Vol. 45, No. 2, pp. 96–111, http://dx.doi.org/10.5741/GEMS.45.2.96

Breeding C.M., Rockwell K.M. (2009) Lab Notes: "Black" diamond with deep violet color. *G&G*, Vol. 45, No. 2, p. 135.

Breeding C.M., Eaton-Magaña S.C., Shigley J.E. (2018) Natural-color green diamonds: A beautiful conundrum. *G&G*, Vol. 54, No. 1, pp. 2–27, http://dx.doi.org/10.5741/GEMS.54.1.2

Collins A.T., Kanda H., Isoya J., Ammerlaan C.A.J., van Wyk J.A. (1998) Correlation between optical absorption and EPR in high-pressure diamond grown from a nickel solvent catalyst. *Diamond and Related Materials,* Vol. 7, No. 2/5, pp. 333–338, http://dx.doi.org/10.1016/S0925-9635(97)00270-7

De Corte K., Kerremans Y., Nouven B., Van Royen J. (2004) Characterization of carbonado as a gem. *Gemmologie - Zeitschrift der Deutschen Gemmologischen Gesellschaft*, Vol. 53, No. 1, pp. 5–22.

Eaton-Magaña S., Ardon T., Zaitsev A.M. (2017) Inclusion and point defect characteristics of Marange graphite-bearing diamonds after high temperature annealing. *Diamond and Related Materials,* Vol. 71, pp. 20–29, http://dx.doi.org/10.1016/j.diamond.2016.11.011

Eaton-Magaña S.C., Breeding C.M., Shigley J.E. (2018a) Natural-color blue, gray, and violet diamonds: Allure of the deep. *G&G*, Vol. 54, No. 2, pp. 112–131, http://dx.doi.org/10.5741/GEMS.54.2.112

Eaton-Magaña S.C., Ardon, T., Smit K.V. Breeding C.M., Shigley J.E. (2018b) Natural-color pink, purple, red, and brown diamonds: Band of many colors. *G&G*, Vol. 54, No. 4, pp. 352–377, http://dx.doi.org/10.5741/GEMS.54.2.352

Evans T., Kiflawi I., Luyten W., Van Tendeloo G., Woods G.S. (1995) Conversion of platelets into dislocation loops and voidite formation in type IaB diamonds. *Proceedings of the Royal Society of London. Series A: Mathematical and Physical Sciences*, Vol. 449, No. 1936, pp. 295–313, http://dx.doi.org/10.1098/rspa.1995.0045

Fritsch E., Hainschwang T., Massi L., Rondeau B. (2007) Hydrogen-related optical centers in natural diamond: An update. *New Diamond and Frontier Carbon Technology*, Vol. 17, No. 2, pp. 63–89.

Goss J.P., Briddon P.R., Hill V., Jones R., Rayson M.J. (2014) Identification of the structure of the 3107 cm^{-1} H-related defect in

diamond. *Journal of Physics: Condensed Matter*, Vol. 26, No. 14, pp. 1–6, http://dx.doi.org/10.1088/0953-8984/26/14/145801
Gu T., Wang W. (2017) IaB diamond and its geological implications. *International Kimberlite Conference: Extended Abstracts*. Vol. 11.
Gu T., Wang W. (2018) Optical defects in milky type IaB diamonds. *Diamond and Related Materials,* Vol. 89, pp. 322–329, http://dx.doi.org/10.1016/j.diamond.2018.09.010
Gu T., Ohfuji H., Wang W. (2019) Origin of milky optical features in type IaB diamonds: dislocations, nano-inclusions, and polycrystalline diamond. *American Mineralogist*, Vol. 104, No. 5, pp. 652–658, http://dx.doi.org/10.2138/am-2019-6699
Haggerty S.E. (2017) Carbonado diamond: A review of properties and origin. *G&G*, Vol. 53 No. 2, pp. 168–179, http://dx.doi.org/10.5741/GEMS.53.2.168
Hainschwang T., Simic D., Fritsch E., Deljanin B., Woodring S., Del Re N. (2005) A gemological study of a collection of chameleon diamonds. *G&G*, Vol. 41, No. 1, pp. 20–35, http://dx.doi.org/10.5741/GEMS.41.1.20
Hainschwang T., Respinger A., Notari F., Hartmann H.J., Gunthard C. (2009) A comparison of diamonds irradiated by high fluence of neutrons or electrons, before and after annealing. *Diamond and Related Materials,* Vol. 18, No. 10, pp. 1223–1234, http://dx.doi.org/10.1016/j.diamond.2009.04.011
Humble P. (1982) The structure and mechanism of formation of platelets in natural type Ia diamond. *Proceedings of the Royal Society of London A*, Vol. 381, No. 1780, pp. 65–81, http://dx.doi.org/10.1098/rspa.1982.0059
Jang-Green H. (2006) Lab Notes: Unusually large Fancy white diamond with whitish banding. *G&G*, Vol. 42, No. 4, pp. 262–263.
Johnson P. (2008) Lab Notes: Black diamonds colored by hydrogen clouds. *G&G*, Vol. 44, No. 3, p. 254.
Johnson P. (2011) Lab Notes: A strongly purple-colored black diamond. *G&G*, Vol. 47, No. 4, p. 309.
Kagi H., Zedgenizov D.A., Ohfuji H., Ishibashi H. (2016) Micro- and nano-inclusions in a superdeep diamond from São Luiz, Brazil. *Geochemistry International*, Vol. 54, No. 10, pp. 834–838, http://dx.doi.org/10.1134/S0016702916100062
Kammerling R.C., Kane R.E., Koivula J.I., McClure S.F. (1990) An investigation of a suite of black diamond jewelry. *G&G*, Vol. 26, No. 4, pp. 282–287, http://dx.doi.org/10.5741/GEMS.26.4.282
Klein-BenDavid O., Wirth R., Navon O. (2007) Micrometer-scale cavities in fibrous and cloudy diamonds —A glance into diamond dissolution events. *Earth and Planetary Science Letters*, Vol. 264, No. 1/2, pp. 89–103, http://dx.doi.org/10.1016/j.epsl.2007.09.004
Koivula J.I., Kammerling R.C., Fritsch E. (1992) Gem News: Tucson '92 report. *G&G*, Vol. 28, No. 1, p. 58.
Kupriyanov I.N., Pal'yanov Y.N., Shatsky V.S., Kalinin A.A., Nadolinnyi V.A., Yur'eva O.P. (2006) Study of the transformation of hydrogen-containing centers in diamond at high PT parameters. *Doklady Earth Science*, Vol. 406, No. 1, pp. 69–73.
Lang A.R. (1974) On the growth-sectorial dependence of defects in natural diamonds. *Proceedings of Royal Society A*, Vol. 340, No. 1621, pp. 233–248, http://dx.doi.org/10.1098/rspa.1974.0150
Moses T.M., Reinitz I.M., Johnson M.L., King J.M., Shigley J.E. (1997) A contribution to understanding the effect of blue fluorescence on the appearance of diamonds. *G&G*, Vol. 33, No. 4, pp. 244–259, http://dx.doi.org/10.5741/GEMS.33.4.244
Nasdala L., Grambole D., Wildner M., Gigler A.M., Hainschwang T., Zaitsev A.M., Harris J.W., Milledge J., Schulze D., Hofmeister W., Balmer W.A. (2013) Radio-colouration of diamond: A spectroscopic study. *Contributions to Mineralogy and Petrology*, Vol. 165, No. 5, pp. 843–861, http://dx.doi.org/10.1007/s00410-012-0838-1
Navon O., Wirth R., Schmidt C., Jablon B.M., Schreiber A., Emmanuel S. (2017) Solid molecular nitrogen (δ -N_2) inclusions in Juina diamonds: Exsolution at the base of the transition zone. *Earth and Planetary Science Letters*, pp. 1–11. Vol. 464, pp. 237–247.
Overton T.W., Shigley J.E. (2008) A history of diamond treatments. *G&G*, Vol. 44, No. 1, pp. 32–55, http://dx.doi.org/10.5741/GEMS.44.1.32
Renfro N. (2015) Digital photomicrography for gemologists. *G&G*, Vol. 51, No. 2, pp. 144–159, http://dx.doi.org/10.5741/GEMS.51.2.144
Rudloff-Grund J., Brenker F.E., Marquardt K., Howell D., Schreiber A., O'Reilly S.Y., Griffin W.L., Kaminsky F.V. (2016) Nitrogen nanoinclusions in milky diamonds from Juina area, Mato Grosso State, Brazil. *Lithos*, Vol. 265, pp. 57–67, http://dx.doi.org/10.1016/j.lithos.2016.09.022
Shirey S.B., Shigley J.E. (2013) Recent advances in understanding the geology of diamonds. *G&G*, Vol. 49, No. 4, pp. 188–222, http://dx.doi.org/10.5741/GEMS.49.4.188
Smit K.V., Shirey S.B., Stern R.A., Steele A., Wang W. (2016) Diamond growth from C–H–N–O fluids in the lithosphere: evidence from CH_4 micro-inclusions and $\delta^{13}C$–$\delta^{15}N$–N content in Marange mixed-habit diamonds. *Lithos*, Vol. 265, pp. 68–81, http://dx.doi.org/10.1016/j.lithos.2016.03.015
Smit K.V., Myagkaya E., Persaud S., Wang W. (2018) Black diamonds from Marange (Zimbabwe): A result of natural irradiation and graphite inclusions. *G&G*, Vol. 54, No. 2, pp. 132–148, http://dx.doi.org/10.5741/GEMS.54.2.132
Smith E.M., Shirey S.B., Nestola F., Bullock E.S., Wang J., Richardson S.H., Wang W. (2016) Large gem diamonds from metallic liquid in Earth's deep mantle. *Science*, Vol. 354, No. 6318, pp. 1403–1405, http://dx.doi.org/10.1126/science.aal1303
Smith E.M., Shirey S.B., Richardson S.H., Nestola F., Bullock E.S., Wang J., Wang W. (2018) Blue boron-bearing diamonds from Earth's lower mantle. *Nature*, Vol. 560, No. 7716, pp. 84–87, http://dx.doi.org/10.1038/s41586-018-0334-5
Speich L., Kohn S.C., Wirth R., Smith C.B. (2017) The relationship between platelet size and the B′ infrared peak of natural diamonds revisited. *Lithos*, Vols. 278-281, pp. 419–426, http://dx.doi.org/10.1016/j.lithos.2017.02.010
Stukowski A., Bulatov V.V., Arsenlis A. (2012). Automated identification and indexing of dislocations in crystal interfaces. *Modelling and Simulation in Materials Science and Engineering*, Vol. 20, No. 8, p. 085007, http://dx.doi.org/10.1088/0965-0393/20/8/085007
Tang C.J., Neves A.J., Carmo M.C. (2005) On the two-phonon absorption of CVD diamond films. *Diamond and Related Materials,* Vol. 14, No. 11/12, pp. 1943–1949, http://dx.doi.org/10.1016/j.diamond.2005.08.060
Titkov S.V., Zudin N.G., Gorshkov A.I., Sivtsov A.V., Magazina L.O. (2003) An investigation into the cause of color in natural black diamonds from Siberia. *G&G*, Vol. 39, No. 3, pp. 200–209, http://dx.doi.org/10.5741/GEMS.39.3.200
Titkov S.V., Shigley J.E., Breeding C.M., Mineeva R.M., Zudin N.G., Sergeev A.M. (2008) Natural-color purple diamonds from Siberia. *G&G*, Vol. 44, No. 1, pp. 56–64, http://dx.doi.org/10.5741/GEMS.44.1.56
Wang W., Lu R., Moses T. (2009) Photoluminescence features of carbonado diamonds. *GIA Research News*, July 21, www.gia.edu/doc/Photoluminescence-Features-of-Carbonado-Diamonds.pdf
Win W.L., Lu R. (2009) Lab Notes: Assemblages of K-feldspar, hematite-magnetite, and quartz in etch channels. *G&G*, Vol. 45, No. 1, pp. 54–55.
Woods G.S. (1986) Platelets and the infrared absorption of type Ia diamonds. *Proceedings of the Royal Society A*, Vol. 407, No. 1832, pp. 219–238, http://dx.doi.org/10.1098/rspa.1986.0094

Unique Vanadium-Rich Emerald From Malipo, China

Yang Hu and Ren Lu

Emeralds were discovered in Malipo County in southwestern China more than 30 years ago. Malipo emeralds are still being extracted and are expected to be available over the next decade. This study provides a full set of data through standard gemological properties, inclusion scenes, color characteristics, and advanced spectroscopic and chemical analyses including Raman, XRD, micro UV-Vis-NIR, EPR, and LA-ICP-MS. Multiphase inclusions in Malipo emerald are distinct with various shapes and occasionally a colorless transparent crystal. Abundant vanadium substitutes for aluminum in the octahedral site and serves as the predominant coloring agent, leading to a yellowish green color. Among significant known deposits, Malipo emerald has a unique chemical composition in its combination of high V, low Cr, and moderate Fe, as well as high Li and Cs concentrations.

Malipo County in Yunnan Province of southwestern China is a valuable source of emerald (figure 1). The mine is located near the village of Dayakou in the Wenshan Autonomous Prefecture, about 30 km from the border city of Ha Giang, Vietnam (figure 2). Emerald was first mined as an accessory mineral from a tungsten deposit. Over the past two decades, large quantities of emerald have been extracted and collected as mineral crystal specimens or fashioned into carvings of traditional Chinese objects and themes. Some gem-quality crystals have been cut into cabochons for jewelry use (figure 3). This is the only commercial emerald source being actively mined in China.

Previous studies of Malipo emeralds focused mainly on the regional geology, metallogenic conditions, and mineralogical properties (Zhang et al., 1998, 1999; Zhang and Lan, 1999; Xue et al., 2010; Huang et al., 2015, 2017). However, some significant gemological features of these emeralds were still insufficiently studied, including multiphase inclusion scenes, color characteristics, and chemical composition analysis. These features significantly affect identification and evaluation, as well as geographic origin determination.

This article provides an overview of the history, resource potential, and geology for Malipo emeralds. Standard gemological techniques were used to characterize this material. Multiphase inclusion scenes

Figure 1. A traditional carved snuff bottle (7.5 × 11 cm) of emerald from Malipo with a lid made of garnet from the nearby town of Maguan. The carving also contains associated quartz at the bottom of bottle. Photo courtesy of Daowen Ye.

See end of article for About the Authors and Acknowledgments.
Gems & Gemology, Vol. 55, No. 3, pp. 338–352,
http://dx.doi.org/10.5741/GEMS.55.3.338

Figure 2. The emerald mine in Malipo County is located near the village of Dayakou in the southeastern region of Yunnan Province, about 20 km from the Vietnamese border. The red rectangle on the right corresponds to the geologic map of the emerald deposits in Dayakou in figure 6.

were summarized, and some inclusions and accessory minerals were identified by Raman and XRD. Above all, micro UV-Vis-NIR, LA-ICP-MS, and EPR were used to investigate the chemical composition, optical absorption, and color features of Malipo emeralds.

CULTURAL HERITAGE AND RESOURCE

Malipo County is part of Wenshan Autonomous Prefecture, known for the cultural heritage of its minority ethnic groups. Two prominent ethnic groups, the Miao and the Zhuang, wear distinctive ethnic dress and sumptuous silver jewelry (http://m.visitourchina.com/blog/detail-348.html). Numerous minority groups there have given birth to a rich and colorful culture that has been passed down from generation to generation. Wenshan Autonomous Prefecture's cultural heritage includes traditional folk literature, music, dance, art, architecture, crafts, and drama. In addition to this important cultural resource,

Figure 3. These gem-quality rough and polished emeralds from Malipo, used in the present study, show medium to intense yellowish green color. The polished emeralds range from 0.20 to 1.00 ct and the rough crystals from 1.75 to 3.00 ct. Photo by Yang Hu.

Figure 4. A collector's item, found in 2011, of emerald crystal specimens in matrix from the Dayakou mine in Malipo County, China. The longest emerald crystal measures about 93 mm. The matrix mainly consists of quartz, feldspar, and dark muscovite. Courtesy of Arkenstone, Robert Lavinsky collection.

Malipo County is known for its rich ore resources, namely the strategically important metal tungsten. Significant tungsten deposits were first discovered in 1943 (Jin et al., 1943), and 23 occurrences were located by 2012.

Emeralds were first discovered in the Malipo region in the late 1980s as associated minerals during tungsten mining. From 1996 to 1997, the regional geology and emerald resources in the area were systematically surveyed by the Yunnan Bureau of Geology and Mineral Resources. According to Wang et al. (1996), 22 pegmatites and 8 quartz veins related to emerald had been documented, with an estimated emerald reserve of about 7 tons.

Local villagers were collecting minerals and ore materials sporadically for years before government regulation. In 2009, the local government authorized a mining company to extract tungsten ore, and the associated emeralds were mined specifically from then on. Some of these emerald specimens have been acquired by domestic and international museums and private collectors (figure 4). At present, the tungsten mine is still in operation, and emeralds have also been produced in Dayakou (figure 5). But no emerald mining activity or production are reported officially by this government-authorized tungsten mining company.

With China's increasing awareness and interest in gems, the local government started to promote Malipo emerald as "Chinese emerald." Indeed, China's emerald industry is supported and protected by the local government. Public auctions for Malipo emeralds have been organized, and trading centers have been established. Moreover, gem and jewelry processing companies were created and introduced new techniques. Policies were enacted to protect emerald resources and to regulate the mining activity.

In Brief

- Emeralds from Malipo County, in southwest China's Yunnan Province, occur in association with quartz and pegmatite veins and Proterozoic granofels.
- The Malipo emerald deposit has produced mineral specimens, traditional carvings, and cabochons.
- Abundant V^{3+} in octahedral coordination is the predominant chromophore, leading to a yellowish green color.
- A distinctive combination of high V, low Cr, and moderate Fe, as well as high Li and Cs concentrations, helps separate Malipo emerald from other deposits.

Figure 5. The Malipo emerald mine is located to the right of the middle mountain ridge, about 1,800 meters above sea level. Residences are located at the foot of the mountain. Photo by Daowen Ye.

GEOLOGY

The Dayakou emerald occurrence lies in the northern part of the Laojunshan–Song Chay metamorphic core complex (Zhang et al., 1999; Feng et al., 2000). The core complex covers an area of approximately 2,000 km^2, and nearly one-third of that is in China. The Chinese counties of Malipo and Maguan and the Ha Giang Province of northern Vietnam are all in this area. The core complex is composed of a Proterozoic metamorphosed core and an upper cover of Paleozoic metasedimentary rocks (Zhang et al., 1998). The metamorphosed core consists of Silurian gneiss granites, Cretaceous porphyritic granites, and granitic to pegmatitic intrusions. Patches of the Proterozoic Mengdong succession are also situated locally within the core. The Mengdong succession consists of structurally layered metamorphic rocks: the basal Nanyangtian unit and the overlying Saxi unit (Zhang et al., 1999) (figure 6). The Nanyangtian unit is generally composed of schist. The Saxi unit is comprised of granofels, gneiss, amphibolites, and calcareous sedimentary rocks, with granofels as the main host rock for emerald mineralization at Dayakou (Xue et al., 2010).

Emerald at Dayakou generally occurs in northwest-southeast-trending quartz veins and northeast-southwest-trending pegmatite veins intruding deformed Proterozoic granofels, gneiss, and schist of the Nanyangtian and overlying Saxi units (Xue et al., 2010) (figure 6). Some emeralds also mineralize in the contact zone with host rocks. Dozens of emerald-bearing pegmatite veins cover an area of 10 km^2. The length of the ore body is between 20 and 280 m, and the width is 0.2 to 1.5 m. According to the classification of emerald type provided by Schwarz and Giuliani (2001), this is a granite-related emerald deposit (Groat et al., 2008).

In general, the emeralds that occur in the quartz veins at Dayakou are of better quality, with saturated green color and high transparency. In contrast, the emeralds within the pegmatite veins are larger, more abundant, and idiomorphic. Various associated minerals occur in emerald-bearing quartz and pegmatitic veins, such as potassic feldspar and mica, as well as minor scheelite, fluorite, calcite, tourmaline, and some sulfide assemblages (Zhang et al., 1999; Feng et al., 2000).

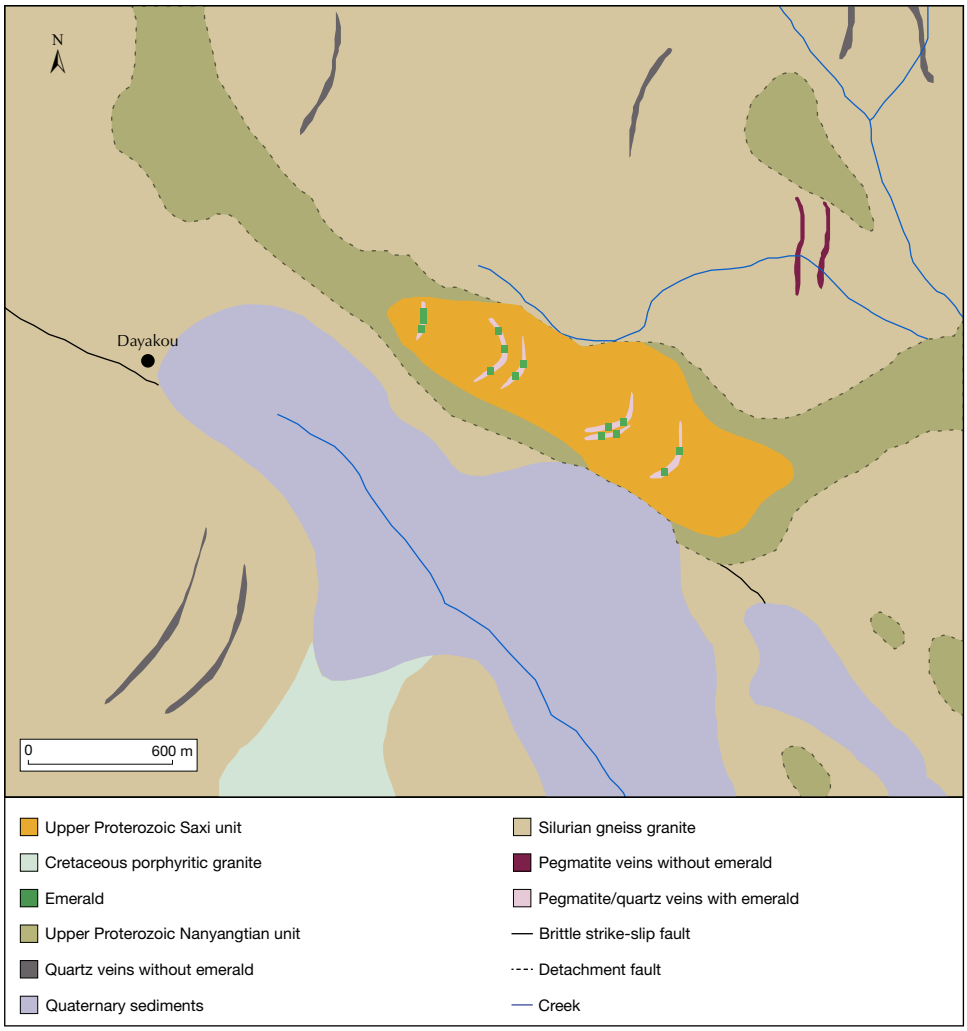

Figure 6. This simplified geologic map of the emerald deposit in Dayakou shows the distribution of major rock types and the main emerald occurrence. Modified from Wang et al. (1996).

MATERIALS AND METHODS

Twenty polished emeralds (figure 3), twenty-three rough crystals (three in figure 3 and twenty in figure 7), and three emerald-in-matrix specimens (one of them in figure 11) were gathered from local miners for this study. The miners extracted these samples privately in the area of the Dayakou emerald deposit. On average, the crystals measured a few centimeters in length, and the longest was 5 cm (figure 7). The cut emeralds ranged from 0.20 to 1.00 ct. Some crystals were contaminated by a brown material, possibly iron oxide, along the fractures and cavities.

All the emerald samples had been oiled by miners after extracting and/or polishing. Eight of the twenty rough samples in figure 7 were immersed in alcohol for two days to remove the oil before sample processing. Then they were fabricated as optical wafers (1.5–2 mm thick) oriented either perpendicular or parallel to the crystal's c-axis. In addition, the black matrix (see figure 11) was prepared as optical wafers to determine the associated minerals.

Gemological properties were measured on eight emerald wafers and twenty polished stones. Refractive indices and birefringence were obtained with a gem refractometer. UV fluorescence was examined under a UV lamp with long-wave (365 nm) and short-wave (254 nm) light in a darkened box. We also tested their reaction under the Chelsea filter. Dichroism was observed and photographed under a polarizing film. Specific gravity was determined by the hydrostatic method. The wafers' optical path length was measured using a digital caliper with an accuracy of 20 microns. Inclusions were observed and photographed at up to 256× magnification by a Leica M205A microscopic system equipped with bright-field and fiber-optic illumination as well as a polarizing attachment.

Raman spectra were obtained with a Bruker Senterra R200 spectrometer coupled with a 532 nm laser to identify the associated mineral assemblages of the host rock and inclusions. The resolution was set at 5 cm^{-1}, and the laser energy was 20 mW. Two scans with 20 s integration time for each scan were taken for a single spectrum. Raman spectra from at least three spots on each sample were recorded to ensure the consistency of the data. X-ray powder diffraction (XRPD) was carried out on associated mineral assemblages from 3° to 64° on a PANalytical X'pert Pro diffractometer with Cu-Kα radiation (λ = 1.5405 Å, 40 kV, 40 mA), using a step size (2θ) of 0.02° and a step time of 0.15 s each.

Trace element contents of eight emerald wafers were analyzed by laser ablation–inductively coupled plasma–mass spectrometry (LA-LCP-MS) using an Agilent 7700 ICP-MS combined with a GeoLas 193 nm laser. We set the laser fluence at 9 J/cm^2 with a 6 Hz repetition rate and the laser spot size at 44 μm diameter. Element concentrations were calibrated against multiple reference materials (BCR-2G, BHVO-2G, and BIR-1G) without using an internal standard (Liu et al., 2008), and Al was chosen as the normalizing element. Standard reference material NIST 610 glass was also applied to time-drift correction. Three laser spots for each sample were applied on a clean area with uniform yellowish green color, where UV-Vis-NIR spectra were also collected.

The absorption coefficients were calculated based on the Beer-Lambert Law with polarized ultraviolet/visible/near-infrared (UV-Vis-NIR) spectra of eight emerald wafers. These spectra were recorded by a Jasco MSV-5200 micro-spectrometer equipped with a microscope and a Glan-Taylor polarizer system over the range of 250–2500 nm with 1 nm bandwidth in the UV-Vis region and 8 nm bandwidth in the NIR region, at a scan speed of 200 nm/min. The optical aperture was set at 200 nm and 0.5 nm data interval. Both ordinary ray (o-ray) and extraordinary ray (e-ray) spectra were obtained for each sample. Electron paramagnetic resonance (EPR) spectroscopy was performed by a JEOL JES-FA200 EPR spectrometer at the X-band (9.1536 GHz microwave frequency, 5 mW microwave power) with the crystal c-axis parallel and normal to the magnetic field H (H∥c and H⊥c) at room temperature (300K). Measurement parameters were set at 3200 Gauss center field, 5000 Gauss sweep width, 30 s sweep time, 0.03 ms time constant, and 100 kHz modulation frequency.

RESULTS

Gemological Properties. The Malipo emeralds typically showed medium to intense yellowish green color. Color zoning was present in some crystals per-

Figure 7. A group of medium- to low-quality rough Malipo emerald crystals were investigated in this study. Eight of them were processed as optical wafers for LA-ICP-MS, UV-Vis-NIR, and EPR measurements, as well as for color zoning study. Associated minerals and brown contaminant were present on some crystals. The crystals shown here average a few centimeters in length. Photo by Yang Hu.

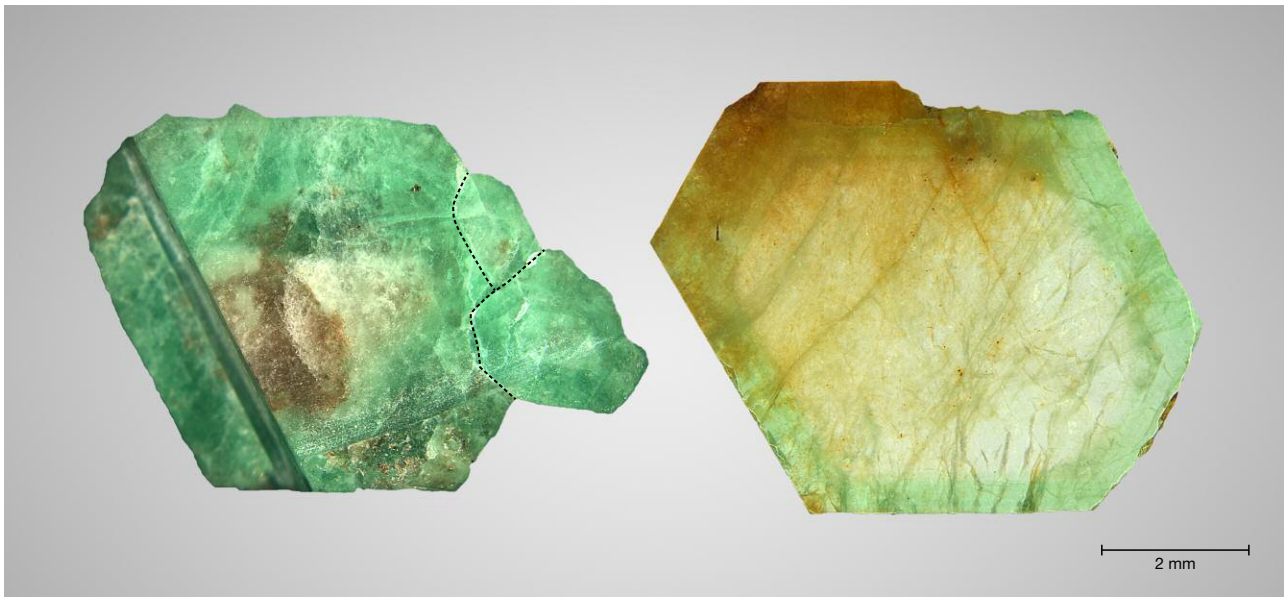

Figure 8. Color zoning in Malipo emerald crystals perpendicular to the c-axis ranges from a yellowish green rim to a colorless or white core. The sample on the left shows parallel intergrowth of at least three crystals (labeled by the black dotted line). Photo by Yang Hu.

pendicular to the c-axis, ranging from a yellowish green rim to a colorless core (figure 8). Some samples were near-transparent to translucent owing to the presence of fractures along and/or normal to the c-axis. Parallel growth striations were seen on prismatic faces. In addition, we observed parallel intergrowth for some emerald crystals (e.g., the one on the left in figure 8).

The refractive indices varied from 1.576–1.582 for n_e and 1.582–1.589 for n_o. Birefringence ranged from 0.006 to 0.008. Specific gravity was 2.66–2.71. Malipo emerald had no reaction under the Chelsea filter. No fluorescence was shown under either long-wave or short-wave UV. Under a polarizing film, bluish green could be observed along the e-ray and yellowish green along the o-ray.

Microscopic Characteristics. Two-phase inclusions with a gas bubble suspended in fluid were the most common inclusion in Malipo emeralds (figure 9). These two-phase inclusions were several to hundreds of microns long, and the width ranged from several to tens of microns. The inclusions displayed various shapes: rectangular, rod-like, needle-like, jagged, and oval or some irregular shapes. The gas bubble usually occupied less than one-third of the volume of the cavity hosting the two-phase inclusion at room temperature. Gas bubbles were sometimes deformed and flattened owing to the outline of the two-phase inclusions. The hosted gaseous phase was identified by Raman spectra as CO_2 and N_2. In addition, dense growth tubes oriented parallel to the c-axis were present in some samples.

Occasionally, a colorless transparent crystal was observed in the multiphase inclusions (figure 10). When observed, these crystals were slightly smaller than the accompanying gas bubbles. The outline of the crystals was near-cubic or irregular, and they were absent in adjacent multiphase inclusions of the same mineralization period. They were somewhat different from the common cubic halite in multiphase inclusions. It was also difficult to determine if they were singly or doubly refractive under cross-polarized illumination. Therefore, we could not confirm whether the crystal was halite, or beryl itself, or other minerals. Huang et al. (2017) determined the presence of halite in Malipo emeralds based only on the oval outline of the crystal. Thus far, no specific evidence of halite in multiphase inclusions has been confirmed in Malipo emeralds.

Various associated minerals were identified by Raman spectra and XRPD in the host rock of our samples, including microcline, calcite, quartz, tourmaline (likely foitite), fluorite, phlogopite, pale yel-

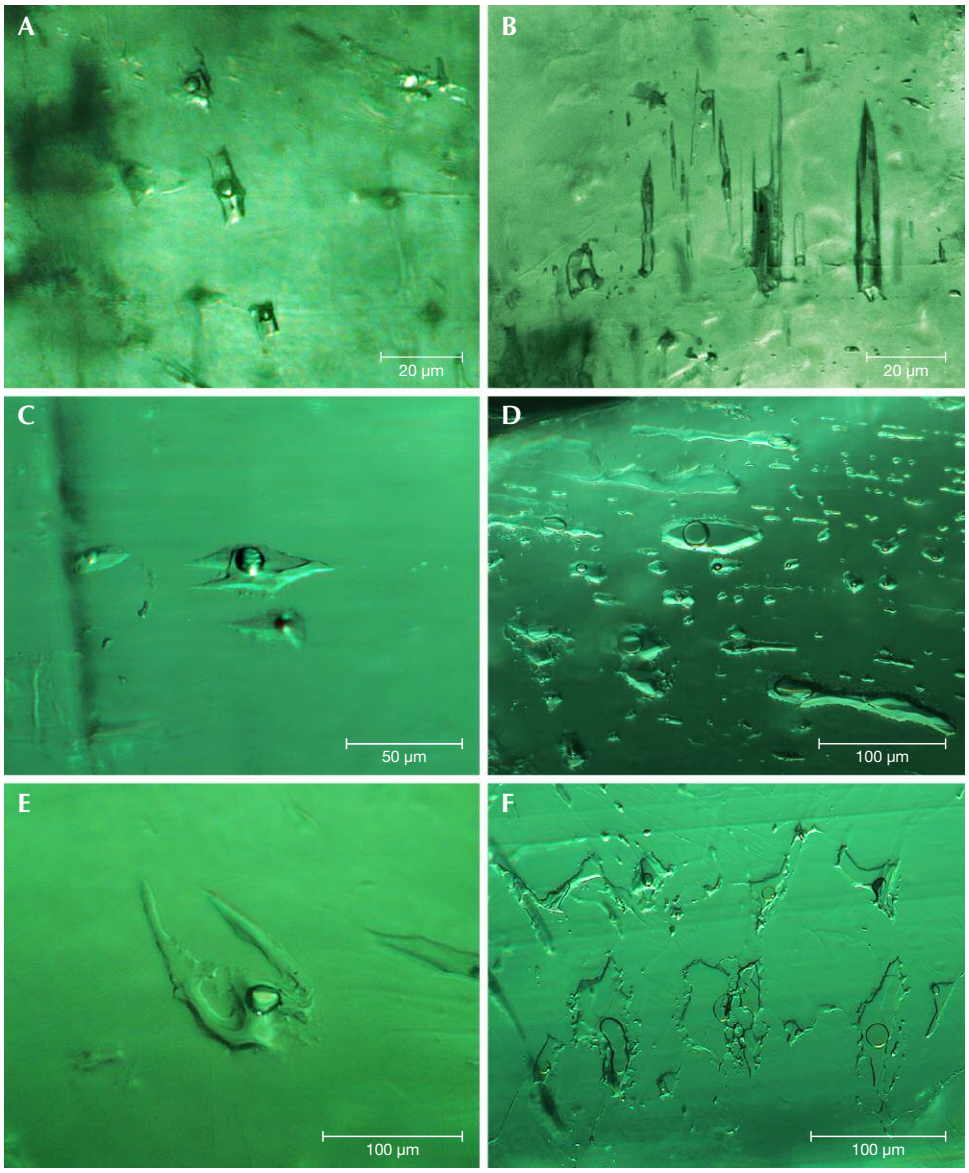

Figure 9. Variously shaped two-phase inclusions in Malipo emeralds. A: Rectangular two-phase inclusions containing round gas bubbles. B: Needle-like two-phase inclusions hosting small gas bubbles. C: A jagged two-phase inclusion with a round gas bubble inside. D: Rod-like and oval two-phase inclusions parallel to the c-axis. E and F: Irregular two-phase inclusions hosting round or deformed bubbles. Photomicrographs by Yang Hu, brightfield illumination.

low scheelite, and pyrrhotite (figure 11). Scheelite is an especially significant ore mineral for extracting tungsten in the nearby Dayakou tungsten mine. It displayed pale orange color, octahedral shape, and strong bluish fluorescence under short-wave UV. Some of these associated minerals were sometimes seen in Malipo emeralds as single-phase inclusions.

Trace Element Analysis. Eight Malipo emerald wafers were analyzed by LA-ICP-MS, and the results are shown in table 1. Concentrations of alkali metals ranged from highest content to lowest as follows: Na 6003–9481 ppmw (averaging 7524 ppmw), Cs 1730–2560 ppmw (averaging 2087 ppmw), Li 259–350 ppmw (averaging 306 ppmw), K 83–301 ppmw (averaging 155 ppmw), and Rb 18–32 ppmw (averaging 25 ppmw). Total alkali element concentrations including Li, Na, K, Rb, and Cs ranged from 8318 to 12403 ppmw. Malipo emerald also contained a significant amount of Mg (3941–7406 ppmw), and trace amounts of Sc (71–168 ppmw), Zn (17–187 ppmw), and Ga (12–15 ppmw).

The emerald samples contained abundant transition element V from 966 to 4568 ppmw, averaging 3473 ppmw, and a lower amount of Cr (3–870 ppmw, averaging 186 ppmw). Chromium content was as low as 3 ppmw in sample E4. The ratio of Cr to V was between 0.001 and 0.20. Iron content varied in a relatively narrow range from 2519 to 3770 ppmw and averaged 3474 ppmw. Trace amounts of Mn (averag-

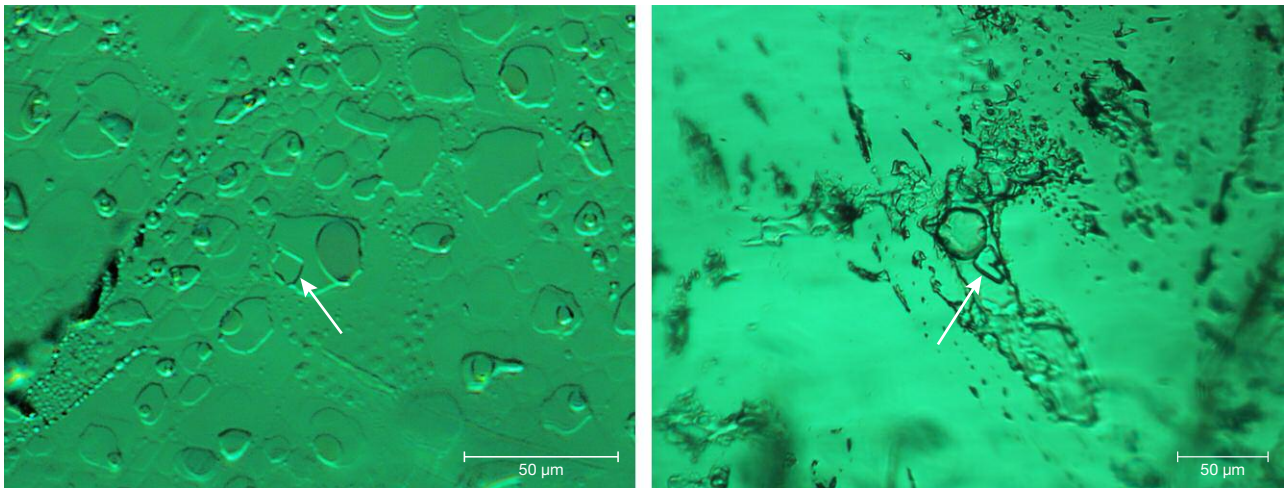

Figure 10. Three-phase inclusions in Malipo emeralds, shown in brightfield illumination. Colorless transparent crystals with near-cubic (left) or irregular shape (right) were visible (indicated by the arrows), along with oval to near-round gas bubbles in the blocky and irregular multiphase inclusions. Photomicrographs by Yang Hu.

ing 70 ppmw) were also detected. It is worth noting that the low Cr concentrations listed in table 1 were all detected from yellowish green zones instead of colorless zones. The low Cr content and the presence of Fe could be responsible for the lack of UV fluorescence in Malipo emeralds.

Figure 11. An emerald-in-matrix hand specimen associated with microcline, quartz, pale yellow scheelite, phlogopite, and pyrrhotite. Photo by Yang Hu.

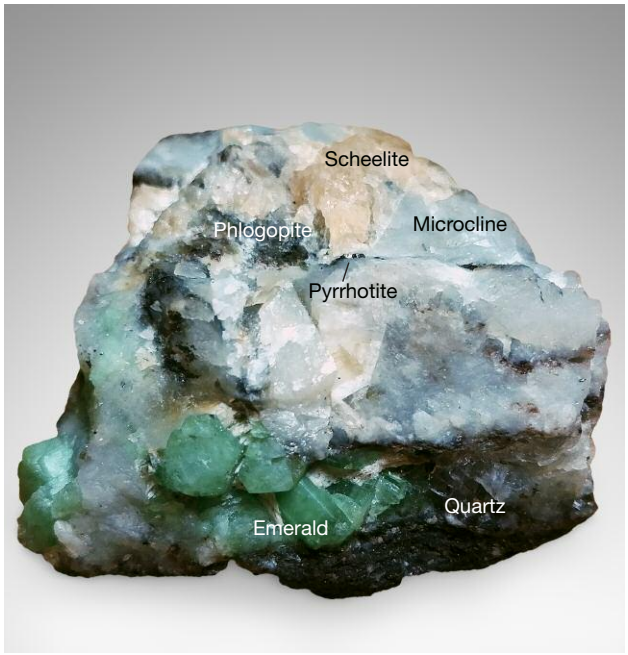

UV-Vis-NIR Spectroscopy. Representative UV-Vis-NIR spectra of Malipo emerald samples showed quantitative information on chromophoric absorption (250–1100 nm) and water molecular vibrations (900–2500 nm); see figure 12. Relative contributions from all absorption features are readily compared across the whole spectral range.

The region of chromophoric absorption (250–1100 nm) showed the main absorption of trivalent vanadium ions. Two absorption maxima at 432 and 611 nm (o-ray) and 425 and 644 nm (e-ray), as well as an absorption shoulder at 395 nm for the o-ray and e-ray in sample E7, were assigned to V^{3+} ions, according to the absorption of vanadium-doped synthetic emerald (Schmetzer et al., 2006). This absorption assignment was in agreement with our EPR result, theoretical crystal field energy levels of V^{3+} in beryl (Beckwith and Troup, 1973; Schmetzer et al., 1978), and distinctly higher vanadium content in Malipo emerald. These absorptions of V^{3+} were prominent in all of our emerald samples.

The anisotropic absorption of V^{3+} at 425–432 nm was obvious. The maximum absorption coefficient at 425–432 nm in the o-ray was nearly twice as high as in the e-ray. In addition, a weak shoulder centered at 675 nm was present for the o-ray. It was not a sharp line and obvious in the o-ray, distinguished

TABLE 1. Chemical composition (in ppmw) of eight Malipo emeralds, obtained by LA-ICP-MS.

	E2			E3			E4			E6			E7			E8			E9			E10			Detection limit (ppmw)
Li	347	343	333	285	288	342	315	308	309	302	308	300	259	264	261	326	306	312	338	350	341	267	274	273	0.2
Na	9481	8749	8725	6003	6095	7375	9344	9180	9186	7236	7301	7585	6340	6173	6381	7970	8261	8053	6489	6924	6253	7123	7053	7286	4.8
Mg	7406	6609	6853	3941	4002	4981	7349	7375	7216	5432	5430	5783	4363	4387	4512	5977	6301	6257	4787	4895	4581	5438	5360	5624	0.2
K	159	284	155	122	97	125	229	196	200	146	151	161	128	128	128	115	126	123	83	301	97	159	148	172	14.7
Sc	168	160	164	82	79	71	142	152	154	113	108	104	143	132	137	100	114	119	156	159	163	126	128	129	0.3
V	4015	3349	3502	1013	999	966	4416	4554	4654	3368	3313	3420	3814	3757	3811	3346	3384	3479	4568	4489	4455	3464	3485	3731	0.1
Cr	118	99	109	65	66	67	3	3	4	20	18	225	109	99	110	115	108	105	857	847	870	133	132	182	1.8
Mn	71	89	68	68	64	96	66	68	66	74	73	76	53	52	53	78	83	86	68	72	69	65	66	64	1.1
Fe	3545	3133	3248	2810	2706	3088	3728	3689	3770	3260	3554	3537	2809	2886	2850	3182	3429	3392	2588	3064	2519	3486	3518	3578	30.2
Zn	27	187	27	17	22	17	35	34	31	33	32	35	29	25	27	23	21	24	15	19	16	32	34	30	0.5
Ga	13	13	13	14	13	14	15	14	15	15	13	14	13	13	12	13	14	13	13	12	13	15	15	14	0.2
Rb	27	25	28	20	21	22	30	32	31	26	22	28	22	23	23	22	24	25	18	18	19	27	26	29	0.2
Cs	1876	2117	2158	1990	1915	2103	2485	2405	2317	1976	2028	1841	1730	1731	1752	2029	2179	2205	2513	2498	2560	1900	1898	1888	0.1
Cr/V	0.029	0.030	0.031	0.065	0.066	0.070	0.001	0.001	0.001	0.006	0.005	0.066	0.029	0.026	0.029	0.035	0.032	0.030	0.188	0.189	0.195	0.038	0.038	0.049	

Data of three spots in yellowish green area for each sample were reported.
ppmw = parts per million by weight.

from *R* lines of Cr^{3+}. This shoulder was also shown in emerald sample E4, which had almost no Cr (3–4 ppmw). Therefore, this 675 nm shoulder should also be attributed to vanadium ions.

A moderate 830 nm absorption band was present for the o-ray of sample E7. This band has usually been attributed to specific Fe^{2+} ions (Wood and Nassau, 1968). All other emerald samples showed a similar 830 nm band height and an absorption coefficient unit no higher than 4 cm^{-1}, consistent with the narrow range of Fe content (2519 to 3770 ppmw). This band height range was typical for Malipo emeralds.

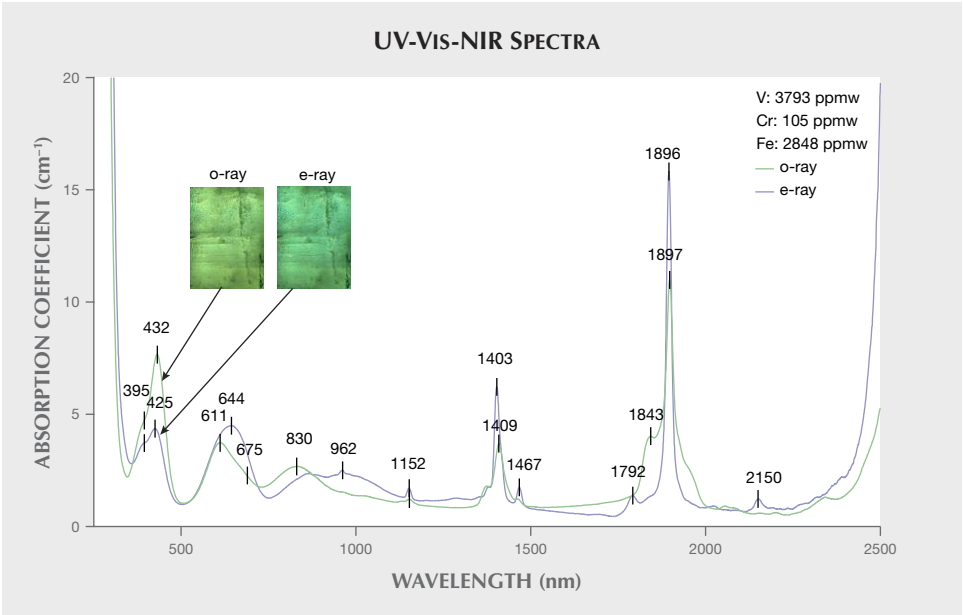

Figure 12. Representative UV-Vis-NIR spectra of sample E7. In the region of chromophoric absorption, it shows intense V^{3+} absorption (432 and 611 nm for the o-ray, 425 and 644 nm for the e-ray, and a 395 nm shoulder for the o- and e-rays) and moderate Fe^{2+} absorption (830 nm for the o-ray). Type I water absorption is shown at 1897, 1896, 1792, 1467, and 1403 nm. The inset photos display obvious dichroism: a yellowish green color for the o-ray and a bluish green color for the e-ray. Chromophore element contents of sample E7 are shown on the top right.

No other Fe-related absorption was observed in any of the samples, such as the band centered at 620 nm or the 427 and 372 nm peaks seen in emeralds from other localities.

Weak Cr^{3+} absorption was sometimes accompanied by absorptions of V^{3+} and Fe^{2+} ions in the samples. According to Wood and Nassau (1968), Cr^{3+} in emerald could lead to the main absorption bands at approximately 430 and 600 nm for the o-ray and 420 and 630 nm for the e-ray. These absorption bands were superimposed over those of vanadium ions, but a series of weak peaks at 658, 646, and 637 nm and sharp *R* lines at 680/683 nm were distinctive for Cr^{3+} in emerald, especially for the e-ray. Absorption of Cr^{3+} ions was not observed for the low Cr content (105 ppmw) in sample E7. But other Malipo emerald samples with slightly higher Cr content displayed a series of weak peaks (658, 646, and 637 nm) and *R* lines, such as sample E9, which averaged 858 ppmw Cr. Specifically, 680/683 nm *R* lines were superimposed on the broad V^{3+} shoulder centered at 675 nm for the o-ray.

In the region of water molecular vibrations (900–2500 nm), Malipo emerald showed absorption of type I water molecules. Water molecules in beryl occur in two configurations in structural channels called "type I" and "type II" (Wood and Nassau, 1967). Peaks between 1100 and 2500 nm were attributed to the overtone and combination vibrations of type I and/or type II water molecules. Strong peaks at 1897 nm (5271 cm^{-1}), 1896 nm (5274 cm^{-1}), and 1403 nm (7127 cm^{-1}), as well as weak peaks at 1792 nm (5580 cm^{-1}) and 1467 nm (6816 cm^{-1}), were displayed for all the samples (figure 12), and these peaks were assigned to type I water (Wood and Nassau, 1967). So Malipo emeralds were dominated by type I water, the same as most emeralds from other major sources except Kafubu, Zambia (Saeseaw et al., 2014). Sodium ions interacted with adjacent type II water molecules in the channels, and the low content of type II water was in agreement with the low Na content in Malipo emeralds.

EPR Spectra. Electron paramagnetic resonance (EPR) is an electron absorption technique using magnetic fields to measure transition energy of impurity elements, radicals, or defects with unpaired electrons. EPR spectra can provide useful information for transition metal impurities on valence, ion occupation, site symmetry, and pair arrangements in crystals.

For the EPR of Malipo emeralds (figure 13), the signal of transition metal impurities differed greatly, with the c-axis either parallel to the magnetic field H (H∥c) or normal to the magnetic field H (H⊥c). Two strong peaks were detected at g = 2.866 and g = 1.968 in orientation H∥c. Peaks centered at g = 1.968 and their side peaks were assigned to Cr^{3+} ions. Because of the large zero-field splitting of Cr^{3+} ions, only one set of EPR (transition from m_s = +1/2 to –1/2) could be seen in the X-band (Ohkura et al., 1987). This Cr^{3+} center may also be overlapped by Fe^{3+} ion–related centers for similar g factors. The assignment of the peak at g = 2.866 was uncertain. In orientation H⊥c, the characteristic six-fold hyperfine structure of Mn^{2+} (m_s = +1/2 to –1/2) was shown (Gaite et al., 2001). The peak at g = 3.893 probably arose from the Fe^{3+} ion (Lin et al., 2013).

The super-hyperfine structure of V^{2+} and V^{4+} in the form of vanadyl ions (VO^{2+}) was previously detected in Australian emerald and Biron gamma-irradiated vanadium-doped synthetic emerald by X-band EPR at room temperature (Hutton et al., 1991). But we were unable to detect any obvious EPR signal of V^{2+} or V^{4+}, indicating that the abundant vanadium detected in Malipo emerald should be in another valence state. Vanadium in minerals is usually present in the valence of +3 and +4 (Rossman, 2014). V^{3+} ($3d^2$) was hardly detectable by room temperature X-band EPR due to outer paired electrons. Thus, we concluded that nearly all vanadium in Malipo emerald was in the trivalent state.

Figure 13. EPR spectra of Malipo emerald E7 showed signals of Cr^{3+}, Mn^{2+}, and possibly the Fe^{3+} center, and no indications of any vanadium signal measured at 300 K.

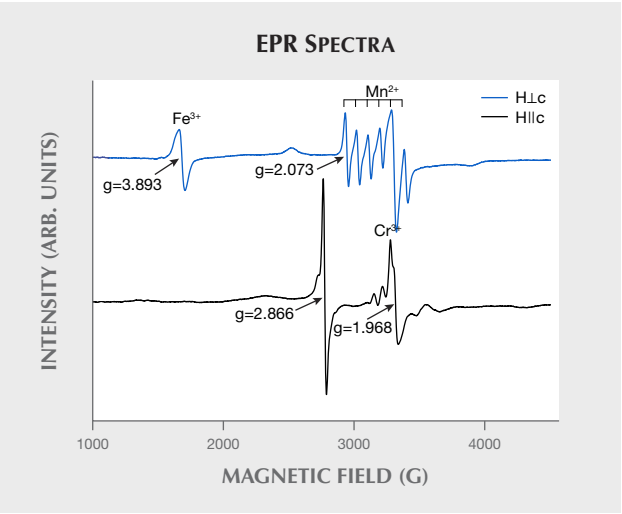

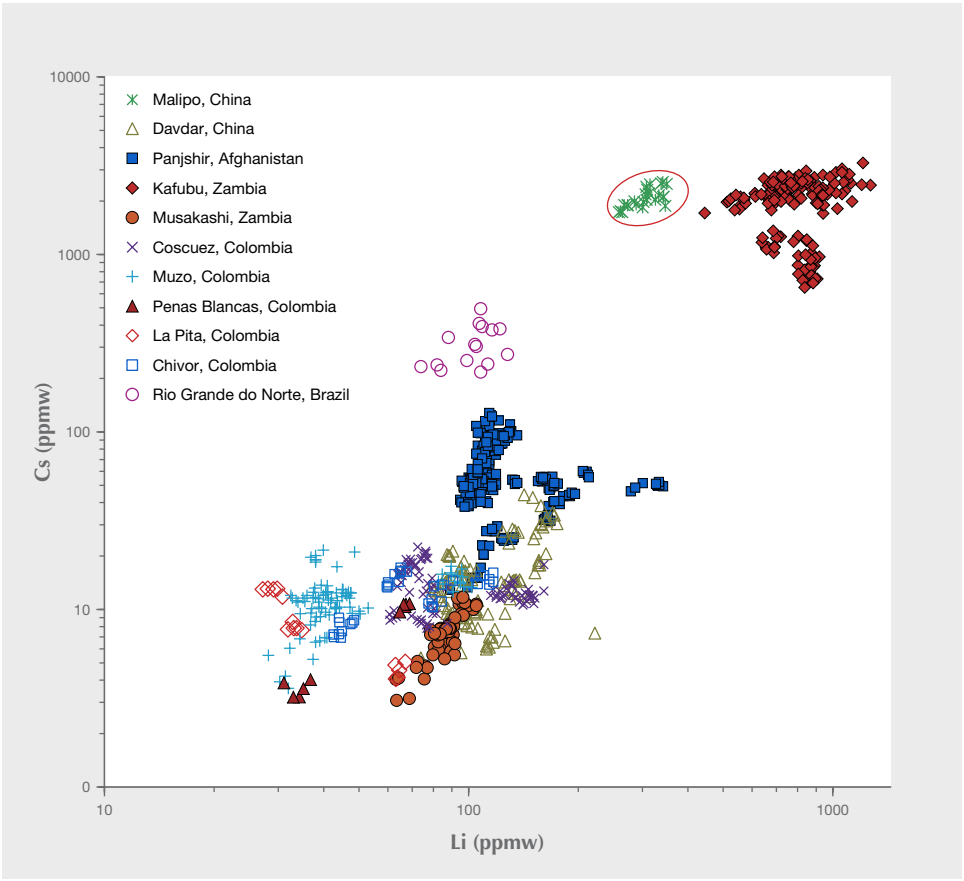

Figure 14. Malipo emeralds contained high concentrations of Li and Cs (within the red oval) and a unique ratio of Li to Cs among significant deposits. Other sources are from Saeseaw et al. (2014).

DISCUSSION

Multiphase Inclusions. The multiphase inclusion scene in Malipo emerald was quite distinct from that of other deposits investigated by Saeseaw et al. (2014). First, the multiphase inclusions in Malipo emerald were relatively small, less than two hundred microns in length and width. Second, multiphase inclusions in Malipo emerald displayed rectangular, rod-like, needle-like, jagged, and other irregular shapes. The rectangular multiphase inclusions were similar to those of emerald from Kafubu, Zambia. Elongated needle-like multiphase inclusions somewhat resembled those in emerald from Panjshir Valley, Afghanistan. Jagged multiphase inclusions resembled classic jagged multiphase inclusions in Colombian emeralds. Moreover, the crystal phase as part of a multiphase inclusion was occasionally observed in our samples. But emeralds from Kafubu, Panjshir, and Colombia usually host one or more crystals.

Trace Element Analysis. Malipo emeralds contained large amounts of Li and Cs, and the ratio of Cs to Li distinguished them from emeralds of all other significant localities. Li concentration in our emerald samples was relatively high (259–350 ppmw), just below that of Kafubu, Zambia, despite a slight overlap with emeralds from Panjshir, Afghanistan (see figure 14). Meanwhile, Cs concentration was the highest (1730–2560 ppmw) among all other deposits except Kafubu, which has a similar range of Cs content. Therefore, the ratio of Cs to Li was exclusively separate from other significant deposits. Concentrations of other alkali elements (Na, K, and Rb) and Mg, Sc, Zn, and Ga were low to moderate in Malipo emeralds, and more or less overlapped with those from some other deposits.

The combination of high V, low Cr, and moderate Fe content was distinctive for Malipo emeralds, as seen in the Fe-Cr-V ternary diagram in figure 15. V content was relatively high (averaging 3473 ppmw), just below some emeralds from Colombia and Norway, behaving as the most significant chromophore element in Malipo emerald. Meanwhile, Cr content was extremely low (averaging 186 ppmw) and similar to emeralds from Lened, Canada, and Gandao, Pakistan. Fe concentration was medium (averaging 3474 ppmw), in the same range as emeralds from many lo-

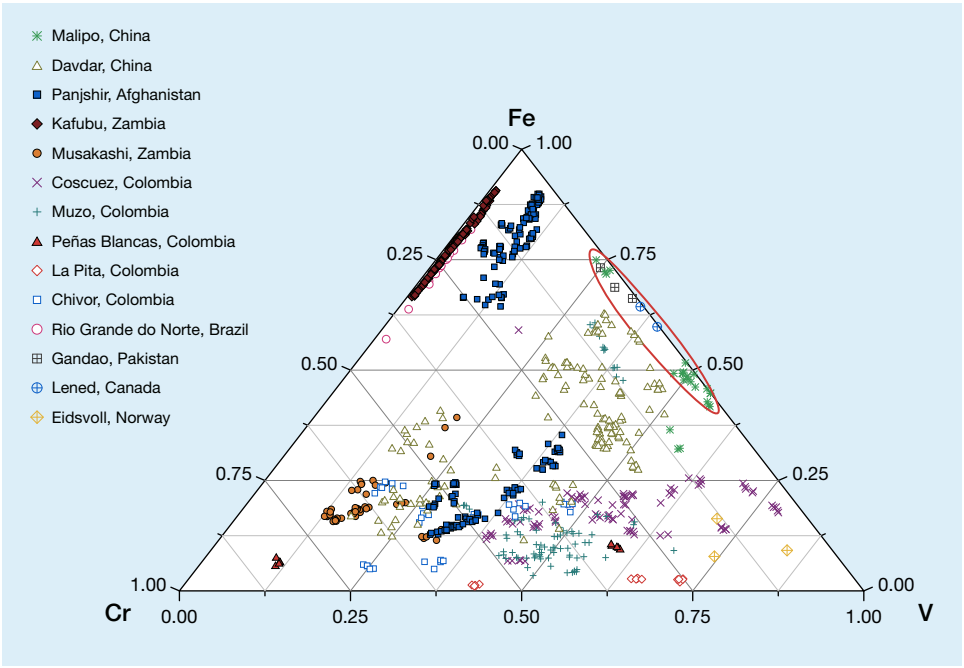

Figure 15. Plot of Fe–Cr–V (ppmw) chemical composition for emeralds from Malipo and other localities. The plot field of Malipo emeralds (within the red oval) was distinctive for the combination of high V, low Cr, and moderate Fe content. Other sources are from Hammarstrom (1989), Marshall et al. (2004), Rondeau et al. (2008), Marshall et al. (2012), Zwaan et al. (2012), and Saeseaw et al. (2014).

calities. Moreover, the plot field of Fe-Cr-V chemical composition was quite distinctive for Malipo emerald, though there was some overlap with Gandao and Lened emeralds. Li and Cs contents were previously unreported for Gandao emerald, and Cs content (850–1590 ppmw) of Lened emerald (Marshall et al., 2004) was just slightly lower than that of Malipo emerald. Therefore, concentrations of Li and Cs were not available to effectively separate Gandao and Lened emeralds. As emeralds from these two deposits are not found in large quantities on the gem market, this overlap has little influence on geographic origin determination. In addition, Li and Cs concentrations of Malipo emerald were close to Kafubu, but the difference in Fe-Cr-V chemical composition offered a straightforward means to distinguish them.

Color Characteristics. Trivalent vanadium was the predominant chromophore for Malipo emeralds, leading to a typically yellowish green color. Malipo emerald contained distinctly high vanadium content and showed the main absorption of V^{3+} ions in the visible light region. Ionic radii of V^{3+} (0.640 Å) were close to Al^{3+} (0.535 Å) in the six-fold coordinated octahedral site (Shannon, 1976), facilitating effective substitution of isovalent V^{3+} for Al^{3+} in the AlO_6 octahedral site. The AlO_6 octahedron is the key coloring structural unit in both beryl and a few important gems (e.g., sapphire, jadeite, and chrysoberyl). Their coloring characteristics from Cr^{3+}, Fe^{2+}, Fe^{3+}, and V^{3+} appear to follow the typical crystal field behaviors of AlO_6 octahedra, which directly lead to gem colors. Incorporation of abundant V^{3+} ions in the AlO_6 octahedral site was responsible for the yellowish green color of Malipo emeralds. Compared with emerald colored by Cr^{3+} ions, the color caused by V^{3+} tended to be more yellowish, owing to stronger absorption in the violet to blue region.

A significant anisotropic absorption band at 425–432 nm is an important spectral feature of V^{3+} in the AlO_6 octahedral site of beryl and other minerals, such as corundum. V^{3+} ions substituting in similar AlO_6 octahedra led to the anisotropic absorption centered at 400 nm in synthetic vanadium-dominated corundum (author's unpublished data). The absorption coefficient in the o-ray was twice as high as in the e-ray for emerald sample E4, which had almost no Cr (3–4 ppmw). This coefficient difference is the maximum value. With the ratio of V to Cr increasing, the difference of absorption coefficient between the o-ray and the e-ray would become larger (o-ray>e-ray), no more than double in emerald. Moreover, this absorption difference led to a noticeable yellowish green color in the o-ray and bluish green color in the e-ray under a polarized film (see inset photos in figure 12). And the color of the o-ray tended to be more yellowish as the V to Cr ratio increased.

The chromophore effectiveness of V^{3+} was expected to be comparable to that of Cr^{3+} ions in emerald. Absorption cross section is a constant for a particular chromophore in a specific matrix and could be used as an indication of chromophore effec-

tiveness. Because an accurate cross section of V^{3+} and Cr^{3+} ions in emerald had not been investigated in previous studies, we estimated the cross section based on the Beer-Lambert law. Malipo emerald E7 contained V (3793 ppmw), a similar concentration level as the Cr (3347 ppmw) in Cr-dominated emerald (figure 21B in Saeseaw et al., 2014). The atomic weights of V and Cr are similar, and so are their atomic concentrations in ppma, which are used to compare the cross sections and chromophore effectiveness. At the same time, concentrations of Cr in sample E7 (105 ppmw) and V in Cr-dominated emerald (116 ppmw) were relatively low, so it was suitable to obtain the cross section of relatively pure V and Cr. These two emerald samples showed a similar range of absorption coefficients, less than 7 cm^{-1} for V^{3+} and Cr^{3+} absorption. So the calculated cross section of V^{3+} and Cr^{3+} should be similar. We concluded that the color effectiveness of Cr^{3+} and V^{3+} were comparable. In addition, Malipo V-rich emeralds and other Cr-rich emeralds containing similar amounts of V and Cr, respectively, demonstrated a similar range of color saturations. Several thousand ppma of V or Cr could lead to a relatively saturated greenish color for emerald. More quantitative data are needed to compare color effectiveness of Cr^{3+} and V^{3+} in the future.

Transition elements other than vanadium had little effect on coloration in our samples. The Cr ion absorption was rather weak for the low level of Cr content determined, so the coloration produced by Cr was weak for Malipo emeralds. The broad absorption band centered at 620 nm could add a bluish color to emerald, especially in the e-ray, caused by Fe^{2+}-Fe^{3+} pairs (Lin et al., 2013). However, this band was nearly invisible because of insufficient Fe content in Malipo emeralds. The tail of a moderate 830 nm Fe^{2+}-related band seems to extend slightly into the visible light region (again, see figure 12). Because the strong tail was also present in colorless beryl, this tail could not produce any visible color for the emerald samples.

CONCLUSIONS

A significant granite-related emerald occurrence is situated in Malipo County in China, a region with rich natural mineral and strategic ore resources. Mineral specimens, carvings, and faceted gems from the Malipo emerald deposit have been produced since the 1990s.

The scene of multiphase inclusions in Malipo emerald is distinctive, with various shapes and occasionally a colorless transparent crystal. Abundant vanadium (averaging 3473 ppmw) is the predominant chromophore, leading to a typically yellowish green color. Inadequate Fe and Cr contribute little to the color. The distinctive combination of high V, moderate Fe, and low Cr content separates this locality from most known emerald deposits. Moreover, the high Li and Cs content in Malipo emerald are unique among significant localities in the world, which can help in their geographic origin determination.

Emeralds have become part of the identity of Malipo as awareness of top-color stones has progressed in China in recent years. With abundant remaining emerald reserves, more production can be anticipated in the future.

ABOUT THE AUTHORS

Mr. Hu (huyang_gems@126.com) is a PhD student at the Gemological Institute, China University of Geosciences in Wuhan. Dr. Lu (renlu.cc@gmail.com) is a distinguished professor at the Gemological Institute, China University of Geosciences in Wuhan.

ACKNOWLEDGMENTS

The authors would like to thank Daowen Ye for providing Malipo emerald samples, valuable photos, and related information. We are also grateful to Dr. Robert Lavinsky for providing the photo from his collection. We sincerely thank Dr. George Rossman, Dr. Benjamin Rondeau, and an anonymous reviewer for their constructive comments and suggestions. This study was funded by the Center for Innovative Gem Testing Technology, China University of Geosciences (CIGTXM-S201821).

REFERENCES

Beckwith P.J., Troup G.J. (1973) The optical and infrared absorption of V^{3+} in beryl ($Be_3Al_2Si_6O_{18}$). *Physica Status Solidi*, Vol. 16, No. 1, pp. 181–186, http://dx.doi.org/10.1002/pssa.2210160119

Feng M.G., Zhang S.T., Lu W. (2000) Geological characters of the Chinese emerald deposit. *Yunnan Geology*, Vol. 19, pp. 37–42 [in Chinese].

Gaite J.M., Izotov V.V., Nikitin S.I., Prosvirnin S.Y. (2001) EPR and optical spectroscopy of impurities in two synthetic beryls. *Ap-*

plied Magnetic Resonance, Vol. 20, No. 3, pp. 307–315, http://dx.doi.org/10.1007/BF03162283
Groat L. A., Giuliani G., Marshall, D.D., Turner D. (2008) Emerald deposits and occurrences: a review. *Ore Geology Reviews*, Vol. 34, No. 1-2, pp. 87–112, http://dx.doi.org/10.1016/j.oregeorev.2007.09.003
Hammarstrom J.M. (1989) Mineral chemistry of emeralds and some associated minerals from Pakistan and Afghanistan: An electron microprobe study. In A.H. Kazmi and L.W. Snee, Eds., *Emeralds of Pakistan: Geology, Gemology & Genesis*. Van Nostrand Reinhold, New York, pp. 125–150.
Huang W.Q., Ni P., Shui T., Yang P. (2015) Mineralogical characteristics of emerald from Malipo, Yunnan Province. *Acta Petrologica et Mineralogica*, Vol. 34, No. 1, pp. 103–109 [in Chinese].
Huang W.Q., Shui T., Ni P. (2017) Fluid inclusion studies on emeralds from Malipo area, Yunnan Province, China. *Acta Mineralogica Sinica*, Vol. 37, No. 1/2, pp. 75–82 [in Chinese].
Hutton D.R., Darmann F.A., Troup G.J. (1991) Electron spin resonance of $V^{4+}(VO^{2+})$ in beryl. *Australian Journal of Physics*, Vol. 44, No. 4, pp. 429–434, http://dx.doi.org/10.1071/PH910429
Jin Y.H., Yang B.Q. (1943) Genesis and significance of Laojunshan scheelite deposit in Wenshan, Yunnan. *Geological Review*, Vol. 8, No. Z1, pp. 170–171 [in Chinese].
Lin J., Chen N., Huang D., Pan Y. (2013) Iron pairs in beryl: New insights from electron paramagnetic resonance, synchrotron X-ray absorption spectroscopy, and ab initio calculations. *American Mineralogist*, Vol. 98, No. 10, pp. 1745–1753, http://dx.doi.org/10.2138/am.2013.4472
Liu Y.S., Hu Z.C., Gao S., Günther D., Xu J., Gao C.G., Chen H.H. (2008) In situ analysis of major and trace elements of anhydrous minerals by LA-ICP-MS without applying an internal standard. *Chemical Geology*, Vol. 257, No. 1-2, pp. 34–43, http://dx.doi.org/10.1016/j.chemgeo.2008.08.004
Marshall D.D., Groat L.A., Falck H., Giuliani G., Neufeld H. (2004) The Lened emerald prospect, Northwest Territories, Canada: Insights from fluid inclusions and stable isotopes, with implications for Northern Cordilleran emerald. *Canadian Mineralogist*, Vol. 42, No. 5, pp. 1523–1539, http://dx.doi.org/10.2113/gscanmin.42.5.1523
Marshall D.D., Pardieu V., Loughrey L., Jones P., Xue G. (2012) Conditions for emerald formation at Davdar, China: fluid inclusions, trace element and stable isotope studies. *Mineralogical Magazine*, Vol. 76, No. 1, pp. 213–226, http://dx.doi.org/10.1180/minmag.2012.076.1.213
Ohkura H., Hashimoto H., Mori Y., Chiba Y., Isotani S. (1987) The luminescence and ESR of a synthetic emerald and the natural ones mined from Santa Terezinha in Brazil. *Japanese Journal of Applied Physics*, Vol. 26, No. 26, pp. 1422–1428, http://dx.doi.org/10.1143/JJAP.26.1422
Rondeau B., Fritsch E., Peucat J.J., Nordrum F.S., Groat L. (2008) Characterization of emeralds from a historical deposit: Byrud (Eidsvoll), Norway. *G&G*, Vol. 44, No. 2, pp. 108–122, http://dx.doi.org/10.5741/GEMS.44.2.108
Rossman G.R. (2014) Optical spectroscopy. *Reviews in Mineralogy and Geochemistry*, Vol. 78, No, 1, pp. 371–398, http://dx.doi.org/10.2138/rmg.2014.78.9
Saeseaw S., Pardieu V., Sangsawong S. (2014) Three-phase inclusions in emerald and their impact on origin determination. *G&G*, Vol. 50, No. 2, pp. 114–132, http://dx.doi.org/10.5741/GEMS.50.2.114
Schmetzer K. (1978) Vanadium III als Farbträger bei natürlichen Silikaten und Oxiden – ein Beitrag zur Kristallchemie des Vanadiums. Inaugural-Dissertation zue Erlangung der Doktorwürde des Naturwissenschaftlichen Gesamtfakultät der Ruprecht-Karl-Universität Heidelberg, 200 pp. [in German].
Schmetzer K., Schwarz D., Bernhardt H.J., Häger T. (2006) A new type of Tairus hydrothermally-grown synthetic emerald, coloured by vanadium and copper. *Journal of Gemmology*, Vol. 30, No 1/2, pp. 59–74.
Schwarz D., Giuliani G. (2001) Emerald deposits—a review. *Australian Gemmologist*, Vol. 21, pp. 17–23.
Shannon R.D. (1976) Revised effective ionic radii and systematic studies of interatomic distances in halides and chalcogenides. *Acta Crystallographica Section A*, Vol. 32, Part 5, pp. 751–767, http://dx.doi.org/10.1107/S0567739476001551
Wang H.Q., Zhang S.T., Zhang M.W., Lu W., Li K.G. (1996) 1:10000 geologic mapping at the Dyakou emerald showing: Yunnan, China. *Yunnan Geological Survey Report*, 33 pp. [in Chinese].
Wood D.L., Nassau K. (1967) Infrared spectra of foreign molecules in beryl. *The Journal of Chemical Physics*, Vol. 47, No. 7, pp. 2220–2228, http://dx.doi.org/10.1063/1.1703295
Wood D.L., Nassau K. (1968) The characterization of beryl and emerald by visible and infrared absorption spectroscopy. *American Mineralogist*, Vol. 53, No. 5, pp. 777–800.
Xue G., Marshall D., Zhang S., Ullrich T.D., Bishop T., Groat L.A., Thorkelson D.J., Giuliani G., Fallick A.E. (2010) Conditions for Early Cretaceous emerald formation at Dyakou, China: Fluid inclusion, Ar-Ar, and stable isotope studies. *Economic Geology*, Vol. 105, No. 2, pp. 339–349, http://dx.doi.org/10.2113/gsecongeo.105.2.339
Zhang L.J., Lan Y. (1999) Gemological characteristics and deposit geology of Yunnan emerald. *Acta Mineralogica Sinica*, Vol. 19, No. 2, pp. 189–197 [in Chinese].
Zhang S.T., Feng M.G., Lu W. (1998) Analysis of the Nanwenhe metamorphic core complex in southeastern Yunnan. *Regional Geology of China*, Vol. 17, p. 390–397 [in Chinese].
Zhang S.T., Feng M.G., Wang H.Q., Lu W., Yang M. (1999) Geological features and genesis of emerald deposit in Malipo County, Yunnan Province, China. *Geological Science and Technology Information*, Vol. 18, No. 1, pp. 50–54 [in Chinese].
Zwaan J.C., Jacob D.E., Häger T., Cavalcanti Neto M.T.O., Kanis J. (2012) Emeralds from the Fazenda Bonfim region, Rio Grande do Norte, Brazil. *G&G*, Vol. 48, No. 1, pp. 2–17, http://dx.doi.org/10.5741/GEMS.48.1.2

GEMS & GEMOLOGY® 2019

CONGRATULATIONS

This year, hundreds of readers participated in the 2019 *Gems & Gemology* Challenge. Entries arrived from around the world as readers tested their gemological knowledge by answering questions listed in the Spring 2019 issue. Those who earned a score of 75% or better received a GIA Certificate of Completion recognizing their achievement. Participants who scored a perfect 100% are listed below.

G&G Challenge Winners

Australia
Donna Drummond-Cooper
Hendrik Holmer
John Newman
Barbara Wodecki
Dennis C. Woods
Janet Woods

Belarus
Dmitry Stepanenko

Belgium
Sheila Sylvester

India
Sane Hemant

Italy
Chiara Piussi

Spain
Fernando Vázquez Garranzo

United Kingdom
Francesca Lawley

United States
Jean Bonebreak
Robert Campbell
Tameka Nicole Clark
Kenneth Fogelberg
Anna Gibbs
Douglas Kennedy
Paul Mattlin
Tim Richardson
Geraldine Vest
Colleen Walsh
Thomas Wendt
Alvin Zimmer

Answers

See pages 89–90 of the Spring 2019 issue for the questions.

1 (a), 2 (a), 3 (d), 4 (d), 5 (c), 6 (d), 7 (c), 8 (d), 9 (d), 10 (d), 11 (c), 12 (d), 13 (c), 14 (b), 15 (d), 16 (d), 17 (d), 18 (b), 19 (c), 20 (c), 21 (d), 22 (a), 23 (a), 24 (d), 25 (b)

Mineral Inclusions in Ruby and Sapphire from the Bo Welu Gem Deposit in Chanthaburi, Thailand

Supparat Promwongnan and Chakkaphan Sutthirat

The mineral inclusions of alluvial ruby and sapphire from the Bo Welu gem deposit in Thailand's Chanthaburi Province were collected and investigated. This deposit is directly related to a basaltic terrain. Raman spectroscopy and electron probe micro-analyzer (EPMA) measurements allow the identification of mineral inclusions of pyrope-rich garnet, sillimanite, high-Al diopside, sapphirine, nepheline, quartz, feldspar (mostly plagioclase), spinel, sulfide, anhydrite, and silicate melts in ruby and purple sapphire. Zircon, alkali feldspar (mostly with high Na content), monazite, columbite, and sulfide were identified in blue sapphire. This study represents the first report of several inclusions in ruby and sapphire from this gem deposit.

Occurrences of gem ruby and sapphire in Thailand are located in the provinces of Chanthaburi-Trat, Kanchanaburi, Phrae-Sukhothai, Ubon Ratchathani, Si Sa Ket, and Phetchabun (figure 1). However, a few main areas have been economically mined and supplied gems to the world market. Sapphire mines were once extensively operated in Kanchanaburi, but most have recently closed down. The Chanthaburi-Trat area has been the most significant source of Thai corundum, and a few small mines are still in operation there. The most famous source of Thai rubies is located in the Bo Rai deposit in the eastern part of Trat Province, close to the Cambodian province of Pailin (figure 1). What became known as "Siamese ruby" was first named from here and adjacent areas. Meanwhile, the main gem mining area for sapphire (yellow, green, and blue, along with golden star and black star sapphires) is the Bang Ka Cha deposit in western Chanthaburi (again, see figure 1). Most gem mines in the central deposits, around Khlung District within Chanthaburi Province, have supplied more sapphire than ruby (Vichit, 1992; Pattamalai, 2015).

The focus of this study, the Bo Welu gem field located in the central gem deposits, has been mined for both ruby and sapphire. Corundum from this area is generally heat-treated to enhance its color, especially the red (or purplish red) ruby and the blue sapphire (figure 2), which are in high demand, particularly within Thailand.

In Brief

- Various mineral inclusions are observed in Bo Welu ruby and sapphire. Although some of these minerals have already been reported as inclusions in Thai corundum, others are first reported here.
- Among the observations were nepheline, sillimanite, spinel, alkali feldspar, quartz, and anhydrite inclusions in ruby and purple sapphire, and columbite and sulfide inclusions in blue sapphire.
- Common mineral inclusions and their chemical compositions indicate different original formations of ruby and sapphire that appear to have the same thermal history of basaltic activity in this region.

Although gem mines in this area are not currently in operation, a few artisanal miners can be found working along streams during the rainy season. The rarity of Thai ruby ensures strong demand in the local and international markets and high value. The sapphires, meanwhile, possess a natural greenish blue color that becomes an intense blue after heating.

In this study, ruby and sapphire from Bo Welu were investigated to determine their mineral inclu-

See end of article for About the Authors and Acknowledgments.
Gems & Gemology, Vol. 55, No. 3, pp. 354–369,
http://dx.doi.org/10.5741/GEMS.55.3.354

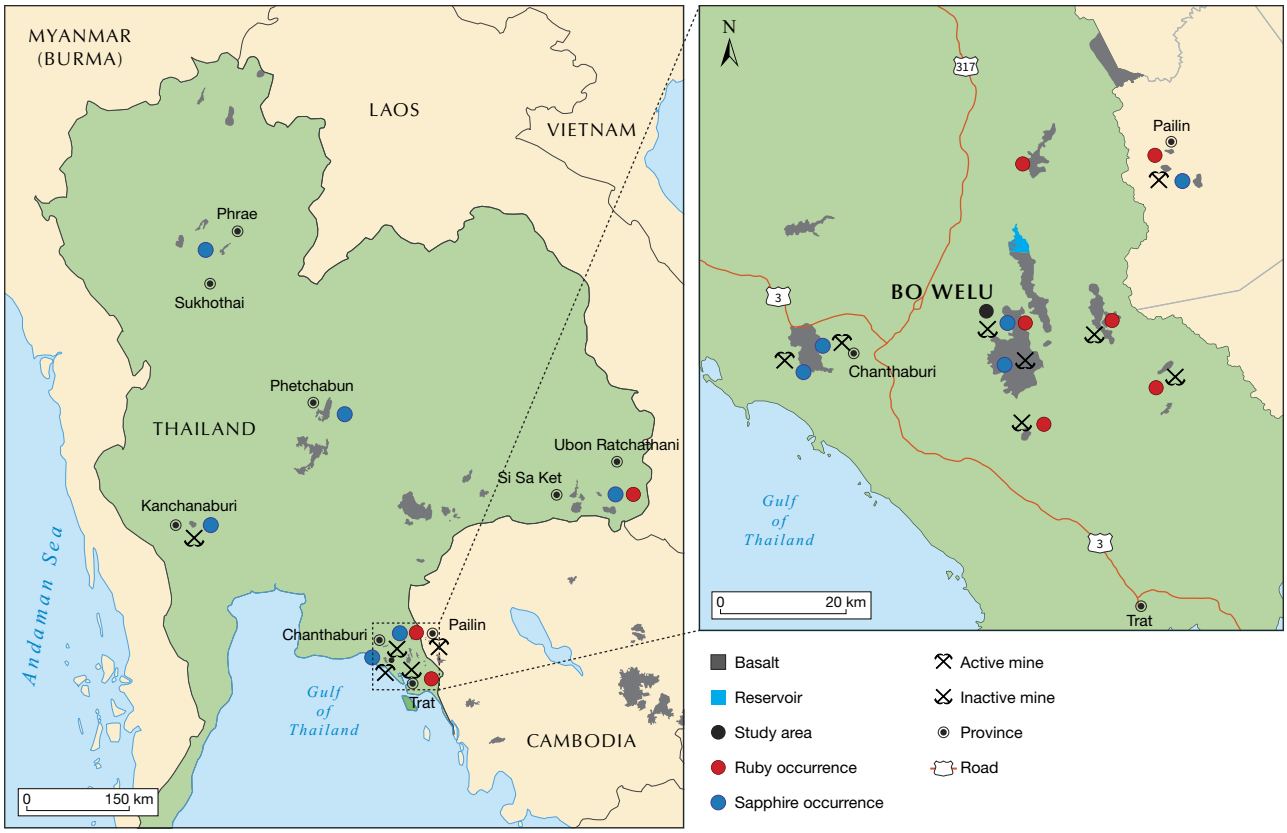

Figure 1. Left: Map of Thailand showing the distribution of basalt and corundum occurrences. Right: Ruby and sapphire deposits and associated basalts in Chanthaburi-Trat Province in eastern Thailand and Pailin Province in western Cambodia. Modified after Hughes (1997), Sutthirat et al. (2001), Barr and Cooper (2013), and Pattamalai (2015).

sions and compared with other Thai corundum and basaltic corundum from other deposits. In this study, rubies and purple sapphires are considered together as a single genetic group that is presented in contrast to the blue sapphires, which are presumed have a different geologic origin. The results of this study may improve the understanding of genetic models of formation of basaltic ruby and sapphire in Thailand.

Figure 2. Bo Welu ruby and sapphires set in rings. The intense blue sapphires are nearly 6 ct (left) and 8 ct (right). The deep red ruby in the middle is approximately 1 ct. These stones were heated to improve their color. Photo by Supparat Promwongnan, courtesy of Kannikar Rojvanakarn.

MATERIALS AND METHODS

More than 1,000 corundum grains from Bo Welu were collected from local miners nearly 20 years ago. The samples were examined under an optical microscope to search for mineral inclusions before the selected stones were carefully polished as slabs by a Facetron faceting machine to expose the mineral inclusions. A total of 99 corundum samples containing 191 tiny mineral inclusions were then selected for further investigation.

General properties such as size, color, specific gravity (SG), and refractive indices (RI) were measured using standard gemological equipment. External and internal features were observed under a gemological microscope.

Figure 3. These representative ruby and sapphire samples collected from Bo Welu were polished for analyses in the study. Photo by S. Promwongnan.

The selected samples, after pre-screening of mineral inclusions by Raman spectroscopy, were polished and mounted in epoxy resin prior to carbon coating. The JEOL JXA-8100 electron probe microanalyzer (EPMA) at the geology department of Chulalongkorn University was used to analyze major and minor compositions. Operating conditions were set at 15 kV accelerating voltage and about 25 nA sample current in the focused beam (smaller than 1 µm). Measurement times for each element were set at 30 seconds for peak counts and 10 seconds for background counts. For special analyses of zircon and monazite inclusions, an accelerating voltage of 20 kV was set to achieve more accurate results. Appropriate standard reference materials, including natural minerals, pure oxides, and pure elements, were used for calibration. Detection limits may reach 100–300 ppm under these conditions. An automatic ZAF correction was applied to the analytical results before reporting percent oxides. Fe^{2+} and Fe^{3+} ratios of minerals such as garnet, pyroxene, sapphirine, and spinel were recalculated using the method of Droop (1987).

RESULTS

General Characteristics. Most of the ruby and purple sapphire samples were less than 0.7 ct and measured up to 6 mm in length. Colors included purplish red, purple-red, reddish purple, and purple. The crystals generally displayed normal tabular habits with slightly rounded edges (figure 3). They were doubly refractive, with an RI of 1.760 to 1.770 and a birefringence of 0.009 to 0.010. Most of the samples displayed weak to moderate red fluorescence under long-wave UV radiation and were inert under short-wave UV.

The blue sapphire samples ranged from 0.2 to 6.9 ct and measured up to 1 cm long. These crystals were mostly characterized by a hexagonal habit with parting along basal planes. Some stones without crystal faces (figure 3) were rounded due to corrosion in the carrier magma (see Coenraads, 1992). They had semi-transparent to transparent blue to greenish blue and green-blue colors with medium to dark tones. They had an RI ranging from 1.760 to 1.771, with a corresponding birefringence of 0.009 to 0.010. These samples were generally inert under long-wave and short-wave UV. Moreover, these rough rubies and sapphires sometimes presented a primary corroded surface (figure 4) caused by hot magma, which is typically observed in corundum from basaltic terrain (Coenraads, 1992).

Mineral Inclusions in Ruby and Purple Sapphire. Various microscopic features were observed in Bo Welu ruby and purple sapphire, such as healed fractures or

Figure 4. Photomicrographs of rough samples of ruby and sapphire, taken under reflected light. Left: Etched features on a ruby's surface (field of view 2.70 mm). Center: Triangular etch marks on a ruby's surface (field of view 1.30 mm). Right: Dissolved features on a sapphire's surface (field of view 3.78 mm). Photomicrographs by S. Promwongnan.

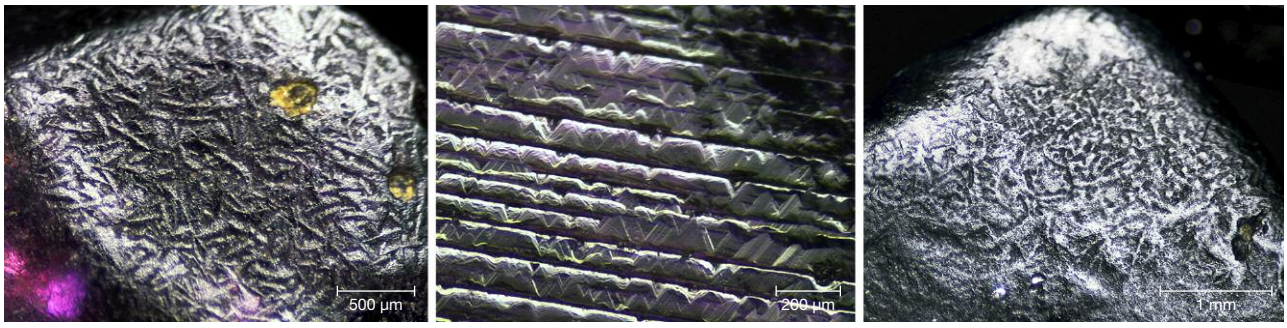

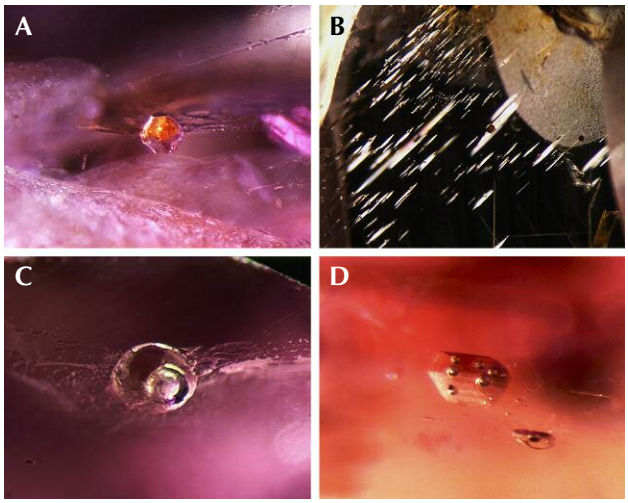

Figure 5. Some internal features observed in Bo Welu ruby and purple sapphire. A: Euhedral crystal surrounded by tension cracks (field of view 1.1 mm). B: Tiny crystals surrounded by thin films (field of view 3.0 mm). C and D: Two-phase inclusions (fields of view 1.4 mm and 0.7 mm). Photomicrographs by S. Promwongnan; darkfield illumination with fiber-optic light.

fingerprints, networks of tiny crystals, euhedral crystals surrounded by tension cracks (figure 5A), and tiny crystal inclusions with equatorial thin films (figure 5B). The last is a typical feature observed in ruby from Thailand. Many two-phase inclusions were captured using a combination of fiber-optic and darkfield illumination (figure 5, C and D). Previous researchers proposed the presence of various mineral inclusions in ruby from Thailand as well as from Pailin, Cambodia. A few analytical techniques were engaged to identify these mineral inclusions, such as optical microscopy and Raman spectroscopy (e.g., Gübelin and Koivula, 1986; Hughes, 1997; Intasopa et al., 1999; Khamloet et al., 2014; Saeseaw et al., 2017; Sangsawong et al., 2017) and X-ray powder diffraction (XRD) (Koivula and Fryer, 1987). Moreover, mineral inclusion chemistries were also reported using EPMA (Gübelin, 1971; Guo et al., 1994; Sutherland et al., 1998a; Sutthirat et al., 2001; Khamloet et al., 2014), proton microprobe analysis (PMP) (Guo et al., 1994), and scanning electron microscopy with energy dispersive X-ray spectrometry (SEM-EDX) (Saminpanya and Sutherland, 2011).

For this study, exposed mineral inclusions were initially identified using Raman spectroscopy before their chemical compositions were analyzed by EPMA. It is noteworthy that a number of mineral inclusions in Thai ruby and purple sapphire are first reported in this study (table 1). For comparison, mineral inclusions found in rubies from nearby mining areas in Chanthaburi-Trat and Pailin are summarized in the same table. Chemical analyses of these inclusions are also provided for further discussion.

TABLE 1. Summary of mineral inclusions discovered in Bo Welu ruby and sapphire, compared to those reported from surrounding basaltic gem fields.

		Ruby, Purple Sapphire				Blue Sapphire				
Mineral group	Mineral inclusions	Cambodia-Pailin	Trat–Bo Rai	Trat–Na Wong	Chanthaburi-Trat–Bo Welu	Chanthaburi-Trat–Bo Welu	Chanthaburi–Khao Wua	Kanchanaburi–Bo Phloi	Phrae–Den Chai	Cambodia-Pailin
Silicates	Zircon	–	–	–	–	✓*	✓[6]	✓[3,4]	–	–
	Garnet	–	✓[2,3,9]	–	✓*	–	–	✓[4]	–	–
	Sillimanite	–	✓[9]	–	✓*	–	–	–	–	–
	Staurolite	–	–	–	–		–	✓[4]	–	–
	Diopside	✓[7]	✓[2,3,9]	–	✓*	–	–	–	–	–
	Enstatite	–	–	–	–	–	–	✓[4]	–	–
	Sapphirine	✓[7]	✓[5]	✓[2,3]	✓*	–	–	✓[4]	–	–
	Nepheline	–	–	–	✓*	–	–	✓[3,4]	–	–
	Quartz	–	–	–	✓*	–	–	–	–	–
	Alkali feldspar	–	–	–	✓*	✓*	–	✓[3,4]	✓[3]	–
	Plagioclase	–	✓[8,9]	–	✓*	–	–	–	–	–
Oxides	Spinel	✓[7]	✓[9]	–	✓*	–	–	✓[1,3]	–	✓[7]
	Ilmenite	–	–	–	–	–	–	✓[4]	–	–
Niobium	Columbite	–	–	–	–	✓*	–	–	–	–
Phosphates	Monazite	–	–	–	–	✓*	–	✓[4]	–	–
Carbonates	Calcite	–	–	–	–	–	–	✓[4]	–	–
	Sulfide	–	✓[8,9]	–	✓*	✓*	–	–	–	–
Sulfates	Anhydrite	–	–	–	✓*	–	–	–	–	–

**This study, using Raman and EPMA*
[1]Guo et al. (1994), using EPMA and PMP
[2]Sutthirat et al. (2001), using EPMA
[3]Saminpanya and Sutherland (2011), using SEM-EDS
[4]Khamloet et al. (2014), using Raman and EPMA
[5]Koivula and Fryer (1987), using XRD
[6]Sutherland et al. (1998a), using EPMA
[7]Sutherland et al. (1998b), using EPMA
[8]Gübelin (1971), using EPMA
[9]Promwongnan and Sutthirat (2019), using Raman and EPMA

Garnet with very low chromium content is often found in Bo Welu ruby and purple sapphire. The crystals usually occur as ellipsoidal, irregular shapes with poorly formed crystal faces (figure 6A) that are either colorless or pale purplish red. They have a pyrope-rich

TABLE 2. EPMA analyses of garnet, sillimanite, pyroxene, sapphirine, nepheline, and quartz inclusions in Bo Welu ruby and purple sapphire samples.

Mineral phase analysis (wt.%)	Garnet		Sillimanite	Diopside		Sapphirine	Nepheline		Quartz
	PR	P	rP	PR	rP	PR	rP	rP	PR
	9TWL059-1	9TWL092-2	9TWL152-1	9TWL029-1	9TWL035-1	9TWL160 -1	9TWL012-1	9TWL153-1	9TWL095-2
SiO_2	42.03	42.57	36.38	44.85	49.28	13.97	47.61	45.99	99.61
TiO_2	0.07	0.10	0.01	0.24	0.75	nd	nd	0.07	nd
Al_2O_3	23.26	23.17	61.62	16.5	8.82	61.06	30.79	34.02	0.05
Cr_2O_3	0.02	0.05	nd	0.17	0.13	0.31	nd	nd	nd
FeO	9.71	10.33	1.43	3.04	3.28	3.32	0.22	0.15	0.28
MnO	0.20	0.19	nd	nd	0.01	0.03	nd	nd	nd
MgO	15.82	15.21	0.50	11.41	12.88	19.62	0.20	0.05	nd
NiO	na	na	na	na	na	0.41	na	na	na
CaO	8.85	8.17	0.15	22.52	23.99	0.14	4.67	3.09	0.01
K_2O	0.01	0.02	0.01	0.02	nd	0.02	15.10	14.80	nd
Na_2O	nd	0.02	nd	1.11	0.76	nd	1.32	1.84	nd
Total	99.98	99.82	100.10	99.85	99.90	98.87	99.91	100.01	99.95
Formula	**12(O)**		**20(O)**	**6(O)**		**20(O)**	**4(O)**		**2(O)**
Si	3.026	3.026	3.958	1.639	1.805	1.655	1.116	1.074	0.998
Ti	0.004	0.004	0.001	0.006	0.021	0.000	0.000	0.001	0.000
Al	1.974	1.974	7.902	0.711	0.381	8.527	0.851	0.936	0.001
Cr	0.001	0.001	0.000	0.005	0.004	0.029	0.000	0.000	0.000
$^{a}Fe^{3+}$	0.000	0.000	0.130	0.11	0.027	0.196	0.000	0.000	0.002
$^{a}Fe^{2+}$	0.584	0.584	0.000	0.000	0.073	0.133	0.004	0.003	0.000
Mn	0.012	0.012	0.000	0.000	0.000	0.003	0.000	0.000	0.000
Mg	1.698	1.698	0.081	0.622	0.703	3.466	0.007	0.002	0.000
Ni	–	–	–	–	–	0.039	–	–	–
Ca	0.683	0.683	0.017	0.882	0.942	0.017	0.117	0.077	0.000
K	0.001	0.001	0.002	0.001	0.000	0.003	0.686	0.670	0.000
Na	0.000	0.000	0.000	0.079	0.054	0.000	0.039	0.055	0.000
Total	7.983	7.983	12.091	4.037	4.009	14.069	2.821	2.819	1.001

$^{a}Fe^{2+}$ and Fe^{3+} were recalculated from total FeO after the method of Droop (1987) and assigned using ideal formula cations.
nd = not detected
na = not analyzed
PR = purple-red, rP = reddish purple, P = purple

composition (high Mg; see table 2), which is similar to garnet inclusions in Bo Rai ruby and purple sapphire located about 30 km southeast of the study area, previously reported by Sutthirat et al. (2001), Saminpanya and Sutherland (2011), and Promwongnan and Sutthirat (2019).

Sillimanite occurred rarely in this study, displaying a subhedral shape with a hexagonal habit surrounded by healed fractures (figure 6B). These inclusions contained major contents of SiO_2 and Al_2O_3 and traces of FeO and MgO (again, see table 2). Sillimanite inclusions have recently been reported in ruby and purple sapphire from the Bo Rai gem field (Promwongnan and Sutthirat, 2019). Therefore, these two studies represent the first discovery of sillimanite inclusions in Thai ruby and purple sapphire.

High-alumina diopside was the most common inclusion found in Bo Welu ruby and purple sapphire. They usually formed colorless rounded or ellipsoidal crystals (figure 6C), with twinning lamella sometimes observed. These inclusions were composed of an Al-rich component (0.38–0.71 Al) with slightly higher Ca and lower Mg components (see table 2). Diopside inclusions were previously reported in alluvial ruby and purple sapphire from Bo Rai (e.g., Sutthirat et al., 2001; Saminpanya and Sutherland, 2011; Promwong-

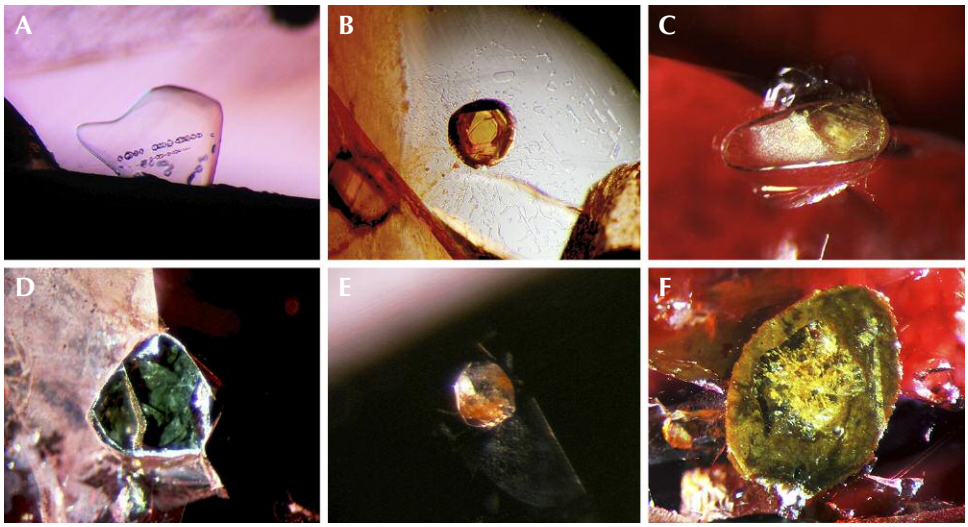

Figure 6. A: Irregularly shaped garnet (field of view 0.95 mm). B: Hexagonal-shaped sillimanite (field of view 1.3 mm). C: Ellipsoidal diopside (field of view 1.6 mm). D: Sapphirine (field of view 1.2 mm). E: Rounded nepheline (field of view 0.8 mm). F: Quartz with an iron-stained edge (field of view 1.4 mm). Photomicrographs by S. Promwongnan; brightfield illumination with fiber-optic light (A and B) and darkfield illumination (C–F).

nan and Sutthirat, 2019) and Pailin rubies (Sutherland et al., 1998b). However, diopsides found in Bo Welu ruby and purple sapphire had a wider range of composition, encompassing the compositions of diopside inclusions in both Bo Rai and Pailin rubies.

Sapphirine was recognized in a purple-red ruby (sample 9TWL160); it was a subhedral crystal surrounded by fractures (figure 6D) and showed strong green-blue pleochroism similar to that reported by Koivula and Fryer (1987). Its chemical composition (table 2) was similar to that of sapphirine inclusions found in alluvial rubies from the Na Wong gem field (Sutthirat et al., 2001; Saminpanya and Sutherland, 2011), located about 20 km south of Bo Welu (again, see figure 1). Sapphirine inclusions were also reported in ruby from Bo Rai (Koivula and Fryer, 1987) and Pailin (Sutherland et al., 1998b). Sapphirine inclusions in rubies from Bo Na Wong, Pailin, and Bo Welu all have similar mineral chemistry.

Nepheline inclusions were occasionally recognized in purple-red and reddish purple samples. They formed as rounded crystals (figure 6E) and contained major contents of SiO_2 and Al_2O_3 with traces of CaO, K_2O, Na_2O, and FeO (table 2). This is the first report of nepheline inclusions in Thai ruby.

Quartz appeared to have formed as an exogenous inclusion in a purple-red ruby (sample 9TWL095). Its euhedral core was surrounded by an iron-stained yellow rim (figure 6F), and its composition was almost pure silica (99.6% SiO_2) with iron traces (table 2). The unusual quartz inclusion in Thai ruby is first reported here.

Feldspar inclusions were often observed in purple-red and reddish purple samples from Bo Welu. They usually formed as single grains with a rounded or irregular shape (figure 7A). Most feldspar inclusions were characterized by plagioclase compositions ranging widely from bytownite to andesine

Figure 7. Feldspar and spinel inclusions in Bo Welu ruby. A: Irregularly shaped feldspar (field of view 0.6 mm, brightfield illumination). B: Feldspar-spinel composite (field of view 0.7 mm, darkfield illumination). C: BSE image of the same inclusion in figure B revealing feldspar intergrowth with spinel (field of view 0.25 mm). Photomicrographs by S. Promwongnan.

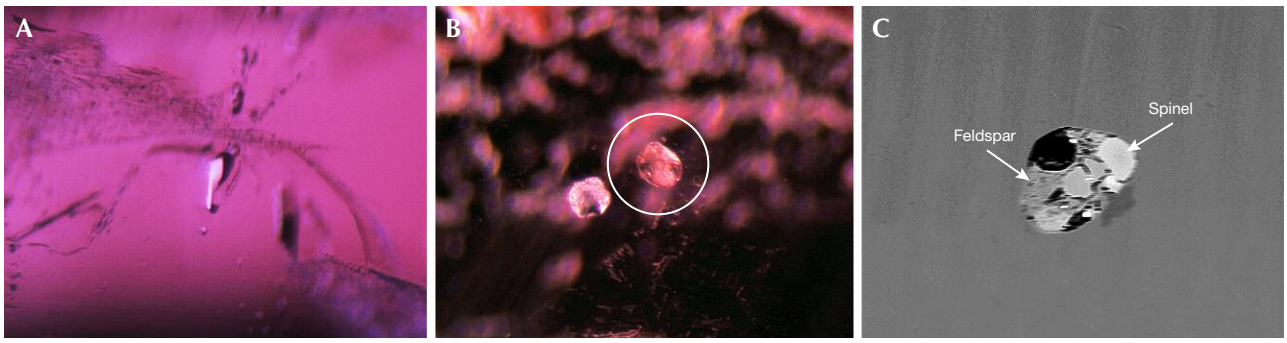

TABLE 3. EPMA analyses of feldspar inclusions in Bo Welu ruby and purple sapphire compared to blue sapphire samples.

Mineral phase analysis (wt.%)	Ruby and Purple Sapphire					Blue Sapphire			
	Plagioclase feldspars				Alkali feldspars	Alkali feldspars			
	PR	rP	rP	PR	rP	gB	gB	B	gB
	9TWL055-1	9TWL122-4	9TWL176-1	9TWL154-1[a]	9TWL012-2	8TWL083-2	8TWL018-3	8TWL114-25[b]	8TWL093-5
SiO_2	58.02	48.61	61.34	55.99	64.91	66.19	66.97	66.47	69.26
TiO_2	0.04	nd	0.07	0.03	0.03	nd	0.02	0.01	0.06
Al_2O_3	26.36	32.46	23.67	26.97	21.54	20.85	21.40	20.92	16.47
FeO	0.09	0.07	0.46	0.25	0.12	0.08	0.65	0.59	0.31
MnO	0.04	0.03	nd	nd	0.01	nd	0.04	0.04	nd
MgO	0.05	0.03	0.20	0.03	nd	nd	nd	0.02	nd
CaO	7.30	16.51	6.29	11.04	1.48	2.50	0.73	0.02	0.14
K_2O	1.35	0.12	0.07	0.02	3.08	1.07	2.69	1.40	7.43
Na_2O	6.66	2.14	7.76	5.51	7.71	8.54	8.47	9.45	6.25
Total	99.91	99.97	99.86	99.84	98.88	99.23	100.97	98.92	99.92
Formula 8(O)									
Si	2.606	2.228	2.732	2.527	2.899	2.926	2.925	2.944	3.095
Ti	0.001	0.000	0.002	0.001	0.001	0.000	0.001	0.000	0.002
Al	1.396	1.753	1.243	1.435	1.134	1.086	1.102	1.092	0.868
Fe	0.004	0.003	0.017	0.010	0.004	0.118	0.034	0.001	0.011
Mn	0.002	0.001	0.000	0.000	0.000	0.003	0.024	0.022	0.000
Mg	0.003	0.002	0.013	0.002	0.000	0.000	0.001	0.001	0.000
Ca	0.352	0.811	0.300	0.534	0.071	0.000	0.000	0.001	0.007
K	0.077	0.007	0.004	0.001	0.175	0.060	0.150	0.079	0.424
Na	0.580	0.190	0.670	0.482	0.668	0.732	0.718	0.811	0.542
Total	5.021	4.995	4.981	4.992	4.952	4.925	4.955	4.951	4.949
Atomic%									
Ca	34.86	80.47	30.82	52.46	7.74	13.01	3.79	0.10	0.69
K	7.66	0.67	0.41	0.12	19.18	6.62	16.62	8.89	43.58
Na	57.49	18.85	68.77	47.42	73.08	80.37	79.60	91.01	55.72
Total	100.00	100.00	100.00	100.00	100.00	100.00	100.00	100.00	100.00

[a]*Feldspar combined with spinel inclusion*
[b]*Feldspar combined with monazite inclusion*
nd = not detected
PR = purple-red, rP = reddish purple, P = purple, gB = greenish blue, B = blue

($Ab_{19–69}An_{31–80}Or_{<8}$; see table 3 and figure 8). Moreover, an unusual rounded alkali feldspar of anorthoclase composition ($Ab_{73}An_8Or_{19}$) was recognized in reddish purple sample 9TWL012; its Raman spectrum was similar to other feldspar inclusions, but the peaks were shifted slightly to the right. Feldspar-spinel composite inclusions were also observed in ruby and purple sapphire (samples 9TWL019, 9TWL154, and 9TWL180); their compositions fell mostly within the labradorite range ($Ab_{38–48}An_{51–62}Or_{0.01–3}$). The composite feldspar and colorless spinel inclusions were found in a few ruby samples such as purple-red sample 9TWL154 (figure 7B), which can be observed clearly under backscattered-electron (BSE) images (figure 7C). The composition range of feldspar inclusions in Bo Welu ruby and purple sapphire was wider than that found in Bo Rai ruby, which indicates only bytownite ($Ab_{11–15}An_{85–89}Or_{0.1–0.2}$) and andesine ($Ab_{56}An_{38}Or_6$) (Promwongnan and Sutthirat, 2019). Although Gübelin (1971) and Promwongnan and Sutthirat (2019) previously reported plagioclase feldspar inclusions in Thai ruby and purple sapphire, this is the first report of them containing a feldspar-spinel composite inclusion as well as alkali feldspar.

Apart from spinel-feldspar composite inclusions, a single tiny rounded spinel inclusion was observed in a

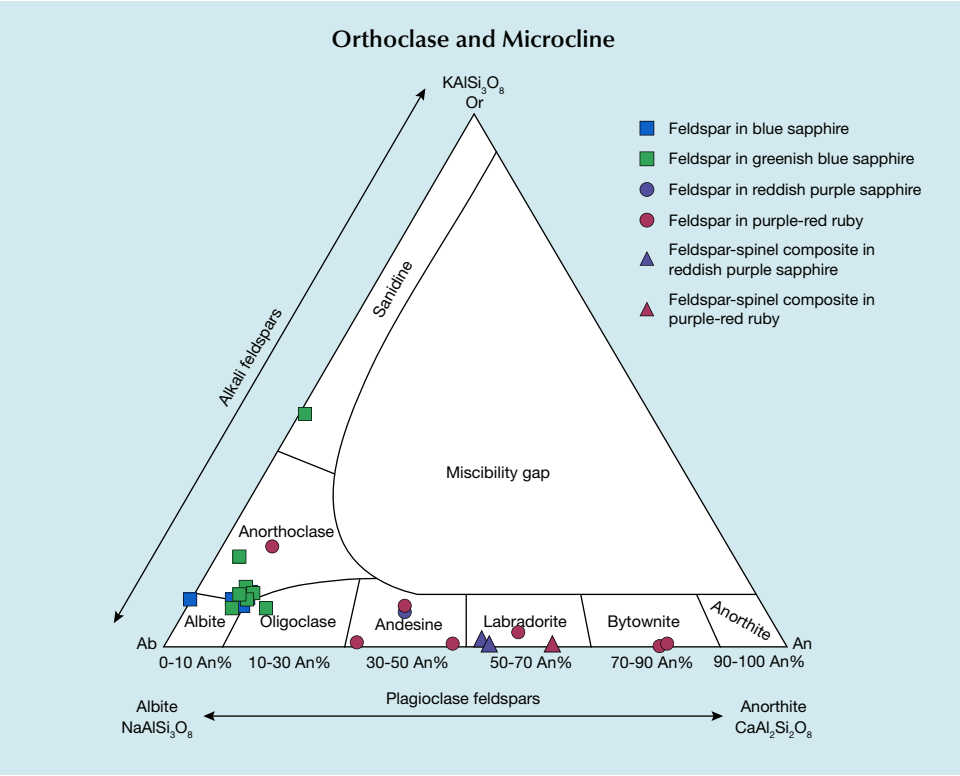

Figure 8. Ternary plot of feldspar inclusions in rubies and sapphires from Bo Welu. Most feldspar inclusions in the ruby and purple sapphire samples fell within the range of plagioclase. One with anorthoclase composition was recognized in a reddish purple sapphire (9TWL012). Most feldspar inclusions in the blue sapphire samples were alkali feldspar. Only one sanidine inclusion was recorded, in a greenish blue sapphire (8TWL093).

purple-red sample (9TWL085). All spinel inclusions appeared to have similar composition, with high contents of Al and Mg greater than Fe (average $Mg_{0.77}Fe_{0.23}Al_2O_4$ or $Spl_{77}Hc_{23}$; table 4). Recently, a spinel inclusion with a composition of $Mg_{0.83}Fe_{0.17}Al_2O_4$ (or $Spl_{83}Hc_{17}$) was reported in ruby and purple sapphire from Bo Rai (Promwongnan and Sutthirat, 2019). Moreover, a pleonaste spinel inclusion was reported in ruby from West Pailin, Cambodia (Sutherland et al., 1998b), with Mg content clearly lower than the spinel inclusions in Thai ruby.

Sulfide was sometimes observed as subhexagonal or rounded metallic opaque inclusions (figure 9A). Their compositions clearly did not match with the ideal formula of pyrrhotite (FeS), but they also contained additional nickel and copper, similar to sulfide inclusions in Bo Rai ruby and purple sapphire reported by Promwongnan and Sutthirat (2019). Moreover, subhexagonal to rounded opaque metallic chalcopyrite ($CuFeS_2$) inclusions in Thai rubies were reported by Gübelin (1971).

Figure 9. A: Rounded sulfide inclusion surrounded by a tension disk (field of view 0.95 mm). B: Euhedral anhydrite containing subhedral black sulfide (pyrrhotite) (field of view 0.8 mm). C: Rounded two-phase inclusion containing a gas bubble and silica melt (field of view 1.0 mm). Photomicrographs by S. Promwongnan; darkfield illumination with fiber-optic light (A) and brightfield illumination with fiber-optic light (B–C).

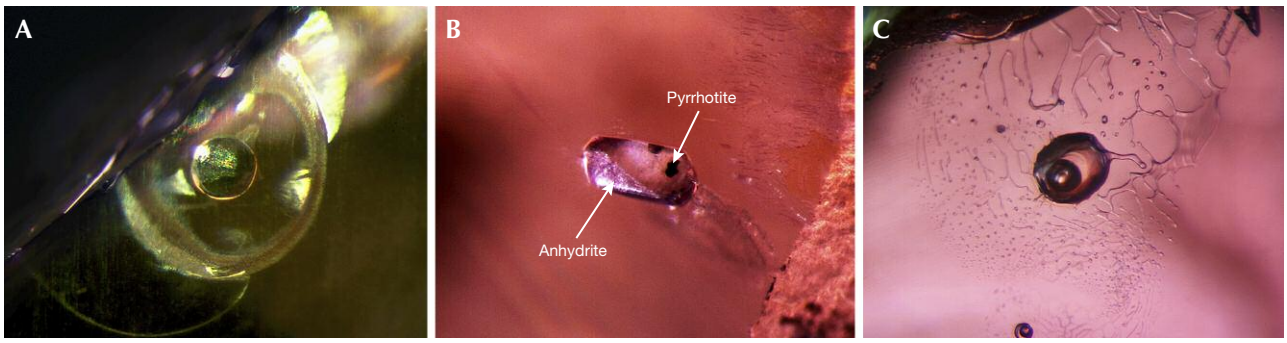

TABLE 4. EPMA analyses of spinel, anhydrite, and sulfide inclusions in Bo Welu ruby and purple sapphire samples.

Mineral phase analysis (wt.%)	Spinel				Anhydrite	Sulfide
	PR	PR	rP	PR	rP	
	9TWL019-2[a]	9TWL154-2[a]	9TWL180-2[a]	9TWL085-2	9TWL096	
SO_3	na	na	na	na	55.62	53.72
SiO_2	0.04	0.10	0.06	0.09	0.03	0.02
TiO_2	0.43	2.51	1.09	nd	nd	0.01
Al_2O_3	64.71	63.37	64.25	67.46	0.03	0.03
Cr_2O_3	0.25	1.67	0.13	0.38	nd	0.09
FeO total	13.11	10.61	13.50	11.81	0.02	44.97
MnO	0.09	0.24	0.10	0.27	0.06	nd
MgO	20.19	20.59	20.56	19.96	0.01	0.01
ZnO	0.09	0.04	0.04	na	na	na
CaO	nd	0.01	0.04	0.03	44.23	1.12
K_2O	nd	nd	0.02	nd	nd	0.02
Na_2O	nd	nd	0.03	nd	0.02	nd
Total	98.91	99.14	99.82	100.00	100.00	99.99
Formula		**4(O)**			**4(O)**	**–**
S	-	-	-	-	0.966	1.008
Si	0.001	0.002	0.002	0.002	0.001	0.000
Ti	0.008	0.048	0.021	0.000	0.000	0.000
Al	1.948	1.893	1.921	1.990	0.001	0.001
Cr	0.005	0.033	0.003	0.007	0.000	0.002
[b]Fe^{3+}	0.038	0.000	0.044	0.000	0.000	0.940
[b]Fe^{2+}	0.242	0.225	0.242	0.247	0.000	
Mn	0.002	0.005	0.002	0.006	0.001	0.000
Mg	0.769	0.778	0.778	0.745	0.000	0.001
Zn	0.002	0.001	0.001	–	–	–
Ca	0.000	0.000	0.001	0.001	1.097	0.030
K	0.000	0.000	0.001	0.000	0.000	0.001
Na	0.000	0.000	0.001	0.000	0.001	0.000
Total	3.014	2.986	3.017	2.999	2.067	1.982

[a]*Spinel composition with feldspar inclusion*
[b]*Fe^{2+} and Fe^{3+} recalculated from total FeO after the method of Droop (1987) and assigned using ideal formula cations*
nd = not detected
na = not analyzed
PR = purple-red, rP = reddish purple

An anhydrite-sulfide composite inclusion was found in a reddish purple sapphire (9TWL096). The anhydrite formed a subhedral crystal containing an irregularly shaped sulfide (figure 9B). This sulfide is chemically characterized by a pure pyrrhotite composition ($Fe_{0.94}S$; see table 4). This is the first report of an anhydrite inclusion in Thai reddish purple sapphire.

Two-phase inclusions were sometimes observed in Bo Welu ruby and purple sapphire samples. Rounded two-phase inclusions, consisting of a gas bubble and silicate melt, were situated within healed fractures (figure 9C). The silicate melts contained major contents of SiO_2 and Al_2O_3 with traces of CaO, FeO, and MgO.

Mineral Inclusions in Blue Sapphire. The most common internal features in Bo Welu blue sapphire were strong color zoning (figure 10A) and orientation of fine minute particles (figure 10B). Other features such as oriented silk inclusions, thin films (figure

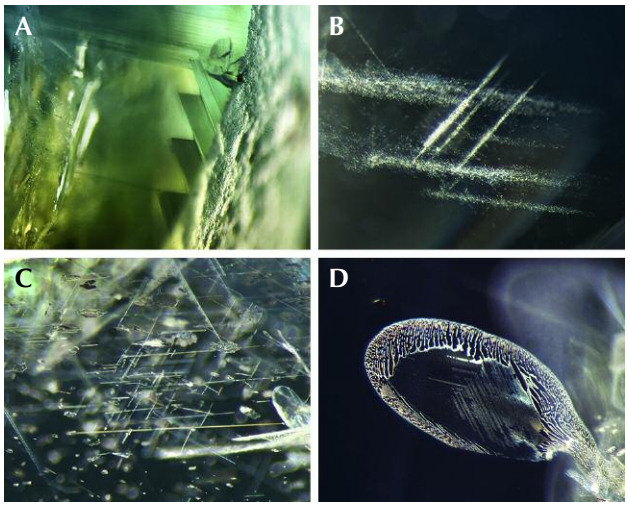

Figure 10. Common internal features found in Bo Welu blue sapphire, viewed using a combination of fiber-optic with darkfield illumination. A: Strong color zoning (field of view 2.3 mm). B: Oriented fine minute particles (field of view 1.3 mm). C: Oriented silk inclusions and a thin film (field of view 1.6 mm). D: Healed fractures (field of view 1.2 mm). Photomicrographs by S. Promwongnan.

10C), and healed fractures (figure 10D) could be observed clearly under darkfield illumination. Moreover, varieties of mineral inclusions were also recognized in these samples. Some had never been documented in blue sapphire from either Thailand or Pailin, Cambodia (see table 1).

Zircon characterized by tetragonal prismatic (figure 11A) or bipyramidal crystals (figure 11B), in this case displaying stress fractures, was sometimes observed in the blue sapphires. They had a narrow compositional range of about 2–3 wt.% HfO_2, ≤1.1 wt.% UO_2, mostly <1.2 wt.% ThO_2, <0.9 wt.% Y_2O_3, and <1.1 wt.% rare earth elements (see table 5). The zircon inclusions in this study were similar to those in sapphire from Bo Phloi, Kanchanaburi (Saminpanya and Sutherland, 2011; Khamloet et al., 2014), but they contained higher HfO_2 content than those from Kao Wua, Chanthaburi (Sutherland et al., 1998a).

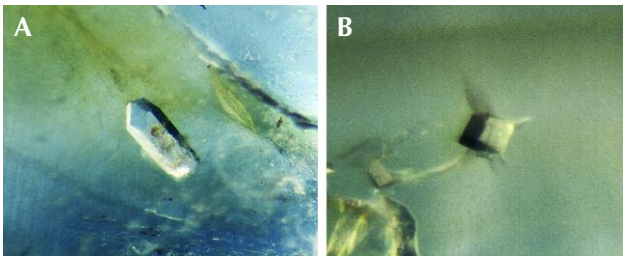

Figure 11. A: Prismatic zircon inclusion in blue sapphire (field of view 1.0 mm). B: Bipyramidal zircon without pyramidal face associated with stress fissure (field of view 0.2 mm). Photomicrographs by S. Promwongnan; darkfield illumination.

Feldspar was the most common inclusion in Bo Welu blue sapphire, typically formed as euhedral to subhedral crystals (figure 12A). Some were also associated with healed fractures or tension cracks (figure 12B). Most of the feldspar inclusions contained a Na-rich (albite) component with low K and Ca contents ranging between $Ab_{80–91}An_{0.1–13}Or_{7–17}$ (table 3, figure 8); surprisingly, feldspar composition ($Ab_{56}An_{0.7}Or_{44}$) was determined from a subhedral inclusion surrounded by a tension crack in greenish blue sapphire sample 8TWL093 (figure 12C) that displayed a Raman spectrum matching that of sanidine. Albite and sanidine inclusions were previously reported in Bo Phloi sapphire in Kanchanaburi and Den Chai

Figure 12. A: Euhedral feldspar inclusion in blue sapphire (field of view 0.8 mm, darkfield illumination). B: Feldspar crystals situated in healed fractures (field of view 0.6 mm, darkfield illumination). C: Subhedral sanidine inclusion surrounded by a tension crack (field of view 0.7 mm, brightfield illumination). Photomicrographs by S. Promwongnan.

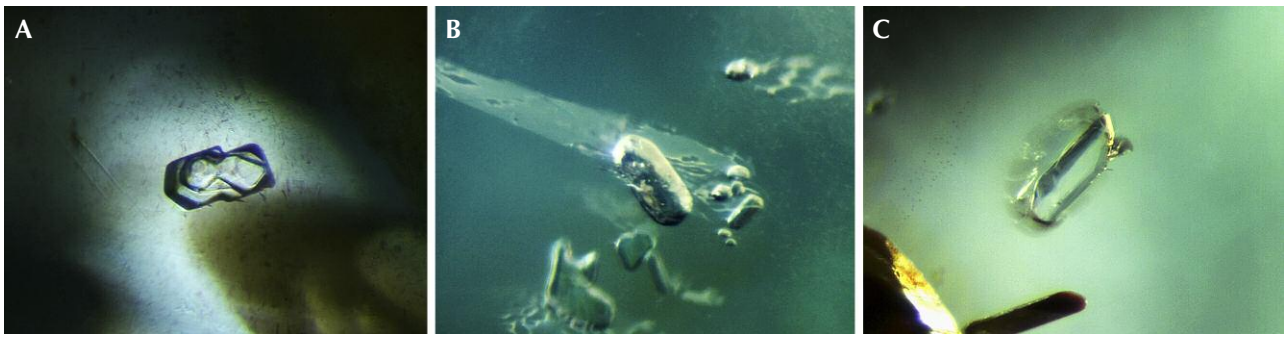

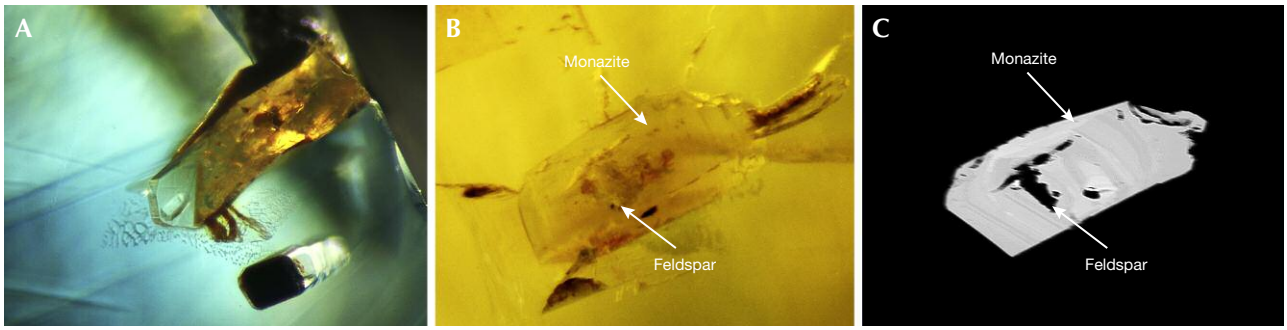

Figure 13. A: Colorless subhedral monazite crystal (field of view 1.0 mm). B: Monazite inclusion containing albite feldspar (field of view 0.7 mm). C: BSE image of the same inclusion in figure B (field of view 0.65 mm). Photomicrographs by S. Promwongnan, brightfield illumination.

sapphire in Phrae Province (Saminpanya and Sutherland, 2011; Khamloet et al., 2014).

Monazite was observed in some of the blue sapphire samples. These were typically colorless to very light yellow crystals that usually occurred as prisms (figure 13A). An unusual composite inclusion combining monazite and albite feldspar ($Ab_{8.9}An_{0.1}Or_{91.0}$; see table 3) was recognized in sample 8TWL114 (figure 13B), clearly visible with BSE imaging (figure 13C). Most of the monazite inclusions varied in composition from about 35–46 wt.% ThO_2, 15–24 wt.% Ce_2O_3, and 16–22 wt.% P_2O_5 (see table 5). Monazite inclusions in sapphire have also been reported in basaltic sapphires from southwest Rwanda (Krzemnicki et al., 1996), Tok Phrom in Chanthaburi and Bo Phloi in Kanchanaburi (Intasopa et al., 1998; Khamloet et al., 2014), and Laos (Singbamroong and Thanasuthipitak, 2004).

Columbite was often found in the blue sapphire samples, usually as black grains with an irregular or flat shape or as orthorhombic crystals (figure 14A), with some surrounded by tension cracks. Some dark red columbite inclusions also presented comet-like dust trails (figure 14B). Their compositions varied in narrow ranges of 74–75 wt.% Nb_2O_5, ≤0.3 wt.% Ta_2O_5, ≤0.4 wt.% TiO_2, ≤0.2 wt.% MgO, and <10.5 wt.% FeO (table 5). Their compositions are plotted on the $FeTa_2O_6$-$FeNb_2O_6$-$MnNb_2O_6$-$MnTa_2O_6$ quadrilateral diagram for columbite-tantalite classification (Černý and Ercit, 1985; see figure 15). The recalculated atomic formula of these columbite inclusions, based on six oxygens, seems to have some cations missing; they fall distinctly in the field of ferro-columbite. Their compositions have less Ti, Ta, and Fe oxides than columbite inclusions in basaltic sapphires from New South Wales in Australia, previously reported by Sutherland et al. (1998a). Moreover, columbite inclusions in sapphire from Tok Phrom in Chanthaburi and Pailin in Cambodia were also reported by Intasopa et al. (1998).

Sulfide was rarely found as an inclusion in the blue sapphire samples; however, some small black

Figure 14. A: Subhedral columbite inclusion (field of view 1.0 mm, brightfield illumination). B: Dark red columbite inclusions presenting comet-like dust trails (field of view 0.8 mm, darkfield illumination). C: Tiny black opaque sulfide inclusions, shown using fiber-optic reflection (field of view 1.0 mm). Photomicrographs by S. Promwongnan.

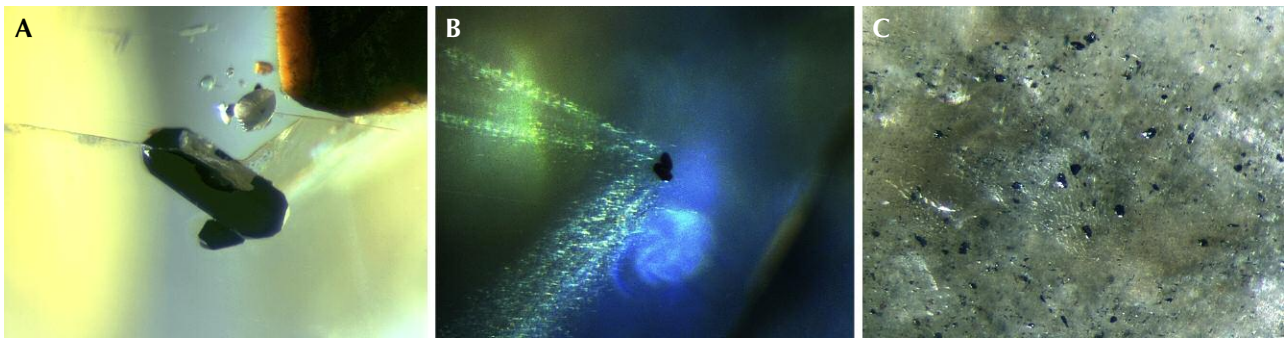

TABLE 5. EPMA analyses of zircon, monazite, and columbite inclusions in Bo Welu blue sapphire samples.

Mineral phase analysis (wt.%)	Zircon			Monazite				Columbite		
	B	B	gB	gB	gB	gB	B	gB	gB	gB
	8TWL040-2	8TWL059-2	8TWL059-6	8TWL036-4	8TWL036-7	8TWL082-7	8TWL114-24[a]	8TWL064-1	8TWL036-2	8TWL097-7
Nb_2O_5	na	na	na	na	0.12	0.01	nd	74.37	74.39	74.57
P_2O_5	nd	0.57	0.49	15.81	21.62	18.72	18.14	na	na	na
Ta_2O_5	na	na	na	na	0.51	0.15	0.41	0.25	0.31	0.16
HfO_2	2.09	2.62	2.80	na	0.13	nd	0.28	na	na	na
SiO_2	34.78	33.63	33.86	3.71	4.59	5.31	4.80	na	na	na
ThO_2	0.07	1.21	0.47	46.46	35.15	45.12	38.14	0.85	0.87	0.11
TiO_2	na	na	na	na	na	na	na	0.43	0.37	0.40
UO_2	0.24	1.13	0.75	0.95	nd	nd	0.05	3.50	3.45	2.10
ZrO_2	61.13	59.39	60.66	na	0.02	nd	nd	0.78	0.57	0.83
Al_2O_3	0.07	0.01	nd	0.07	nd	nd	nd	0.29	0.15	0.14
Ce_2O_3	na	na	na	19.28	24.32	15.38	24.30	1.36	1.27	1.85
Dy_2O_3	0.06	0.09	0.12	0.60	0.06	0.22	0.07	na	na	na
Gd_2O_3	na	na	na	1.14	0.57	0.92	0.71	na	na	na
La_2O_3	na	na	na	1.04	nd	nd	nd	na	na	na
Nd_2O_3	0.02	nd	nd	5.33	6.94	7.33	6.41	1.42	1.46	1.93
Pr_2O_3	nd	nd	0.97	3.04	4.50	2.80	4.80	na	na	na
Sm_2O_3	na	na	na	0.80	0.24	0.20	0.12	0.72	0.76	0.77
Y_2O_3	0.17	0.85	0.81	0.08	0.22	0.99	0.48	2.76	3.19	3.46
FeO	0.08	0.07	0.08	0.09	0.20	0.07	nd	9.79	10.37	10.45
MnO	na	na	na	na	na	na	na	1.58	1.48	1.24
MgO	na	na	na	na	na	na	na	0.08	0.09	0.16
CaO	na	na	na	0.24	0.24	2.19	1.70	0.42	0.47	0.81
Na_2O	na	na	na	na	na	na	na	nd	nd	nd
Total	98.71	99.57	101.01	98.64	99.40	99.39	100.41	98.61	99.18	98.97
Formula		**4(O)**			**4(O)**			**6(O)**		
Nb	–	–	–	–	0.002	0.000	0.000	1.97	1.97	1.96
P	0.000	0.013	0.015	0.669	0.795	0.715	0.699	–	–	–
Ta	–	–	–	–	0.006	0.002	0.005	0.00	0.01	0.00
Hf	0.018	0.023	0.024	–	0.002	0.000	0.004	–	–	–
Si	1.062	1.035	1.027	0.186	0.199	0.240	0.219	–	–	–
Th	0.000	0.008	0.003	0.529	0.347	0.463	0.395	0.011	0.012	0.001
Ti	–	–	–	–	–	–	0.000	0.019	0.016	0.018
U	0.002	0.008	0.005	0.011	0.000	0.000	0.000	0.046	0.045	0.027
Zr	0.910	0.891	0.897	–	0.000	0.000	0.000	0.022	0.016	0.023
Al	0.003	0.000	0.000	0.004	0.000	0.000	0.000	0.020	0.010	0.010
Ce	–	–	–	0.353	0.387	0.254	0.405	0.029	0.027	0.039
Dy	0.001	0.001	0.001	0.010	0.001	0.003	0.001	–	–	–
Gd	–	–	–	0.019	0.008	0.014	0.011	–	–	–
La	–	–	–	0.019	0.000	0.000	0.000	–	–	–
Nd	0.000	0.000	0.000	0.095	0.108	0.118	0.104	0.030	0.030	0.040
Pr	0.000	0.000	0.011	0.055	0.071	0.046	0.080	–	–	–
Sm	–	–	–	0.014	0.004	0.003	0.002	0.015	0.015	0.015
Y	0.003	0.014	0.013	0.002	0.005	0.024	0.012	0.086	0.099	0.107
Fe	0.002	0.002	0.002	0.004	0.007	0.003	0.000	0.481	0.507	0.508
Mn	–	–	–	–	–	–	–	0.079	0.073	0.061
Mg	–	–	–	–	–	–	–	0.007	0.008	0.014
Ca	–	–	–	0.013	0.011	0.106	0.083	0.026	0.030	0.051
Na	–	–	–	–	–	–	–	0.000	0.000	0.000
Total	2.001	1.995	1.998	1.983	1.954	1.990	2.019	2.847	2.861	2.879

[a]*Monazite combined with feldspar inclusion*
nd = not detected; na = not analyzed
B = blue, gB = greenish blue

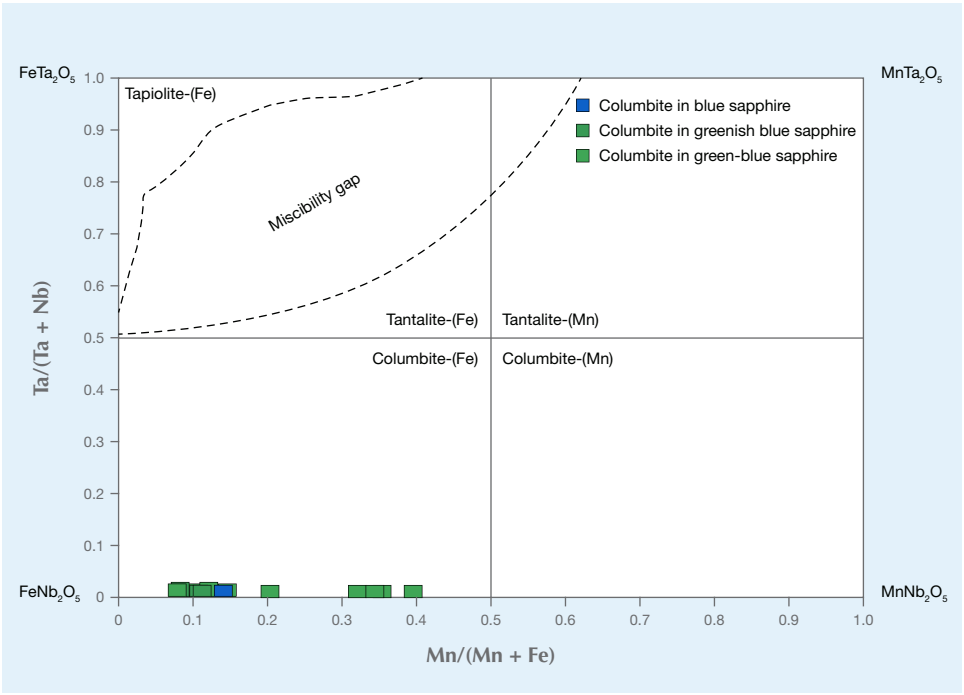

Figure 15. Compositional plots (suggested by Černý and Ercit, 1985) indicating ferrocolumbite inclusions in the Bo Welu blue sapphires analyzed in this study.

opaque crystals oriented along the crystallographic direction of the host sapphire, sample 8TWL046 (figure 14C), were recognized as sulfide. Their composition ($FeS_{1.1}$) was close to the ideal pyrrhotite formula and similar to sulfide in sapphire from New England in Australia (Sutherland et al., 1998a). On the other hand, these compositions are different from sulfide inclusions in sapphire from New South Wales, which contains trace compositions of Cu and Zn (Guo et al., 1996). However, it must be noted that this is the first discovery of sulfide inclusions in Thai blue sapphire.

DISCUSSION

Alluvial ruby and sapphire from the Bo Welu area showed characteristics of basaltic-type origin, particularly surface etching by carrier magmas.

Mineral inclusions in Thai corundum have been documented for almost eight decades (Gübelin, 1940). In this study, high-alumina diopside was the most common mineral inclusion in ruby and purple sapphire from Bo Welu. Mineral inclusions of pyrope garnet, sapphirine, quartz, feldspar, and sulfide were also identified. These inclusions have been mentioned in earlier studies on Thai ruby (e.g., Gübelin, 1940; Koivula and Fryer, 1987; Sutthirat et al., 2001; Saminpanya and Sutherland, 2011). Sillimanite, nepheline, quartz, alkali feldspar, spinel, and anhydrite are newly reported in this study as inclusions in ruby and purple sapphire from Bo Welu; this is also the first report for most of them in any such samples from Thailand. These minerals can provide more information about the environment of the host's crystallization before they traveled rapidly to the surface during magmatic eruption. Sillimanite, spinel, and melt inclusions, reported recently in Bo Rai ruby and purple sapphire (Promwongnan and Sutthirat, 2019), offer new evidence to support a high-temperature environment of the original host's formation in the following discussion.

Cr-rich content in the host and Al-rich content in mafic mineral inclusions such as pyroxene, pyrope garnet, plagioclase, nepheline, and sapphirine indicate a deep-seated source (most likely mantle or lower crust). Pyroxenes are inosilicate minerals and a key constituent of mafic igneous rocks. High-alumina diopside usually occurs in granulitic xenoliths in alkali basalts (Sutherland et al., 2003). Pyrope-rich end-member garnet inclusions are related to a liquid magmatic occurrence (Gübelin and Koivula, 1986). More than 55% of pyrope compositions of garnet in this study are classified as Group A eclogitic garnets (Coleman et al., 1965), which usually occur in layers in ultramafic rocks. Most of the feldspar inclusions in these rubies and purple sapphires are plagioclase, with the exception of one alkali feldspar inclusion with anorthoclase composition. Anorthoclase and sanidine crystals are intergrown with sapphire in xenoliths from alkali basalt that suggest crystallization from intermediate magmas in the lower crust/upper mantle (Upton et al., 1983; Aspen et al.,

1990; Coenraads et al., 1990). The compositions of the pyroxene, garnet, plagioclase, and spinel inclusions support mafic granulites as the possible source of ruby and purple sapphire, as reported by Sutthirat et al. (2018) and Promprated et al. (2003). Nepheline, the most common of the feldspathoid minerals, occurs in alkaline rocks (Deer et al., 2013). Sapphirine inclusions support the equilibrium of garnet, corundum, spinel, and sapphirine. Anorthoclase, sillimanite, and silicate melt inclusions offer further evidence that the host formed from partial melting at high temperature (Palke et al., 2018). The exogenous mineral inclusions such as anhydrite, sulfide, and quartz observed in Bo Welu ruby and purple sapphire may be due to submarine volcanism prior to subduction, when these shallow crustal materials moved downward and mixed with mafic materials at the mantle. The chemical composition data of the mineral inclusions implies that these samples crystallized at high temperature through partial melting of hybrid mantle material affected by ancient subduction. Therefore, their original source is confirmed to be mafic granulites characterized by high pressure and very high temperature.

The inclusions in Bo Welu blue sapphire consist of alkaline-related minerals that crystallized from alkaline felsic magma, such as alkali feldspar, monazite, columbite, and zircon. The feldspar inclusions found in this study were mainly Na-rich alkali feldspar (albite), with an unusual sanidine. The low Ca content of the feldspars indicates that the source rock was felsic. Sanidine suggests that the crystallization of blue sapphire may be related to high-temperature metamorphism. Saminpanya and Sutherland (2011) proposed that sanidine inclusions in Den Chai sapphire may have crystallized at a minimum temperature of about 1000ºC. Monazite inclusions in sapphires suggest that crystallization of basaltic sapphire is related to highly evolved melt (Krzemnicki et al., 1996; Intasopa et al., 1998; Singbamroong and Thanasuthipitak, 2004; Khamloet et al., 2014). Columbite generally occurs in various granitic rocks (Guo et al., 1996). Chemical characteristics of zircons (e.g., high Hf, Y, and rare earth elements) have been found in sapphires from basaltic terrains elsewhere, possible evidence that the host sapphire crystallized from alkaline and highly evolved source material under conditions unrelated to the associated basaltic magma (e.g., Coenraads et al., 1990, 1995; Guo et al., 1996; Sutherland et al., 2002; Khamloet et al., 2014). In addition, the exogenous inclusions in sapphire such as sulfides indicate starting materials related to subduction and hybridization within the deep crust and later partial melting of initial magma-related sapphire formation. The occurrence of mineral inclusions in Bo Welu blue sapphire strongly supports crystallization from highly evolved alkali-rich, silica-poor magma (syenite) (e.g., Coenraads et al., 1990; Ding, 1991; Coenraads et al., 1995; Guo et al., 1996; Sutherland et al., 2002; Khamloet et al., 2014).

The Chanthaburi-Trat placer rubies and sapphires should have a somewhat different crystallization environment, as suggested by previous research (e.g., Yui et al., 2006; Saminpanya and Sutherland, 2011). The ruby formed at greater depths (the upper mantle) than the sapphire (crust/upper mantle). However, ruby and sapphire have been found together in the central Chanthaburi-Trat deposits, including Bo Welu, which should have geological linkage between deeper ruby formation, narrower sapphire formation, and the deepest basaltic magma source prior to basaltic magma that has risen and then brought ruby, sapphire, and other associated assemblages up to the surface via volcanic eruption. More detailed investigation and further discussion of this complex geological process can be carried out on the basis of this study.

CONCLUSIONS

Although ruby and sapphire production from Bo Welu has declined since the 1970s, a few artisanal miners are still supplying the market. These stones are in high demand for their colors: purplish red ruby and green-blue sapphire. They are clearly characterized as basaltic-type corundum, based on their primary corroded surface.

Various types of mineral inclusions have been identified in this study, and their chemical composition can be used to interpret the conditions in which ruby and sapphire crystallized prior to being transported to the surface by basaltic magma. Many of these inclusions are common; for others, such as sillimanite, nepheline, quartz, alkali feldspar, spinel, and anhydrite for ruby and purple sapphire, and sulfide for blue sapphire, this is a newly reported occurrence in Thai corundum. These inclusions can be used to support origin determination. The original deep-seated formations of Thai ruby and sapphire as well as transportation by basaltic volcanism are actually complicated geological processes that must take place under very specific conditions. Therefore, these rubies and sapphires should be valued not only for their rarity and quality but also their unique geological history.

ABOUT THE AUTHORS
Ms. Promwongnan is a master's degree student in geology at Chulalongkorn University and a gemologist at the Gem Testing Laboratory of the Gem and Jewelry Institute of Thailand (GIT). Dr. Sutthirat (chakkaphan.s@chula.ac.th) is a professor of earth sciences at the Geology Department, Faculty of Science, Chulalongkorn University. He has also served as an academic advisor to the GIT's Gem Testing Laboratory.

ACKNOWLEDGMENTS
This research is financially supported by the 90th Anniversary of Chulalongkorn University, Rachadapisek Sompote Fund of Chulalongkorn University. All analyses were carried out at the Geology Department, Faculty of Science, Chulalongkorn University and the GIT's Gem Testing Laboratory. The first author would like to thank Duangkamol Jiambutr (GIT director), Wilawan Atichat, Visut Pisutha-Arnond, Thanong Leelawattanasuk, and Sakonvan Chawchai for their suggestions and encouragement. Special thanks are also be given to Sopit Poompeang for assistance with sample preparation and EPMA analysis. Finally, we must thank all the technical reviewers for handling the manuscript with very constructive comments and kind support.

REFERENCES

Aspen P., Upton B.G.J., Dickin A.P. (1990) Anorthoclase, sanidine and associated megacrysts in Scottish alkali basalts: high-pressure syenitic debris from upper mantle sources? *European Journal of Mineralogy*, Vol. 2, No. 4, pp. 503–517, http://dx.doi.org/10.1127/ejm/2/4/0503

Barr S., Cooper M. (2013) Late Cenozoic basalt and gabbro in the subsurface in the Phetchabun Basin, Thailand: Implications for the Southeast Asian Volcanic Province. *Journal of Asian Earth Sciences*, Vol. 76, pp. 169–184, http://dx.doi.org/10.1016/j.jseaes.2013.01.013

Černý P., Ercit T.S. (1985) Some recent advances in the mineralogy and geochemistry of Nb and Ta in rare-element granitic pegmatites. *Bulletin de Mineralogie*, Vol. 108, pp. 499–532, http://dx.doi.org/10.3406/bulmi.1985.7846

Coenraads R.R. (1992) Surface features on natural rubies and sapphires derived from volcanic provinces. *Journal of Gemmology*, Vol. 23, No. 3, pp. 151–160.

Coenraads R.R., Sutherland F.L., Kinny P.D. (1990) The origin of sapphires: U–Pb dating of zircon inclusions sheds new light. *Mineralogical Magazine*, Vol. 54, No. 374, pp. 113–122, http://dx.doi.org/10.1180/minmag.1990.054.374.13

Coenraads R.R., Vichit P., Sutherland F.L. (1995) An unusual sapphire-zircon-magnetite xenolith from the Chanthaburi Gem Province, Thailand. *Mineralogical Magazine*, Vol. 59, No. 396, pp. 465–479, http://dx.doi.org/10.1180/minmag.1995.059.396.08

Coleman R.G., Lee D.E., Beatty L.B., Brannock W.W. (1965) Eclogites and eclogites: their differences and similarities. *Geological Society of America Bulletin*, Vol. 76, No. 5, pp. 483–508, http://dx.doi.org/10.1130/0016-7606(1965)76%5B483:EAETDA%5D2.0.CO;2

Deer W.A., Howie R.A., Zussman J. (2013) *An Introduction to the Rock-forming Minerals*, 3rd ed. Longman, Essex, UK, 696 pp.

Ding Z. (1991) Mineralogical studies on Shandong sapphires (unpublished). MSc thesis, Academia Sinica Inst Geochem, Guiyang, China.

Droop G. (1987) A general equation for estimating Fe^{3+} concentrations in ferromagnesian silicates and oxides from microprobe analyses, using stoichiometric criteria. *Mineralogical Magazine*, Vol. 51, No. 361, pp. 431–435, http://dx.doi.org/10.1180/minmag.1987.051.361.10

Gübelin E.J. (1940) Differences between Burma and Siam rubies. *G&G*, Vol. 3, No. 5, pp. 69–72.

Gübelin E.J. (1971) New analytical results of the inclusions in Siam rubies. *Journal of Australian Gemmology*, Vol. 12, No. 7, pp. 242–252.

Gübelin E.J., Koivula J.I. (1986) *Photoatlas of Inclusions in Gemstones*, Volume 1. ABC Edition, Zurich, 532 pp.

Guo J., Griffin W.L., O'Reilly S.Y. (1994) A cobalt-rich spinel inclusion in a sapphire from Bo Ploi, Thailand. *Mineralogical Magazine*, Vol. 58, No. 391, pp. 247–258, http://dx.doi.org/10.1180/minmag.1994.058.391.07

Guo J., O'Reilly S.Y., Griffin W.L. (1996) Corundum from basaltic terrains: a mineral inclusion approach to the enigma. *Contributions to Mineralogy and Petrology*, Vol. 122, No. 4, pp. 368–386, http://dx.doi.org/10.1007/s004100050134

Hughes R.W. (1997) *Ruby & Sapphire*. RWH Publishing, Boulder, Colorado.

Intasopa S., Atichat W., Pisutha-Arnond V. (1998) Inclusions in corundum: A new approach to the definition of standards for origin determination. *Science and Technology for Gem and Jewelry Industry Thailand Research Fund* [in Thai].

Intasopa S., Atichat W., Pisutha-Arnond V., Sriprasert B., Narudeesombat N., Phuttarat T. (1999) Inclusions in Chanthaburi – Trat corundums: A clue to their genesis, in Thai. *Proceedings of the Symposium on Mineral, Energy, and Water Resources of Thailand: Towards the Year 2000, October 28–29, 1999, Bangkok, Thailand*, pp. 471–484.

Khamloet P., Pisutha-Arnond V., Sutthirat C. (2014) Mineral inclusions in sapphire from the basalt-related deposit in Bo Phloi, Kanchanaburi, Western Thailand: indication of their genesis. *Russian Geology and Geophysics*, Vol. 55, No. 9, pp. 1087–1102, http://dx.doi.org/10.1016/j.rgg.2014.08.004

Koivula J.I., Fryer C.W. (1987) Sapphirine (not sapphire) in a ruby from Bo Rai, Thailand. *Journal of Gemmology*, Vol. 20, No. 6, pp. 369–370.

Krzemnicki M.S., Hänni H.A., Guggenheim R., Mathys D. (1996) Investigations on sapphires from an alkali basalt, South West Rwanda. *Journal of Gemmology*, Vol. 25, No. 2, pp. 90–106.

Palke A.C., Wong J., Verdel C., Ávila J.N. (2018) A common origin for Thai/Cambodian rubies and blue and violet sapphires from Yogo Gulch, Montana, U.S.A? *American Mineralogist*, Vol. 103, No. 3, pp. 469–479, http://dx.doi.org/10.2138/am-2018-6164

Pattamalai K. (2015) Chanthaburi-Trat corundum deposits, Eastern Thailand. *Proceedings of The 3rd Lao-Thai Technical Conference, July 7–8, 2015*, pp. 219–229.

Promprated P., Taylor L.A., Neal C.R. (2003) Petrochemistry of mafic granulite xenoliths from the Chantaburi basaltic field: implications for the nature of the lower crust beneath Thailand. *International Geology Review*, Vol. 45, No. 5, pp. 383–406, http://dx.doi.org/10.2747/0020-6814.45.5.383

Promwongnan S., Sutthirat C. (2019) An update on mineral inclusions and their composition in ruby from the Bo Rai gem field in Trat Province, eastern Thailand. *Journal of Gemmology*, Vol. 36, No. 7, pp. 634–645, http://doi.org/10.15506/JoG.2019.36.7.634

Saeseaw S., Sangsawong S., Vertriest W., Atikarnsakul U., Liliane

R.-F.V., Khowpong C., Weeramonkhonlert V. (2017) A study of sapphire from Chanthaburi, Thailand and its gemological characteristics. *GIA Research News*, www.gia.edu/gia-news-research/sapphire-chanthaburi-thailand-gemological-characteristics

Saminpanya S., Sutherland F.L. (2011) Different origins of Thai area sapphire and ruby, derived from mineral inclusions and co-existing minerals. *European Journal of Mineralogy*, Vol. 23, No. 4, pp. 683–694.

Sangsawong S., Vertriest W., Saeseaw S., Pardieu V., Muyal J., Khowpong C., Atikarnsakul U., Weeramonkhonlert V. (2017) A study of rubies from Cambodia & Thailand. *GIA Research News*, https://www.gia.edu/gia-news-research/study-rubies-cambodia-thailand

Singbamroong S., Thanasuthipitak T. (2004) Study of solid mineral inclusions in sapphires from Ban Huai Sai area, Laos, by Raman spectroscopy. *Chiang Mai Journal of Science*, Vol. 31, No. 3, pp. 251–263.

Sutherland F.L., Hoskin P.W., Fanning C.M., Coenraads R.R. (1998a) Models of corundum origin from alkali basaltic terrains: a reappraisal. *Mineralogy and Petrology*, Vol. 133, No. 4, pp. 356–372.

Sutherland F.L., Schwarz D., Jobbins E.A., Coenraads R.R., Webb G. (1998b) Distinctive gem corundum suits from discrete basalt fields: a comparative study of Barrington, Australia, and West Pailin, Cambodia, gemfields. *Journal of Gemmology*, Vol. 26, No. 2, pp. 65–85.

Sutherland F.L., Bosshart G., Fanning C.M., Hoskin P.W.O., Coenraads R.R. (2002) Sapphire crystallization, age and origin, Ban Huai Sai Laos: age based on zircon inclusions. *Journal of Asian Earth Sciences*, Vol. 20, No. 7, pp. 841–849.

Sutherland F.L., Coenraads R.R., Schwarz D., Raynor L.R., Barron B.J., Webb G.B. (2003) Al-rich diopside in alluvial ruby and corundum-bearing xenoliths, Australian and SE Asian basalt fields. *Mineralogical Magazine*, Vol. 67, No. 4, pp. 717–732.

Sutthirat C., Saminpanya S., Droop G.T.R., Henderson C.M.B., Manning D.A.C. (2001) Clinopyroxene-corundum assemblages from alkali basalt and alluvium, eastern Thailand: constraints on the origin of Thai rubies. *Mineralogical Magazine*, Vol. 65, No. 2, pp. 277–295.

Sutthirat C., Hauzenberger C., Chualaowanich T., Assawincharoenkij T. (2018) Mantle and deep crustal xenoliths in basalts from the Bo Rai ruby deposit, Eastern Thailand: Original source of basaltic ruby. *Journal of Asian Earth Sciences*, Vol. 164, pp. 366–379.

Upton B.G.J., Aspen P., Chapman N.A. (1983) The upper mantle and deep crust beneath the British Isles: evidence from inclusions in volcanic rocks. *Journal of the Geological Society of Thailand*, Vol. 140, No. 1, pp. 105–121.

Vichit P. (1992) Gemstones in Thailand. In C. Piencharoen, Ed., *Proceedings of a National Conference on Geologic Resources of Thailand—Potential for Future Development: 17–24 November 1992, Bangkok, Thailand*. Department of Mineral Resources, Bangkok.

Yui T.-F., Wu C.-M., Limtrakun P., Sricharn W., Boonsoong A. (2006) Oxygen isotope studies on placer sapphire and ruby in the Chanthaburi-Trat alkali basaltic gemfield, Thailand. *Lithos*, Vol. 86, No. 3-4, pp. 197–211.

Characteristics of Hydrothermally Treated Beeswax Amber

Yamei Wang, Yan Li, Fen Liu, Fangli Liu, and Quanli Chen

The gemological characteristics of natural milky "beeswax" amber are compared with those enhanced by hydrothermal treatment. A layer of variable thickness of yellowish white or greenish yellow hydrothermally treated skin is generated below the natural, weathered skin of rough amber after this treatment. Different-sized pores and newly grown brown or yellowish white crust-like skin appear locally on the surface of the rough amber. Finished products show a white residue of hydrothermally treated spots. The treated beeswax displays abundant gas-liquid inclusions with small and flattened gas bubbles or disk-shaped bubbles accompanied by tiny strain-induced fractures. The gas bubbles are uneven in size and densely distributed, forming a cloud-like effect. A series of comprehensive tests are required to identify hydrothermally treated beeswax amber (HT amber).

Amber is an organic gem, formed tens of millions of years ago when sap from ancient trees hardened and fossilized. Scientists, gemologists, and collectors treasure amber that contains suspended insects or assorted plant fragments, creating a fascinating time capsule (Ross, 2010). Amber has become increasingly popular in the jewelry trade. It is usually translucent to opaque, and its opacity is caused by the reflection and scattering of incident light by an abundance of internal tiny bubbles. "Beeswax," a term commonly used in the Chinese gem trade, refers to amber that is semi-translucent to opaque with greasy luster. Beeswax accounts for about 60% of natural amber production globally. Due to the saying "Millennium amber, million years beeswax" in the Chinese gem market, many Chinese consumers mistakenly believe that beeswax takes much longer to form than amber. This misimpression has driven demand for beeswax and significantly raised its price.

Among beeswax, the "chicken-fat" yellow variety is highly desired in China for its vivid color, but limited in global production. It is worth noting that in the international rough amber trade, transparent and opaque materials are usually mixed together for sale, just as they are mixed together in nature. There is usually a layer of weathered skin on the surface of both transparent and opaque rough amber, making it impossible to choose them individually by hand under normal lighting. There is no price difference between the two. Quality is judged according to weight, size, shape, and impurities.

Due to the popularity of beeswax in the Chinese market, however, amber processing enterprises have preferred to purchase and store rough beeswax materials, artificially driving up the price of the rough material. Numerous researchers (e.g., Brody et al., 2001; Zhang, 2003; Zhang, 2006; Feist et al., 2007; Abduriyim et al., 2009; Ross, 2010; Wang et al., 2010, 2014) have investigated the methods to enhance the quality of amber. Many techniques have been at-

In Brief

- Hydrothermally treated amber is produced by heating the material in an aqueous solution with some catalyst to convert it from transparent to opaque.
- Hydrothermally treated amber shows yellowish white or greenish yellow hydrothermally treated skin below natural weathered skin. Various-sized pores and newly grown cracks or brown crust-like skin are developed on the surface of treated rough amber, and a residue of white spots is left in treated products.
- Hydrothermally treated amber displays abundant gas-liquid inclusions with small and flattened gas bubbles or disk-shaped bubbles accompanied by tiny strain-induced fractures. The bubbles are of different sizes and densely distributed, forming a cloud-like effect.

See end of article for About the Authors and Acknowledgments.
Gems & Gemology, Vol. 55, No. 3, pp. 370–387,
http://dx.doi.org/10.5741/GEMS.55.3.370

Figure 1. Various commercial HT amber products. A: calabash beads (751 g total). B: light yellow and yellow beeswax drop-shaped pendants. C: carved pendant (white HT beeswax). D: roasted "chicken-fat" yellow beads. E and F: good-quality and poor-quality necklaces of roasted HT amber. Photos by Yamei Wang.

tempted to improve the color of beeswax amber, such as heat treatment. Driven by profit, foreign rough suppliers have converted ordinary and low-quality transparent amber to opaque beeswax via hydrothermal treatment to cater to Chinese consumers.

In recent years, Chinese amber manufacturers have gradually mastered hydrothermal treatment through continuous exploration and technology transfer. This is a novel method to optimize the appearance of semi-translucent to opaque amber by heating it with controlled temperature and pressure in a furnace in aqueous solution and inert atmosphere. Submicron- and micron-sized gas bubbles are able to migrate into the amber during this process. As a result, the treated amber exhibits a uniform and compact appearance, and these commercial products are commonly known as hydrothermally treated or "HT" amber. This treatment expands the availability of amber products but leads to identification challenges.

The quality of HT amber varies, since manufacturers employ a range of technologies and rough materials. This method is generally applicable to rough amber materials, semi-finished products, and finished products. Common HT amber products include beads (figure 1A) and some pendants (figure 1, B–C). The majority of HT amber beads are used to produce "roasted old beeswax" (figure 1, D–F; box A details this and other common terms in the Chinese amber trade). Hydrothermal treatment followed by heat treatment can produce beeswax with a "chicken-fat yellow" color (figure 1D).

BOX A: TERMINOLOGY USED IN THE CHINESE AMBER MARKET

Beeswax: a common term in the Chinese gem trade, referring to semi-translucent to opaque amber that has an opalescent, milky appearance with greasy luster (figures A-1C and A-2A).

Chicken-fat yellow beeswax: the most desired beeswax variety, possessing a vivid yellow color (figure A-1D).

Gold-twisted honey amber: amber with semi-transparent and semi-opaque internal features (figure A-1B).

Golden amber: golden transparent amber (figure A-1A).

HT: hydrothermally treated, as in HT amber, beeswax, or copal resin.

Roasted HT beeswax: hydrothermally treated beeswax that subsequently undergoes heat treatment to enhance its color (figure A-2C).

Roasted old beeswax: white or light yellow beeswax that is heat-treated to enhance the color to a dark or saturated yellow (figure A-2B).

Weathered skin: a rough layer developed on the surface of amber after tens of millions of years of exposure to heat and pressure. Due to density variance between different resin layers, evaporation and volatilization occurred together with oxidation, which caused the surface layer to shrink, crack, and form irregular linear features.

Figure A-2. Images of (A) a natural beeswax strand, (B) a roasted old beeswax strand, and (C) a roasted HT beeswax strand. Photos by Yamei Wang.

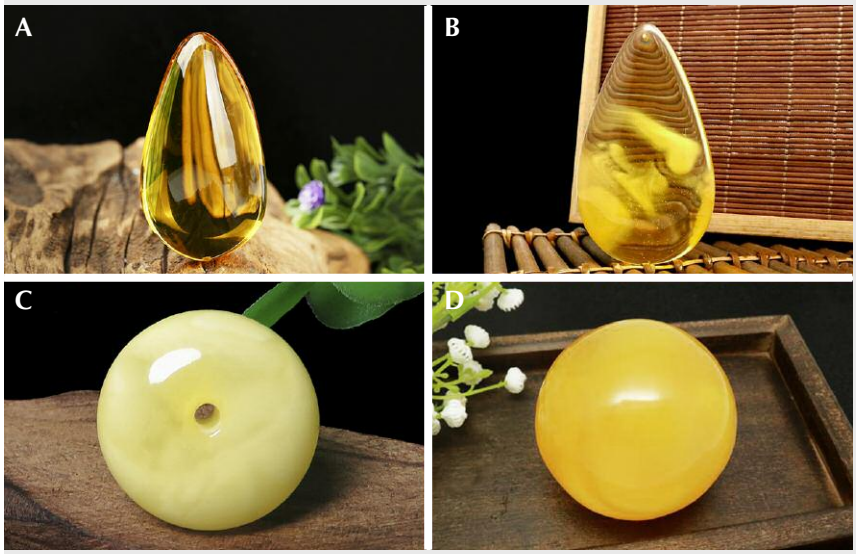

Figure A-1. Images of (A) golden amber, (B) gold-twisted honey amber, (C) beeswax, and (D) chicken-fat yellow beeswax. Photos by Yamei Wang.

Through experiments, investigation of manufacturing processes, and extensive research and identification practice, the authors have developed a method to identify HT amber (Wang et al., 2010, 2014, 2017). In the present work, the authors studied the inclusions and IR spectra of the specimens before and after hydrothermal treatment, providing valuable information regarding the formation mechanisms and identification characteristics of HT amber.

Figure 2. Rough amber materials before hydrothermal treatment, photographed at manufacturing facilities. Gold-twisted honey amber rough is shown on the left, transparent golden amber rough on the right. Photos by Yamei Wang.

MATERIALS AND METHODS

Specimens. The rough amber for hydrothermal treatment experiments in this study was sourced from Kaliningrad, Russia. Beeswax is a unique variety of Baltic amber, and amber rough material for HT is mostly selected from Baltic amber. (The use of Colombian copal resin for HT copal is also found in the market; see the Results section under "Microscopic Characteristics of Hydrothermally Treated Copal Resin.") Two types of commonly used rough materials for hydrothermal treatment were chosen as samples: gold-twisted honey amber (partially transparent and partially opaque) and transparent golden amber (both are shown in figure 2). Three representative specimens, labeled as I, II, and III, were used for the hydrothermal treatment experiment in this study (gemological characteristics of chosen specimens can be found in table 1 and figure 4). Sample III was further heat-treated to mimic old beeswax, since in the trade HT amber is often heated to form roasted old beeswax.

Some rough amber pieces (with and without weathered skin) presented in the Results and Discussion sections were typical HT specimens collected by the authors from Chinese manufacturing facilities. The others were client submissions previously examined at the China University of Geosciences gem testing center in Guangzhou, China. All of these samples, studied by the authors over many years, were used to show identification features of HT amber.

The HT amber finished products and copal resin beads were client submissions previously examined at the gem testing center in Guangzhou. These are typical examples of commercial HT amber and HT copal resin to mimic natural beeswax in the trade. Observations of these products are also presented in this study.

Hydrothermal Treatment Experiment. Hydrothermal treatment aims to introduce an abundance of tiny bubbles (nano- and micron-sized) into the amber in an aqueous solution with some catalyst. Doing so optimizes the appearance of amber by converting it from transparent to opaque to mimic beeswax. Hydrothermal treatment is carried out in a pressure autoclave by controlling the temperature and pressure and selecting an inert atmosphere (figure 3), similar to the pressure furnace established for amber heat treatment (Wang et al., 2014).

Optical Microscopy and Scanning Electron Microscopy. Morphological analysis was carried out via optical microscopy (Olympus BX 60) and scanning electron microscopy (FEI Inspector-F) with an electron beam of 20 kV. SEM was conducted to assess the morphology of the bubbles in the amber with gold coating at room temperature.

Fourier-Transform Infrared Spectrometry. Three amber samples before and after hydrothermal treat-

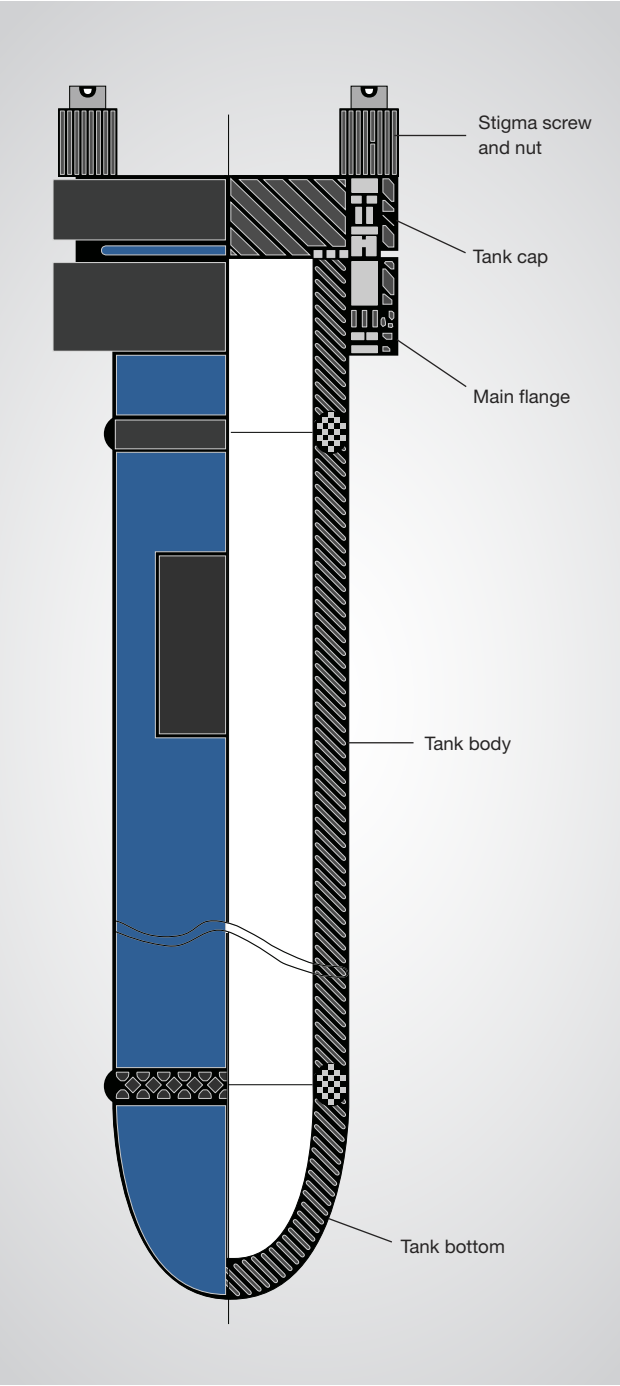

Figure 3. Diagram of the pressure furnace used for hydrothermal treatment.

ment were measured using a Bruker Tensor-27 Fourier transform infrared (FTIR) spectrometer to check the variations among the functional groups of samples. FTIR was used to reflectively scan each sample 32 times in the range of approximately 4000–400 cm^{-1}.

RESULTS

Gemological Characteristics of Rough Amber Before Hydrothermal Treatment. Three semi-finished amber samples were chosen and polished as much as possible to remove their weathered skin before hydrothermal treatment (figure 4). The gemological characteristics of these rough amber specimens (samples I, II, and III) before hydrothermal treatment are listed in table 1. Sample III was heated after hydrothermal treatment.

Characteristics of Rough Amber Material After Hydrothermal Treatment. In our experiment, the three samples changed from transparent to translucent or opaque after hydrothermal treatment, achieving the expectation of treatment (see the characteristics in table 2). The color of the golden amber (samples I and II) became darker, while the gold-twisted honey amber (sample III) became white. All three developed a layer of khaki-colored, hydrothermally treated skin or white hydrothermally treated spots (figure 5, A–F). However, the samples' refractive index and fluorescence intensity did not change much.

There was no significant difference in the infrared absorption spectra of the three samples before and after hydrothermal treatment (figure 5G). Spectra show that the characteristics of the aliphatic skeleton structure consist of absorption peaks caused by the stretching vibration of C-H saturated in the range of approximately 3000 to 2800 cm^{-1} (Wang et al., 2010). The corresponding absorption peaks at 1457 and 1378 cm^{-1} are attributed to δ (CH_2-CH_3) bending vibration and carbonyl stretching vibration absorption peaks ranging from 1695 to 1736 cm^{-1}. In addition, the samples have a wide absorption shoulder (Baltic shoulder) in the range of 1261 to 1164 cm^{-1}, which is attributed to the C-O stretching vibration. This is an unusual peak shape for Baltic amber.

The effect of hydrothermal treatment can vary depending on the starting materials. The gold-twisted honey amber (translucent, semi-beeswax-like) achieves the best appearance after treatment, while golden amber performs the worst. An important value factor of beeswax is "waxiness," a term that describes whether the materials look and feel compact and uniform. Compact and uniform high-quality HT amber only accounts for one-third of the material treated. Waxiness is related to the number and size of the gas bubbles inside the amber. Larger bubbles generate more surface area to diffuse light, but they also make the texture of beeswax rough.

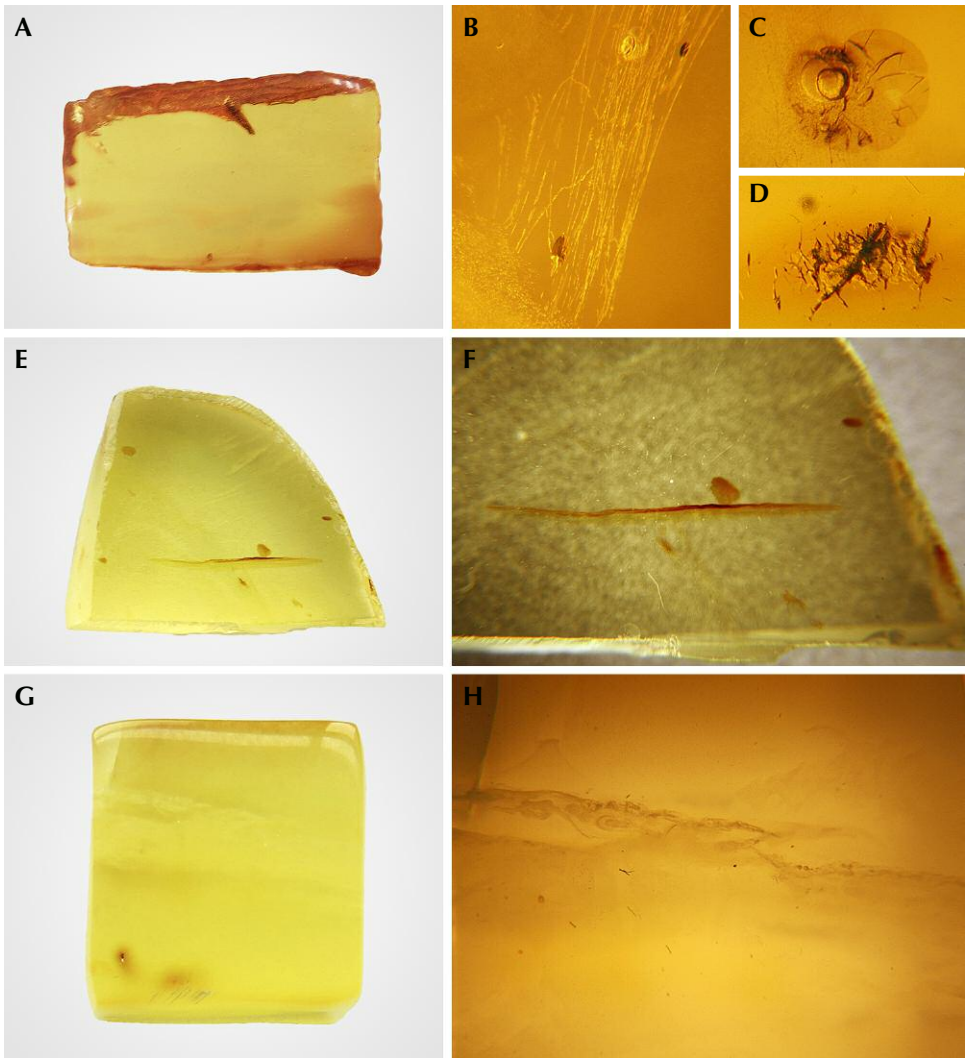

Figure 4. Gemological characteristics of rough amber specimens before hydrothermal treatment. A: sample I (golden amber, 10.20 g). B: filament and flow striation in sample I (field of view 11 mm). C: gas-liquid inclusions in sample I (field of view 5.5 mm). D: internal impurities in sample I (field of view 7 mm). E: sample II (golden amber, 2.24 g). F: internal red crack in sample II (field of view 22 mm). G: sample III (gold-twisted honey amber, 2.39 g). H: translucent, semi wax-like inclusions in sample III (field of view 16 mm). Photos by Yamei Wang.

Therefore, high-quality beeswax needs to have a large amount of small gas bubbles.

Visiting the factory, author WYM also noticed features that developed on HT rough amber. A new layer of greenish yellow, yellowish white HT skin occurred below the natural weathered skin of most HT amber rough materials (figure 6, A–B). This HT layer, which formed when a large amount of tiny gas bubbles quickly gathered in the shallow surface, had a relatively high porosity (figure 6A). A gradual transi-

TABLE 1. Gemological characteristics of the rough amber samples.

Sample no.	Weight (g)	Category	Origin	Color	Transparency	UV fluorescence (LW)	Internal characteristics
I	10.20	Golden amber	Russia	Golden yellow	Transparent	Medium yellowish white	Internally clean, partial flow pattern, gas-liquid inclusions, filaments, and internal impurities
II	2.24	Golden amber	Russia	Bright yellow	Transparent	Strong yellowish white	Internally clean, with only a small red crack
III	2.39	Gold-twisted honey	Ukraine	Yellow	Translucent and semi wax-like	Strong yellowish white	Transparent and opaque beeswax twisted together, as well as various sizes of bubbles

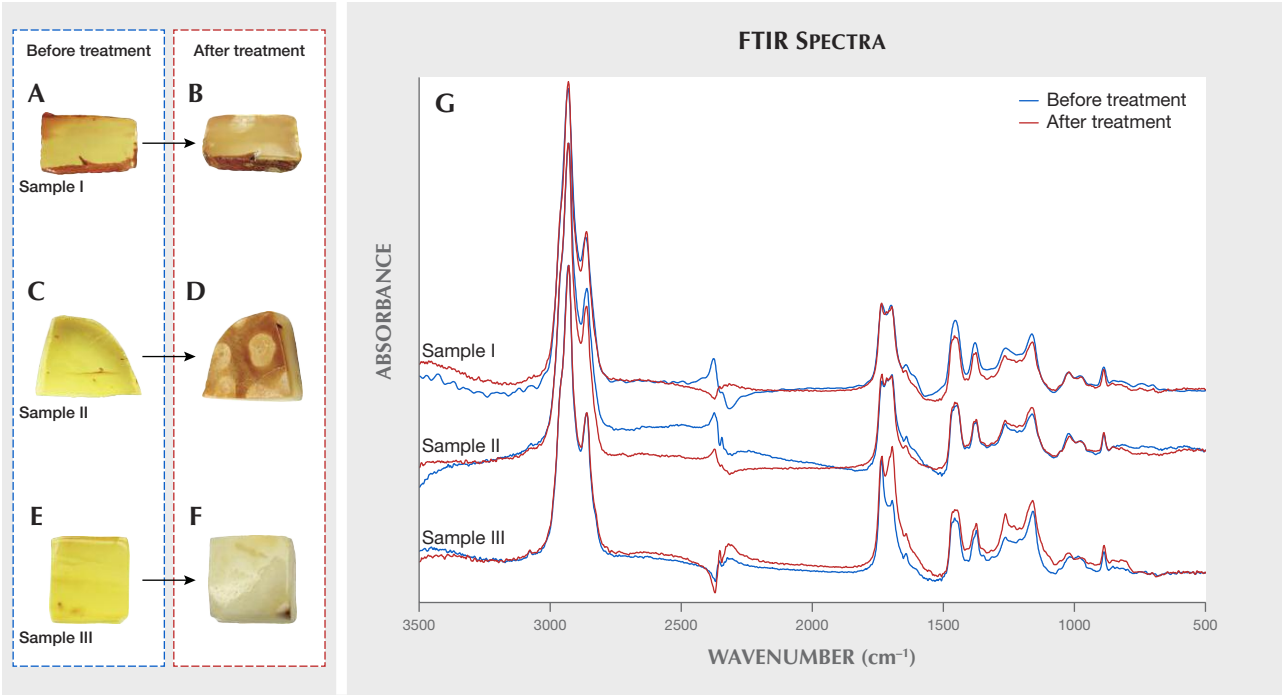

Figure 5. Variations in the appearance of amber samples before and after hydrothermal treatment: samples I (A and B), II (C and D), and III (E and F). G: infrared absorbance before and after hydrothermal treatment. Note that there was no weight change after hydrothermal treatment. Photos by Yamei Wang.

tion was observed (figure 6, C–D) from larger bubbles to smaller bubbles with increasing depth (figure 6, E–F). No such size change was observed within the white HT skin.

A circular weathered disk often forms around HT spots with various sizes, a feature that can be used to distinguish treated beeswax (figure 7, A–B). This disk can penetrate the amber and remain on the surface after polishing (figure 7, C–D). It was speculated that the weathered disk around HT spots formed after prolonged soaking in the condensation water droplets and that HT spots might be caused by vaporization of water molecules in the furnace. Some of the water vapor molecules are recondensed into

TABLE 2. Gemological characteristics of specimens before and after hydrothermal treatment.

Sample no.		Color	Transparency	RI	Fluorescence (LW)	Appearance
I	Before	Gold yellow	Transparent	1.54	Medium yellow	The purpose of treatment was achieved, but the effect was just fair. A white layer of HT skin was developed (figure 5, A and B). The inclusions were invisible after hydrothermal treatment.
	After	Darker yellow-brown	Semi-translucent	1.54	Strong yellow-white	
II	Before	Light yellow	Transparent	1.54	Strong yellow-white	A new layer of HT skin and spots developed (figure 5, C and D).
	After	Darker yellow-brown	Opaque	1.54	Strong yellow-white	
III	Before	Yellow	Translucent and somewhat wax-like	1.54	Strong yellow-white	The amber changed to white and showed uniform wax luster after hydrothermal treatment (figure 5, E and F).
	After	Yellow-white	Opaque	1.54	Strong yellow-white	

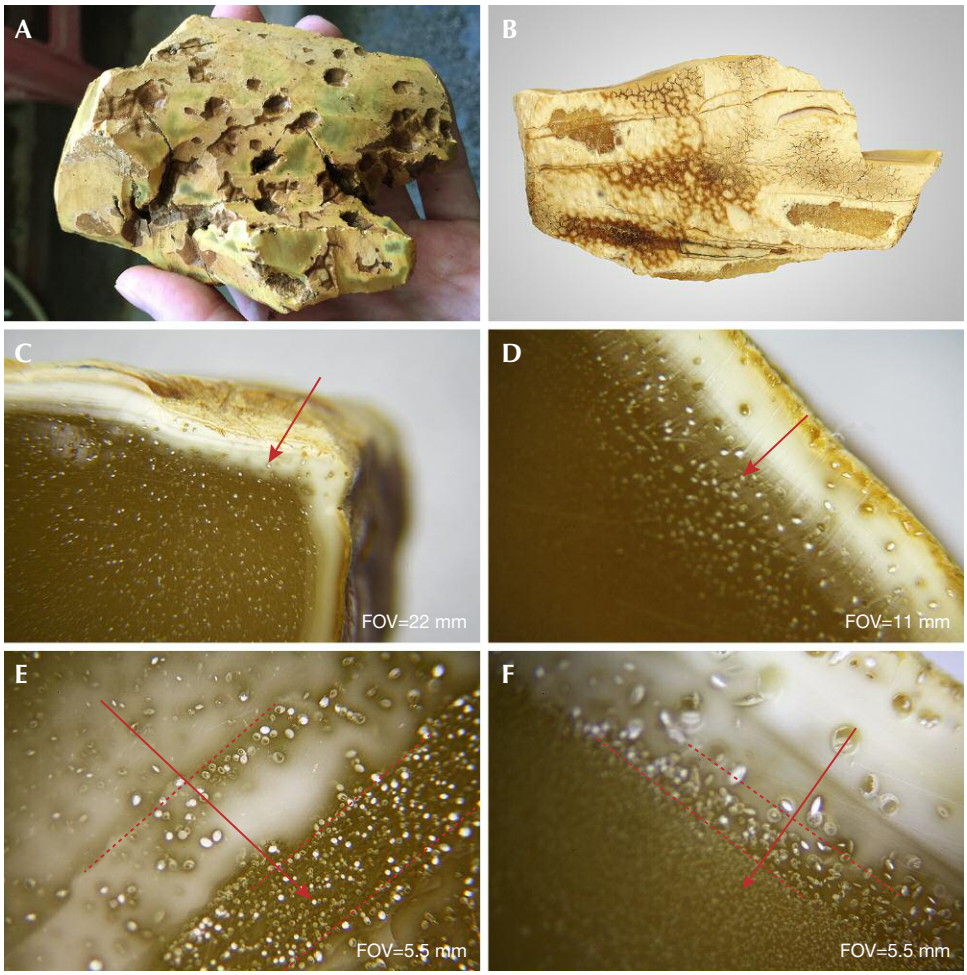

Figure 6. External and internal characteristics of HT amber rough. A: yellowish green HT skin. B: yellowish white HT skin. C and D: HT skin transition phenomenon. E and F: bubble stratification phenomenon. These previously examined samples were collected from manufacturing facilities. Photos by Yamei Wang.

water droplets left on the surface of HT amber (a permanent residue).

The surface of the freshly HT amber shows a "water ripple" structure (figure 8, A–B), and is often locally accompanied by a layer of yellowish white or greenish yellow HT skin with various thicknesses, or a corrugated, crust-like skin containing mostly oval pores (figure 8, C–D). Some surface areas on the HT skin are cracked, forming a crust-like texture (figure 8E). In some cases, yellowish white HT skin is found below the black naturally weathered skin of rough amber (figure 8F). All these features are quite different from the weathered skin or cracks on untreated amber. The HT skin and spots are therefore diagnostic evidence of HT amber.

Microscopic Characteristics of Finished HT Amber. The appearance of HT amber is mostly uniform and waxy (figure 1, B–E) with undeveloped flow lines, sometimes with white HT spots as well as a compact structure. With magnification, one can easily detect an abundance of gas bubbles around HT spots. These bubbles lower the transparency of the amber. A larger number of smaller bubbles provides a higher-quality treated amber (figure 9, A–B). Dense, flat, or disk-shaped gas bubbles or gas-liquid inclusions are commonly found in HT amber (figure 9, C–F). The size range of gas bubbles in HT amber is substantially greater than that in untreated beeswax.

HT amber retains the natural flow lines of gold-twisted honey amber. However, the flow lines appear disordered, less clear, and smoother compared to the pattern in natural beeswax, which may be attributed to the impact of later gas intervention (figure 9, G–H).

In the Chinese market, most HT beeswax materials are further heated to obtain a vivid yellow color. The surface of HT beeswax is slowly oxidized during

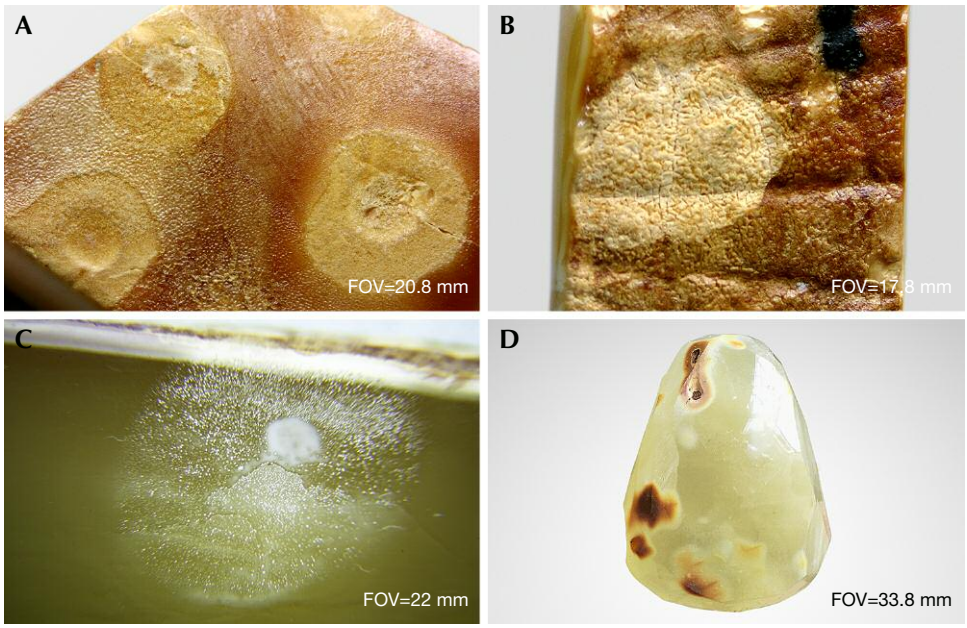

Figure 7. Features of hydrothermally treated spots. A: newly generated spots on the HT skin of sample II. B: newly generated spots on the weathered skin of sample I. C: spots penetrated the HT skin. D: spots on the polished surface. These previously examined samples were collected from amber manufacturing factories. Photos by Yamei Wang.

the heat treatment, and the color may reach chicken-fat yellow. There is an obvious layering of different-sized and different-colored bubbles near the surface of roasted HT amber (figure 9I). There is no color dif-

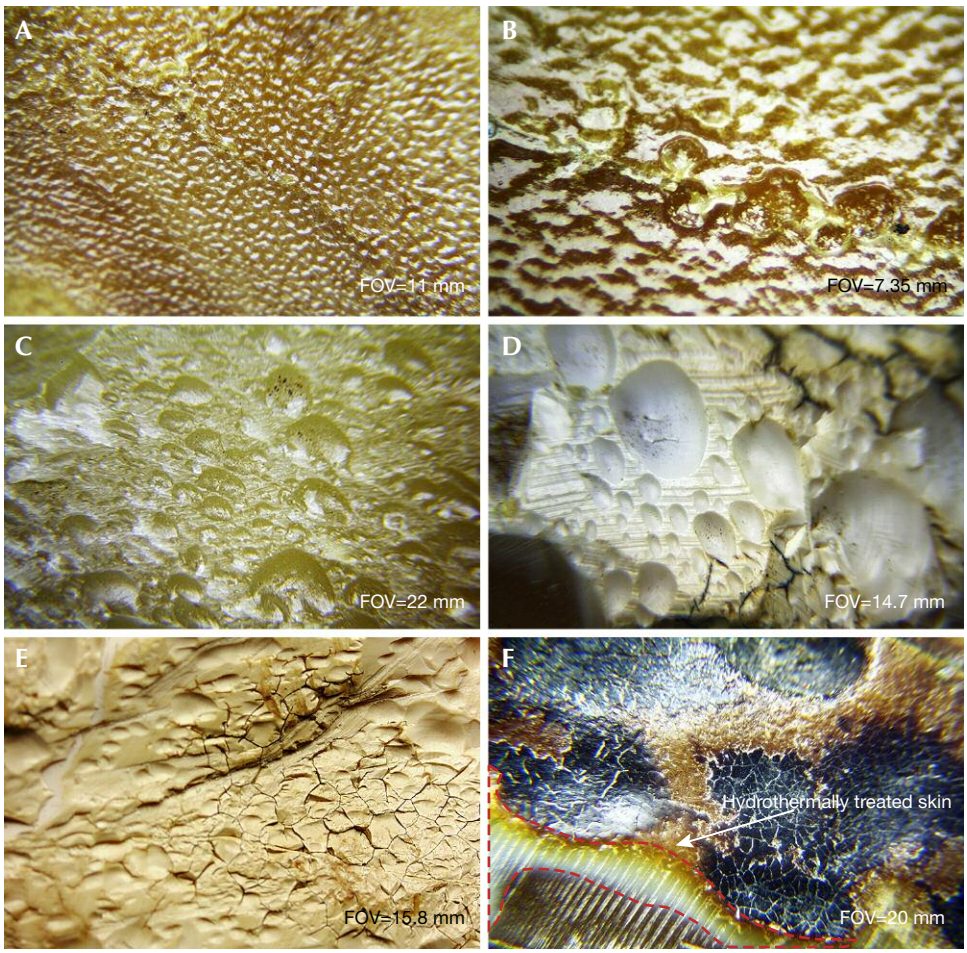

Figure 8. Features of hydrothermally treated skin. A and B: water ripple structure. C and D: oriented and distributed bubbles or residual porosity on HT skin. E: cracked or brown crust-like HT skin. F: yellowish white HT skin below the weathered skin of rough amber material. These previously examined samples were collected from amber manufacturing facilities. Photos by Yamei Wang.

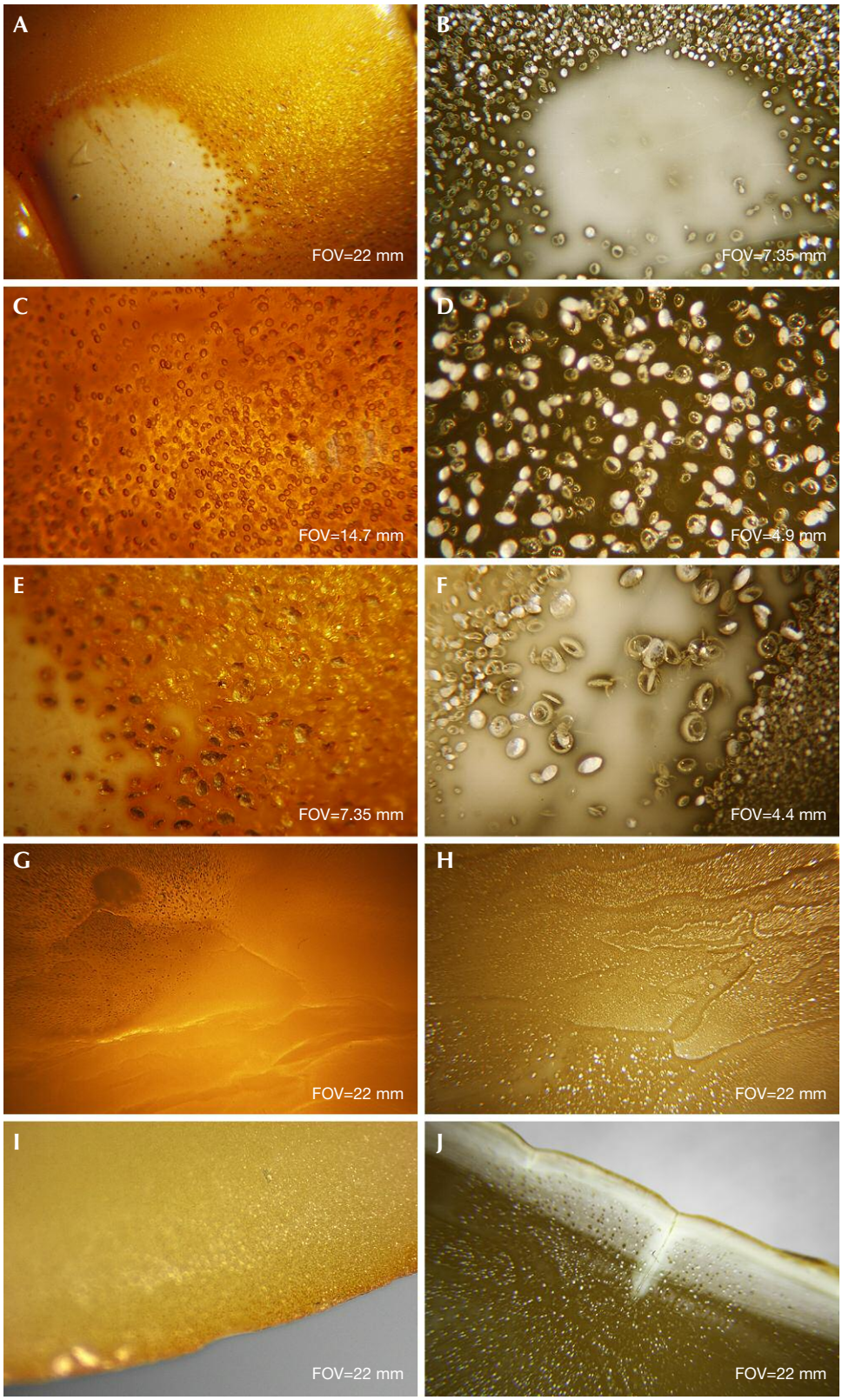

Figure 9. Inclusions in HT amber. A: HT spots on the surface of roasted HT amber. B: HT spots on finished amber surface. C: dense, flat gas bubbles. D: dense, disk-shaped gas inclusions. E: bubble cluster near the HT spots. F: enriched gas-liquid phase inclusions. G: fuzzy flow lines. H: disordered flow lines. I: color zoning close to the surface of roasted HT amber. J: a spread white pattern along the crack. These previously examined samples were collected from amber manufacturing facilities. Photos by Yamei Wang.

ference if the sample is not roasted but only hydrothermally treated. A white diffusion pattern appears along the cracks after hydrothermal treatment of originally cracked amber (figure 9J).

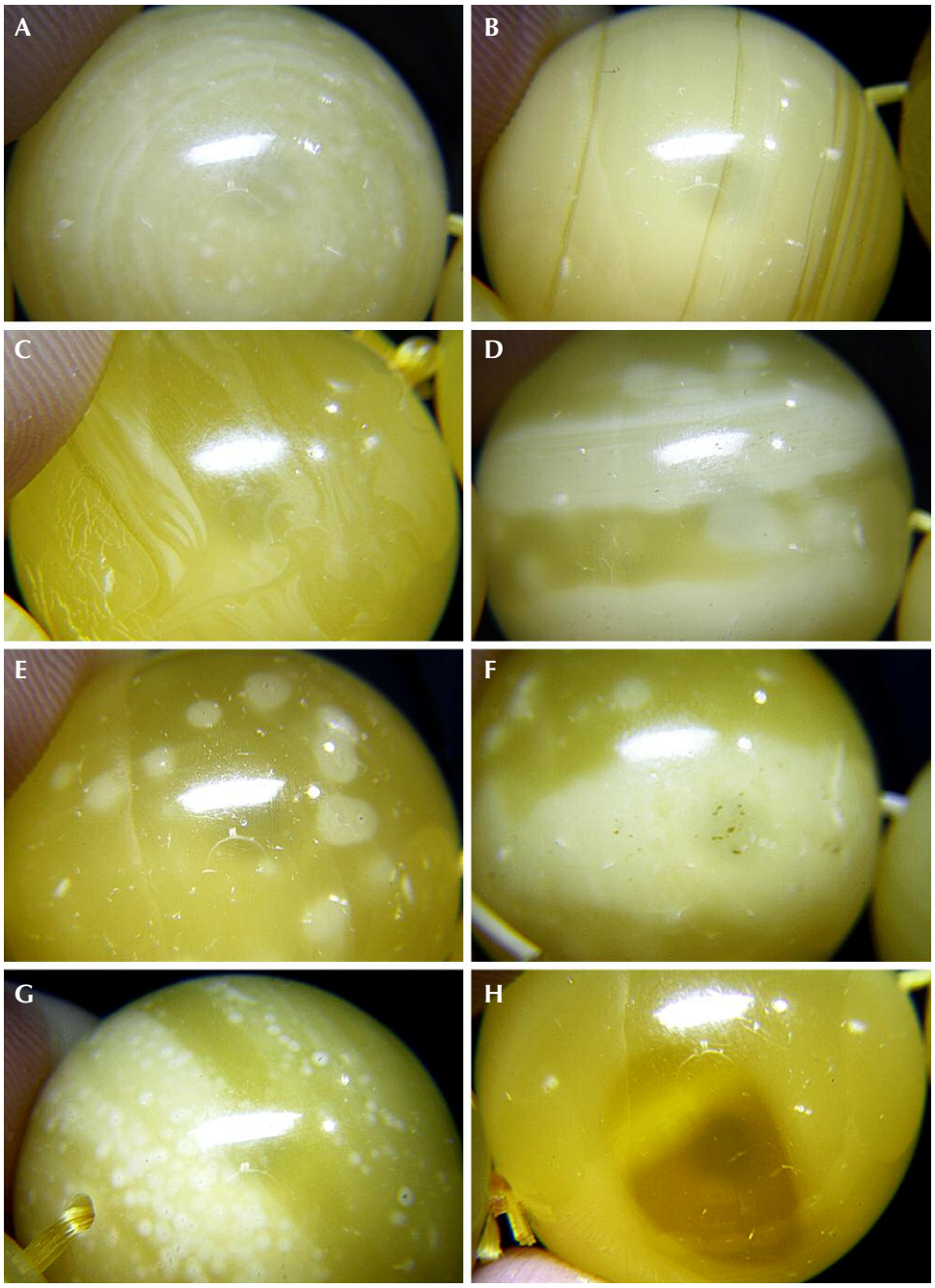

Figure 10. A: concentric structures of HT copal beads. B: thick and thin straight lines of HT copal beads. C: flow lines similar to beeswax. D: striped structures of HT copal beads. E: round dot-like HT spots. F: large HT spots. G: densely distributed HT spots along the white belt. H: obvious boundaries between the opaque and transparent areas (the diameter of the bead is around 11–12 mm). These previously examined samples were from a client's collection. Photos by Yamei Wang.

Microscopic Characteristics of Hydrothermally Treated Copal Resin. The HT copal resin finished products (figure 10) mimic the appearance of natural beeswax. For example, Colombian copal resin can be transformed into yellow or yellow-green opaque copal after hydrothermal treatment. The client who sent the copal resin beads for examination acknowledged that they went through multiple cycles of hydrothermal treatment, around 20 hours total. Since the original copal resin material is transparent without flow lines, the HT copal will not show the flow patterns. This is very different from HT amber, which often starts with gold-twisted honey amber full of flow lines. These flow lines are often retained in the HT products. HT copal resin instead shows more concentric rings and a straight, irregular, and banded or striped texture (figure 10, A–D). There are various forms of HT spots (figure 10, E–G), and the boundaries between the opaque and transparent areas of copal are often very obvious (figure 10H). There

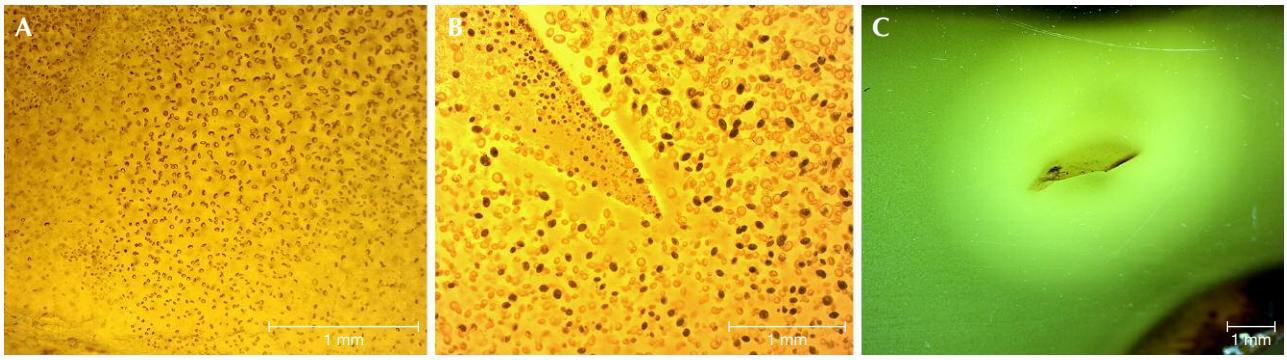

Figure 11. A and B: Disk-like bubbles in HT copal resin. C: Large HT spots on the surface of a copal resin sample. These samples were from a client's collection. Photos by Yamei Wang.

are obvious disk-like bubbles in the HT copal resin and large HT spot residues on the surface of copal resin (figure 11).

DISCUSSION

The Mechanism of Hydrothermal Treatment. The purpose of hydrothermal treatment is to generate the same mechanism that turns natural beeswax opaque by adjusting the temperature, pressure (inert gas), and saturated vapor pressure inside the furnace to make the water vapor penetrate the softened amber. To better illustrate the equilibrium of two-phase wet steam on the amber surface, the hydrothermal treatment process is illustrated in figure 12A. The effect is similar to when a tap water valve is opened all the way and the high water pressure in the pipe causes bubbles to form as air is trapped within the water, making it appear white and opaque. When the water pressure is reduced close to atmospheric pressure, the flowing water does not contain so many air bubbles and becomes transparent (figure 12B, top).

There are two types of vaporization: evaporation and boiling. Evaporation occurs on the surface, while boiling occurs when the saturated vapor pressure is equal to the external pressure. Both forms are suitable for hydrothermal treatment of amber. First of all, amber in the furnace will be affected by the dual role of temperature and pressure, resulting in softening

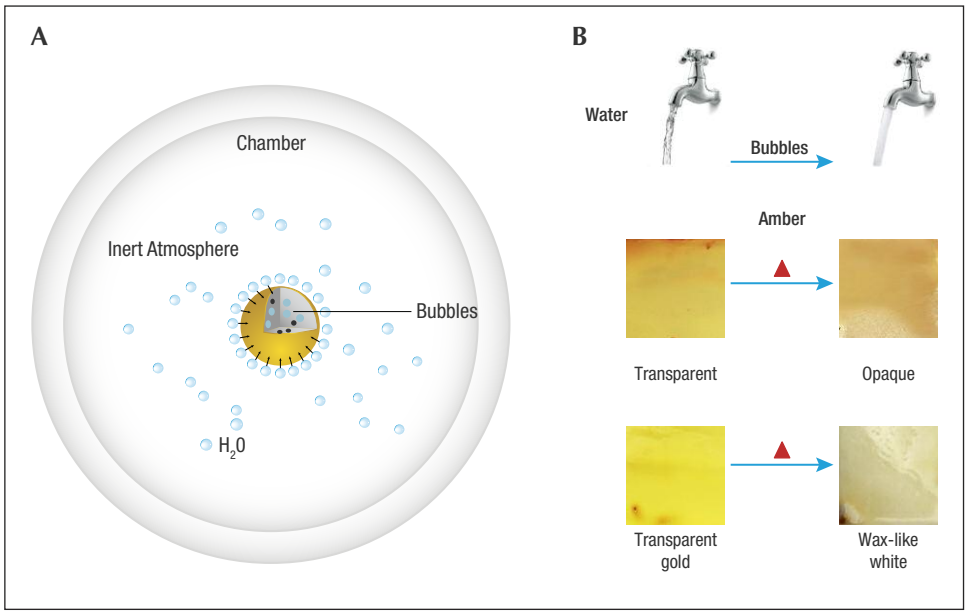

Figure 12. A: Evaporation of H_2O steam on amber in the chamber under inert atmosphere. B: Hydrothermal treatment introduces tiny bubbles into transparent amber (the red triangle represents hydrothermal treatment). Illustrations by Yan Li.

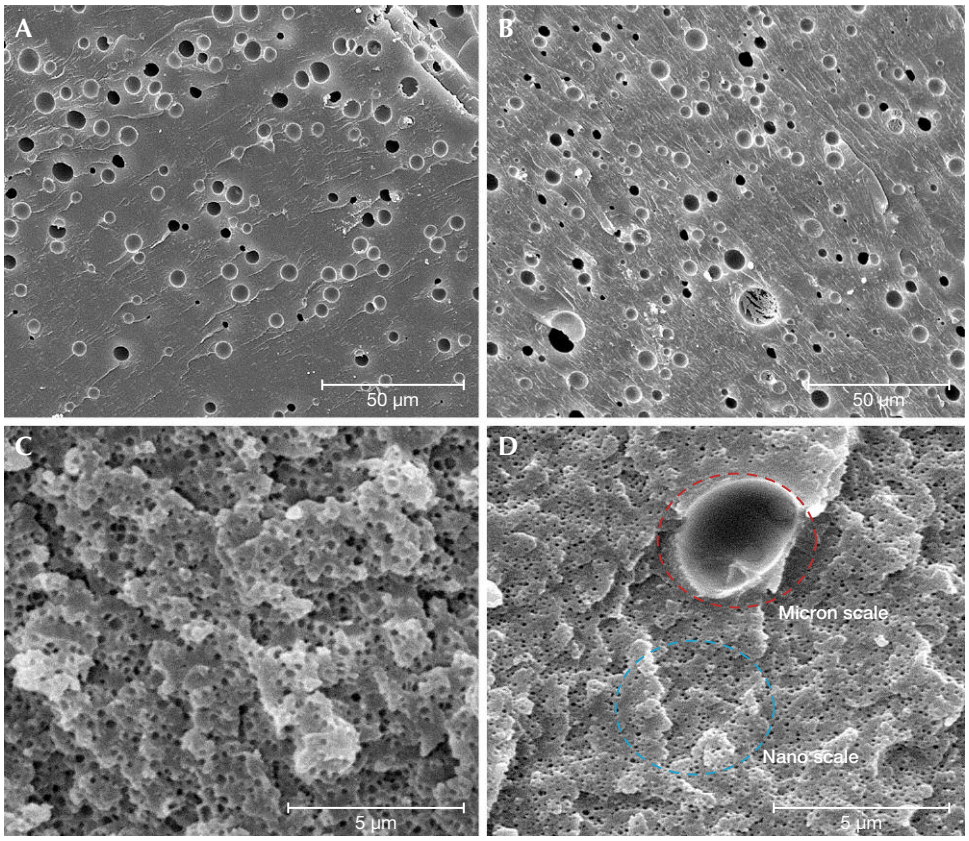

Figure 13. SEM images of bubbles in (A) natural beeswax and (B) HT beeswax amber. SEM images of (C) natural white beeswax and (D) crust of HT white beeswax. Samples were collected from amber manufacturing facilities. Photos by Yamei Wang.

(making it rubbery). Meanwhile, at a certain temperature when the conditions in the chamber are adequate to give the water molecules enough kinetic energy to break away from the surrounding molecules, steam will form. Water vapor in the chamber by means of steam pressure and the pressure of external inert gas constantly penetrates the softened amber in the form of wrapped bubbles; the amber becomes opaque, with a wax-like or milky color, achieving the appearance of beeswax.

Beeswax is translucent to opaque and milky in appearance, the result of reflection and scattering of light by abundant tiny gas bubbles in the amber. Wang et al. (2016) used SEM to observe the size and distribution of bubbles per unit area and the area ratio of bubbles in a variety of amber specimens. The gas bubbles, caused by the volatile materials within amber, have a round shape (ranging from 100 nm to 15 µm, with a density of hundreds to thousands of bubbles per mm^2) and are uniformly distributed. The density of the gas bubbles is positively related to the amber's opacity. The higher density of the gas bubbles leads to a less transparent appearance. The smaller the gas bubbles, the smoother or more compact the texture is.

HT Amber Quality and Durability. Softening the amber is a prerequisite of treatment. Once softened, the amount of gas bubbles penetrating the amber during hydrothermal treatment is related to pressure. There is no obvious difference in the size range of gas bubbles in natural beeswax and HT beeswax under SEM because of the much smaller area of observation (figure 13, A–B). However, the observation is dramatically different under an optical microscope: The gas bubbles in HT beeswax are small and flattened or disk-shaped and densely distributed (figure 9D). Gas bubbles in natural white beeswax can only be observed under SEM of 5000–10,000× magnification. In general, 30× or higher magnification is required to see bubbles in natural beeswax, while 10× magnification is sufficient for HT amber. The white HT skin is caused by rapid accumulation of tiny gas bubbles in the highly porous shallow surface of the amber. Gas bubbles can be divided into two different groups: the micron-scale bubbles that are clearly visible at 800× magnification (figure 13B and 13D, red circle) and the secondary nano-scale bubbles visible at 10,000× magnification (figure 13D, blue circle). The density of bubbles in beeswax is positively related to opacity. Both the porcelain white color and the com-

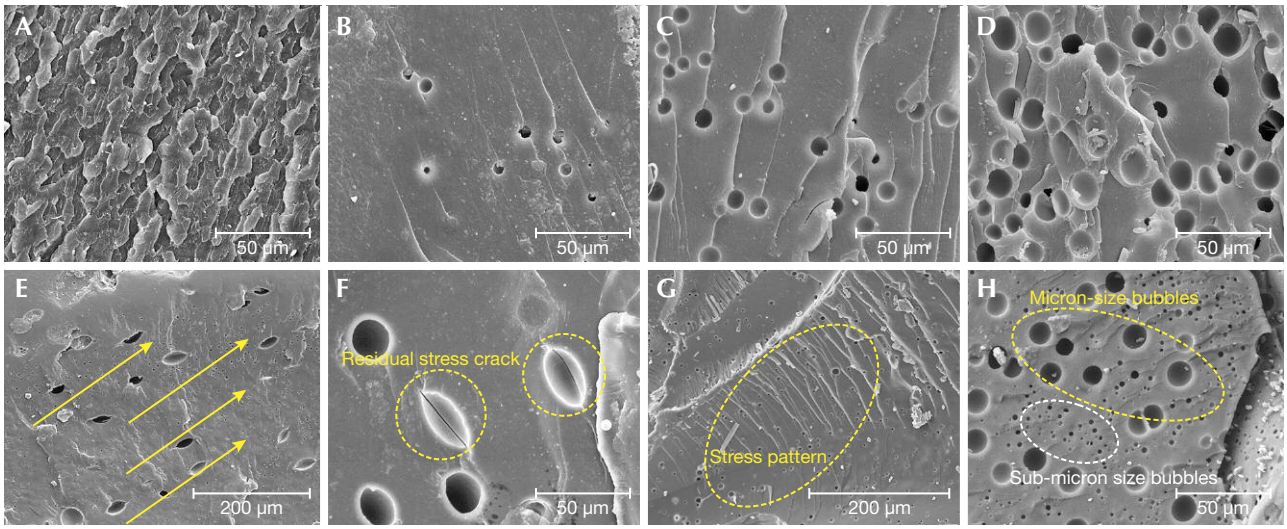

Figure 14. SEM images A–D show the characteristics of natural beeswax. A: layering structure. B: gas bubbles scattered in the amber matrix. C: gas bubbles with a size of 8–11 µm, uniformly dispersed in the matrix. D: closely distributed gas bubbles, 8–17 µm. SEM images E–H show the characteristics of hydrothermally treated beeswax. E: oval bubbles oriented along the long axis. F: residual stress cracks along the oval bubbles. G: a parallel stress pattern. H: submicron-/micron-sized bubbles. These previously examined samples were collected from amber manufacturing facilities. Photos by Yan Li.

pact structure of high-quality natural white beeswax are attributed to the nano-scale bubbles (figure 13C). Hence, the large amount of artificially introduced nano-scale bubbles (figure 13D, blue circle) in the treated samples will lead to an even more compact structure of white HT skin and a milky appearance.

HT beeswax beads are especially prone to breaking or cracking in the process of drilling. In comparison, natural beeswax has high toughness, possibly due to its layering structure (figure 14A). The distribution, amount, and density of tiny gas bubbles in the HT amber was different from that in natural beeswax (figure 14, B–D). Depending on the cutting direction, it is possible to see both circular and oval bubbles in HT amber, and figure 14E shows an orientation along the bubbles' long axis direction and residual stress cracks along the oval bubbles (figure 14F), accompanied by small but obvious stress patterns (figure 14G). HT beeswax is easily burst during processing due to residual stress cracks. The submicron-/micron-sized bubbles (figure 14H) penetrating the HT amber are associated with a certain pressure that has not been disclosed. It is presumed that gas bubbles form in HT beeswax from the synergistic effect of temperature and pressure during the hydrothermal treatment process. Adjacent gas bubbles may squeeze each other, resulting in deformation and forming stress patterns or lines.

Definition and Identification of Hydrothermally Treated Amber. *Definition and Naming.* Since HT amber is a new product, the authors suggest that several factors be taken into consideration for defining it:

1. The hydrothermal treatment process is similar to heat treatment in practice, as both are completed in a pressure furnace. They have opposite outcomes, however (Wang et al., 2010). Heat treatment is a purification process for squeezing gas inclusions out of the amber to form transparent golden amber, while hydrothermal treatment aims to introduce submicron-/micron-sized bubbles into the amber to create a milky appearance (figure 15).
2. Hydrothermal treatment aims to improve the appearance of amber by artificially creating inclusions, causing the appearance of natural beeswax. Translucent amber, semi-beeswax, gold-twisted honey amber, transparent gold amber, and low-quality beeswax usually serve as the starting materials for hydrothermal treatment.
3. HT amber (figure 16, left) is mostly used for further heat treatment to produce roasted old beeswax (figure 16, right; see definition in box

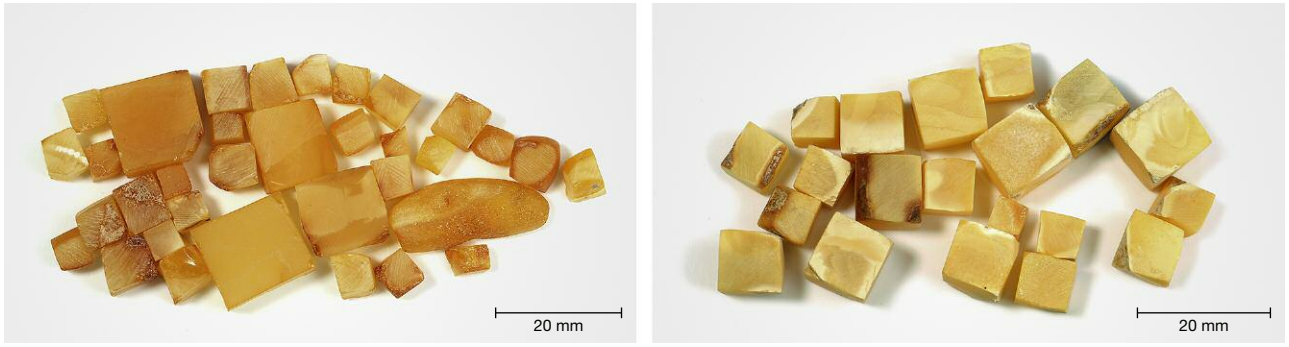

Figure 15. Semi-finished amber before and after hydrothermal treatment, photographed at the factory. Photos by Yamei Wang.

A). Natural beeswax with a faint yellow color could be heat-treated to mimic saturated yellow or dark yellow beeswax (see figure A-2C). The roasted old beeswax formed slowly due to oxidation from more than 15 days of continuous heat treatment at 60–90°C under atmospheric pressure (figure 1, D–F). However, the structure of the roasted HT amber did not change significantly, indicating its durability.

4. HT amber is mainly composed of foreign gas bubbles in the structure through physical introduction, but natural beeswax contains its own volatile ingredients (Yang et al., 2002). A series of processes take place during the formation of amber from resinite. Two key processes have been recognized by researchers, namely polymerization and volatilization (Scalarone et al., 2003; Guiliano et al., 2007). Volatilization refers to the process in which volatile components (VCs) contained in the original resinite continuously escape during the geological process. The VCs mainly include terpenes, unsaturated compounds, and carboxylic acids (Matuszewska and John, 2004). According to the shape and distribution of bubbles in amber, it is speculated that the formation of bubbles is related to terpenes, succinic acid, and other volatiles carried by amber itself. This is distinctly different from gas-liquid inclusions, which are isolated, gas-liquid two-phase inclusions (figure 9F, observed by gemological microscope).

Baltic amber comes from pine and cypress trees. Infrared spectroscopy shows that it has a higher content of volatile components and succinic acid in the initial resinite than amber from other areas (such as Myanmar, Mexico, China, and the Dominican Republic). FTIR results show that almost all Baltic amber without heat treatment has a set of absorption peaks near 3070, 1645, and 888 cm^{-1} caused by C=C stretching vibration and out-of-plane bending vibration of C-H on the double bond of methylene outside the ring (Wang et al., 2016). These absorption peaks reflect the fact that while the evolution of Baltic amber took place over a period of 50 million years, a small amount of volatile terpenes containing unsaturated bonds remained. The VCs were buried together with the resinite, leading to the change in shape and distribution of bubbles with the variations of temperature, pressure, wall rock type, and other geological conditions. Since the Tertiary period, the geological conditions of the Baltic Sea area have continuously evolved. The volatile components of buried resin fossils have continuously escaped over that time. However, amber can be found in geological environments with high pressure (for example, the surrounding rock of amber in the Baltic Sea was

Figure 16. Left: HT amber beads. Right: The roasted HT amber with enhanced color. Samples were collected from the factory. Photos by Yamei Wang.

Figure 17. Flowchart for the identification of hydrothermally treated amber. Photos by Yamei Wang.

mainly a blue mud layer). Occasionally bubbles are enclosed in amber to form beeswax, and they tend to become smaller. Gas chromatography coupled with mass spectrometry has been successfully used for identification of VCs contained in the fossil resin matrix (Stout et al., 2000; Vîrgolici et al., 2010), and the results confirmed that the VCs mainly consist of aromatic compounds such as terpenes, semiquinones, and biguanides.

The authors believe that hydrothermal treatment is a practical and acceptable method to enhance the appearance of amber to fulfill market demand in certain locations. Western markets might not enjoy the opaque products as much as the Chinese market. This belief is based on a comprehensive analysis of the nature of the HT treatment materials, technical process, purpose, effect, stability, market acceptance, and detection standards. In recent years, it has been used more and more widely in the market and accounts for a relatively large proportion of bead products. In order to ensure that consumers are informed, it should be referred to as *amber* rather than *beeswax*. However, the use of hydrothermal treatment needs to be disclosed.

Identification of Hydrothermally Treated Amber. As explained above, it is feasible for experienced gemologists to definitively identify HT amber pieces. Identification focuses on external and internal characteristics (figure 17):

1. The appearance of HT amber is mostly uniform and waxy.
2. It sometimes displays white HT spots as well as a compact structure.
3. There are usually dense, flat, or disk-shaped gas bubbles or gas-liquid inclusions in HT amber. Also, the gas bubbles in HT amber are generally much larger than those in natural beeswax.
4. HT amber retains the natural flow lines of gold-twisted honey amber. However, the flow lines appear disordered, less well-defined and smooth than the pattern of natural beeswax, which may be attributed to the impact of later gas interventions.
5. A white diffusion pattern appears along cracks after treatment of original cracked amber.

CONCLUSIONS

Hydrothermal treatment can be used to improve the appearance of amber materials (from transparent to opaque) to cater to Chinese consumers. During the process, an abundance of tiny submicron-/micron-sized bubbles penetrate the amber in an aqueous solution (with some catalyst) through controlling the temperature and pressure and selecting an inert atmosphere environment. After treatment, the inner layer of the weathered skin of rough amber material will generate a layer of yellowish white or greenish yellow HT skin of various thicknesses, or a corrugated crust containing pores. The finished amber shows a residue of hydrothermally treated spots of different sizes, which may penetrate the amber's interior or remain on the polished surface. It is recommended to look for dense, flat, or disk-shaped bubbles and gas-liquid inclusions in the finished products. In addition, the original flow pattern in the gold-twisted honey amber affected by the subsequent interference of tiny bubbles appears disorderly, unclear, and less smooth. Because the infrared spectra data of the experimental samples before and after the treatment showed little difference, FTIR spectra cannot be considered conclusive (though they do facilitate the identification). A series of careful observations and tests are needed to identify HT amber.

ABOUT THE AUTHORS

Ms. Wang is an associate professor at the Gemological Institute, China University of Geosciences in Wuhan, and the director of the university's gem testing center in Guangzhou. Dr. Li (yanli@cug.edu.cn, corresponding author) is an associate professor at the Gemological Institute and Advanced Manufacturing Centre, China University of Geosciences in Wuhan. Ms. Fen Liu and Ms. Fangli Liu are gemologists in the Gem Testing Center, China University of Geosciences in Wuhan. Dr. Chen is an associate professor at the Gemological Institute, China University of Geosciences in Wuhan.

ACKNOWLEDGMENTS

The authors thank all the parties who have contributed to the project, especially the anonymous companies for their great support and fruitful discussions. The thoughtful and constructive comments by reviewers and technical editors are gratefully acknowledged. This research was financially supported by Grant No. 2018YFF0215403 from the National Key R&D Program of China. The project was partially supported by the Fundamental Research Funds for the Central Universities, China University of Geosciences (Wuhan) (No. CUG170677).

REFERENCES

Abduriyim A., Kimura H., Yokoyama Y., Nakazono H., Wakatsuki M., Shimizu T., Tansho M., Ohki S. (2009) Characterization of "green amber" with infrared and nuclear magnetic resonance spectroscopy. *G&G*, Vol. 45, No. 3, pp. 159–171, http://dx.doi.org/10.5741/GEMS.45.3.158

Brody R.H., Edwards H.G.M., Pollard A.M. (2001) A study of amber and copal samples using FT-Raman spectroscopy. *Spectrochimica Acta Part A: Molecular and Biomolecular Spectroscopy*, Vol. 57, No. 6, pp. 1325–1338, http://dx.doi.org/10.1016/S1386-1425(01)00387-0

Feist M., Lamprecht I., Müller F. (2007) Thermal investigations of amber and copal. *Thermochimica Acta*, Vol. 458, No. 1-2, pp. 162–170, http://dx.doi.org/10.1016/j.tca.2007.01.029

Guiliano M., Asia L., Onoratini G., Mille G. (2007) Applications of diamond crystal ATR FTIR spectroscopy to the characterization of ambers. *Spectrochimica Acta Part A: Molecular and Biomolecular Spectroscopy*, Vol. 67, No. 5, pp. 1407–1411, http://dx.doi.org/10.1016/j.saa.2006.10.033

Matuszewska A., John A. (2004) Some possibilities of thin layer chromatographic analysis of the molecular phase of Baltic

amber and other natural resins. *Acta Chromatographica*, No. 14, pp. 82–91.
Ross A. (2010) *Amber: The Natural Time Capsule.* Firefly Books Ltd., Ontario, Canada.
Scalarone D., Lazzari M., Chiantore O. (2003) Ageing behaviour and analytical pyrolysis characterisation of diterpenic resins used as art materials: Manila copal and sandarac. *Journal of Analytical and Applied Pyrolysis*, Vol. 68-69, pp. 115–136, http://dx.doi.org/10.1016/S0165-2370(03)00005-6
Stout E.C., Beck C.W., Anderson K.B. (2000) Identification of rumanite (Romanian amber) as thermally altered succinite (Baltic amber). *Physics and Chemistry of Minerals*, Vol. 27, No. 9, pp. 665–678, http://dx.doi.org/10.1007/s002690000111
Vîrgolici M., Ponta C., Manea M., Negut D., Cutrubinis M., Moise I., Suvaila R., Teodor E., Sarbu C., Medvedovici A. (2010) Thermal desorption/gas chromatography/mass spectrometry approach for characterization of the volatile fraction from amber specimens: A possibility of tracking geological origins. *Journal of Chromatography A*, Vol. 1217, No. 12, pp. 1977–1987, http://dx.doi.org/10.1016/j.chroma.2010.01.075
Wang Y., Yang Y., Yang M. (2010) Experimental study on enhancement technique of amber. *Journal of Gems and Gemmology*, Vol. 12, No. 1, pp. 6–11 (in Chinese with English abstract).
Wang Y., Yang M., Yang Y. (2014) Experimental studies on the heat treatment of Baltic amber. *G&G*, Vol. 50, No. 2, pp. 142–150, http://dx.doi.org/10.5741/GEMS.50.2.142
Wang Y., Wang Q.Y, Nie S. (2016) Gas bubble characteristic of translucent to opaque amber and its relationship to quality assessment. *Journal of Gems and Gemmology*, Vol. 18, No. 5, pp. 20–27 (in Chinese with English abstract).
Wang Y., Yang M., Nie S., Liu F. (2017) Gemological and spectroscopic features of untreated vs. heated amber. *Journal of Gemmology,* Vol. 35, No. 6, pp. 530–542.
Yang J., Dong X., Guo L., Li H. (2002) The chemical research development of amber. *Beijing Traditional Chinese Medicine,* Vol. 21, No. 4, pp. 245–248 (in Chinese).
Yang Y., Wang Y. (2010) Summary on organic components and relevant spectral characteristics of amber and copal. *Journal of Gems and Gemmology*, Vol. 12, No. 1, pp. 16–22 (in Chinese with English abstract).
Zhang S.H. (2003) Can heat treatment change refractive index? *Journal of Gems and Gemmology*, Vol. 5, No. 2, pp. 14–15 (in Chinese with English abstract).
Zhang P.L. (2006) *Systematic Gemology*, 2nd ed. Geology Press, Beijing (in Chinese).

Effects of Mollusk Size on Growth And Color of Cultured Half-Pearls From Phuket, Thailand

Kannika Kanjanachatree, Napapit Limsathapornkul, Amorn Inthonjaroen, and Raymond J. Ritchie

The pearl mollusk *Pteria penguin* is popular for the production of half-pearls (mabe or cultured blister pearls). Research was carried out on two shell size classes implanted with half-pearl nuclei: the standard 140–145 mm size class (n = 200) was the control, and the smaller 130–135 mm size class (n = 200) was the test group. The mollusks were hung on strings at a sea depth of 2 m for up to 10 months. Implant rejection rates for the two mollusk groups were not significantly different, but the small mollusks had much lower mortality and grew faster. Nacre growth was not significantly different. Digital spectral analysis showed that the three red-green-blue (RGB) colors of the cultured half-pearls followed independent sinusoidal seasonal patterns with time periods of about 10 ± 0.3 months. The amplitude of variation in the RGB colors of the cultured half-pearls were all larger in the small pearl mollusks.

Most of the pearl farms in Phuket, Thailand, use *Pteria penguin* (Röding, 1798) to produce half-pearls (Kanjanachatree et al., 2003, 2019). These typically have a cream and white color (figure 1), but the mollusk also produces yellow pearls, black half-pearls, and bicolor half-pearls (Shor, 2007). The major determining factor in the viability of the cultured half-pearl industry is consistent production of good-quality half-pearls as demanded by the market (Ky et al., 2014a,b). Research is needed to improve quality and consistency. In addition to size, thickness, and weight, consideration should also be given to the luster, darkness, shape, and visible color. The color of pearls is defined by two main criteria: the overall bodycolor of the pearl, a combination of many pigments; and secondary color that is due to refraction and wavelength interference effects, with some colors scattered on the pearl surface (Karampelas et al., 2011; Abduriyim, 2018). Some pearls are bicolor (white and yellow or black and yellow) (Kanjanachatree et al., 2019). The factors that contribute to different colors are the mollusk species, pearl thickness, water quality of the pearl farm, plankton density (food quality and quantity) (Snow et al., 2004; Shor, 2007), and the genetics of the mollusk population (Ky et al., 2014a,b, 2018).

In Brief

- Color development of half pearls in *Pteria penguin* in small and standard-sized mollusks was followed over 10 months. The smaller mollusks grew faster and had better nacre growth.
- RBG (red-green-blue) color analysis showed that the colors of the half-pearls varied during development following sine curves.
- The sinusoidal curves of red, green, and blue colors were out of phase, and so the overall color varied with age and size class of the host mollusk.
- The periodicity of color development has important consequences for color-matching of half-pearls.

Plankton are small organisms that float freely in the water. Almost all types of algae, including some bacteria and molds, are also present. Zooplankton consist of single- and multi-celled organisms, including small invertebrates, and also include the larvae of fish and invertebrates. Phytoplankton are small single-celled or multi-celled or colonial algae. They are the most abundant of all plankton and the major

See end of article for About the Authors and Acknowledgments.
Gems & Gemology, Vol. 55, No. 3, pp. 388–397,
http://dx.doi.org/10.5741/GEMS.55.3.388

Figure 1. Cultured half-pearls from different-sized Pteria penguin *mollusks. Photo by Kannika Kanjanachatree.*

photosynthetic primary producers in marine ecosystems (Falkowski and Raven, 2007). They float in the water freely, but there are some mobile species with flagella. Although some are large enough to see with the naked eye, most are well below this in size. Phytoplankton use solar energy to fix inorganic carbon and convert nutrients. The primary photosynthetic pigment, chlorophyll *a*, is routinely measured to indicate the biomass of phytoplankton in water (Falkowski and Raven, 2007; Kanjanachatree et al., 2019).

The purpose of this research was to find ways to increase the overall production and value of cultured half-pearls. We set out to determine the optimum mollusk size and compare the rejection rate, the mortality rate of the seeded mollusks, and the color and quality of the cultured half-pearl, particularly any changes in the quality of the color from month to month in the cultivation of *Pteria penguin*.

MATERIALS AND METHODS

Collection and Sorting of Mollusks. A batch of more than 400 wild mollusks were collected from the Sapum Bay area of Phuket, near the pearl farm, in August 2015. In Phuket, this is the middle of the wet season. They were measured for overall length and divided into two classes. Based on the breeding seasons for *Pteria penguin*, these young mollusks were probably all 2–2½ years of age (Milione and Southgate, 2012; Kanjanachatree et al., 2019).

Of these, 200 pearl mollusks were designated the large or standard mollusk class, measuring 140–145 mm in length. Because this is the size class typically used for half-pearl cultivation, we made this the control group (figure 2). The second class consisted of 200 smaller mollusks, measuring 130–135 mm in length. These formed the test group for the experiment.

Implantation Procedure. Half-pearl nuclei (17 mm diameter) were implanted in August 2015, and the experiment was run for 10 months. Standard half-pearl cultivation practices were followed as described by Taylor and Strack (2008) and in our previous publications (Kanjanachatree et al., 2003, 2019). The mollusk was left in the air for 30 minutes, or in

Figure 2. Different size classes of Pteria penguin *pearl mollusks: small (130–135 mm) and standard (140–145 mm). Photo by Kannika Kanjanachatree.*

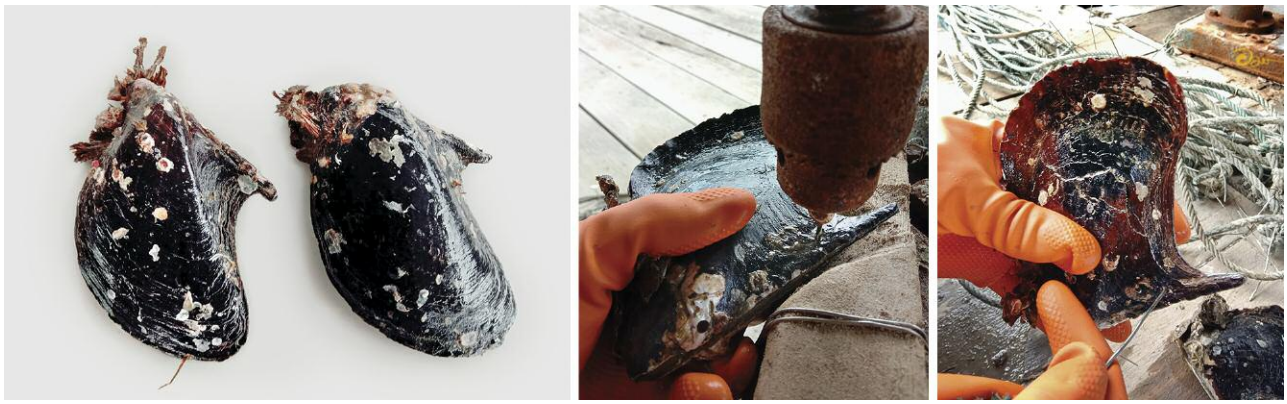

Figure 3. Drilling shells for hanging mollusks on strings: a pearl mollusk prepared for drilling (left), the drilling procedure (center), and the stringing (right). Photos by Kannika Kanjanachatree.

continuously running seawater. Shells began to open, and then a small wooden wedge was inserted into the mollusk to hold it open (Shor, 2007). Shells were placed in a clamp, pliers were used to insert the speculum, and the mollusk was held open using a metal spatula. The nucleus is made from resin and has a base length of 17 mm. It is attached to the shell with a glue containing ethyl-2-cyanoacrylate. Nuclei were placed near the adductor muscle in the standard position used for mabe (cultured blister) half-pearls.

A small hole was drilled in each shell so the mollusks could be hung in the water in strings, two meters below the surface to avoid excessive sunlight (figures 3 and 4). Mollusks also receive a larger amount of plankton at this depth (Kanjanachatree et al., 2003). All mollusks were checked each month and scrubbed to remove fouling organisms (Taylor and Strack, 2008). Harsher methods for removing fouling organisms were avoided.

Assessment of Growth of Cultured Half-Pearls, Food Resources, and Half-Pearl Quality. Ten mollusks were randomly selected each month for assessment. These mollusks were removed from the experiment,

Figure 4. Preparation and hanging the mollusks on strings two meters below the water's surface on the floating raft pearl farm. Photo by Kannika Kanjanachatree.

so the cohort decreased from 200 at month 0 to 100 at month 10. In our previous study (Kanjanachatree et al., 2019) the parameters could be measured nondestructively and the mollusks were returned to the water, but the measurements made in the present study necessarily involved the death of the mollusks.

The assessed parameters were mortality, rejection of nucleus by the mollusk, half-pearl nacre formation, pearl nacre thickness, and growth of shell from the differently sized *Pteria penguin* mollusks. Data were recorded over the 10 months of the project (mean ± 95% confidence limits, n = 10).

Chlorophyll Analysis. Chlorophyll measurements were made on water samples taken for the environmental monitoring. The water samples were collected from the pearl farm at four points to determine the average chlorophyll and carotene content. Cells were filtered using standard 0.45 µm filter disks. Chlorophyll was assayed using a formula for a mixed phytoplankton population (Ritchie, 2006) using ethanol solvent and a Shimadzu UV-1601 UV-visible dual beam spectrophotometer. Water sample volumes were 500 mL. Chlorophyll content was expressed as µg/L of water sample. The monthly results (see supplementary table 1 at https://www.gia.edu/doc/FA19-Phuket-Half-Pearls-Supplementary-Table1.pdf) were similar to those published previously in Kanjanachatree et al. (2019).

Color of Cultured Half-Pearls. There has been a resurgence of interest in quantitative color analysis of pearls (Ky et al., 2014a,b, 2018), particularly as a result of the finding that selective breeding for color is possible. The color of the half-pearls was measured using the method and simple apparatus described by Choodum et al. (2014) for use on drug samples. The device uses readily accessible mobile phone technology for digital image analysis of red, green, and blue (RGB) light. The device is a simple light box fitted with a white LED light source and constructed using minimal equipment, as opposed to an integrating sphere scanning spectrophotometer that is highly specialized and not readily available. The measured colors of the half-pearls were compared month to month and compared to a set of cultured half-pearl standard colors (Phuket Pearl Industry Standards).

Statistical Analysis. Completely randomized design data were analyzed by one-way analysis of variance (ANOVA), and comparisons of mean values were made using Duncan's new multiple range test (DMRT) using standard statistical analysis packages. The confidence level of $p < 5\%$ was chosen as the significant difference criterion. Samples with the same superscript letter were not significantly different ($p < 0.05$). Standard linear regression methods were used to fit linear regressions ($Y = mx + b$) to data. The seasonal sinusoidal fit to the half-pearl color data was performed using non-linear least squares methods, and the asymptotic errors of the fitted parameters were calculated by matrix inversion. The standard statistical reference text used was Snedecor and Cochran (1980).

RESULTS AND DISCUSSION

Water Quality and Chlorophyll Content Over the Course of This Study. Phuket has a wet maritime monsoonal climate, with a wet season from April to November each year (about 300 mm/month) and a dry season the rest of the year (about 100 mm/month) (Kanjanachatree et al., 2019). The dry season drought is therefore not as severe as in mainland Asia. The study was begun in August and continued over 10 months, so it extended from the middle of the wet season to the beginning of the next wet season. During the monthly monitoring of the mollusks, midday measurements were made of Secchi depth (cm), air temperature (°C), surface water temperature (°C), salinity in parts per thousand (‰), and pH using standard methods for measurements of water and wastewater (Cleseri et al., 1998, known as the APHA manual). Similar monthly results have been published previously in Kanjanachatree et al. (2019). Overall, the results in the present study were very uniform, with little seasonality in the five parameters of water quality just mentioned, so overall values were calculated (see supplementary table 2 at https://www.gia.edu/doc/FA19-Phuket-Half-Pearls-Supplementary-Table2.pdf). The calculated values compared well with previous environmental data for the study site (Kanjanachatree et al., 2019). The Secchi disk depth was 106 ± 12 cm, the water temperature was 29 ± 0.8°C (range of 26–32°C), the salinity was 30 ± 0.5 ppt (range of 27–35 ppt), and the dissolved oxygen was typically high (5.63 ± 0.64 mg/L ≈ 87% saturation, range of 5.2–7.3), and the overall pH was typical for seawater (8.3). Seawater becomes more acidic when CO_2 levels are high and more alkaline when phytoplankton remove CO_2. There was very little seasonality of conditions at the study site compared to other pearl-growing areas in more tem-

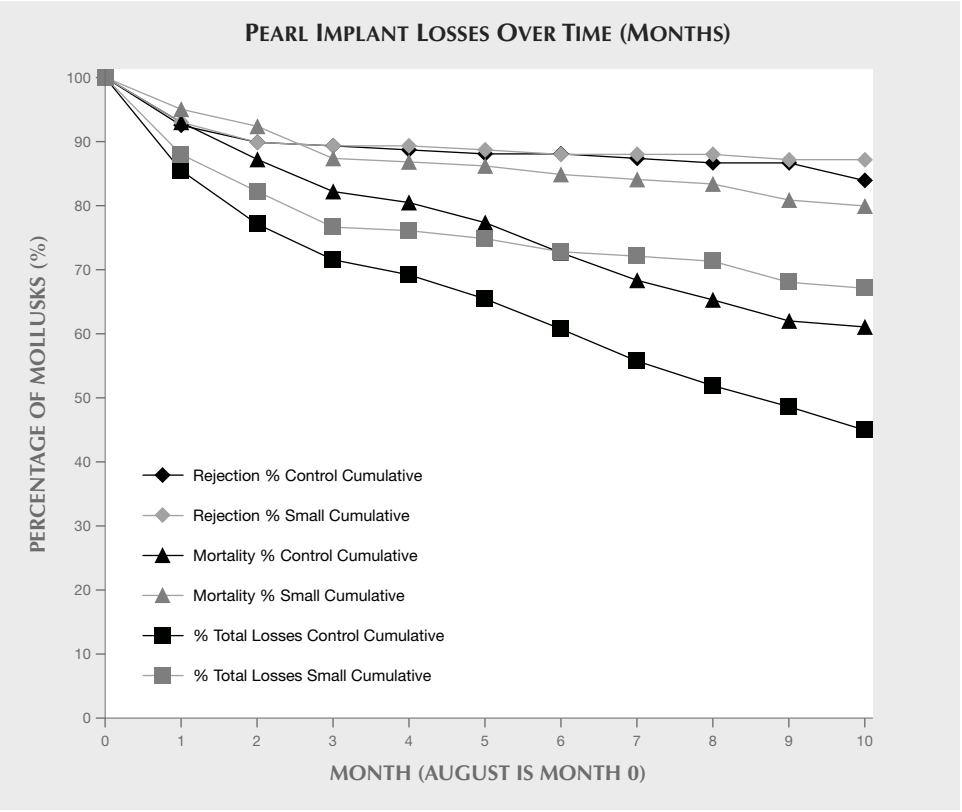

Figure 5. Rejection, mortality, and total losses of the control group and the test group after implantation of a half-pearl nucleus over time. The control mollusks had higher mortality rates and overall losses than the small mollusks.

perate climates such as Japan (Tomaru et al., 2002a,b; Muhammad et al., 2017), Mexico (Ruiz-Rubio et al., 2006), and Australia (Milione and Southgate, 2012).

The chlorophyll *a* levels in the water column were remarkably constant over the growing period used in this study, about 0.8 µg/L (0.868 ± 0.046) except for a January high level of about 1.0 µg/L (1.02 ± 0.079). Overall mean values and ± 95% confidence limits have been calculated (again, see supplementary table 1). The relative amounts of chlorophylls *a*, *b*, and *c* are a guide to the predominant types of plankton present over the year (Falkowski and Raven, 2007): Chlorophyll *b* indicates the presence of green algae (Chl *a* + *b*), and chlorophyll *c* indicates the predominance of chromo flagellates and diatoms. High carotenoids indicate a heavy presence of Chl *a* + *c* organisms. By such criteria, the relative abundance of algae containing chlorophyll *b* was more or less constant over the year, but there were high levels of Chl *c* and carotenoids in October (month 2) at the end of the wet season and in December (month 4), which is in the first half of the dry season. Large algal blooms did not occur during the course of the study, and the plankton food supply for the mollusks was remarkably constant, reflecting Phuket's tropical maritime climate.

Performance of the Different-Sized *Pteria penguin* Pearl Mollusks. The mollusks used in the study would have been about 2 to 2½ years old (Milione and Southgate, 2012; Kanjanachatree et al., 2019). Smaller pearl mollusks had better growth, much lower mortality, and lower overall losses than the larger mollusks in the control group (supplementary table 2; figure 5). The first-month rejection rates, mortality rates, and total losses for the control group and the small mollusks were not significantly different (rejection 7.3 ± 3.6%; mortality 6.0 ± 3.3%; overall losses 13.3 ± 4.7%, n = 400). The 10-month rejection rate (16% vs. 13%) was not significantly different, either, but there was a large difference in the mortality rate (39% vs. 20% respectively, $p < 0.001$). The sum of rejection + mortality was consequently much higher in the control group than in the small mollusks (55% vs. 33% respectively, $p < 0.001$). After the losses in the first month, the rejection rate, mortality, and overall losses were approximately linear over time ($p << 0.001$), with no obvious seasonal effect (figure 5). After the first month, the rejection rate was not significantly different for the two mollusk sizes, and so the overall mean rejection rate was only about 0.606 ± 0.151% per month ($r = 0.8924$). The mortality rate and hence overall loss (above) were much higher for the

control mollusks (3.575 ± 0.340% per month vs. 1.490 ± 0.364% per month), resulting in a total loss rate of 4.288 ± 0.389% per month (r = 0.9939) for the control mollusks vs. 1.989 ± 0.544% per month (r = 0.9482) for the small mollusks. The rejection rates, mortalities, and total losses for the control mollusks in this study are comparable to those found previously in Phuket pearl mollusks (Kanjanachatree et al., 2018a,b). Growth rates of shell and half-pearls were determined by linear regression (supplementary table 2; figure 5). The shells of the small mollusks grew faster (3.274 ± 0.177 vs. 2.231 ± 0.927 mm/month, mean values ± 95% confidence limits), but their pearl nacre did not (0.3134 ± 0.05334 vs. 0.2458 ± 0.1349 mm/month). The standard-sized mollusks routinely used for half-pearl farming using *Pteria penguin* are actually suboptimal for shell growth, though not for nacre growth of the half-pearls, but their mortality rate is unacceptably high.

Feeding. Tomaru et al. (2002a,b) studied the relationship between akoya pearl mollusks and chlorophyll *a* concentration in phytopigment extracts of the wet mollusk tissue (basically a measure of the stomach contents) and the dry tissue weight in the pearl mollusks at Ago Bay (1967–1969) and Ohmura Bay (1984–1985) in Japan. Their study showed that the concentration of chlorophyll *a* as a measure of the mollusks' diet affected their growth and growth of the implanted pearls. However, Japan has a temperate climate with four distinct seasons and a spring plankton bloom, and so plankton availability was much more seasonal than in Phuket. The dry season in Phuket is not a period of extreme drought as it is in many monsoonal climates: There is at least some rain all year.

Pearl mollusks feed by filtration, either of live food or dead food. Sometimes they absorb dissolved organic matter (DOM), but the importance of this as a source of nutrition has not been well documented or quantified. Very small plankton (picoplankton, ≈1 µm) are very important to pearl mollusks. They feed on other picoplankton and nanoplankton much smaller than the effective mesh size of their filtration apparatus because their gills are covered in a sticky mucus that traps nanoplankton (Tomaru et al., 2002a). *Bacteriastrum*, *Leptocylindrus*, *Melosira*, *Nitzschia*, *Rhizoslovenia*, *Skeletonema*, *Thalassionema*, and *Thalassiosira* are all consumed by the mollusks (Martinez-Fernandez et al., 2006). Some of these species were found at the Phuket pearl farm, but the more common species were the diatoms *Chaetoceros* and *Skeletonema*, which are generally regarded as non-toxic. Some species such as the *Nitzschia* species are also blamed for shellfish food poisoning and mortality. Where *Nitzschia* were found in large quantities and for a prolonged period of time, the mortality rate of the shellfish was found to increase. Tomaru et al. (2002a) reported that the *Nitzschia* species that bloomed in a bay in Japan's Uchiumi Prefecture caused the death of akoya pearl mollusks in 1998. *Nitzschia* contains chlorophyll *a* + *b*, so such blooms would be indicated by very high levels of Chl *a* + *b*, which did not occur at the Phuket pearl farm during this study (Kanjanachatree et al., 2018a,b). Similarly, other harmful blooms are often caused by dinoflagellates, which have high levels of chlorophyll *a* + *c* and high carotenoids. See Tun (2000), Shor (2007), and Taylor and Strack (2008) for overviews of mass mortalities in pearl mollusks and their consequences.

Temperature. The present study measured the water quality of the pearl farm, which was within the standard for aquaculture in Thailand. Conditions on the farm, with a temperature range of 26–32°C, do not cause death of the mollusks (Kanjanachatree et al., 2019). This is consistent with the study of Tomaru et al. (2002a,b) on Japanese pearl farms that have a temperate climate. At temperatures above 20°C, food availability and metabolism increase and have positive effects on shell thickness, but this does not affect the size of the shells. Yukihira et al. (2000) reported that at temperatures below 12°C, akoya pearl mollusks (*Pinctada fucata*) in Nagoya have reduced nacre secretion, which affects the production of pearls and reduces the weight of the shellfish. But at either 7.5°C or 35°C, the mollusks ate less. Eventually, excessively cold or hot temperatures stop both the movement of the cilia and the heartbeat of mollusk larvae. But the response to temperature depends on the stage of the larva. High temperatures make mollusks more vulnerable to disease by increasing their stress levels, making them less able to cope with infections (Mannion, 1983).

Mollusks are ectothermic animals, so the ambient temperature affects their metabolism and survival rate. Metabolism affects respiratory processes, absorption, excretion, and growth of tissues, as well as reproductive cells and vulnerability to diseases. Higher temperatures are not always good; usually there is an optimum temperature, and higher temperatures are progressively harmful. High temperatures can destroy enzymes (Yukihira et al., 2000) and

promote diseases in pearl mollusks (Mannion, 1983). High-temperature fatalities in aquatic organisms are often a consequence of oxygen stress because O_2 solubility decreases with temperature (Yamamoto et al., 1999; Yukihira et al., 2000). Water temperatures at the Phuket pearl farm are exceptionally stable throughout the year, with no sudden cold or hot events (Kanjanachatree et al., 2019). Temperatures of 7.5°C and 35°C (Yukihira et al., 2000) are both outside the range found at the Phuket pearl farm.

Fouling of cultivated pearl mollusks is an expensive nuisance (Dharmaraj et al., 1987; O'Connor and Newman, 2001; Guenther et al., 2006). In the present study, a monthly scrubbing was sufficient to prevent overgrowth by fouling organisms. Salinity changes are often used to control nuisance fouling organisms. Salinities outside the normal seawater range are generally fatal. In a study by Dharmaraj et al. (1987), pearl mollusks at Veppalodai, India (Gulf of Mannar), had 100% mortality at salinities of 14‰, 55‰, and 58‰. The mollusks were resistant to salinity ranges of 17–45‰, had a mortality rate of 0%, and could withstand fatal salinities for very brief periods by tightly closing their shells. Encrustations of fouling invertebrates and unwanted algae can be killed by soaking akoya mollusks in fresh water for 15 minutes. Brines (saltwater 60‰) can be used to kill *Polydora* ciliates and tubeworms (O'Connor and Newman, 2001). The mollusks lack access to oxygen when their shell lid is tightly closed. *Pinctada sugillata* from the Gulf of Mannar (India) are resistant to low oxygen levels for up to 24–27 hours (Dharmaraj et al., 1987). Low-oxygen stress leads to glycolytic acid accumulation in tissues. Yamamoto et al. (1999) reported that low oxygen levels in rapidly growing plankton blooms encourage the growth of dinoflagellates. The pearl farm in their study had a dense planting of mollusks. There were high suspended solids after heavy rain, some minor pollution, and limited circulation in deeper water. Water temperatures at the Phuket pearl farm are sometimes as high as >32°C (Kanjanachatree et al., 2019), but mass mortalities are rare in Phuket and similar locales (Tun, 2000). All of the factors mentioned above can result in reduced oxygen levels, leading to physiological stress. Extreme treatments to control fouling are best avoided if possible because they are likely to interfere with shell growth and nacre formation. The overall loss rate of *Pteria penguin* mollusks with implanted half-pearls was already high (figure 5). Any activities that might increase mortality are best avoided since they would make cultivation uneconomical (Kanjanachatree et al., 2019).

Phuket has two tidal cycles a day, so there is a continuous flow of water at the pearl farm. But because it is a floating raft, the depth at which the mollusks were suspended was constant. The farm is located in a strait behind a barrier island and has a very favorable circulation pattern, so the environmental conditions there are never unfavorable (Kanjanachatree et al., 2019) and mass mortalities are rare. The water quality at the pearl farm easily met the physical and chemical standards for aquaculture in Thailand (Yukihira et al., 2006). The water currents allowed the pearl mollusks to receive oxygen and filter feed. During the breeding season, the currents also help spread the reproductive cells and larvae of the shellfish. But during the low tide, the water carried by currents from the coastline was turbid, which may cause sediment to accumulate on the shell. The decrease in plankton and oxygen levels at low tide can cause the mollusk to become temporarily deprived of oxygen (Condie et al., 2006), but this was not a problem at the Phuket pearl farm, which is in a well-circulated site and located on a floating raft in about 10 m of water: The farm has never had a mass mortality event (Kanjanachatree et al., 2019). Poor growth conditions seem to increase pearl secretion, resulting in a faster pearl coating, but with lower production quality (Condie et al., 2006). In addition, there are tidal effects on the diet of *P. margaritifera* in more marginal farm locations (such as enclosed bays) because it does not tolerate high suspended solids in water, whereas *P. maxima* is more resistant to turbidity (Yukihira et al., 2006).

Color Analysis of Cultured Half-Pearls. Supplementary table 3 at https://www.gia.edu/doc/FA19-Phuket-Half-Pearls-Supplementary-Table3.pdf shows the color indices of the cultured half-pearls over the course of the study, and the data is plotted in figures 5 and 6. The RGB indices showed no significant linear increase or decrease over time (linear regression: $y = mx + b$, $p >> 0.05$). However, there was a noticeable sinusoidal periodic difference in color over time, with maxima at months 4 and 5 (December and January) after the start of the experiment (figures 6 and 7). The effect on the blue indices is the most noticeable, with the blue indices higher in December and January at the beginning of the dry season. The % reflectance appears to go up in the dry season and goes down in the wet season in a seasonal pattern.

A complex sinusoidal model was fitted to the RGB data by the equation:

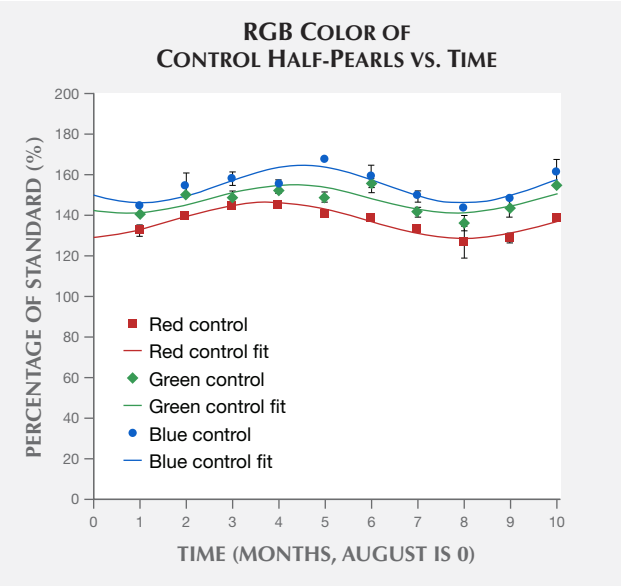

Figure 6. Cyclic nature of red-green-blue (RGB) color properties of cultured half-pearls from the control group over the course of the project. The mollusks were implanted in August, month 0.

$$Y = A \times \mathrm{Sin}\,(\varpi.T + D) + C \qquad (1)$$

The period for this function is:

$$2\pi = \varpi.Tp + D$$
$$\therefore Tp = \frac{2\pi - D}{\omega}$$

where *Y* is the % reflectance compared to an industry standard, *A* is an amplitude scaling factor for the sine function, *T* is time in months, ω is the period scaling factor (ω = 0.5236 for T in months), *D* is a displacement factor for adjusting where to start the sine function, *C* is a scaling constant (average *Y* over the time period), and *Tp* is the repeat period of the sine function (in months). Parameters A, ω, D, and C for Equation 1 could be estimated using Microsoft Excel's Solver tool, and their asymptotic errors could be estimated by matrix inversion (Snedecor and Cochran, 1980).

Figures 6 and 7 show mean values ± 95% confidence limits of standardized reflectance in half-pearls of standard- and small-sized mollusks over the course of the 10-month experiment starting in August 2015. The curve fits were all highly statistically significant ($p < 0.001$), and all means of the fitted parameters were significantly different from zero (see analysis in supplementary table 1). The period scaling factor (ω) would have been 0.5236 if the period were exactly one year: The experimentally determined ω values were all greater than ω = 0.5236. Only one ω value was significantly different from the others (red, control), and since the Tp value was not different, an overall value for ω = 0.8430 ± 0.0284 could be calculated. The amplitude (A) of the seasonal effect was greatest in the case of the blue color of cultured half-pearls from small mollusks and least in the case of the green color index of half-pearls from the control group. The amplitude (A) was noticeably higher in the cultured half-pearls from the small mollusks for all RBG colors (figures 6 and 7; supplementary table 1). The range in color was nearly ±30% in the case of the blue color of the half-pearls from the small group. The mean color was measured by the constant parameter (C). As would be expected, the average % colors for red, green, and blue were significantly different, but the three colors were not significantly different when the control group and the small mollusks were compared as pairs. The displacement parameter (D) shifted the sine curve timewise to optimize the fit. On an annual scale, 0.5236 radians is equivalent to one month, and so D was equivalent to –2 to –5 months in most cases. If the changes in color over time were synchronous, the parameter D would not be significantly different for the different RGB colors: Supplementary table 2 shows that D is significantly different even though the pe-

Figure 7. Sinusoidal character of RGB color properties of the cultured half-pearls grown in small mollusks. The cyclic nature of the color of the cultured half-pearls is more apparent in the small pearl mollusks.

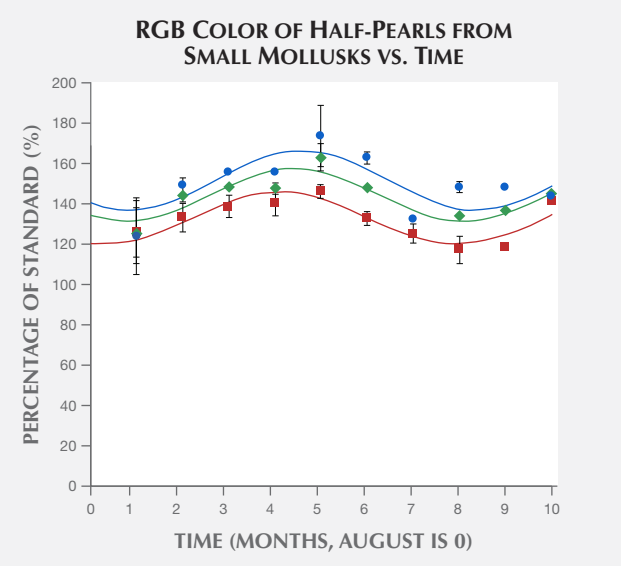

riod parameter ω was only marginally significant and the time period (Tp) of the sine curves was not significantly different. The RGB color of the cultured half-pearls thus shows an asynchronous seasonality (figures 6 and 7). Growth of the half-pearls was linear over time (supplementary table 2). The available phytoplankton also appeared to be more or less constant, with no strong seasonality as would be found in a temperate climate (Yukihira et al., 2000, 2006; Tomaru et al., 2002a,b).

These color trends are not readily noticeable to human color matchers of pearls, but some matchers do note that there appears to be a relationship between harvest time and color. Comparison of figures 6 and 7 (supplementary table 1) shows that the seasonal sinusoidal effect is more obvious in the cultured half-pearl from the small mollusks (figure 7) than in the standard-sized group (figure 6). The seasonal effect is least apparent in green light (human eyesight happens to be most sensitive to green light). These findings are important considerations in color-matching of the pearls (Shor, 2007). The seasonal effect is nearly ±30% of standardized reflectance in the case of blue color, and so would be important in color matching and in displaying the pearls for sale. Modern "white" light diodes have a very heavy blue component compared to green and red light and so are not well color balanced compared to natural sunlight or other common light sources. Hence, display cases using "white" diodes will cause differences in blue light reflectance to be more conspicuous than, for example, under typical fluorescent lighting. More sophisticated color analysis using integrating sphere technology is needed to resolve color issues of pearls, following the work of Karampelas et al. (2011) on marine pearl mollusks and Abduriyim (2018) on freshwater pearl mollusks.

CONCLUSIONS

The rate of nacre deposition on half-pearl nucleus is not significantly different between small and large *Pteria penguin* mollusks, but there are significant RGB color differences (supplementary table 1). The growth of the mollusk contributes to the rate of half-pearl nacre deposition. In this study, the small mollusks grew faster and had a much better survival rate than the larger ones that are the industry standard (figure 5). To achieve the highest quality, the half-pearls should be harvested in the seventh month because the thickness of the nucleus plus pearl layer is up to 19.4 mm (nacre 1.2 mm thick), which is the optimum for buttons and for button-shaped jewelry. Longer incubations produce pearls of increasingly uneven shape, which are less useful for buttons and jewelry.

The RGB color of the cultured half-pearls seems to be little affected by the month if a simple linear regression is fitted to the data. However, more sophisticated analysis shows that there is a seasonal (sinusoidal) effect on color reflectance, particularly in blue light (figures 6 and 7; supplementary table 1). The smaller mollusks produced better-quality cultured half-pearls and had a lower mortality and rejection rate. However, the RGB colors of the cultured half-pearls had larger amplitudes of color variation over the incubation period than the colors in the larger pearl mollusks. The phases of the sinusoidal changes in RBG colors of the half-pearls are not in-phase (synchronous), so the overall color of the pearls changes over the year. This has important consequences for color matching.

ABOUT THE AUTHORS

Ms. Kanjanachatree is an assistant professor, Ms. Limsathapornkul is a technical officer, and Dr. Ritchie is an associate professor, at Prince of Songkla University in Phuket, Thailand. Mr. Inthonjaroen is director of at Phuket Pearl Industry, Co. Ltd.

ACKNOWLEDGMENTS

The authors wish to thank Phuket Pearl Industry Co. Ltd. for providing access to the pearl farm facilities. Prince of Songkla University in Phuket provided access to equipment for analyses done as part of the study.

REFERENCES

Abduriyim A. (2018) Cultured pearls from Lake Kasumigaura: Production and gemological characteristics. *G&G*, Vol. 54, No. 2, pp. 166–183, http://dx.doi.org/10.5741/GEMS.54.2.166

Choodum A., Parabun K., Klawach N., Daeid N.N., Kanatharana P., Wongniramaikul W. (2014) Real time quantitative colourimetric test for methamphetamine detection using digital and mobile phone technology. *Forensic Science International*, Vol. 235, pp. 8–13, http://dx.doi.org/10.1016/j.forsciint.2013.11.018

Cleseri L.S., Greenberg A.E., Eaton A.D., Franson M.A.H., Eds. (1998) *Standard Methods for the Examination of Water and Wastewater (APHA)*, 20th ed. American Public Health Association, Washington, DC, pp. 1189.

Condie S.A., Mansbridge J.V., Hart A.M., Andrewartha J.R. (2006) Transport and recruitment of silver-lip pearl oyster larvae on Australia's North West Shelf. *Journal of Shellfish Research*, Vol. 25, No. 1, pp. 179–185, http://dx.doi.org/10.2983/0730-8000(2006)25%5B179:TAROSP%5D2.0.CO;2

Dharmaraj S., Chellam A., Velayudhan T.S. (1987) Biofouling, boring and predation of pearl oyster. In K. Alagarswami, Ed., *Pearl Culture*. Central Marine Fisheries Research Institute (CMFRI), Indian Council of Agricultural Research, Bulletin No. 39, Chapter 14, pp. 92–97.

Falkowski P.G., Raven J.A. (2007) *Aquatic Photosynthesis*, 2nd ed. Princeton University Press, Princeton, New Jersey.

Guenther J., Southgate P.C., De Nys R. (2006) The effect of age and shell size on accumulation of fouling organisms on the akoya pearl oyster *Pinctada fucata* (Gould). *Aquaculture*, Vol. 253, No. 1-4, pp. 366–373, http://dx.doi.org/10.1016/j.aquaculture.2005.08.003

Kanjanachatree K., Piyathamrongrut K., Inthonjaroen N. (2003) Effects of sea depths and sizes of winged pearl oysters (*Pteria penguin*) on pearl culture. *Songklanakarin Journal of Science and Technology*, Vol. 25, No. 5, pp. 659–671.

Kanjanachatree K., Limsathapornkul N., Inthonjaroen A., Ritchie R.J. (2019) Implanting half-pearl nuclei in different positions in mabe pearls (*Pteria penguin*, Röding, 1798). *Thalassas*, Vol. 35, No. 1, pp. 167–175, http://dx.doi.org/10.1007/s41208-018-0106-x.

Karampelas S., Fritsch E., Gauthier J.-P., Hainschwang T. (2011) UV-Vis-NIR reflectance spectroscopy of natural-color seawater cultured pearls from *Pinctada margaritifera*. *G&G*, Vol. 47, No. 1, pp. 31–35.

Ky C.-L., Blay C., Sham-Koua M., Vanaa V., Lo C., Cabral P. (2014a) Family effect on cultured pearl quality in black-lipped pearl oyster *Pinctada margaritifera* and insights for genetic improvement. *Aquatic Living Resources*, Vol. 26, No. 2, pp. 133–145, http://dx.doi.org/10.1051/alr/2013055

Ky C.-L., Blay C., Sham-Koua M., Lo C., Cabral P. (2014b) Indirect improvement of pearl grade and shape in farmed *Pinctada margaritifera* by donor "oyster" selection for green pearls. *Aquaculture*, Vol. 432, pp. 154–162, http://dx.doi.org/10.1016/j.aquaculture.2014.05.002

Ky C.-L., Sham-Koua M., Gilles Le Moullac G. (2018) Impact of spat shell colour selection in hatchery-produced *Pinctada margaritifera* on cultured pearl colour. *Aquaculture Reports*, Vol. 9, pp. 62–67, http://dx.doi.org/10.1016/j.aqrep.2017.12.002

Mannion M.M. (1983) Pathogenesis of a marine *Vibrio* species and *Pseudomonas putrefaciens* infections in adult pearl oysters, *Pinctada maxima* (Mollusca: Pelecypoda). Thesis, Honours Degree in Veterinary Biology, Murdoch University, Australia, 130 pp.

Martinez-Fernandez E., Acosta-Salman H., Southgate P.C. (2006) The nutritional value of seven species of tropical microalgae for black-lip pearl oyster (*Pinctada margaritifera*, L.) larvae. *Aquaculture*, Vol. 257, pp. 491–503, http://dx.doi.org/10.1016/j.aquaculture.2006.03.022

Milione M., Southgate P. (2012) Growth of winged pearl oyster, *Pteria penguin*, at dissimilar sites in northeastern Australia. *Journal of Shellfish Research*, Vol. 31, No. 1, pp. 13–20, http://dx.doi.org/10.2983/035.031.0102

Muhammad G., Atsumi T., Sunardi, Komaru A. (2017) Nacre growth and thickness of akoya pearls from Japanese and hybrid *Pinctada fucata* in response to the aquaculture temperature condition in Ago Bay, Japan. *Aquaculture*, Vol. 477, pp. 35–42, http://dx.doi.org/10.1016/j.aquaculture.2017.04.032

O'Connor W.A., Newman L.J. (2001) Halotolerance of the oyster predator, *Imogine mcgrathi*, a Stylochid flatworm from Port Stephens, New South Wales, Australia. *Hydrobiologia*, Vol. 459, No. 1-3, pp. 157–163, http://dx.doi.org/10.1023/A:1012525015850

Ritchie R.J. (2006) Consistent sets of spectrophotometric equations for acetone, methanol and ethanol solvents. *Photosynthesis Research*, Vol. 89, No. 1, pp. 27–41, http://dx.doi.org/10.1007/s11120-006-9065-9

Ruiz-Rubio H., Acosta-Salmón H., Olivera A., Southgate P.C., Rangel-Dávalos C. (2006) The influence of culture method and culture period on quality of half-pearls ('mabe') from the winged pearl oyster *Pteria sterna*. *Aquaculture*, Vol. 254, pp. 269–274.

Shor R. (2007) From single source to global free market: the transformation of the cultured pearl industry. *G&G*, Vol. 43, No. 3, pp. 200–226, http://dx.doi.org/10.5741/GEMS.43.3.200

Snedecor G.W., Cochran W.G. (1980) *Statistical Methods*. The Iowa State University Press, Ames, Iowa.

Snow M.R., Pring A., Self P., Losic D. (2004) The origin of the colour of pearls in iridescence from nano-composite structures of the nacre. *American Mineralogist*, Vol. 89, No. 10, pp. 1353–1358.

Taylor J., Strack E. (2008) Pearl production. In P.C. Southgate and J.S. Lucas, Eds., *The Pearl Oyster*. Elsevier, Oxford, UK. Chapter 8, pp. 273–302.

Tomaru Y., Udaka N., Kawabata Z., Nakano S. (2002a) Seasonal change of seston size distribution and phytoplankton composition in bivalve pearl oyster *Pinctada fucata martensii* culture farm. *Hydrobiologia*, Vol. 481, pp. 181–185.

Tomaru Y., Kumatabara Y., Kawabata Z., Nakano S. (2002b) Effect of water temperature and chlorophyll abundance on shell growth of the Japanese pearl oyster, *Pinctada fucata martensii*, in suspended culture at different depths and site. *Aquacultural Research*, Vol. 33, No. 2, pp. 109–116, http://dx.doi.org/10.1046/j.1365-2109.2002.00653.x

Tun T. (2000) A review of mass mortalities in pearl oyster. *SPC Pearl Oyster Information Bulletin*, Vol. 14, pp. 1–6.

Yamamoto K., Adachi S., Koube H. (1999) Effects of hypoxia on respiration in the pearl oyster, *Pinctada fucata martensii*. *Aquaculture Science*, Vol. 47, pp. 539–544, http://dx.doi.org/10.11233/aquaculturesci1953.47.539

Yukihira H., Lucas J.S., Klumpp D.W. (2000) Comparative effects of temperature on suspension feeding and energy budgets of the pearl oysters *Pinctada margaritifera* and *P. maxima*. *Marine Ecology Progress Series*, Vol. 195, pp. 179–188, http://dx.doi.org/10.3354/meps195179

Yukihira H., Lucas J.S., Klumpp D.W. (2006) The pearl oysters, *Pinctada maxima* and *P. margaritifera*, respond in different ways to culture in dissimilar environments. *Aquaculture*, Vol. 252, No. 2-4, pp. 208–224, http://dx.doi.org/10.1016/j.aquaculture.2005.06.032

Hydrogen-Rich Green Diamond Color-Treated by Multi-Step Processing

Wenqing Huang, Pei Ni, Ting Shui, and Guanghai Shi

A cut diamond of intense yellowish green color has been characterized using microscopy and spectroscopic techniques. The diamond has been unambiguously identified as color-treated. The simultaneous presence of multiple centers related to irradiation and annealing—including H1a, H1b, NV^0, NV^-, H3, H4, GR1, and H2—was revealed. UV-Vis-NIR absorption spectroscopy showed that the diamond owes its color to the two major bands related to H3 and GR1. The combination of these spectroscopic features in one diamond has not been reported in the gemological literature, suggesting that this diamond was subjected to a complex treatment procedure that is not frequently applied. Taking into account the thermal stability of the defects involved and the defect transformations at high temperatures, two possible treatment procedures explaining the observed combination of spectroscopic features are proposed.

Although a number of color centers such as GR1 (neutral vacancies), H3 (N-V-N defects), and some hydrogen- and nickel-related centers can impart green coloration to diamonds (Breeding et al., 2018), diamonds with a natural saturated green color are among the rarest. In the laboratory, attempts have been made to artificially induce green color in diamonds. This can be done with high-energy electron irradiation of yellowish diamonds (Collins, 1982; Wang et al., 2018), followed by prolonged annealing at a temperature of 1400°C for colorless type Ia diamonds (Collins, 2001), or using high-pressure, high-temperature (HPHT) annealing for brown type Ia diamonds (Collins et al., 2000; Collins, 2001, 2003). A multi-step processing that probably involved irradiation, annealing, and re-irradiation was documented by GIA researchers (Fritsch et al., 1988).

Although many features of color-treated (Fritsch et al., 1988; Collins et al., 2000; Collins, 2003) and untreated (Reinitz et al., 1998; Breeding et al., 2018) green diamonds have been established, determining the color origin of some green diamonds still poses a challenge due to the similarity of natural and laboratory radiation and annealing processes (Overton and Shigley, 2008; Breeding et al., 2018). Therefore, a deeper understanding of the thermal stability and transformations of the color-causing defects in diamonds subjected to irradiation and annealing is crucial for reliable reporting of color treatment.

Although two multi-step treated green diamonds were reported more than 30 years ago (Fritsch et al., 1988), treated-color green diamonds enhanced by a multi-step process involving three or more steps are rarely encountered by gemological labs, to the best of our knowledge. Here we report a combination of spectroscopic features that has not been previously documented in a single gem diamond and propose two possible treatment procedures to explain the results of our observations. The aim of this study is to characterize a green diamond color-treated by multi-step processing and to provide a supplementary database for the correct determination of color origin for gemological laboratories.

In Brief

- Determining the color origin of some green diamonds still poses a challenge for gemological laboratories.
- A 0.25 ct diamond of intense yellowish green color showed a rare combination of multiple centers related to irradiation and annealing, providing conclusive proof of treatment.
- Two alternative multi-step treatment procedures are proposed to interpret the observed combination of spectral features.

See end of article for About the Authors and Acknowledgments.
Gems & Gemology, Vol. 55, No. 3, pp. 398–405,
http://dx.doi.org/10.5741/GEMS.55.3.398

MATERIALS AND METHODS

The studied sample was a yellowish green round brilliant cut diamond weighing 0.25 ct (figure 1), provided to us by Mr. Congsen Zhang. The internal and external structural features of the diamond were examined with a standard gemological binocular microscope using a variety of illumination techniques. The UV-Vis-NIR absorption spectrum in the range of 225–1000 nm was recorded at the National Center of Supervision and Inspection of Quality of Gold and Silver Products (NGSTC) using a Spec GEM-3000 fiber-optic instrument equipped with an Ocean Optics QE65Pro spectrometer (1 nm spectral resolution). The sample was immersed in liquid nitrogen for a few seconds and then taken out for immediate UV-Vis-NIR measurement. Room-temperature FTIR absorption measurements in the spectral range 400–6000 cm^{-1} with a resolution of 4 cm^{-1} were performed at NGSTC using a Nicolet iN10 spectrometer. Photoluminescence (PL) spectra were collected at liquid nitrogen temperature in the laboratory of the National Gemstone Testing Center (NGTC) using a Renishaw InVia Raman confocal spectrometer equipped with 473 and 532 nm lasers.

RESULTS

Microscopic Features. Examination with the microscope revealed that the green color was evenly distributed over the stone. No green-brown stains characteristic of natural irradiation were observed. Patterned clouds and several fractures under the table were observed. A black graphitized surface-reaching fracture was seen near the girdle (figure 2).

Figure 1. This 0.25 ct yellowish green diamond is a multi-step treated diamond. Photo by Wenqing Huang; courtesy of Congsen Zhang.

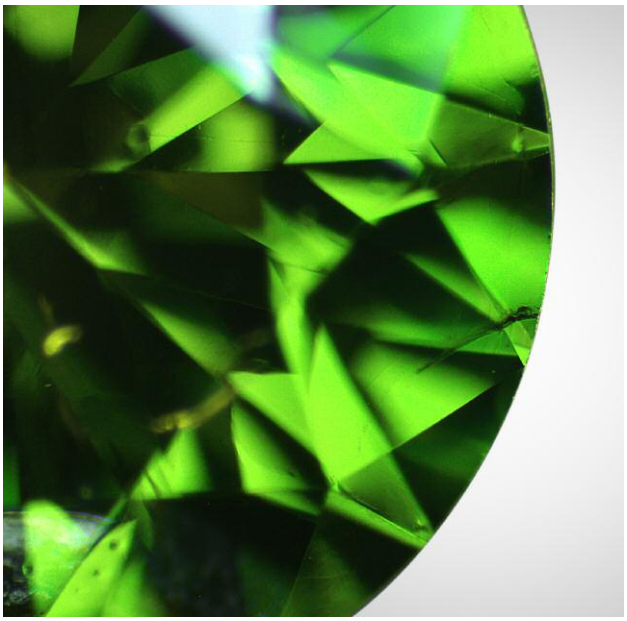

Figure 2. Graphitization along a surface-reaching fracture was evident. Photomicrograph by Wenqing Huang; field of view 4.6 mm.

Spectra. FTIR analysis provided important information about the impurity-related defects from nitrogen and hydrogen (Zaitsev et al., 1996). The spectra revealed that the diamond was type IaAB and had high nitrogen content. A minor line detected at 1362 cm^{-1} (figure 3) was probably an auxiliary peak to isolated nitrogen, given its sharp shape. These features unambiguously pointed to a naturally grown diamond. Hydrogen is a common impurity in diamonds, giving rise to a number of sharp absorption peaks in the IR spectral range from 2700 to 3500 cm^{-1} (Woods and Collins, 1983; Ardon, 2014; Zaitsev et al., 2016). Many of these hydrogen-related peaks were present in the FTIR spectrum of the studied diamond: strong absorption at 1405 cm^{-1} and several sharp peaks between 3300 and 2700 cm^{-1}, with the three strongest ones at 3237, 3107, and 2785 cm^{-1}. Weak lines at 4496 and 4168 cm^{-1} were also detected (figure 3). Besides these features, a strong absorption at 1450 cm^{-1} (H1a center, an interstitial nitrogen defect; Woods, 1984; Zaitsev, 2001) and a relatively weak absorption at 4930 cm^{-1} (H1b center) were recorded.

UV-Vis-NIR absorption spectra revealed the strong absorption band of the GR1 center in the spec-

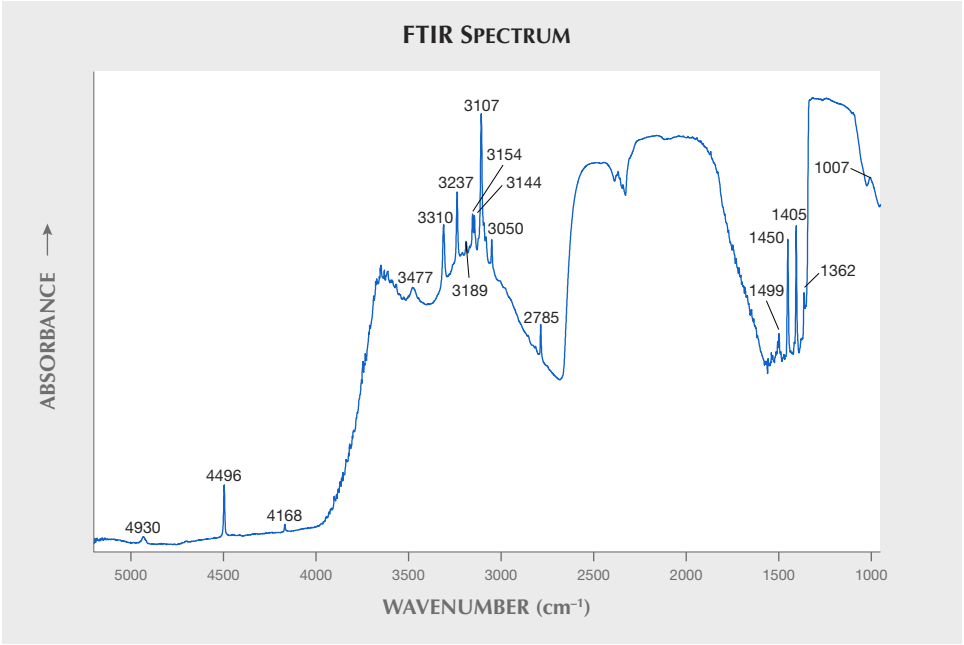

Figure 3. The FTIR absorption spectrum of the 0.25 ct diamond showed a consistent pattern of nitrogen aggregation (type Ia). This diamond was characterized by multiple strong, hydrogen-related peaks, including the 3107 cm^{-1} peak and those at 3237, 2785, and 1405 cm^{-1}. In addition, it revealed absorptions at H1a (1450 cm^{-1}) and H1b (4930 cm^{-1}) that were related to irradiation and annealing.

tral range from about 550 to 750 nm with a zero-phonon line (ZPL) at 741 nm, and a broad structureless band spreading from 410 to 510 nm that was presumably due to the H3 center (Dobrinets et al., 2013; Breeding et al., 2018) (figure 4). The H2 center (negatively charged N-V-N defect) with its ZPL at 985 nm was also clearly seen.

PL spectra recorded at 473 nm laser excitation displayed a strong H3 center with a ZPL at 503.2 nm and characteristic phonon side bands at 512 and 520

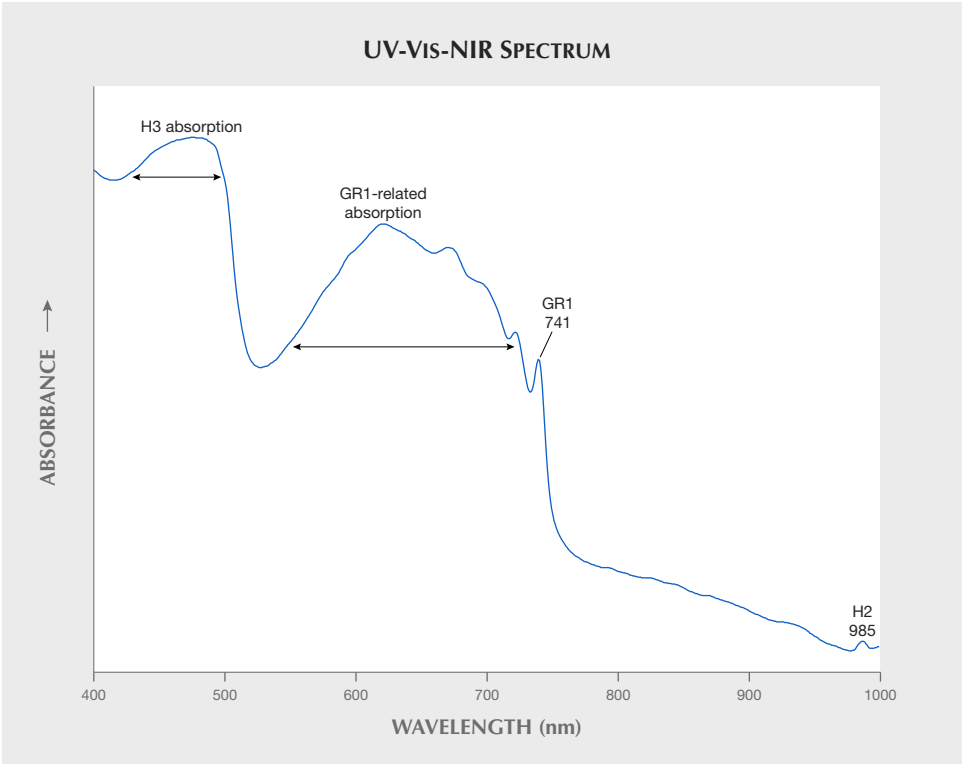

Figure 4. The UV-Vis-NIR spectrum of the 0.25 ct color-treated diamond revealed a moderate irradiation-related GR1 ZPL at 741 nm, with associated broad absorption extending from approximately 550 to 750 nm. Also detected were the H2 defect with ZPL at 985 nm and an H3 center with absorption band spreading from 410 to 510 nm.

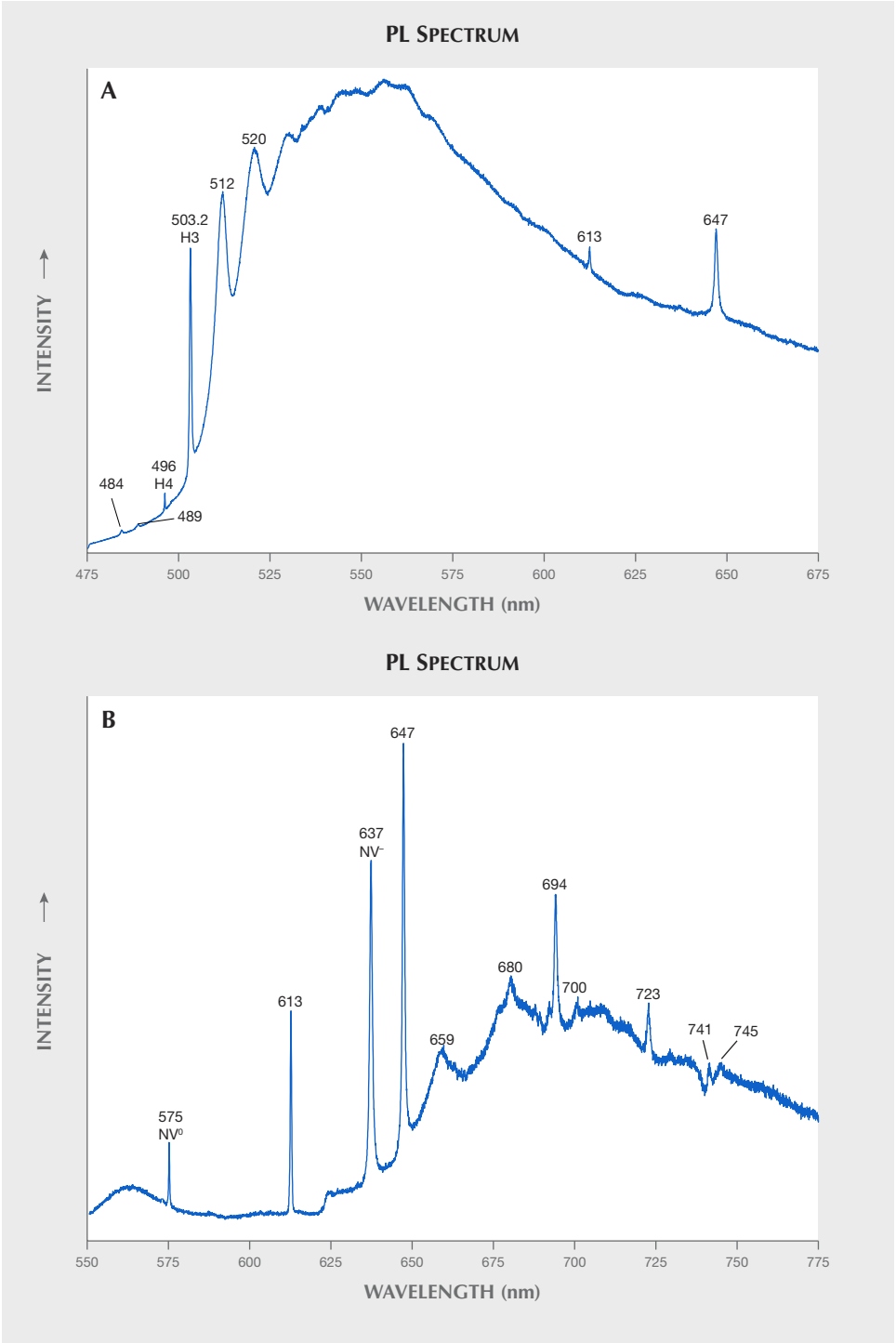

Figure 5. Photoluminescence spectra collected using 473 nm excitation (A) and 532 excitation (B) showed features attributed to H3, H4, NV^0, NV^-, and GR1 centers and Ni-related defects. Intrinsic diamond Raman lines have been removed for clarity.

nm (Zaitsev, 2001) (figure 5A). The emission related to the H4 center was recorded at a wavelength of 496 nm. Lines at wavelengths 484, 489, 613 (612.5 nm in some publications), and 647 nm were also detected. All these features with the exception of the 647 line are common for type Ia diamonds (Zaitsev, 2001). Brown and pink type Ia diamonds frequently reveal a strong 613 nm center in their PL spectra (Tretiakova and Tretyakova, 2008; Gaillou et al., 2010). A ZPL at 613 nm center with its vibrational feature at 625 nm (a weak hillock in spectrum shown in figure 5A) is also a common feature of purple diamonds

(Titkov et al., 2008). The 647 nm center has been reported in irradiation-treated diamonds (Wang et al., 2018) and is believed to be an irradiation-related defect (Zaitsev et al., 2018).

Photoluminescence spectra taken with 532 nm laser excitation revealed pronounced emissions of NV^0 and NV^- centers. Intensity of the NV^- center (ZPL at 637 nm, or 638 nm in some publications) was much stronger than that of the NV^0 center (ZPL at 575 nm) (figure 5B). Pronounced broad bands at 659 and 680 nm in this spectrum are due to electron-phonon transitions at NV^- and 647 nm centers. A doublet line feature at wavelengths 741 and 745 nm is a strongly suppressed and distorted ZPL of the GR1 center. This distortion is a result of strong self-absorption in the ZPL. Self-absorption in the ZPL is a common effect observed in PL spectra of optical centers with strong absorption. For instance, self-absorption can be very pronounced for NV^- and H3 centers (Dobrinets et al., 2013). Also detected were lines at 694, 700, and 723 nm of presumably nickel-related centers (Lang et al., 2004; Fritsch et al., 2007; Dobrinets et al., 2013).

DISCUSSION

Characterization of the Sample and Identification of Features. Although graphitization may occur naturally, it is not frequently observed in untreated cut diamonds. If present, the graphitized features are usually considered "suspicious" features, possibly the result of high-temperature treatment. Typical graphitized features in HPHT-treated diamonds have been described in detail by numerous researchers (e.g., Reinitz et al., 2000; Wang et al., 2005). However, the presence of graphitization alone is not reliable proof of HPHT treatment (Overton and Shigley, 2008).

The absence of strong hydrogen-related absorption bands (centered at 730 and 835 nm) and/or a Ni-related band (from approximately 620 to 710 nm), which could contribute to the green color of the diamond, suggests that other optical centers are responsible for the observed color. As shown in figure 4, the strong absorptions in the H3 and GR1 bands result in a transmission window at wavelengths from about 500 to 600 nm. The dominating transmission in this spectral range is the main cause of the yellowish green color. Natural-color green diamonds in which GR1 and H3 centers are the substantial chromophores are relatively common. According to Breeding et al. (2018), they may account for about 8% of the natural-color green diamonds submitted to GIA labs over the last decade. However, the simultaneous presence of these two centers in treated stones is a rare event (Buerki et al., 1999; Reinitz et al., 2000) and thus gives little indication of color treatment.

Indicators of color treatment are seen in IR absorption spectra. It is known that the H1a center, a radiation-related defect, may occur as a weak peak in FTIR spectra of some type Ia diamonds with intense green natural color (Breeding et al., 2018). Consequently, the presence of H1a alone is not a reliable indicator of the origin of green coloration. However, strong H1a absorption is unusual in untreated diamonds and always interpreted as a feature of possible treatment. For instance, a strong H1a center is always observed in multi-step treated "Imperial Red diamonds" (Wang et al., 2005). The H1b center, which is believed to be formed by trapping the 595 nm center on the A-aggregate of nitrogen during annealing at temperatures above 650°C (Woods, 1984; Zaitsev, 2001), is also generally deemed a strong indication of multi-step treatment processes involving radiation and subsequent annealing (Woods and Collins, 1986; Fritsch et al., 1988; Collins, 2003).

Substantial absorption strength of the H2 center contrasts with the vast majority of untreated diamonds, which do not exhibit an H2 center strong enough to be detected in their absorption spectra (Shigley and Fritsch, 1990; Buerki et al., 1999; Dobrinets et al., 2013). Yet the H2 center does occur naturally in type Ia diamonds exposed to natural irradiation and natural annealing at temperatures of about 1000 to 1200°C during geological processes and is, on very rare occasions, seen in absorption. Consequently, pronounced H2 center absorption generally serves as a valuable diagnostic feature for the determination of treatment in diamonds with a green color component (Reinitz and Moses, 1997; Buerki et al., 1999). There are two explanations for the elevated intensity of the H2 center. One is the formation of the negatively charged N-V-N defects (H2 center) in the course of the collapse of H1a and/or H1b defects in irradiated diamonds during their annealing at temperatures above 1300°C (Collins et al., 2005). The other involves HPHT treatment of type Ia diamonds when the dissociation of some nitrogen aggregates produces a measurable amount of single substitutional nitrogen atoms (C defects). C defects are donors in the diamond lattice and negatively charge the naturally occurring N-V-N defects (Collins et al., 2000). This change in the charge state

of N-V-N defects is seen as the formation of H2 centers at the expense of H3 centers. The latter model is commonly used to explain the conversion from brown color to green color in type Ia diamonds by HPHT treatment. In the case of brown diamonds, the role of HPHT annealing is to produce C defects and to increase the concentration of N-V-N defects (Dobrinets et al., 2013).

Much stronger intensity of the NV^- center relative to the NV^0 center also raises suspicion of treatment (Hainschwang et al., 2005; Sriprasert et al., 2007). Those authors regarded the intensity ratio $I_{637}/I_{575}>1$ as a manifestation of HPHT treatment for type Ia diamonds. For untreated diamonds, the 637 nm center is generally minor with respect to that of the 575 nm center (Dobrinets et al., 2013). It should be noted that the luminescence efficiency of the differently charged NV defects can vary depending on the intensity of the laser excitation (higher-power laser excitation may decrease the I_{637}/I_{575} ratio). Because of this effect, some natural-color diamonds could reveal an I_{637}/I_{575} intensity ratio similar to that of HPHT-treated diamonds (e.g., figure 3 in Lim et al., 2006). Unfortunately, the intensity ratio $I_{637}/I_{575}>1$ as an indicator of treatment does not work well for type Ia diamonds that have remnants of natural C defects sufficient for the enhancement of NV^- center luminescence. Thus, this criterion alone cannot be used as a reliable proof of treatment (Dobrinets et al., 2013).

While none of the above features alone provides conclusive proof of treatment, taken together they leave no doubt that the studied diamond is color-treated. Although these features of color treatment are not new, their combination in a single stone does not appear to have been explicitly documented in the literature and as such is worthy of reporting.

Possible Treatment Process. On the basis of the visual microscopic examination and spectroscopic analyses, it is evident that this sample was treated by a complex, multi-step procedure. Taking into account the stability and the transformation pathways of nitrogen-related and radiation defects in diamonds exposed to high-temperature annealing, the treatment processes involved and their sequence could be:

(I) HPHT + Irradiation + Annealing + Irradiation, or

(II) Irradiation + High-Temperature Annealing (about 1400°C) + Irradiation

Detailed analysis of these two treatment procedures is given below.

Treatment Procedure I. Since graphitization is a characteristic feature of HPHT treatment, it offers a hint of HPHT annealing. A much stronger NV^- center than the NV^0 center is the next clue. The detection of H2 absorption also points to possible HPHT annealing. Evidence of the irradiation-annealing procedure is provided by the presence of H1a and/or H1b centers. It should be noted that the H1a center is destroyed by HPHT annealing (H1a anneals out at a temperature above 1500°C; Zaitsev, 2001; Zaitsev et al., 2018). Thus, assuming the initial HPHT treatment, we also have to assume that after HPHT annealing the diamond was irradiated and annealed again. The very strong GR1 center presented in the absorption spectrum leaves no doubt that there was one more exposure to irradiation. Due to low thermal stability, vacancies cannot survive the temperature required to produce the H1b center. The presence of the GR1 center therefore provides strong evidence that irradiation was the final step of treatment.

Treatment Procedure II. Graphitization of diamond is indicative of high-temperature annealing (usually above 1400°C). It should be noted that the presence of graphitized features does not necessarily imply that annealing was performed under high pressure. After irradiation, therefore, the studied diamond could have been subjected to conventional annealing at high temperature without high pressure. As a result of the annealing, the graphitization and the centers H3, H2, H1a, and H1b appeared. During this course, the newly formed H1a and H1b centers could have been partially annealed out and contributed to the growth of the H2 center (Collins et al., 2005). Taking into account the temperature stability of the H1a and H1b centers, we speculate that the annealing at this temperature was performed for a relatively short time to allow a partial survival of the H1a and H1b centers (prolonged heating at temperatures over 1400°C is needed to completely eliminate H1a or H1b absorption; e.g., Woods, 1984; Collins et al., 2005; Eaton-Magaña et al., 2017; Zaitsev et al., 2018) and the H4 center (Woods and Collins, 1986; Buerki et al., 1999). Besides, type Ia diamonds colored by strong H3 and H2 centers that were produced via irradiation and subsequent prolonged annealing at 1400°C may have an unappealing appearance (a drab, unattractive green color) (Woods and Collins, 1986). A shorter annealing results in a moderate H2 absorption, and diamonds treated in this way tend to have more attractive yellow color, or to show greenish yel-

low color when H2 absorption is relatively strong (Buerki et al., 1999). If a stronger green color component is needed, the diamond can be re-irradiated. Strong GR1 center in the absorption spectrum offers unambiguous proof that the studied diamond was re-irradiated after the first two steps of treatment with irradiation and annealing.

The treatment process with irradiation, subsequent annealing, and re-irradiation described above resembles the process reported for two green diamonds in Fritsch et al. (1988). However, the substantial presence of H2 absorption suggests that in our case the annealing temperature was higher than that used for the treatment reported by Fritsch et al. (1988).

CONCLUSIONS

We performed detailed studies of a yellowish green diamond that exhibited a range of features indicative of color treatment. Numerous spectroscopic and structural indicators of treatment were identified using microscopy, low-temperature PL spectroscopy, and absorption spectroscopy in a broad spectral range. While the color of this diamond has been unambiguously determined as artificially enhanced, the exact treatment procedure could not be established with certainty. Analyzing the available data, however, we came up with two possible treatment procedures that could explain the results of our measurements. One is a sequence of HPHT annealing, irradiation, conventional annealing, and re-irradiation. The other involves irradiation followed by brief high-temperature annealing at a temperature of about 1400°C and the final re-irradiation.

The major difference between these two procedures is the initial HPHT treatment. HPHT annealing is commonly used for reduction (and eventual elimination) of brown color in type IIa and type IaB diamonds. Applied to type Ia diamonds, HPHT annealing renders conversion of the brown color to a more attractive yellow-green color. Furthermore, HPHT annealing is an effective technique to enhance pink color in some initially brown type IIa diamonds, and to enhance blue color in originally grayish type IIb diamonds. Application of HPHT treatment for a colorless diamond is essentially useless.

Color treatment of colorless diamonds makes economic sense only for low-clarity stones, when it is desirable to conceal their highly included interior. Low-clarity stones have low value, so they can have a higher value as a colored diamond, where clarity is a lesser consideration. Color treatment of pale yellowish diamonds of low color grade is also used as a way to improve their yellow color, or to convert them to green diamonds. These pale yellowish diamonds can be of relatively high clarity grade. Since the studied diamond was not highly included, we assume that the choice of the treatment procedure was dictated by its initial color. If the color was brown, initial HPHT annealing was a likely step. If the color was light brown or yellowish brown, HPHT annealing was not needed and the initial treatment was irradiation. Unfortunately, based on the available spectroscopic data we cannot give a meaningful assumption about the original color of the diamond.

ABOUT THE AUTHORS

Mr. Huang is a doctoral candidate at Nanjing University, and is also affiliated with the National Center of Supervision and Inspection on Quality of Gold and Silver Products Nanjing, China. Dr. Ni (corresponding author, peini@nju.edu.cn) is a professor in the State Key Laboratory for Mineral Deposit Research, Institute of Geo-Fluids, School of Earth Science and Engineering, Nanjing University. Mr. Shui is a professor at Nanjing Center, China Geological Survey. Dr. Shi is a professor in the State Key Laboratory of Geological Processes and Mineral Resources, China University of Geosciences, Beijing.

ACKNOWLEDGMENTS

The authors are grateful to Huihuang Li and Yan Lan, staff members of the National Gem Testing Center, for offering assistance with PL analysis. Many thanks go to Dr. Ilene Reinitz and Troy Ardon of GIA for helpful comments and suggestions. In particular, they thank Dr. Alexander Zaitsev of the Department of Physics and Astronomy at City University of New York for his thoughtful comments and help during revising the manuscript. They are also thankful to Congsen Zhang for providing the sample for this research.

REFERENCES

Ardon T. (2014) Spatial correlation of infrared and PL optical centers in hydrogen-rich diamonds. 2014 GSA Annual Meeting in Vancouver, British Columbia, October 19–22.

Breeding C.M., Eaton-Magaña S., Shigley J.E. (2018) Natural-color green diamonds: A beautiful conundrum. *G&G*, Vol. 54, No. 1, pp. 2–27, http://dx.doi.org/10.5741/GEMS.54.1.2

Buerki P.R., Reinitz I.M., Muhlmeister S., Elen S. (1999) Observation of the H2 defect in gem-quality type Ia diamond. *Diamond and Related Materials*, Vol. 8, No. 6, pp. 1061–1066, http://dx.doi.org/10.1016/S0925-9635(99)00094-1

Collins A.T. (1982) Colour centers in diamond. *Journal of Gemmology*, Vol. 18, No. 1, pp. 37–75.

Collins A.T. (2001) The colour of diamond and how it may be changed. *Journal of Gemmology*, Vol. 27, No. 6, pp. 341–359.

Collins A.T. (2003) The detection of colour-enhanced and synthetic gem diamonds by optical spectroscopy. *Diamond and Related Materials*, Vol. 12, No. 10-11, pp. 1976–1983, http://dx.doi.org/10.1016/S0925-9635(03)00262-0

Collins A.T., Kanda, H., Kitawaki H. (2000) Colour changes produced in natural brown diamonds by high-pressure, high-temperature treatment. *Diamond and Related Materials*, Vol. 9, No. 2, pp. 113–122, http://dx.doi.org/10.1016/S0925-9635(00)00249-1

Collins A.T., Connor A., Ly C. H., Shareef A., Spear P.M. (2005) High-temperature annealing of optical centers in type-I diamond. *Journal of Applied Physics*, Vol. 97, No. 8, 083517, http://dx.doi.org/10.1063/1.1866501

Dobrinets I.A., Vins V.G., Zaitsev A.M. (2013) *HPHT-Treated Diamonds*. Springer-Verlag, Berlin.

Eaton-Magaña S., Ardon T., Zaitsev A.M. (2017) LPHT annealing of brown-to-yellow type Ia diamonds. *Diamond and Related Materials*, Vol. 77, pp. 159–170, http://dx.doi.org/10.1016/j.diamond.2017.06.008

Fritsch E., Shigley J.E., Stockton C.M., Koivula J.I. (1988) Detection of treatment in two unusual green diamonds. *G&G*, Vol. 24, No. 3, pp. 165–168, http://dx.doi.org/10.5741/GEMS.24.3.165

Fritsch E., Massi L., Rossman G.R., Hainschwang T., Jobic S., Dessapt R. (2007) Thermochromic and photochromic behavior of "chameleon" diamonds. *Diamond and Related Materials*, Vol. 16, No. 2, pp. 401–408, http://dx.doi.org/10.1016/j.diamond.2006.08.014

Gaillou E., Post J., Bassim N., Zaitsev A.M., Rose T., Fries M., Stroud R.M., Steele A., Butler J.E. (2010) Spectroscopic and microscopic characterizations of color lamellae in natural pink diamonds. *Diamond and Related Materials*, Vol. 19, No. 10, pp. 1207–1220, http://dx.doi.org/10.1016/j.diamond.2010.06.015

Hainschwang T., Katrusha A., Vollstaedt H. (2005) HPHT treatment of different classes of type I brown diamonds. *Journal of Gemmology*, Vol. 29, No. 5-6, pp. 261–273.

Lang A.R., Yelisseyev A.P., Pokhilenko N.P., Steeds J.W., Wotherspoon A. (2004) Is dispersed nickel in natural diamonds associated with cuboid growth sectors in diamonds that exhibit a history of mixed-habit growth? *Journal of Crystal Growth*, Vol. 263, No. 1-4, pp. 575–589, http://dx.doi.org/10.1016/j.jcrysgro.2003.11.116

Lim H., Park S., Cheong H., Choi H., Kim Y.C. (2006) Photoluminescence of natural diamonds. *Journal of the Korean Physical Society*, Vol. 48, No. 6, 1556–1559.

Overton T.W., Shigley J.E. (2008) A history of diamond treatments. *G&G*, Vol. 44, No. 1, pp. 32–55, http://dx.doi.org/10.5741/GEMS.44.1.32

Reinitz I.M., Moses T.M. (1997) Lab Notes: Treated-color yellow diamonds with green graining. *G&G*, Vol. 33, No. 2, p. 136.

Reinitz I.M., Fritsch E., Shigley J.E. (1998) An oscillating visible light optical center in some natural green to yellow diamonds. *Diamond and Related Materials*, Vol. 7, No. 2-5, pp. 313–316, http://dx.doi.org/10.1016/S0925-9635(97)00268-9

Reinitz I.M., Buerki P.R., Shigley J.E., McClure S.F., Moses T.M. (2000) Identification of HPHT-treated yellow to green diamonds. *G&G*, Vol. 36, No. 2, pp. 128–137, http://dx.doi.org/10.5741/GEMS.36.2.128

Shigley J.E., Fritsch E. (1990) Optical properties of some greenish blue to green diamonds. *SPIE Proceedings*, Vol. 1325, pp. 315–324.

Sriprasert B., Atichat W., Wathanakul P., Pisutha-Arnond V., Sutthirat C., Leelawattanasuk T., Kim S., Jakkawanvibu C., Saejoo S., Srithunayothin P., Kunwisutthipan C., Susawee N. (2007) Spectroscopic investigation of Bellataire and Iljin treated diamonds. *GEOTHAI'07 International Conference on Geology of Thailand: Towards Sustainable Development and Sufficiency Economy*, pp. 304–312.

Titkov S.V., Shigley J.E., Breeding C.M., Mineeva R.M., Zudin N.G., Sergeev A.M. (2008) Natural-color purple diamonds from Siberia. *G&G*, Vol. 44, No. 1, pp. 56–64, http://dx.doi.org/10.5741/GEMS.44.1.56

Tretiakova L., Tretyakova Yu. (2008) Significance of spectroscopic methods for the identification defects in diamond. *9th International Kimberlite Conference*, Extended Abstract No. 9IKC-A-00042.

Wang M., Shi G., Yuan J.C.C., Han W., Bai Q. (2018) Spectroscopic characteristics of treated-color natural diamonds. *Journal of Spectroscopy*, Vol. 2018, pp. 1–10, http://dx.doi.org/10.1155/2018/8153941

Wang W., Smith C.P., Hall M.S., Breeding C.M., Moses T.M. (2005) Treated-color pink-to-red diamonds from Lucent Diamonds Inc. *G&G*, Vol. 41, No. 1, pp. 6–19, http://dx.doi.org/10.5741/GEMS.41.1.6

Woods G.S. (1984) Infrared absorption studies of the annealing of irradiated diamonds. *Philosophical Magazine B*, Vol. 50, No. 6, pp. 673–688, http://dx.doi.org/10.1080/13642818408238892

Woods G.S., Collins A.T. (1983) Infrared absorption spectra of hydrogen complexes in type I diamonds. *Journal of Physics and Chemistry of Solids*, Vol. 44, No. 5, pp. 471–475, http://dx.doi.org/10.1016/0022-3697(83)90078-1

Woods G.S., Collins A.T. (1986) New developments in spectroscopic methods for detecting artificially coloured diamonds. *Journal of Gemmology*, Vol. 20, No. 2, pp. 75–82.

Zaitsev A.M. (2001) *Optical Properties of Diamond: A Data Handbook*. Springer-Verlag, Berlin.

Zaitsev A.M., Melnikov A.A., Denisenko A.V., Varichenko V.S., Job R., Fahrner W.R. (1996) Luminescence characterization and application of diamond. *Materials Research Society Symposium Proceedings*, Vol. 416, pp. 113–124, http://dx.doi.org/10.1557/PROC-416-113

Zaitsev A.M., Wang W., Moe K.S., Johnson P. (2016) Spectroscopic studies of yellow nitrogen-doped CVD diamonds. *Diamond and Related Materials*, Vol. 68, pp. 51–61, http://dx.doi.org/10.1016/j.diamond.2016.06.002

Zaitsev A.M., Moe K.S., Wang W. (2018) Defect transformations in nitrogen-doped CVD diamond during irradiation and annealing. *Diamond and Related Materials*, Vol. 88, pp. 237–255, http://dx.doi.org/10.1016/j.diamond.2018.07.017

Pressed Gibbsite and Calcite as a Rhodochrosite Imitation

Hanyue Xu and Xiaoyan Yu

A new rhodochrosite imitation has appeared in the market, with gemological properties, chemical composition, and structural characteristics that are different from natural rhodochrosite. In this investigation, four samples—two imitations and two rhodochrosites—were examined by standard gemological testing, scanning electron microscopy, energy-dispersive spectroscopy, X-ray diffraction, FTIR, and Raman microspectroscopy. Examination revealed that the imitations are composed of pressed gibbsite and calcite powder with a granular structure, which are easy to identify through standard gemological testing.

Rhodochrosite ($MnCO_3$), the national stone of Argentina, is known as "Inca Rose" for its red and white bands (Xing, 2015). The most significant producer is the Sweet Home mine in the American state of Colorado, which can produce transparent, vivid red single-crystal rhodochrosite (Knox and Lees, 1997). Rhodochrosite for lapidary and mineral specimens is also found in South Africa, Peru, Australia, Romania, Spain, Russia, Mexico, Japan, China, and the American state of Montana (Yu, 2016).

Rhodochrosite has a beautiful pink to deep red bodycolor and usually occurs as a translucent to opaque stone, mostly showing a white banded pattern (Zwaan, 2015). In recent years, it has been processed into center stones for rings and used in pendants, necklaces, and bracelets. Unique and ornamental pieces are also popular with mineral connoisseurs, and thus the value of rhodochrosite has continued to rise (Knox and Lees, 1997).

Imitation rhodochrosite is rare because the complex banded pattern in the natural material is difficult to mimic. Glass imitations have appeared on the market previously, but they could be distinguished from rhodochrosite by gemological properties (such as color, luster, and transparency), structural differences, and internal air bubbles (Zhang, 2006). Meanwhile, pressed materials are commonly used as imitations of turquoise, coral, and chicken-blood stone (Tian et al., 2004; Teng et al., 2008; Zhang et al., 2014), but not as a rhodochrosite imitation. Therefore, we were surprised to find a new rhodochrosite imitation on the market in the form of a pressed material.

We conducted analyses to study the new imitation's composition and micro-structure characteristics as well as methods for its identification.

MATERIALS AND METHODS

Four samples of rhodochrosite and its imitations ranging from 8.20 to 20.59 ct were analyzed for the study: rhodochrosite samples T1 and T2, and imitation samples F1 and F2 (figure 1). The rhodochrosite samples were from the gem laboratory of China University of Geosciences, and the imitation samples were obtained from the gem market in Wuzhou, Guangxi, China.

In Brief

- New rhodochrosite imitations found in the market have a more natural appearance.
- The imitations are composed of pressed gibbsite and calcite powder with a granular structure. They are easy to identify through their gemological properties, chemical composition, structure, and spectra.
- The matrix of the imitation contains organic material, perhaps a type of styrene or a similar compound.

The samples were examined by standard gemological methods, including basic observation, refractive index measurement, fluorescence reaction under long-wave (365 nm) and short-wave (254 nm) UV, and hydrostatic specific gravity testing.

The micro-structure of the samples was examined by a scanning electron microscope (SEM, JEOL JSM-7800F) with a working voltage of 15 kV and a working distance of 10 mm.

See end of article for About the Authors and Acknowledgments.
Gems & Gemology, Vol. 55, No. 3, pp. 406–415,
http://dx.doi.org/10.5741/GEMS.55.3.406

Figure 1. The imitations are similar to rhodochrosite in terms of appearance. Shown here are the samples from the study. From left: natural rhodochrosites T1 (8.20 ct) and T2 (18.03 ct) and imitations F1 (20.59 ct) and F2 (20.09 ct). Photo by Xiaoyan Yu.

SEM-EDS (Oxford X-Max50) was used to quantitatively analyze the chemical compositions of both the natural and imitation rhodochrosite stones. The chemical compositions in weight percentages were obtained on multiple points in the various red and white regions of each, and elemental mapping allowed us to see the chemical variations of these same regions.

X-ray diffraction (XRD) was performed using a Shimadzu XRD-7000S to conduct phase analyses with the test conditions of Cu target, tube voltage 40 kV, tube current 30 mA, and test angle 5°–90°. We used linkage scanning mode, a scanning speed of 5°/min, and a step size of 0.02°.

Infrared spectra were recorded on a Bruker Tensor 27 infrared spectrometer using the specular reflection method and the KBr pressed-pellet technique with 4 cm^{-1} resolution. The scanning ranges were 2000–400 cm^{-1} and 4000–400 cm^{-1}, respectively. Powder from the sample (about 0.5 mg) was mixed with potassium bromide (about 150 mg) in an agate pestle and mortar during the FTIR analysis. The powder was ground to a particle size of <2.5 μm.

Raman spectra were recorded on the four samples using a Horiba HR-Evolution Raman microspectrometer with an Ar-ion laser operating at 532 nm excitation between 1800 and 100 cm^{-1} and accumulating up to three scans.

RESULTS AND DISCUSSION

Visual Appearance and Standard Gemological Properties. The gemological properties of the samples are summarized in table 1. All four had a pink bodycolor with white bands, but the imitation and natural rhodochrosite were different in terms of band shape, luster, and transparency. Compared with the serrated, lace-like bands of rhodochrosite, the bands of the imitation were not as complex or smooth. The imitations also had lower luster and transparency than the natural samples (again, see figure 1).

TABLE 1. Standard gemological properties of rhodochrosite and imitation rhodochrosite samples.

Sample no.	Color	Luster	Transparency	Specific gravity	Refractive index
T1 (rhodochrosite)	Orangy pink with white and lace-like bands	Vitreous	Translucent	3.66	Red part: 1.60 White part: 1.63
T2 (rhodochrosite)	Orangy pink with white and lace-like bands	Vitreous	Translucent	3.66	Red part: 1.60 White part: 1.63
F1 (imitation)	Pink with white and smooth banding pattern	Resinous	Subtranslucent	2.00	Red part: 1.56 White part: 1.50
F2 (imitation)	Pink with white and smooth banding pattern	Resinous	Subtranslucent	2.00	Red part: 1.56 White part: 1.51

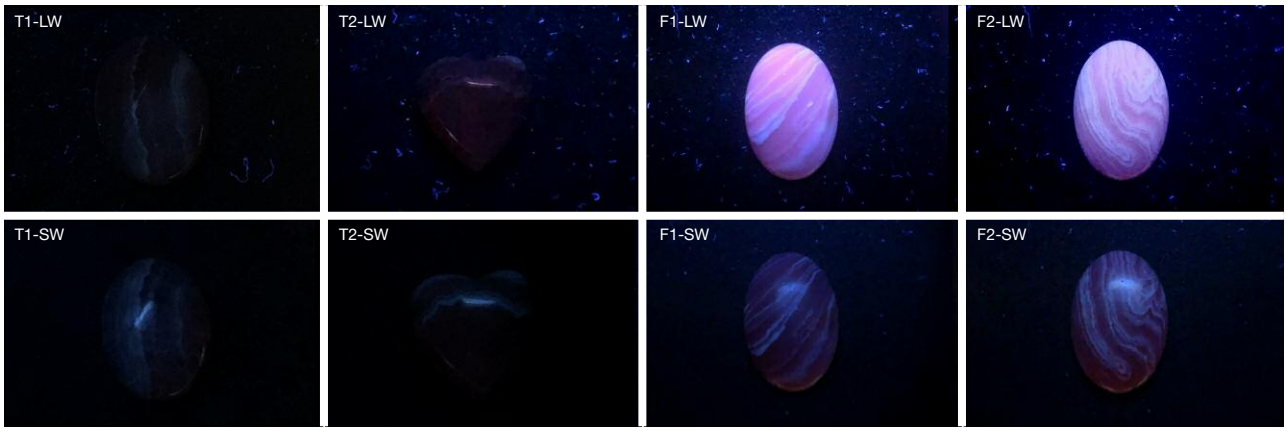

Figure 2. The natural rhodochrosite was inert under the UV lamp, while the imitation showed strong fluorescence. Photo by Hanyue Xu.

These properties were sufficient to identify the imitations. The specific gravity of the imitations was about 2.00, much lower than the rhodochrosite's. Moreover, the refractive index of the white band and the red part were different between the natural and imitation samples. The rhodochrosites had a refractive index of 1.60 in the red part and 1.63 in the white part. Meanwhile, the imitations had a refractive index of 1.56 for the red part and just 1.50 for the white part. The samples' fluorescence responses under long-wave and short-wave UV light were noticeably different. The imitation had strong fluorescence under long-wave UV and weak fluorescence under short-wave, but the natural rhodochrosite was inert (figure 2).

Micro-Structure. The micro-structure was another distinguishing characteristic (figure 3). The natural rhodochrosite had a smooth surface with few pits (figure 3A). Meanwhile, the imitation had a granular

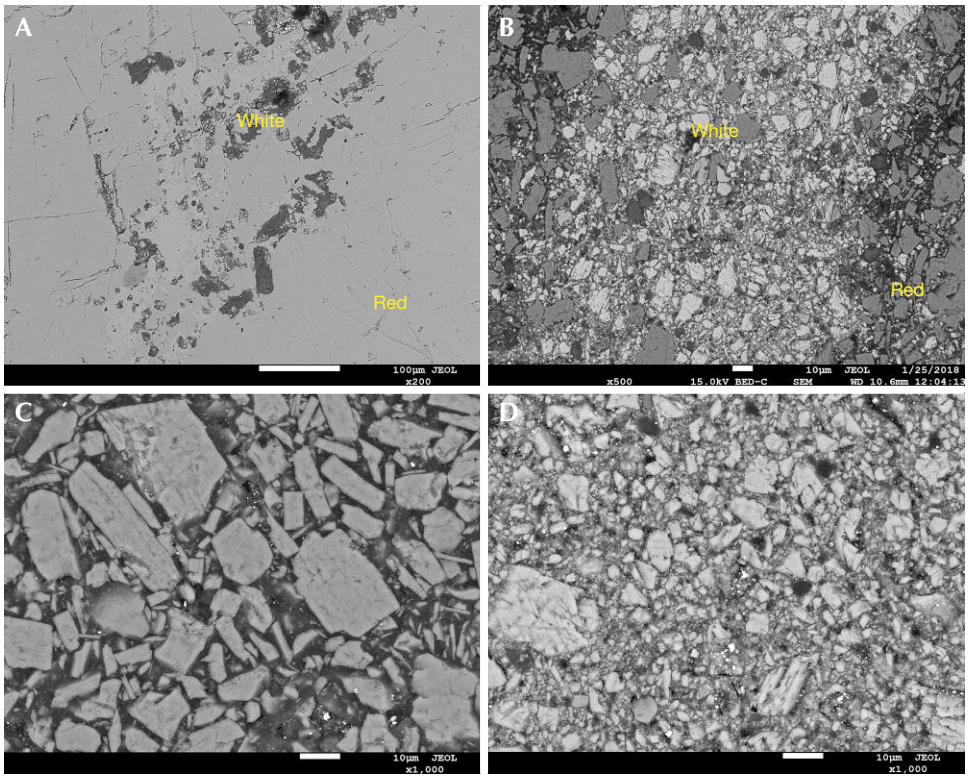

Figure 3. BSE images of samples. A: The junction of the red and white parts of rhodochrosite at 200× magnification. B: The junction of the red and white parts of the imitation at 500× magnification. C: The red part of the imitation showed a coarse granular structure at 1000× magnification. D: The white part of the imitation exhibited a finer granular structure at 1000× magnification.

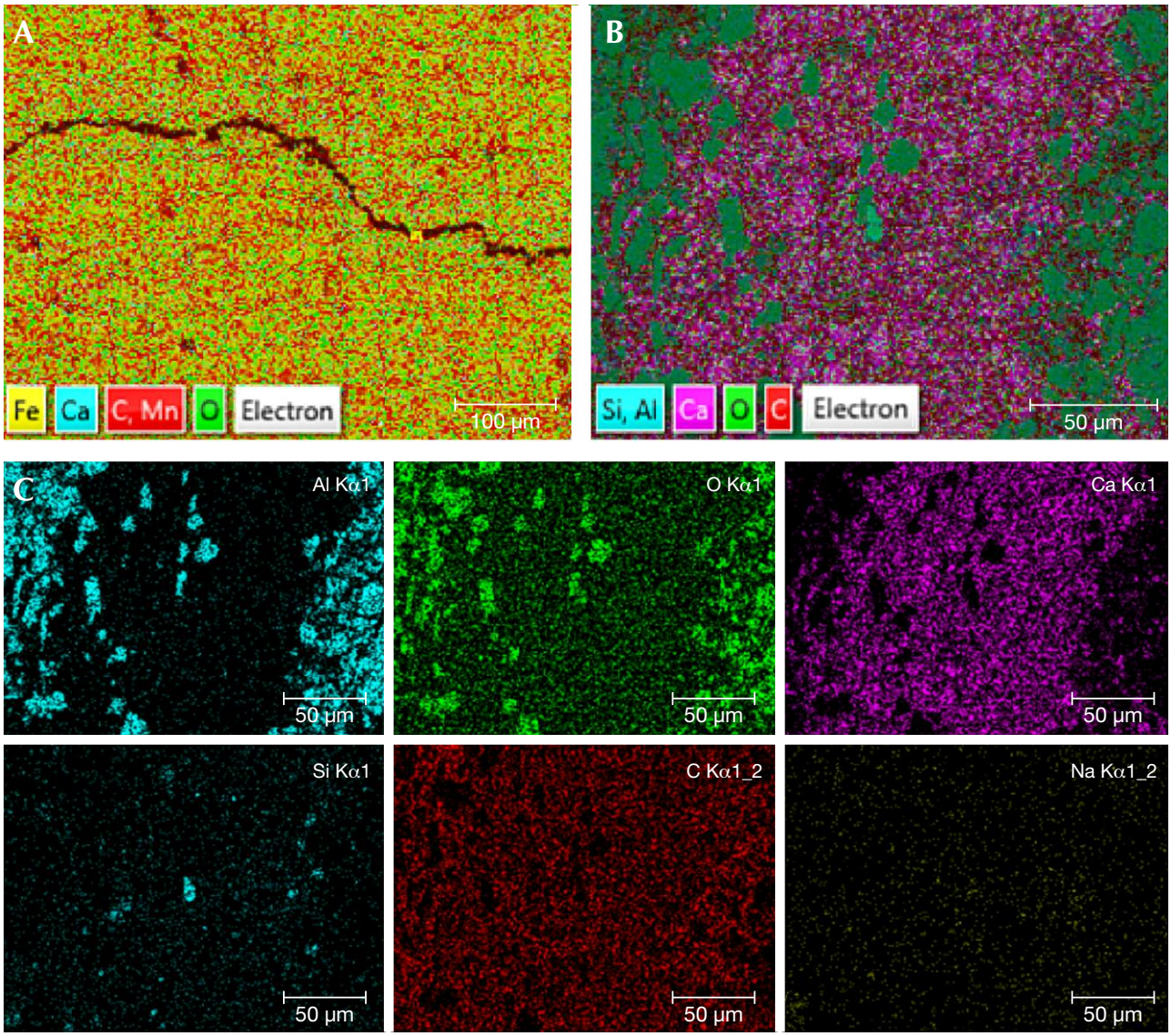

Figure 4. Element mapping of the junction of the red and white parts using EDS on SEM. A: Element mapping for Mn, Ca, O, Fe, and C of the rhodochrosite sample. B and C: Element mapping for Al, O, Ca, C, Si, and Na of the imitation sample.

texture (figure 3B). The mineral particles of the red part were larger than those in the white parts (figure 3, C and D). Observing the junction of the red and white parts (figure 3B), it can be seen that the two kinds of mineral particles are mutually permeable with each other. Thus we came to the conclusion that the imitation is a pressed stone containing two kinds of material.

Element Mapping and Chemical Compositions. According to the element mapping, the natural samples mainly contained Mn, C, O, with few impurity elements of Fe and Ca (figure 4A). Rhodochrosite belongs to the carbonate family. Carbonates are a group of minerals with the same structure but slightly different compositions such as siderite ($FeCO_3$), magnesite ($MgCO_3$), and calcite ($CaCO_3$). Thus some Fe, Ca, and Mg can replace Mn as impurity elements in rhodochrosite (Du and Fan, 2010).

The red and white parts of the imitation had a very different composition from rhodochrosite (figure 4, B and C). The larger mineral particles in the red part

TABLE 2. Chemical composition (in wt.%) of the red part of the rhodochrosite imitations, obtained by EDS.

Sample no.	Elements	C	O	Al	Na	Si	S	Total
F1R	Point 1	4.70	57.12	38.03	0.15			100.00
	Point 2	4.34	58.03	37.38	0.24			99.99
	Point 3	4.17	56.78	38.98	0.07			100.00
	Point 4	68.15	13.28	18.11	0.04	0.19	0.23	100.00
	Point 5	52.99	19.28	27.16	0.09	0.20	0.29	100.01
	Point 6	65.35	19.31	14.98	0.04	0.10	0.22	100.00
F2R	Point 1	6.35	57.90	35.62	0.12			99.99
	Point 2	6.75	58.86	34.23	0.16			100.00
	Point 3	5.79	58.55	35.58	0.08			100.00
	Point 4	64.77	21.01	13.93	0.08	0.13	0.08	100.00
	Point 5	65.25	19.29	15.20	0.06	0.16	0.05	100.01
	Point 6	64.52	21.33	13.70	0.09	0.25	0.11	100.00

mainly contained Al and O, while the smaller particles in the white bands mainly contained Ca, C, and O. The smaller minerals in the white bands also had a small amount of Si and Na as impurity elements. At the same time, we observed that the gap between the particles contained a large amount of C. This indicated that the mineral particles were Al and O compounds in the red part of the imitation, and calcium carbonate in the white part. Moreover, a large amount of C in the gap between the particles revealed that the imitation was perhaps formed by cementing and dyeing with mineral powder and organics.

The EDS data in tables 2 and 3 agree well with the element mapping results. The red part of the imitation samples was mainly composed of Al and O, and contained little Na (F1R and F2R, points 1–3; figure 5); the white part was mainly composed of Ca, C, and O, with a small amount of Si and Na (F1W and F2W, points 1–3; figure 6). The content of C increased sharply (F1R, F2R, F1W, and F2W, points 4–6) when the test points were in the matrix of the imitation. This is probably due to the presence of organics in the mineral particle gap of the imitation.

According to the ICDD powder diffraction file (PDF-2) database and Li et al. (2009), the X-ray diffraction data confirmed the presence of rhodochrosite (figure 7, T1 and T2), matching PDF card 99-0089. Furthermore, according to the previously published report of the imitation turquoise (Zhang et al., 2014) and the chemical composition data ob-

Figure 5. EDS test point of the red part of imitations F1R (left) and F2R (right).

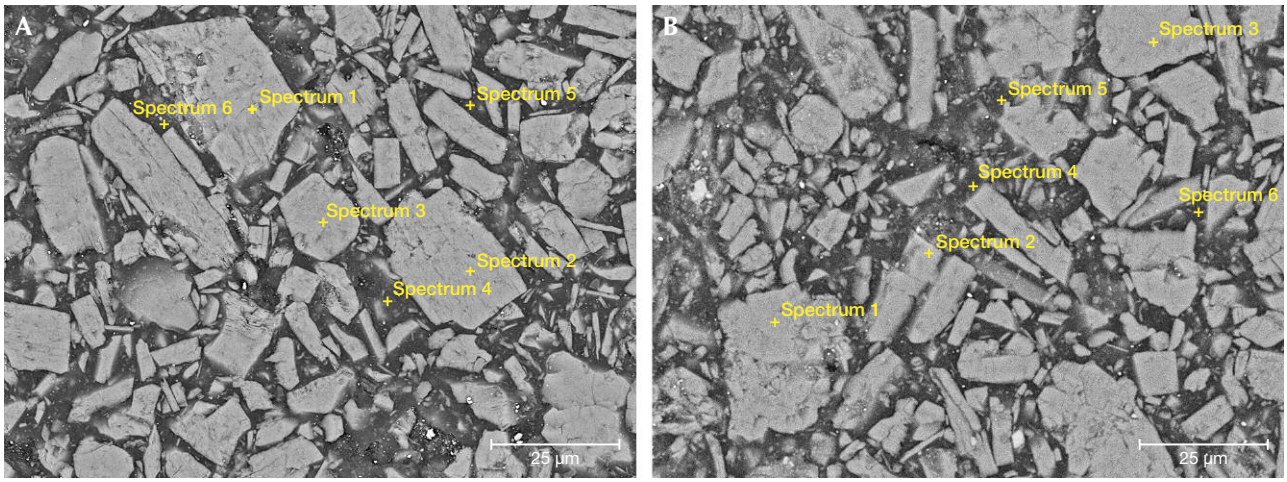

TABLE 3. Chemical composition (in wt.%) of the white part of the rhodochrosite imitations, obtained by EDS.

Sample no.	Elements	C	O	Ca	Mg	Al	Si	Na	Cl	K	Total
F1W	Point 1	11.65	36.30	51.96	0.08						99.99
	Point 2	9.63	31.15	59.16	0.07						100.01
	Point 3	10.35	30.89	58.65	0.11						100.00
	Point 4	38.96	32.73	23.99	0.18	0.53	3.31	0.09	0.06	0.14	99.99
	Point 5	39.48	20.78	35.69	0.27	0.26	3.23	0.13	0.03	0.13	100.00
	Point 6	29.11	25.57	43.19	1.37	0.06	0.46	0.12	0.05	0.05	99.98
F2W	Point 1	10.53	32.61	56.52	0.34						100.00
	Point 2	12.86	32.90	53.87	0.38						100.01
	Point 3	11.01	32.12	56.43	0.44						100.00
	Point 4	31.58	29.73	24.89	0.18	0.67	11.43	0.59	0.35	0.59	100.01
	Point 5	31.38	31.07	25.80	0.09	0.58	9.98	0.31	0.19	0.60	100.00
	Point 6	26.51	27.45	42.67	0.30	0.14	0.33	1.49	0.62	0.48	99.99

tained by EDS (tables 2 and 3), the red part of the imitation is $Al(OH)_3$ (gibbsite), which matches PDF card 33-0018, and the white part is $CaCO_3$ (calcite), matching PDF card 47-1743.

Infrared Spectroscopy. FTIR spectroscopy using the specular reflection method (figure 8) shows large differences between the infrared spectrum of rhodochrosite and the imitations.

According to Farmer (1974), the infrared spectrum of rhodochrosite does not show symmetric stretching vibration, while out-of-plane bending vibration and in-plane bending vibration are sharp absorption peaks that appear at about 900–600 cm^{-1}; asymmetric stretching vibration is a strong and wide absorption peak, appearing near 1400 cm^{-1} (Li et al., 2009; Yang et al., 2015).

The infrared spectra of the red and white parts of the natural rhodochrosite samples are similar (figure 8, T2W and T2R). There are three characteristic absorptions in the range of 2000–400 cm^{-1}: a wide absorption band of 1550–1400 cm^{-1} and sharp absorption peaks of 725 and 874 cm^{-1} in the range of 900–600 cm^{-1}. The absorption of ν(C-O) in the 1550–1400 cm^{-1} range is wide and strong, the absorption at 874 cm^{-1} of $\nu(CO_3^{2-})$ is sharp and strong, and the absorption of ν(O-C-O) near 720 cm^{-1} is sharp but weak. According to Yang et al. (2015), the three characteristic absorptions of the natural rhodochrosite samples correspond to ν(C-O) asymmetric stretching

Figure 6. EDS test point of the white part of imitations F1W (left) and F2W (right).

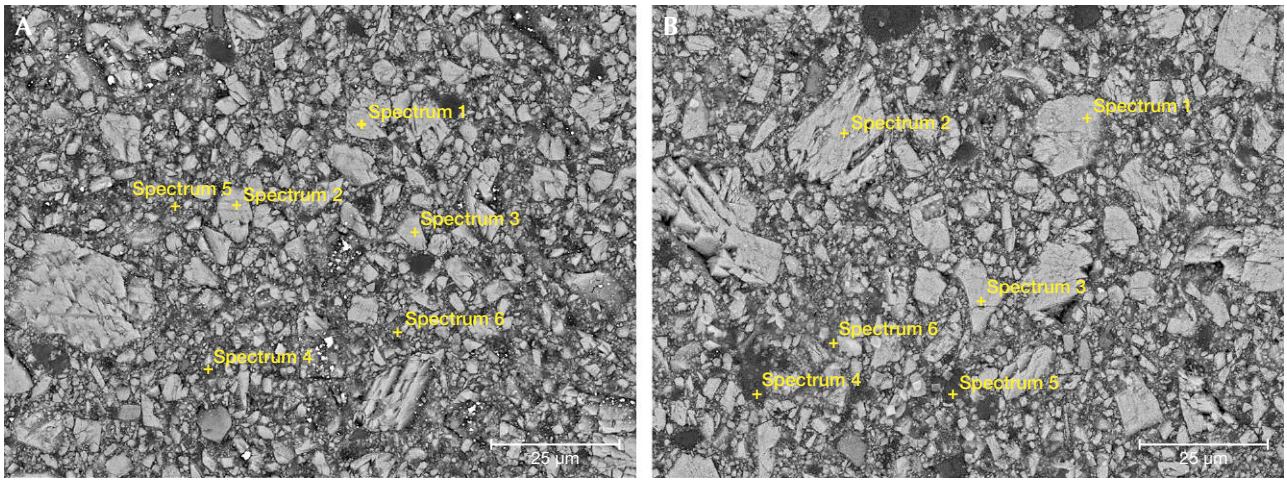

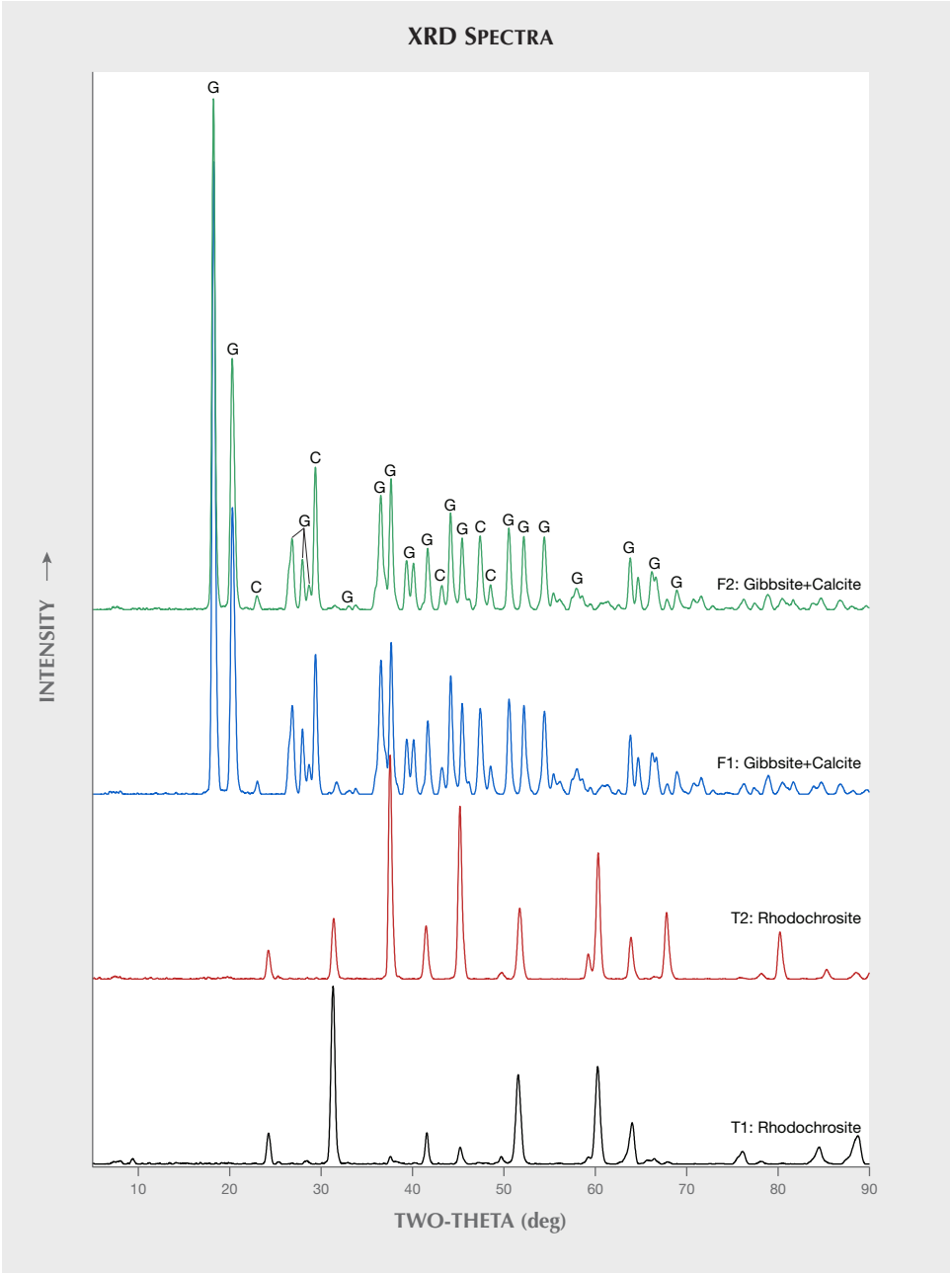

Figure 7. X-ray diffraction results of samples (5°–90°). Spectra are offset for clarity.

vibration, $\gamma(CO_3^{2-})$ out-of-plane bending vibration, and δ(O-C-O) in-plane bending vibration, respectively. These are characteristic absorptions of carbonate minerals.

As figure 8 shows, the infrared spectrum of the white part of the imitation is different from the red part. The main absorption peaks of the red part of the imitation (figure 8, F1R) are the peak at 1020 cm^{-1}, the broad peak at about 800–740 cm^{-1}, and the series of weak and sharp peaks in the 600–400 cm^{-1} range, which correspond to the ν(Al-O-H) stretching vibration and the related vibration of the hydroxyl group (Zhang et al., 2014). According to the attribution of the infrared spectrum peaks, we determined that the red part of the imitation is composed of gibbsite-$Al(OH)_3$.

However, the white part of the imitation (figure 8, F1W) has four characteristic absorptions in the range of 2000–400 cm^{-1}: the stretching vibration peak of ν(C-O) at 1716 cm^{-1}; the asymmetric stretching vibration of ν(C-O) at 1412 cm^{-1}; $\gamma(CO_3^{2-})$, the out-of-plane bending vibration peak at 873 cm^{-1}; and the out-of-plane bending vibration of δ(O-C-O) at 720

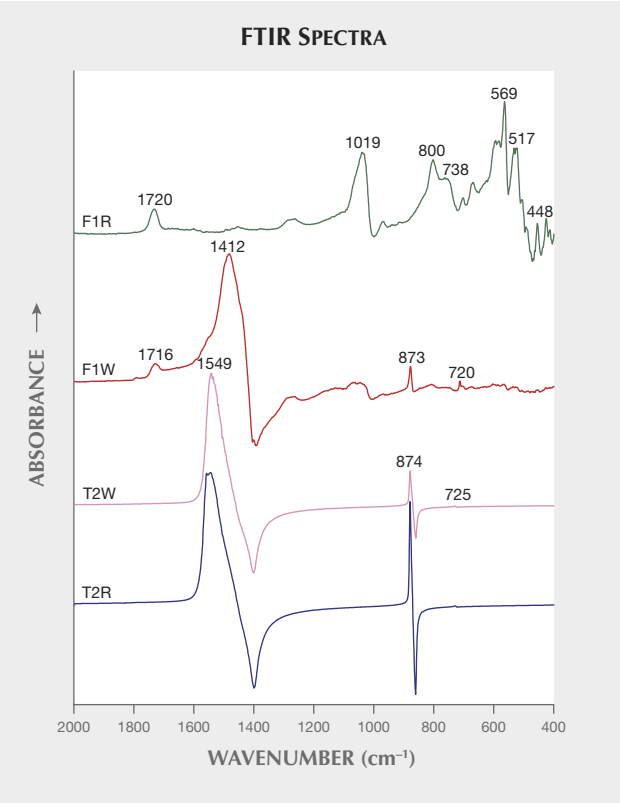

Figure 8. Infrared spectra of the red and white parts of samples using the specular reflection method. Shown from top to bottom are the red and white parts of an imitation and the white and red parts of a rhodochrosite. Spectra are offset for clarity.

cm^{-1}, which are characteristic absorptions of carbonate. In addition to the absorption at 1020 cm^{-1} is the absorption caused by the $Al(OH)_3$ particle mixed in the white part. These peaks are also characteristic absorptions of carbonate minerals, and thus the attribution of peaks is similar to that of natural rhodochrosite (figure 8; Yang et al., 2015).

The KBr pressed-pellet technique was used for more accurate and comprehensive determination of the samples' infrared spectra in the 4000–2000 cm^{-1} range. It can be seen from figure 9 (T1) that the absorption peaks of the natural rhodochrosite sample in the 1500–400 cm^{-1} range were the same as those measured by the reflection method (figure 8). The ν(C-O) stretching vibration peak appears around 1800 cm^{-1} (Li et al., 2009; Yang et al., 2015). The absorption peak at 3446 cm^{-1} could be caused by the water absorption of KBr.

In addition to the characteristic peaks similar to those measured by the reflection method, many characteristic absorptions of the imitation (figure 9, F1) are caused by the organics and water. The absorptions of the ν(OH) symmetric stretching vibration appear at 3621, 3527, 3469, and 3369 cm^{-1} in the range of 4000–3000 cm^{-1}, which may be caused by the (OH) from $Al(OH)_3$ or the organics (Chen et al., 2006).

The absorptions at 2926, 2854, and 1453 cm^{-1} are caused by ν(C-H) asymmetric stretching vibration, ν(C-H) symmetric stretching vibration, and δ(C-H) deformation vibration of CH_2, respectively (Chen et al., 2006; Teng et al., 2008).

Two peaks near 1731 and 1140 cm^{-1} are caused by symmetric stretching vibrations of ν(C=O) and ν(C-O-C) of the ester group. And the absorptions of the asymmetric stretching vibration of ν(C=C) in the benzene ring are at 1600 and 1508 cm^{-1}. Moreover, the absorption peak at 1286 cm^{-1} is caused by OH, and the 968 cm^{-1} peak is caused by the bending vibration of an unsaturated hydrocarbon group (=C-H) (Tian et al., 2004; Chen et al., 2006; Teng et al., 2008).

It can be inferred that the organic material in the matrix of the imitation is a kind of resin used for ce-

Figure 9. Infrared spectra of samples using the KBr pressed-pellet technique: rhodochrosite (top) and imitation rhodochrosite (bottom). Spectra are offset for clarity.

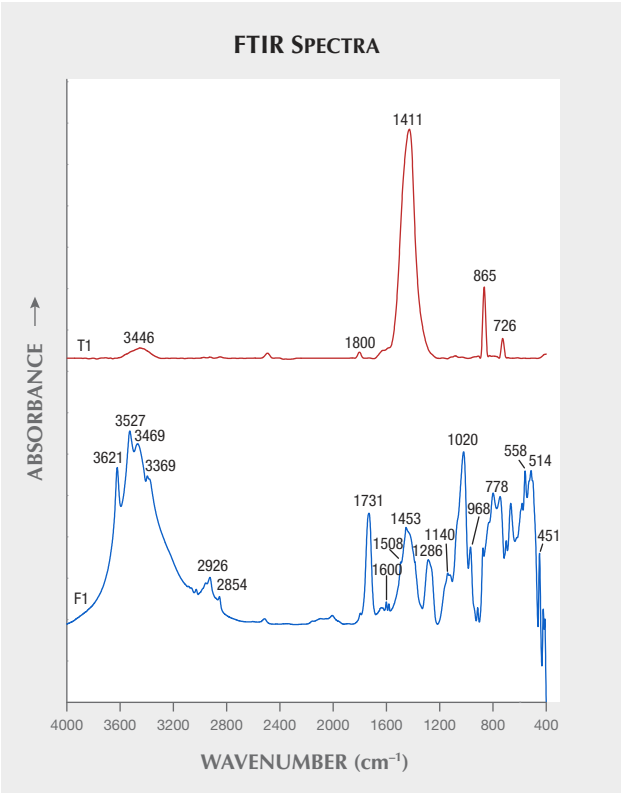

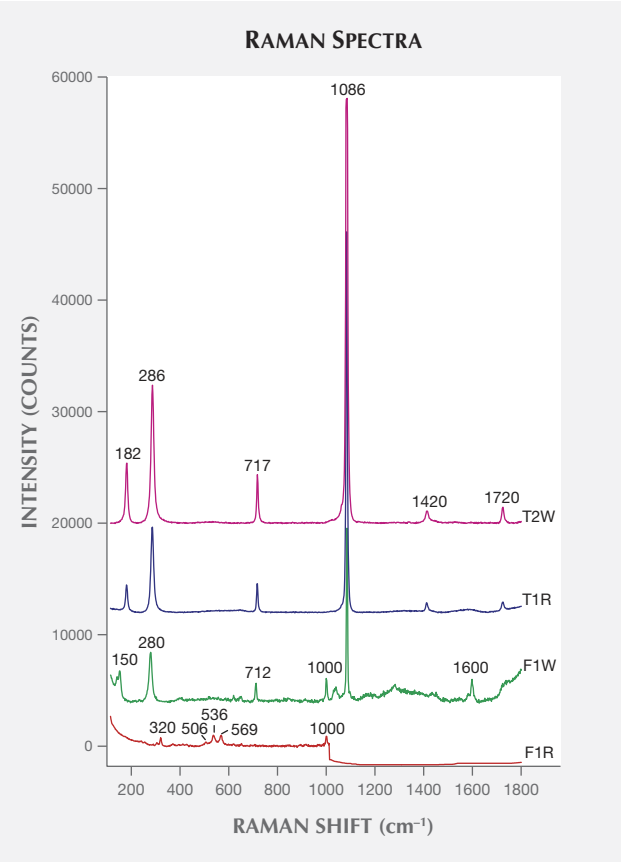

Figure 10. Shown from top to bottom are the Raman spectra of the white and red parts of the rhodochrosite and the imitation rhodochrosite, respectively. Spectra are offset for clarity.

menting or dyeing. According to Chen et al. (2006), it could be styrene or a similar compound.

Raman Spectroscopy. Figure 10 presents the Raman spectra of the red and white parts of the rhodochrosite and the imitation rhodochrosite in the 1800–100 cm^{-1} range. There are six groups of Raman shifts in the rhodochrosites (figure 10, T2W and T1R). The peak at 182 cm^{-1} is related to the lattice vibration of rhodochrosite. The peaks at 286, 717, 1086, 1420, and 1720 cm^{-1} correspond to the vibration of C-O in CO_3^{2-} (the out-of-plane bending vibration, the in-plane bending vibration, the symmetric stretching vibration, the antisymmetric stretching vibration, and the coupled vibration mode, respectively) (Du and Fan, 2010).

The Raman spectrum of the red part of the imitation sample (figure 10, F1R) is attributed to the O-H bending vibration in the range of 1200–200 cm^{-1}, including the Al-OH deformation vibration and the Al-O-Al bending vibration. Among them, the peak at about 1000 cm^{-1} is caused by δ(O-H) in-plane bending vibration, and the peak at 506 cm^{-1} is related to the γ(O-H) out-of-plane bending vibration. The 569 and 536 cm^{-1} peaks are attributed to the out-of-plane bending vibration of γ(Al-O-Al). And the δ(Al-O) bending vibration leads to the peak at 320 cm^{-1}, plus a small shoulder at 306 cm^{-1}. The Raman spectra come to the same conclusion as the infrared spectra.

The Raman shifts of the white part of the imitation sample (figure 10, F1W) are mainly located at 150, 280, 712, 1000, 1085, and 1600 cm^{-1}. The Raman shifts at about 1000 and 1600 cm^{-1} are caused by the $Al(OH)_3$ impurity in the white strip. The remaining absorption peaks at 150, 280, 712, and 1085 cm^{-1} are similar to those in the natural samples but slightly shifted. It is known that as the cation radius increases, the Raman shifts of the calcite group minerals that belong to ν_{ob}, ν_{ib}, and ν_s shift toward the short-wave (Du and Fan, 2010). Through comparison of the peak positions with Fu and Zheng (2013) and Du and Fan (2010), the peak at 150 cm^{-1} is due to the calcite lattice vibration, while the peaks at 280, 712, and 1085 cm^{-1} correspond to the C-O vibration of CO_3^{2-} (the out-of-plane bending vibration, in-plane bending vibration, and symmetric stretching vibration, respectively). From this, we determined that the white part of the imitation is calcite.

CONCLUSIONS

Standard gemological testing was able to distinguish imitations from rhodochrosite by color, structure, band shape, transparency, and UV fluorescence. The imitation samples had brighter color, less-complex banding, lower specific gravity, lower RI, and poor transparency. SEM showed that the imitation had a granular structure, and its red and white parts contained different mineral powder particles. The FTIR, XES, XRD, and Raman spectra showed that the red part of the imitation product consists of granules of gibbsite ($Al(OH)_3$) and the white band part is composed of calcite ($CaCO_3$). Moreover, it is proposed that the matrix contains organic substances, possibly styrene or a similar compound.

ABOUT THE AUTHORS
Ms. Hanyue Xu is obtaining a master's degree in gemology, and Dr. Xiaoyan Yu (yuxy@cugb.edu.cn) is director of the gemology teaching and research group and a professor of gemology and mineralogy, at the School of Gemology, China University of Geosciences in Beijing.

ACKNOWLEDGMENTS
The authors would like to thank Mr. Weiren Wang and Mrs. Ning Xu for supplying the samples, along with Mr. Longquan Xu, Mrs. Xu Fei, and Mrs. Ling Yu at the Instrumental Analysis Center, Dalian Polytechnic University, for assistance with the SEM, FTIR, and XRD experiments. Mr. Zhechen Li at the School of Gemology, China University of Geosciences in Beijing, assisted with the Raman spectra experiment; Mrs. Ying Han provided valuable discussions on the experimental data.

REFERENCES

Chen Q.L., Qi L.J., Zhang Y. (2006) IR absorption spectrum representation of turquoise, treated turquoise and imitation. *Journal of Gems and Gemmology*, Vol. 8, No. 1, pp. 9–12.

Du G.P., Fan J.L. (2010) Characteristics of Raman spectra of calcite group minerals. *Journal of Mineralogy and Petrology*, Vol. 30, No. 4, pp. 32–35.

Farmer V.C. (1974) *The Infrared Spectra of Minerals*. Mineralogical Society Monograph 4, London.

Fu P.G., Zheng H.F. (2013) Raman spectra of aragonite and calcite at high temperature and high pressure. *Spectroscopy and Spectral Analysis*, Vol. 33, No. 6, pp. 1557–1561, http://dx.doi.org/10.3964/j.issn.1000-0593(2013)06-1557-05

Knox K., Lees B.K. (1997) Gem rhodochrosite from the Sweet Home mine, Colorado. *G&G*, Vol. 33, No. 2, pp. 122–133, http://dx.doi.org/10.5741/GEMS.33.2.122

Li N., Wang Q., Zhang L.J., Jiang D. (2009) Study on gemological characteristics of the rhodochrosite in Wutong, Guangxi. *Popular Science & Technology*, No. 6, pp. 129–130.

Teng W.W., Yu W.L., Luo Y.G. (2008) Study on component and structure of a kind of imitated chicken-blood stone. *Journal of Gems and Gemmology*, Vol. 10, No. 1, pp. 25–28.

Tian L.G., Cheng Y.F., Liu H.B., Zhang Z.G. (2004) Identification of treated chicken-blood stones and imitations. *Journal of Gems and Gemmology*, Vol. 6, No. 3, pp. 18–21.

Xing N. (2015) Rhodochrosite Inca Rose. *China Gems*, No. 3, pp. 92–95.

Yang N., Kuang S.Y., Yue Y.H. (2015) Infrared spectra analysis of several common anhydrous carbonate minerals. *Journal of Mineralogy and Petrology*, Vol. 35, No. 4, pp. 37–42.

Yu X.Y. (2016) *Colored Gemmology*, 2nd ed. Geological Publishing House, Beijing.

Zhang P.L. (2006) *Systematic Gemmology*, 2nd ed. Geological Publishing House, Beijing.

Zhang X., Yang M.X., Di J.R., Wang P. (2014) Identification and spectroscopy characteristics of three natural minerals similar to turquoise. *Journal of Gems and Gemmology*, Vol. 16, No. 3, pp. 38–45.

Zwaan J.C. (2015) Rhodochrosite from Brazil. *Journal of Gemmology*, Vol. 34, No. 6, pp. 473–475.

Lab Notes

Editors
Thomas M. Moses | Shane F. McClure

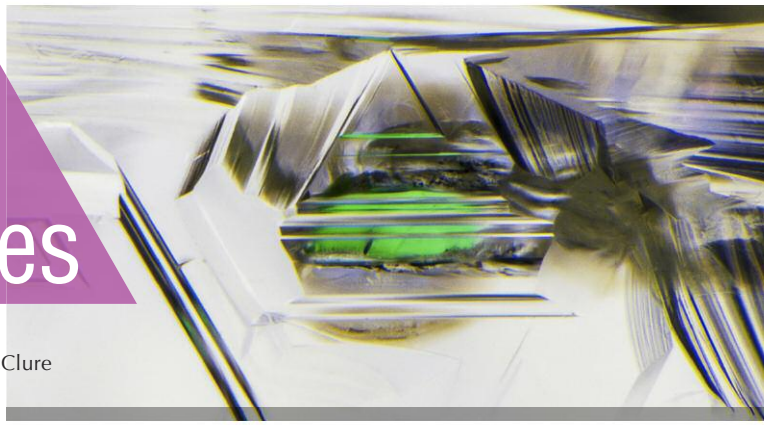

Faceted CHIOLITE

Recently, the GIA lab in Carlsbad received a colorless 1.04 ct gemstone of a material that was new to the lab (figure 1). The measured refractive index was 1.342–1.349 with a birefringence of 0.007 and an optic character of uniaxial negative. The specific gravity, measured hydrostatically, was 3.01. These properties were consistent with the mineral chiolite, which was confirmed by Raman spectroscopy (see figure 2 and http://rruff.info/R050412).

Chiolite is a very rare transparent to translucent colorless or snow-white mineral with a vitreous luster, perfect cleavage in one direction, and a white streak. It crystallizes in the tetragonal system and is composed of sodium and aluminum, with the formula $Na_5Al_3F_{14}$ (the presence of these elements was confirmed with EDXRF). The principal source of gem-quality material is Ivigtut, Greenland, where it occurs in association with cryolite. Other gem-quality sources include Miass in the Ilmen Mountains region of Russia, where it is found in a cryolite pegmatite, and the Morefield pegmatite mine in Virginia (see AZoMining.com). The mineral was first discovered at Miass in 1846. The name is very similar to cryolite, a related mineral. *Cryolite* comes from Greek for "ice stone," while *chiolite* means "snow stone." Like their namesakes, they are sometimes found together, though chiolites are rarer.

Figure 1. This 1.04 ct colorless octagonal cut was identified as chiolite.

This gem has a very low hardness (3.5–4 on the Mohs scale) and perfect cleavage. The stones are usually small and nondescript. Nevertheless, chiolite has joined the ranks of minerals cut by faceters who wish to try their hand at everything clean enough to cut, and a cut stone would make quite a specimen for a gem collection.

Chiolite occurs in some granite pegmatites and is associated with ralstonite, pachnolite, elpasolite, cryolite, thomsenolite, cryolithionite, fluorite, phenakite, and topaz (see mindat.org and rruff.info).

Figure 2. Raman spectroscopy confirmed the colorless stone's identity as chiolite.

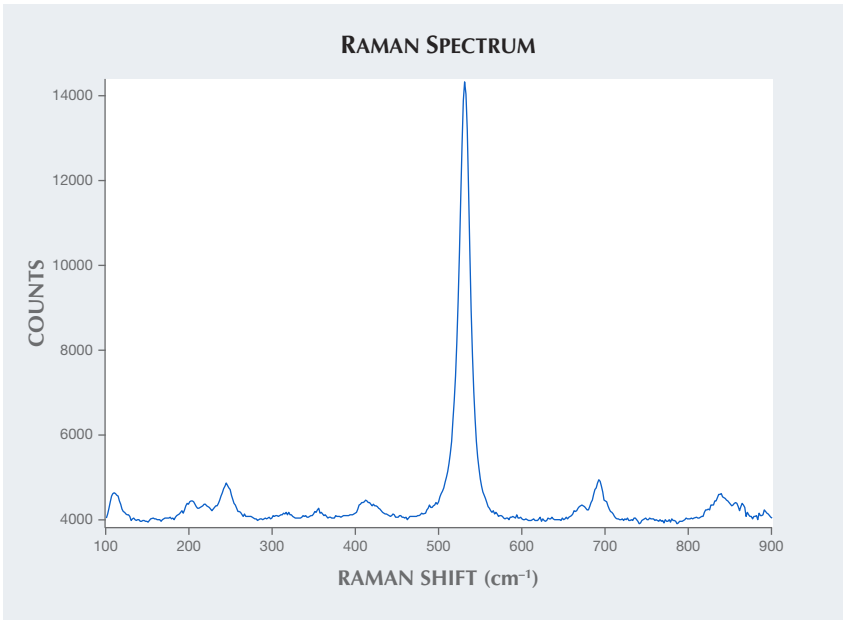

Editors' note: All items were written by staff members of GIA laboratories.

Gems & Gemology, Vol. 55, No. 3, pp. 416–425.

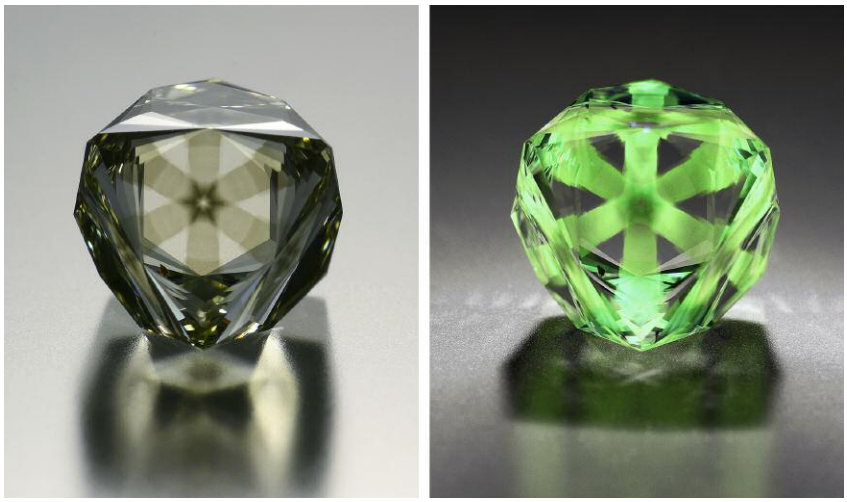

Figure 3. This 3.70 ct brownish greenish yellow faceted octahedron contained a remarkable stellate hydrogen cloud (left) that showed strong yellowish green fluorescence under long-wave UV light (right).

Chiolite is difficult to cut, extremely rare, and has little commercial appeal. It is solely a curiosity in the gem world.

Forozan Zandi

Faceted DIAMOND Octahedron with a Remarkable Stellate Cloud Inclusion

A 3.70 ct faceted Fancy brownish greenish yellow diamond (figure 3, left) was recently submitted to the Carlsbad laboratory for color origin and identification service. The diamond was remarkable in that it contained an eye-visible stellate cloud inclusion consisting of six legs that each radiated to a point on the polished octahedron. Diamonds containing star-like clouds are sometimes referred to as "asteriated" in the trade (T. Hainschwang et al., "The Rhodesian Star: An exceptional asteriated diamond," *Journal of Gemmology*, Vol. 34, No. 4, 2014, pp. 306–315). While GIA occasionally encounters asteriated diamonds, this one was striking due to the well-defined nature of the star and the strong yellowish green color it exhibited under long-wave UV (figure 3, right).

Gemological examination revealed a type Ia diamond, showing a typical cape series in the visible spectrum. Hydrogen bands in the infrared spectrum and the UV-Vis-NIR spectrum were consistent with the observed "hydrogen cloud" inclusions (figure 4). These clouds in diamonds consist of a high density of light scattering micro-inclusions consistent with those that have been reported to be graphite (B. Rondeau et al., "Three historical 'asteriated' hydrogen-rich diamonds: Growth history and sector-dependent impurity incorporation," *Diamond and Related Materials*, Vol. 13, No. 9, 2004, pp. 1658–1673) that correlate strongly with the presence of hydrogen (W. Wang and W. Mayerson, "Symmetrical clouds in diamond—the hydrogen connection," *Journal of Gemmology*, Vol. 28, No. 3, 2002, pp. 143–152). Also observed was brown radiation staining in a shallow feather, indicating that the stone had been exposed to natural alpha radiation (figure 5).

While the cutting style was unconventional, it served to showcase the remarkable inclusion scene contained within the diamond. This is one of the most interesting diamonds of this type examined at GIA's Carlsbad laboratory.

Maryam Mastery Salimi and Nathan Renfro

Figure 4. The six-ray star pattern is composed of microscopic particles commonly referred to as "hydrogen clouds" (left) that fluoresce strong green to long-wave UV (right). Field of view 6.27 mm.

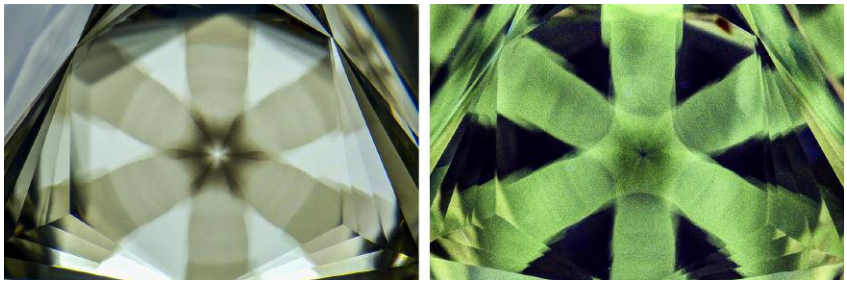

GROSSULAR GARNET Crystals in Demantoid Garnet

Demantoid, the green variety of andradite garnet, is a rare gemstone. It typically possesses high dispersion and diamond-like luster, which is often partly masked by the green and yellow-green bodycolors. Variations

Figure 5. An irregularly shaped dark brown radiation stain on the diamond's surface-reaching inclusion clearly shows that it was exposed to natural alpha radiation. Field of view 3.51 mm.

TABLE 1. LA-ICP-MS results on three areas of the demantoid sample: the host material (spot 1), the outer area of the inclusion (spot 2), and the inner area of the inclusion (spot 3).

Concentration (ppmw) of different elements	Mg	Al	Si	Ca	Ti	V	Cr	Mn	Fe	
Spot 1	449	414	185000	275000	17.7	nd[a]	nd	328	186000	
Spot 2	162	32200	205000	296000	338	4.66	nd	723	152000	
Spot 3	127	85100	192000	271000	3570	10.4	nd	13000	57600	
Detection limits (ppmw)	0.17	0.92	221	36	0.65	0.06	0.80	0.15	5.03	
Wt.% oxides, converted from LA-ICP-MS	**MgO**	**Al_2O_3**	**SiO_2**	**CaO**	**TiO_2**	**V_2O_5**	**Cr_2O_3**	**MnO**	**FeO**	
Spot 1	0.1	0.1	39.6	38.5	0.0	nd	nd	0.0	23.9	
Spot 2	0.0	6.1	43.9	41.4	0.1	0.0	nd	0.1	19.6	
Spot 3	0.0	16.1	41.1	37.9	0.6	0.0	nd	1.7	7.4	
Normalized to 12 oxygen atoms	**Mg**	**Al**	**Si**	**Ca**	**Ti**	**V**	**Cr**	**Mn**	**Fe**	**O**
Spot 1	0.01	0.01	3.38	3.52	0.00	nd	nd	0.00	1.71	12.0
Spot 2	0.00	0.54	3.30	3.34	0.00	0.00	nd	0.01	1.23	12.0
Spot 3	0.00	1.42	3.09	3.05	0.03	0.00	nd	0.11	0.47	12.0

[a]*nd refers to elemental concentrations below the detection limits of LA-ICP-MS.*

in the color of demantoid garnet are generally caused by traces of chromium (Cr^{3+}), ferric iron (Fe^{3+}), Fe^{2+}-Ti^{4+} intervalence charge transfer, and Fe^{2+}-Fe^{3+} interactions (G. Giuliani et al., "Gem andradite garnet deposits demantoid variety," *InColor*, No. 36, Summer 2017, pp. 28–39).

Recently, GIA's Bangkok laboratory received a 4.47 ct yellowish green gemstone for identification. Standard gemological testing, including a refractive index over the limits of the refractometer and a specific gravity of 3.86, and Raman spectroscopy identified it as demantoid garnet. Microscopic examination revealed strong internal graining, fingerprints, and particles mixed with short needles. Interestingly, it also exhibited transparent octahedral crystals at the crown (figure 6). Some of them reached the surface and had a different luster from the host material. Close examination showed that the crystals contained two different luster areas, which also distinguished them from the host demantoid (figures 7 and 8).

Raman spectroscopy was performed on the three different areas to identify the materials. The Raman spectra of the two areas of the crystals were similar to that of the host, matching with andradite garnet. Garnet species typically possess similar physical properties and crystal forms, but differ in chemical composition. For example, andradite is a calcium-iron garnet with the formula $Ca_3Fe_2(SiO_4)_3$, whereas grossular is a calcium-aluminum garnet with the formula $Ca_3Al_2(SiO_4)_3$. Those two garnet species are in the same isomorphous series and therefore have the same general chemical formula, but differ only in containing Fe or Al. Due to their similar Raman spectra, chemical analysis is better suited to separate the species of garnet.

In this case, laser ablation–inductively coupled plasma–mass spectrometry (LA-ICP-MS) was used to compare the chemical composition of the demantoid against that of the surface-reaching inclusions. Spot 1 was on the host material, spot 2 on the outer area of the crystal inclusion, and spot 3 on the inner area of the crystal (figure 8).

Surprisingly, the three spot areas exhibited different chemical compositions, especially between the host demantoid area and the inner area of

Figure 6. A cluster of transparent octahedral crystals observed in a yellowish green demantoid garnet. Field of view 1.2 mm.

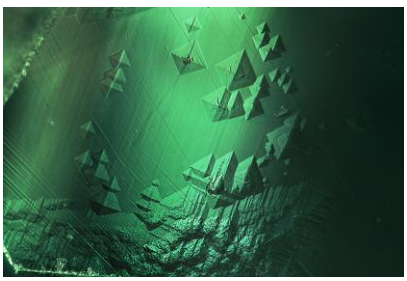

Figure 7. Some of the transparent octahedral crystals reached the surface of the demantoid. Field of view 2.0 mm.

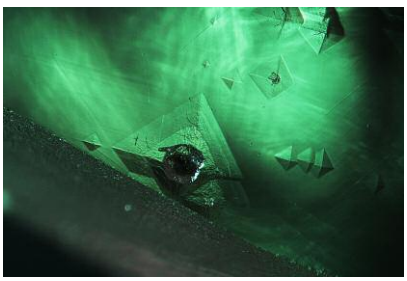

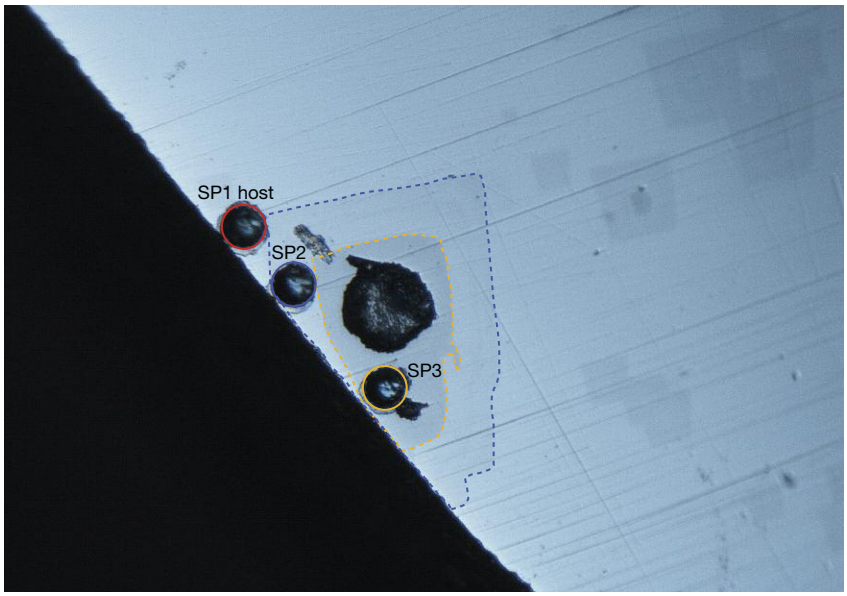

Figure 8. LA-ICP-MS was performed on three different areas: the host demantoid (spot 1), the outer area of the included crystal (spot 2), and the inner area of the included crystal (spot 3). The blue dashed line shows the separation between the demantoid area and the outer area of the inclusion. The yellow dashed line separates the outer and inner areas of the inclusion. Field of view 1.0 mm.

the crystal. This indicated that the crystal inclusion was from a garnet species other than andradite. Table 1 shows the chemical composition of the three spot areas, provided first in parts per million by weight (ppmw) units, followed by wt.% oxides of elements, and then as recalculated cations normalized to 12 oxygen atoms. Spot 1 (the demantoid) contained significantly more Fe than Al, whereas spots 2 and 3 of the crystal inclusion contained both elements. Spot 2 contained a higher concentration of Fe than Al, and the calculation showed a mix of two garnet species. It is possible that the detection area partly included the host material. Spot 3 contained a higher Al concentration than Fe (a 75.36% match with grossular).

Many types of solid inclusions are found in demantoid garnet, such as chromite, apatite, and diopside. From the results obtained here, it is interesting that solid inclusions of a different garnet species—grossular, in this case—can also be trapped in demantoid.

Ungkhana Atikarnsakul

Resin IMITATION IVORY with a Pseudo "Engine-Turned" Structure

Resin materials marketed as imitation ivory were recently acquired by a GIA gemologist. Material A, marketed under the name "Arvorin Plus," was purchased from a billiard store. Material B, sold as "Resin-Ivory+S," was purchased from a guitar store. These are manufactured as rods that can be purchased in a variety of lengths. Both show fine parallel linear striations along their length and a distinct pattern reminiscent of Schreger lines, commonly referred to as an "engine-turned" effect, when viewed across their horizontal plane (figure 9). These are also characteristics seen in genuine elephant and mammoth ivory.

The resin materials were found to have nearly identical gemological properties. Both had a Mohs hardness around 2, indented when pressed firmly with a pointer probe, and melted rapidly when touched with a hot point. They also had a spot refractive index reading of 1.57, a hydrostatic specific gravity of 1.24, and were inert to long-wave and short-wave ultraviolet light. Raman spectroscopy further confirmed their identity as a polymer substance.

Genuine elephant and mammoth ivory typically show a refractive index

Figure 9. Left: Material A, 24.40 mm in diameter and sold under the name "Arvorin Plus," shows parallel linear striations along its length and unorganized perpendicular striations along the horizontal plane. Right: Material B, 18.93 mm in diameter and marketed as "Resin-Ivory+S," exhibits parallel linear striations along its length and perpendicular striations with an average angle of 90° along its horizontal plane.

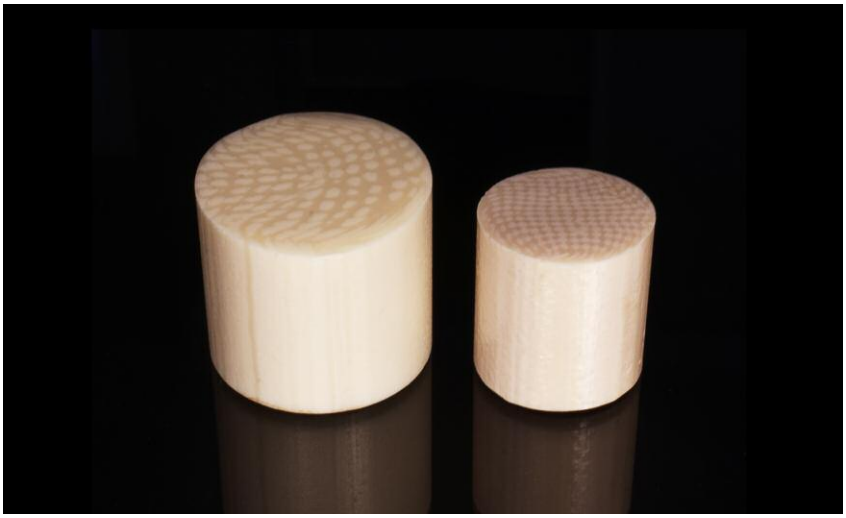

Figure 10. Left: Elephant ivory with Schreger lines intersecting at an average angle of 109°; field of view 19.27 mm. GIA Collection no. 4287. Right: Mammoth ivory with Schreger lines intersecting at an average angle of 69°; field of view 19.27 mm. Part of GIA Collection no. 19267, donated in 1995 by Richard Marcus of Mammoth Enterprises, Inc.

of 1.540, a specific gravity between 1.70 and 2.00, and weak white to blue fluorescence under both long-wave and short-wave UV. Ivory's most distinguishing characteristic is a display of Schreger lines ("engine turning"), an inherent growth property that is visible when specimens are cut perpendicular to the length of the tusk. These Schreger lines create unique angles that distinguish between mammoth and elephant species. When concave angles that open to the inner area of the tusk are measured, mammoth ivory will show an average angle of less than 90°, while elephant ivory will show an average angle greater than 90°. Figure 10 shows elephant and mammoth specimens oriented with their concave angles opening to the inner area of the tusk. Their Schreger lines intersect at average angles of 109° and 69°, respectively. These can be compared to materials A and B. While material A did show perpendicular striations along the horizontal plane, the angles were not particularly organized or consistently measurable. However, material B had "engine-turned" striations at an average angle of 90° along this same plane.

Cabochons were cut from both types of resin, and the form of a small elephant tusk was carved out of material A (figure 11). The resins' low hardness allowed them to be quickly ground down for shaping, while their high toughness prevented any chipping or fracturing even on small details. The resins each consist of two components with slightly different hardness, which produces the engine-turned pattern. One difficulty is that when attempting to shape a smooth surface, the darker and lighter areas erode at different speeds, creating an uneven texture. This effect is minimized, though, at the prepolishing stage of the carving. The low melting point of the ivory imitations posed an added challenge during the polishing process. When attempting to polish with a compound applied to a felt

Figure 11. Three ivory imitations carved for this study. The tusk (52.23 ct) and the cabochon on the right (35.37 ct) were created from material A. The cabochon on the left (14.67 ct) was created from material B. Lapidary by Dylan Hand.

wheel, the resins can melt and deform relatively quickly.

Elephant ivory was first regulated under the Endangered Species Act in 1976, with more recent laws creating a near-total ban on its import and export. Laws regarding mammoth ivory vary by state. Ivory imitations are now commonly used in their place for furniture and musical instrument inlays, jewelry, and various accessories. Both resins are purportedly composed of spun polyester and are being produced in China.

Britni LeCroy and Dylan Hand

Cobalt-Coated SAPPHIRE

Recently, the New York laboratory received a bright blue stone for identification. The blue color closely resembled that of the highly desired cobalt spinel. Advanced testing procedures of Fourier-transform infrared (FTIR), ultraviolet/visible/near-infrared (UV-Vis-NIR), energy-dispersive X-ray fluorescence (EDXRF), and laser Raman spectroscopy were performed to aid in identification. FTIR revealed a corundum spectrum, but with an uncharacteristic rise in the 7000–5800 cm^{-1} region. Laser Raman spectroscopy confirmed corundum, and UV-Vis-NIR yielded a cobalt absorption spectrum similar to that of diffused cobalt spinel.

Magnification revealed the presence of a coating, which was responsible for the observed over-the-limits RI reading. The coating was easily detected by the speckled, uneven surface and lighter facet edges where the coating was damaged (figure 12). EDXRF identified the coating as cobalt, consistent with the UV-Vis-NIR absorption spectrum. The stone possessed typical heated sapphire inclusions, such as altered fingerprints and frosted crystals. In addition, Raman spectroscopy identified glass-filled surface-reaching cavities (figure 13).

Cobalt coating is already a known treatment of tanzanite to improve the blue color component, but GIA has not observed cobalt coating on sapphire in recent years (see Spring 1994 *G&G*, pp. 48–49). Unlike cobalt coating on tanzanite, which has been observed applied only to the pavilion, this coating covered the entirety of the sapphire. This highlights the possibility of cobalt coating on materials other than tanzanite to induce a more pronounced blue color.

Figure 12. Lighter facet junctions and a speckled surface are evidence of coating. Field of view 4.79 mm.

Because of its color, this material is most likely to be mistaken for cobalt spinel, which can easily be eliminated as a possibility through standard gemological testing with the polariscope and specific gravity. The stone tested was doubly refractive and had a specific gravity of 4.00, while spinel is singly refractive and has an SG of 3.60 (+0.10/–0.03). Although the RI was over the limit of

Figure 13. Glass-filled cavities on the sapphire's pavilion. Field of view 3.57 mm.

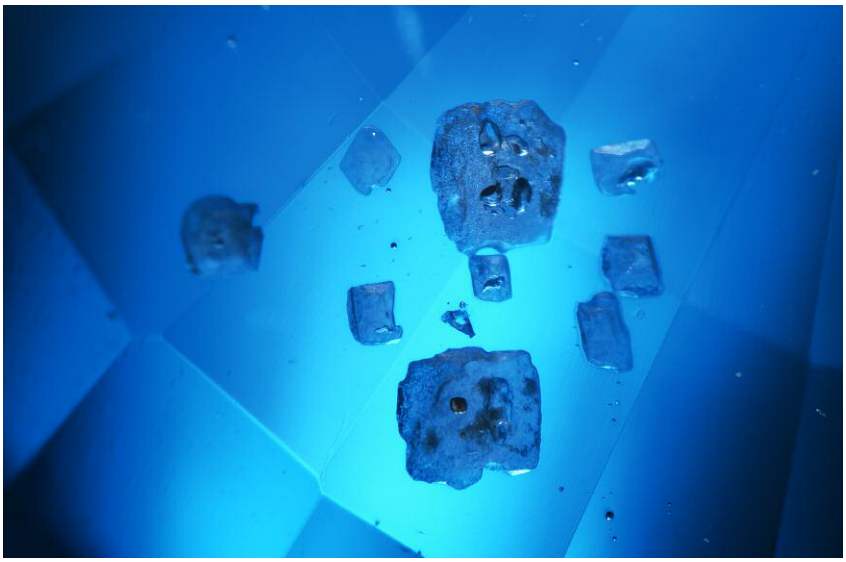

the refractive index liquid, the stone's specific gravity and doubly refractive nature point to sapphire. Advanced testing was useful in confirming the true identity of the stone and the coating.

Virginia Schneider and Jessica Jasso

Possible Natural Abalone SHELL Blister

An intriguing item was sent by KC Bell to GIA's Carlsbad laboratory for examination. Mr. Bell stated that it was found among a group of natural abalone pearls off the coast of Southern California in the Pacific Ocean. The sample (figure 14) weighed 3.00 ct, measured 10.73 × 8.82 × 6.23 mm, and was appealing because "pearl" layers appeared to have formed around a piece of rock. However, its natural or cultured origin and the mollusk species that produced it needed to be determined.

The sample consisted of two main components: an opaque dark body and a translucent cap formed of nacreous layers. The main body looked like a stone with a typical angular baroque shape expected of unfashioned natural material. The exposed areas exhibited a bumpy surface texture, and a strong fiber-optic light revealed a dark greenish bodycolor and some black areas of a different composition. Subsequently, Raman spectroscopic analysis with an 830 nm diode laser verified the dark greenish body was composed of a rock-forming feldspar mineral when the spectrum was matched with the RRUFF mineral database (RRUFF-R040129).

The thin layers partially covering the stone displayed vibrant blue, green, and purple-pink hues. At higher magnifications, a fine platelet structure was clearly visible, together with a characteristic underlying botryoidal-like structure that has been observed through the translucent surface layers of many abalone pearls (Fall 2015 Lab Notes, pp. 319–320). Raman analysis of the surface layers using a 514 nm argon-ion laser revealed peaks at 701, 705, and 1085 cm^{-1}, proving the nacre was composed of aragonite. In pearl testing, the higher excitation power of this laser is generally used in the identification of calcium carbonate polymorphs as well as natural pigments or artificial coloring agents. The 830 nm laser is used to obtain spectra in some situations, such as when high fluorescence is encountered with the 514 nm laser.

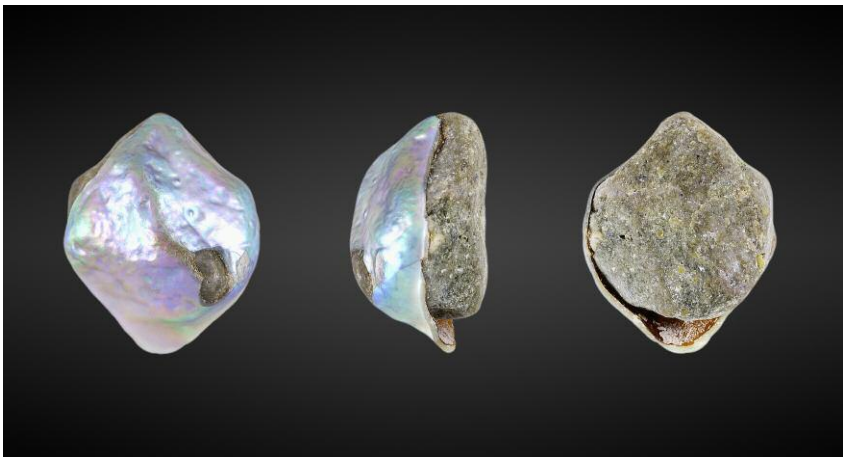

Figure 14. This intriguing abalone sample, shown in three different orientations, weighed 3.00 ct and measured 10.73 × 8.82 × 6.23 mm.

Energy-dispersive X-ray fluorescence (EDXRF) analysis showed that the nacreous surface layers contained low levels of manganese and confirmed a saltwater origin. Moreover, 221 ppm of iodine was detected, typical of many abalone shells and pearls since abalone is an iodine-rich organism (H.S. Doh and H.J. Park, "Speciation of bio-available iodine in abalone (*Haliotis discus hannai*) by high-performance liquid chromatography hyphenated with inductively coupled plasma-mass spectrometry using an *in vitro* method," *Journal of Food Science*, Vol. 83, No. 6, 2018, pp. 1579–1587). GIA has often detected iodine in abalone samples examined (Fall 2015 Lab Notes, pp. 319–320). Surface observation and chemical data confirmed that the nacre layers were produced by a univalve abalone gastropod (*Haliotis* genus), allowing us to confidently identify the mollusk species. Furthermore, EDXRF analysis of the rock surface revealed that it was composed of sodium-rich feldspar.

Closer examination of a small surface opening on the face of the sample (figure 15) and the edge of the nacre where it did not cover the underlying rock (figure 14, center and right) revealed a tight connection between the two main components. No gas bubbles or other features such as flow lines indicating an artificial bonding agent were observed in the translucent brown layer between them. The brown layer appeared to be an organic substance—likely conchiolin, an essential natural substance secreted by mollusks during the formation of pearls, blisters, and shells. The inter-

Figure 15. The overlying nacre tightly conformed to the underlying rock's surface, and a small opening was visible on the face, exposing the material beneath. A translucent brown layer between the two main components is possibly an organic substance, likely conchiolin. Field of view 7.19 mm.

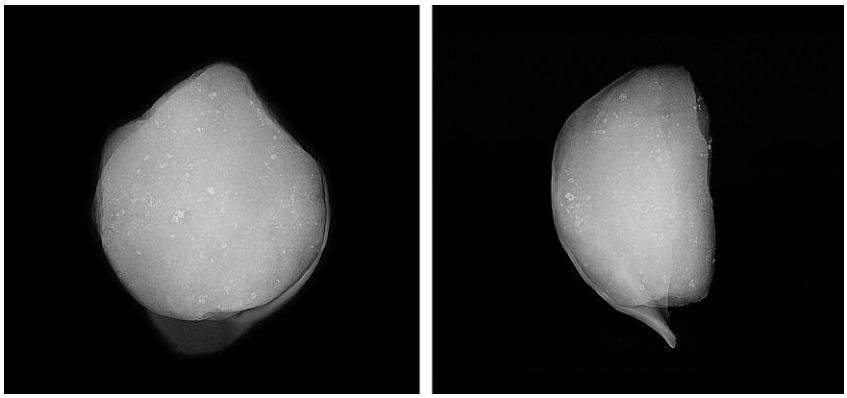

Figure 16. RTX images of the sample's face (left) and side (right) revealed that the thin nacre layer conformed very well to the underlying stone's surface.

nal structure revealed by real-time X-ray microradiography (RTX) supported the observational findings that the thin nacreous overgrowth adhered to the rock's surface in all directions and did not appear to have formed from any culturing process (figure 16).

Abalone are known to produce natural pearls and are also used commercially to produce cultured shell blisters in order to fashion assembled cultured blister "pearls" (mabe). Shell blisters can form naturally when a foreign object accidentally enters the mollusk's body and becomes trapped in between the shell's interior surface and the mantle tissue. If the mollusk survives this experience, the cells within the mantle tissue continue to secrete nacre (commonly biogenic aragonite) to increase the layers and cover the intruder, possibly to ease any discomfort. The intruder eventually becomes a part of the inner shell, resulting in a natural shell blister. Based on this formation mechanism and the gemological evidence obtained, this sample appears to be an unusual natural shell blister in which a small piece of rock acted as the irritant that initiated formation. Since abalone mollusks inhabit rocky areas and attach themselves to rocky surfaces, this scenario is not out of the question.

Artitaya Homkrajae

Large LABORATORY-GROWN STAR RUBY and SAPPHIRE

The Tokyo lab received for a Quality Assurance report two unusually large loose stones with asterism. One was a 4,759 ct red sphere (figure 17, left) with a diameter of approximately 76.96 mm, and the other a 467.2 ct blue cabochon measuring approximately 52.04 × 42.29 × 20.89 mm (figure 17, right).

These stones both had a spot refractive index of 1.77 and were doubly refractive with a uniaxial interference figure. The red sphere displayed a ruby spectrum with a handheld spectroscope. Microscopic observation showed curved bands of gas bubbles, cottony structure on the surface, and Plato striations (figure 18), providing proof of a laboratory-grown star ruby. The cottony structure indicates the possibility of diffusion treatment. The blue cabochon displayed a faint blue sapphire spectrum with the handheld spectroscope. It had a mottled blue color in diffused light (figure 19). Apparently it was a titanium-diffused colorless synthetic sapphire polished to produce asterism. As a result of polishing, the blue color is concentrated on the flat bottom and mottled on the curved top. This is visible when viewed from the side. Microscopic observation showed curved bands of gas bubbles, proof of laboratory growth.

As Schmetzer et al. summarized ("Dual-color double stars in ruby, sap-

Figure 17. A 4,759 ct synthetic star ruby and a 467.2 ct synthetic star sapphire were submitted to GIA's Tokyo lab.

Figure 18. Asterism seen on the surface and irregular grain boundaries (Plato striations). Field of view 11.4 mm.

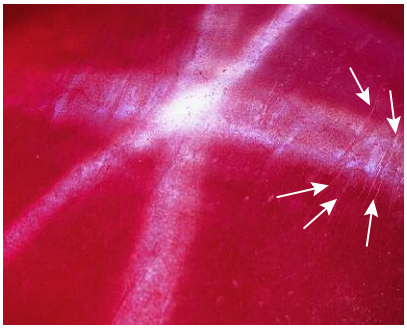

Figure 19. Mottled blue patterns were observed in the synthetic sapphire against transmitted illumination through a diffuser plate.

phire, and quartz: Cause and historical account," Summer 2015 *G&G*, pp. 112–143), the Czochralski pulling technique can produce large crystals. These crystals have a uniform distribution of color and titanium-bearing precipitates compared to other growth methods, and they can be cut from any part of the crystal, regardless of size. Therefore, this laboratory-grown star ruby was most likely produced by the pulling technique. Also, this specimen was too large to have been produced by flame fusion. Detailed information on these two items is not available, but they are probably similar products.

Synthetic star corundum is not rare, but these were among the largest laboratory-grown star rubies and star sapphires submitted to the GIA laboratory.

Masumi Saito and Yusuke Katsurada

LABORATORY-GROWN SAPPHIRE with Unusual Features

The Hong Kong laboratory recently examined a 14.36 ct pink-orange cushion mixed-cut specimen measuring 12.97 × 11.41 × 10.59 mm. Standard gemological testing yielded an RI of 1.760–1.768, a chromium emission line in red using a handheld spectroscope, strong red fluorescence under long-wave UV, and weak red fluorescence under short-wave UV. These properties were consistent with pink sapphire. Magnification revealed large fractures containing orange staining and some partially crystallized foreign material (figure 20). The foreign material partially crystallized in a dendritic pattern resembling that of diaspore (figure 21). Other natural-looking features included a twinning plane and tubules. Nonetheless, the observation of indistinct Plato lines and a slight curvature in the twinning plane raised suspicion about the stone's nature.

Figure 20. This 14.36 ct pink-orange synthetic sapphire contains large fractures with orange staining and some partially crystallized foreign material. Field of view 15.26 mm.

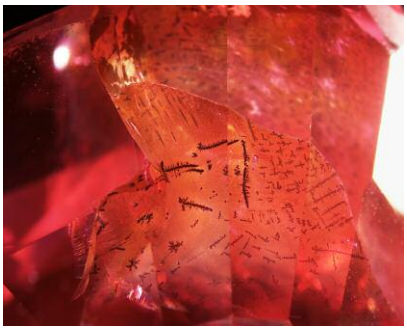

Figure 21. The foreign material partially crystallized in a dendritic pattern in the fractures, reminiscent of diaspore. Field of view 7.64 mm.

A strong red curved band observed in the DiamondView confirmed it was a Verneuil (flame-fusion) synthetic sapphire (figure 22). The absence of Ga, V, and Fe in the specimen, determined using laser ablation–inductively coupled plasma–mass spectrometry (LA-ICP-MS), provided further evidence supporting its synthetic nature. Ti was below detection limit in all six spots. Cr was below the detection limit in one spot and 37.61–44.31 ppma in five other spots.

Although flame-fusion synthetic sapphires are common in the marketplace, it is unusual to encounter a specimen containing such natural-looking orange staining and partially crystallized foreign material in the fractures. Careful observation as well as advanced testing are required for the correct identification of the natural or synthetic origin of such specimens.

Bona Hiu Yan Chow and Mei Mei Sit

VLASOVITE

The Carlsbad laboratory recently received for identification service a stone with properties that were not consistent with stones previously identified at GIA. This yellow octag-

Figure 22. The pink-orange specimen showed a strong red curved band in the DiamondView, confirming its identity as a flame-fusion synthetic sapphire.

Figure 23. This 1.20 ct octagonal modified brilliant was identified as the rare gem vlasovite.

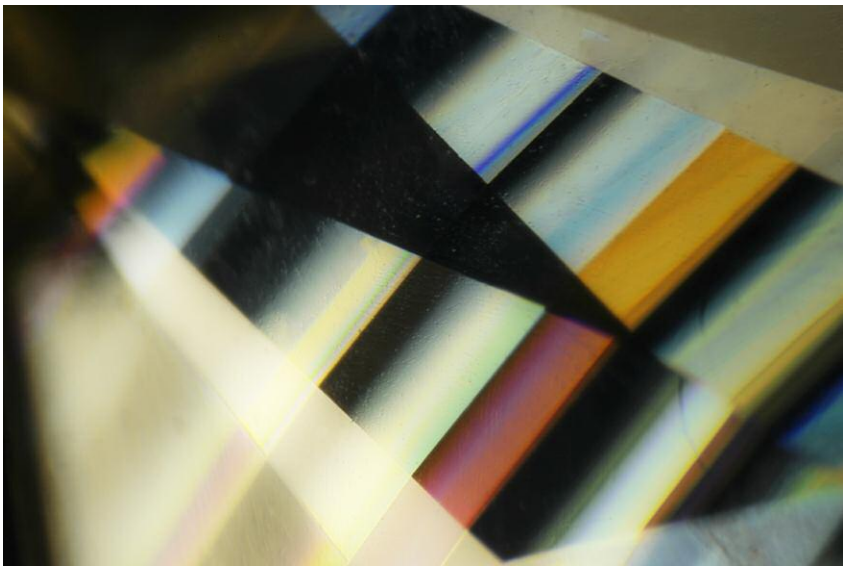

Figure 24. Colorful twinning planes were observed in the faceted vlasovite using polarized light. Field of view 3.23 mm.

onal modified brilliant (figure 23), measuring 6.41 × 5.26 × 4.68 mm, weighed 1.20 ct and had a specific gravity of 3.01. Microscopic features observed included distinct parallel twinning planes (figure 24), iridescent fractures, stringers, and fingerprints. Standard gemological testing revealed that it was doubly refractive, with a biaxial optic figure and a refractive index of 1.608–1.628. It fluoresced a very weak yellow under short-wave UV and had no reaction under long-wave UV. The Raman spectrum of the stone (figure 25) was matched to one in the RRUFF database, which confirmed the gem's identity as vlasovite, an inosilicate mineral with the chemical formula $Na_2ZrSiO_4O_{11}$ (rruff.info/vlasovite/R060913).

Vlasovite is known to be found in pegmatites in northern Russia, Canada, and Portugal. It was named after Kuzma Alekseevich Vlasov, who studied the region where vlasovite originated (handbookofmineralogy.com). Vlasovite is a rare mineral, and faceted stones are especially rare. This is the first faceted example examined at GIA's Carlsbad laboratory.

Jessa Rizzo

Figure 25. Raman spectroscopy confirmed the gem's identity as vlasovite.

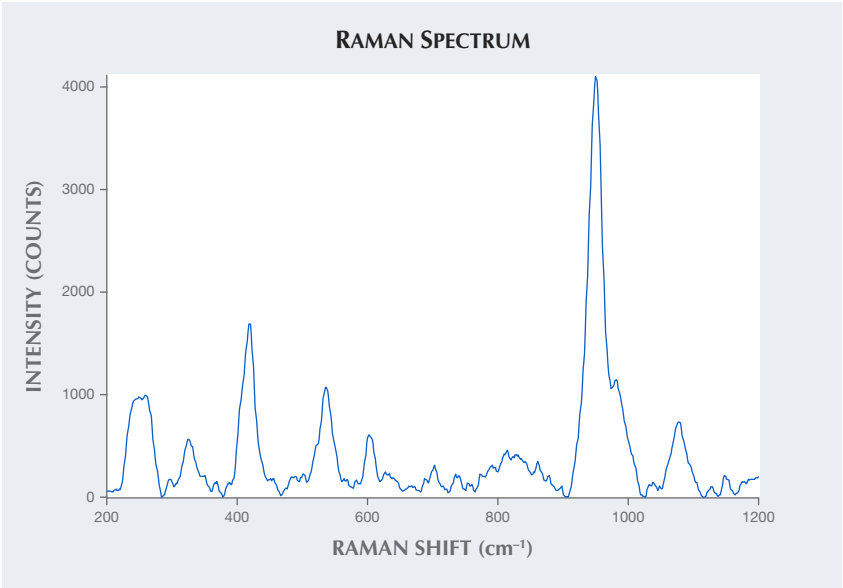

PHOTO CREDITS
Diego Sanchez—1, 3, 14, 23; Nathan Renfro—4; Maryam Mastery Salimi—5; Ungkhana Atikarnsakul—6, 7, 8; Dylan Hand—9, 10, 11; Britni LeCroy—10; Tyler Smith—12, 13; Artitaya Homkrajae—15; Shunsuke Nagai—17, 19; Masumi Saito—18; Moqing Lin—20, 21, 22; Jessa Rizzo—24

Rain Cloud in Alexandrite

An example of nature imitating nature was seen in a 0.73 ct faceted alexandrite showcasing an inclusion reminiscent of a rain cloud (figure 1). The "cloud" was composed of white particles oriented as parallel bands that displayed a cloud-like silhouette when viewed at an angle. The "rain" was composed of fine oriented reflective needles commonly referred to as silk. Fiber-optic lighting allowed for a concentration of white light to be seen under the cloud, creating an appearance of lightning. The inclusion scene observed in this gem is an interesting novelty that any gemologist can appreciate.

Britni LeCroy
GIA, Carlsbad

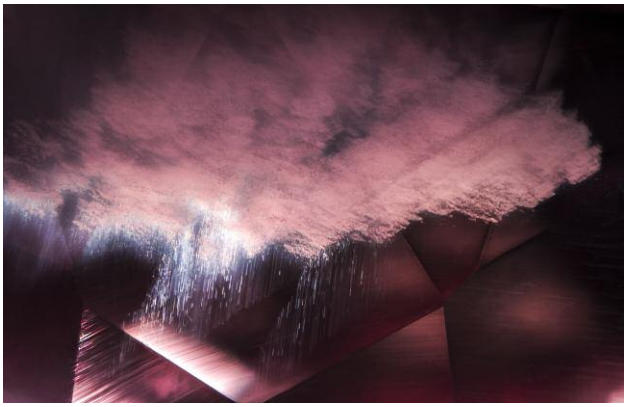

Figure 1. An alexandrite seen with fine milky particles and bands of silk resembling a rain cloud. Photomicrograph by Britni LeCroy; field of view 2.90 mm.

Conichalcite in Quartz Chalcedony

An interesting greenish blue cabochon of chalcedony was examined to determine the identity of some peculiar yellowish green inclusions. The bodycolor offered some clues, as the greenish blue variety of chalcedony, known as "gem silica," is commonly attributed to the copper mineral chrysocolla. Therefore, it was not a surprise when Raman spectrometry identified the yellowish green inclusions as another mineral that contained a significant amount of copper: conichalcite (figure 2).

Conichalcite, $CaCu(AsO_4)(OH)$, is a member of the adelite-descloizite group and occurs in colors from dominantly green to dominantly yellow, with either a yellow or green modifier. Conichalcite is reported to occur with chrysocolla from deposits in the United States (Utah, Arizona, and California), Germany, Peru, and Australia. This particular gem was reportedly from Concepcion Del Oro, Zacatecas, Mexico.

These vibrant inclusions were quite visually striking when seen along with their greenish blue host chalcedony. This is the first time the authors have identified inclusions of conichalcite in chalcedony.

Nathan Renfro and John I. Koivula
GIA, Carlsbad

Emerald in Rock Crystal Quartz

Rock crystal is a transparent and colorless macrocrystalline variety of quartz (SiO_2) that often has cavities containing liq-

About the banner: Fibers of actinolite radiate from a core crystal of chromite in a Russian demantoid garnet. These "horsetail" inclusions are common in demantoid from Russia. Photomicrograph by Nathan Renfro; field of view 1.53 mm. Courtesy of the John Koivula Inclusion Collection.

Editors' note: Interested contributors should contact Nathan Renfro at nrenfro@gia.edu for submission information.

Gems & Gemology, Vol. 55, No. 3, pp. 426–433.

Figure 2. Raman spectrometry identified the yellowish green inclusions in this chalcedony host as the copper mineral conichalcite. Photomicrograph by Nathan Renfro; field of view 7.20 mm.

uid and gas two-phase inclusions. Many different minerals also form as inclusions within rock crystal quartz. Typical varieties of included quartz for gem use are rutilated quartz, tourmalinated quartz, and strawberry quartz. Specimens may also contain several other types of mineral inclusions.

Recently, the author examined a 10.95 ct rock crystal quartz cabochon that contained elongate rod-shaped green crystals (figure 3). The green crystals showed hexagonal cross-section and were identified by Raman spectroscopy as beryl. Ultraviolet/visible/near-infrared (UV-Vis-NIR) spectroscopy showed a chromium (Cr) spectrum, which confirmed that the green crystals were emerald. This amazing inclusion has been previously reported in a rock crystal quartz specimen (Fall 2008 Lab Notes, p. 258), but this is the first time the author has examined a gem-quality rock crystal quartz cabochon with a perfectly hexagonal emerald crystal inclusion.

Figure 3. A prismatic emerald crystal within a rock crystal quartz. Photomicrograph by Nattida Ng-Pooresatien; field of view 12.5 mm.

Nattida Ng-Pooresatien
GIA, Bangkok

Iolite-Sunstone Intergrowth and Inclusions

At the GIA Carlsbad laboratory, the authors recently examined a cabochon of "bloodshot" iolite (containing red, eye-visible platelets of hematite) intergrown with a sunstone (figure 4). This material was reportedly sourced from India. Cordierite (iolite) and plagioclase feldspar is a common metamorphic mineral assemblage, and similar material reportedly from India has been documented in the past (Winter 1991 Gem News, pp. 261–262).

This "double" gem specimen displays a mixture of an attractive bluish violet dichroic color with red hematite platelet inclusions in the iolite half, combined with an orange aventurescence effect from numerous tiny copper-colored hematite platelets in the sunstone half.

Figure 4. An iolite-sunstone overgrowth crystal specimen. Photo by Kevin Schumacher.

Figure 5. This colorful inclusion scene showcases an anthophyllite crystal inclusion, which exhibits high transparency, several cleavage planes, and a thin/bladed prismatic crystal form. Photomicrograph by Jonathan Muyal; field of view 2.34 mm.

Viewing the stone under magnification offers an inclusion scene with a variety of well-formed hematite platelets, crystals, and liquid inclusions. Of particular interest was a fine elongated single-crystal inclusion of anthophyllite (figure 5).

The crystal shape of the anthophyllite could easily be mistaken for phlogopite, which has been documented in cordierite (E.J. Gübelin and J.I. Koivula, *Photoatlas of Inclusions in Gems*, Vol. 1, ABC Edition, Zurich, 1986, p. 268). In fact, several greenish brown prismatic phlogopite crystal inclusions were also observed inside the same specimen. Nevertheless, the anthophyllite crystal was conclusively identified by Raman microspectrometry analysis. The anthophyllite crystal inclusion showed a bladed prismatic crystal form, orangy yellow color, transparency, and several cleavage planes.

Although amphibole mineral inclusions have been documented extensively, distinct prismatic anthophyllite crystal inclusions are very rare and few references are found in the literature. Anthophyllite is more common in lamellar or fibrous form, classified as asbestos.

This combination iolite-sunstone specimen and its inclusions offer a unique visual composition that makes it a desirable piece for a gem collection.

Jonathan Muyal and Paul Mattlin
GIA, Carlsbad

Merelaniite in Gem Diopside from Merelani, Tanzania

A recent Micro-World entry (Summer 2018 *G&G*, pp. 226–227) described merelaniite occurring as dense inclusions in a tanzanite cabochon and as inclusions in two gem tanzanite crystals. While the Merelani tanzanite mines have also become well known for green diopside in recent years, in July 2019 the authors observed, for the first time, dense inclusions of fine merelaniite whiskers in gem-quality yellow-green, prismatic diopside crystals (figure 6, left).

Seven merelaniite-included diopside crystals, reportedly mined in 2018 and obtained by one of the authors (WR),

Figure 6. Left: Prismatic diopside crystal (1.5 cm tall) included with abundant merelaniite whiskers, associated with graphite at the termination, and aggregates of radiating white acicular mesolite crystals on some prism faces. Photo by Tom Stephan. Top right: Close-up of the merelaniite inclusion (field of view ~8 mm), viewed through one polarizer to reduce the effects of diopside's birefringence. Bottom right: Detail of some of the merelaniite inclusions showing spindle structures due to non-uniform layer growth around the whisker axes (field of view 1.5 mm). Photomicrographs by J.A. Jaszczak.

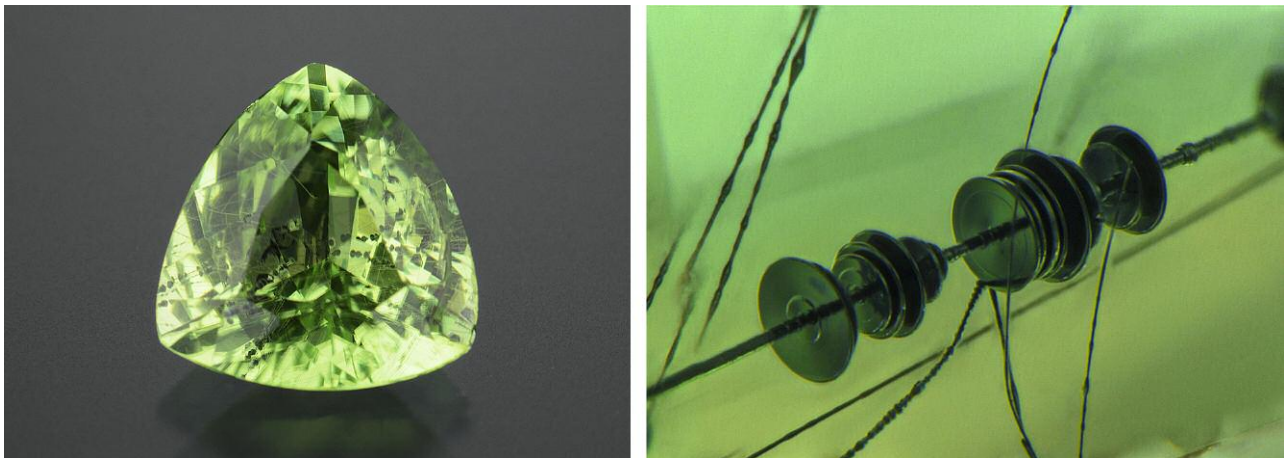

Figure 7. Left: A 1.35 ct faceted gem diopside containing merelaniite inclusions. Photo by Diego Sanchez. Right: Close-up of wheel and whisker morphology of the included merelaniite. Photomicrograph by Nathan Renfro; field of view 1.03 mm. Stone courtesy of Bill Vance.

ranged in size from approximately 1 to 5 cm long. Apart from the merelaniite inclusions, all but the largest had excellent clarity, although one 1.7 cm crystal was so densely filled with merelaniite that half of the sample appeared very dark. Similar to the inclusions observed in tanzanite, the merelaniite inclusions in diopside were predominantly cylindrical whiskers with metallic luster and variable diameters and lengths. The longest whiskers in the largest diopside spanned up to 2 cm (figure 6, top right), and many extended to the surface, where they terminated. Some of the merelaniite whiskers showed a spindle- or wheel-type structure with diameter that varied along the axis of even a single whisker (figure 6, bottom right). Some ribbon-like inclusions also occurred that were likely merelaniite. All of the diopsides were also associated with white spheroidal clusters of radiating acicular mesolite crystals, while several crystals were associated with graphite and one was associated with a transparent blue fluorapatite crystal.

While reviewing an earlier version of this report, GIA's Nathan Renfro made the connection between these included diopside crystals and a faceted Merelani diopside gemstone (figure 7, left) containing dark whisker inclusions. Author JIK obtained that diopside from Bill Vance, the stone's cutter, in approximately 2012. The whiskers in this 1.35 ct stone, some of which were surrounded by remarkable dark circular growths (figure 7, right), have also been confirmed by Raman spectroscopy as merelaniite.

Werner Radl (mawingugems@yahoo.de)
Mawingu Gems
Idar-Oberstein, Germany

John I. Koivula

John A. Jaszczak (jaszczak@mtu.edu)
Michigan Technological University
Houghton, Michigan

Dravite from Mozambique with an Abundance of Pyrite Inclusions

In the summer of 2017, author JP encountered a parcel of transparent yellow to brownish yellow tourmalines at the gemstone market in Chanthaburi, Thailand. The six faceted tourmalines shown in figure 8 revealed properties consistent with tourmaline. LA-ICP-MS analysis was performed to determine their major chemical components, which were: 11.56–12.31% MgO, 9.98–10.34% B_2O_3, 2.62–

Figure 8. Six yellow to brownish yellow faceted dravite tourmalines (0.47–2.8 ct) from Mozambique, many of which contained distinct metallic inclusions of pyrite. Photo by Weizhi Huang.

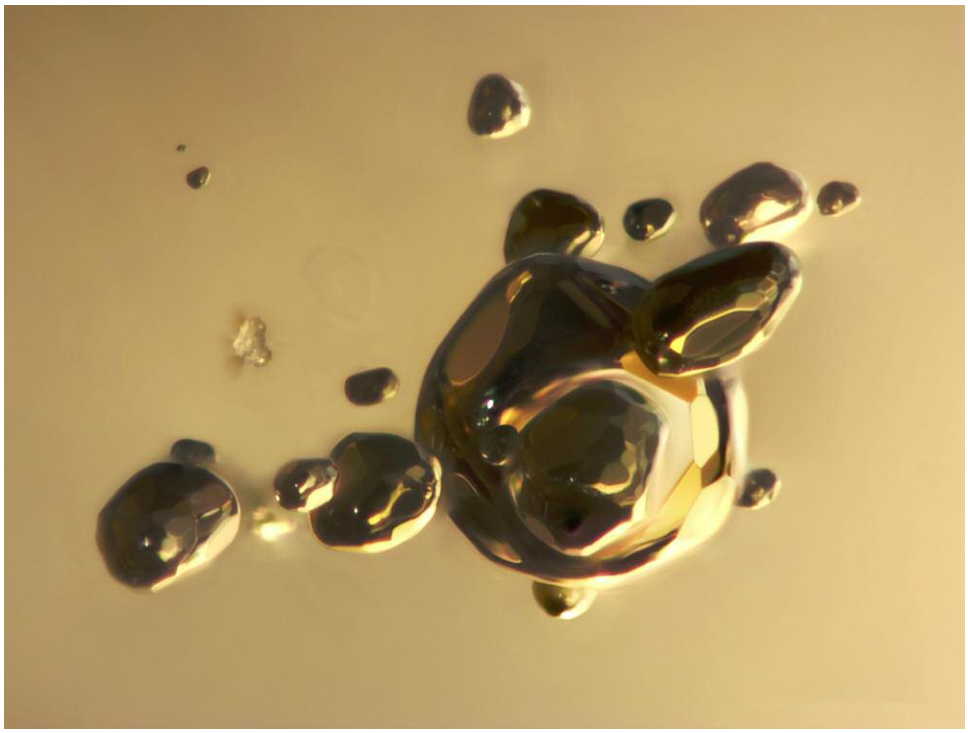

Figure 9. The dravites contained distinctive inclusions of pyrite, which were confirmed by Raman spectrometry. Photomicrograph by Weizhi Huang; field of view 0.8 mm.

2.82% Na_2O, 0.68–1.06% CaO, 0.17–0.45% TiO_2, and 0.11–0.25% FeO (total iron). Minor amounts of Li, K, V, Cr, Mn, Zn, Ga, and Sr were also detected, indicating dravite tourmaline.

These dravites were noteworthy for their numerous euhedral pyrite crystal inclusions (figure 9), confirmed by Raman. This was previously reported without Raman analysis (see Spring 2007 GNI, pp. 73–75). This is the first time the authors have seen so many intact pyrite crystals in yellow to brownish yellow gem-quality dravite from Mozambique.

Weizhi Huang and Jingcheng Pei
Gemmological Institute, China University of Geosciences Wuhan

Dislocation Chain in Oregon Sunstone

The author recently examined a high-quality faceted orangy red Oregon sunstone weighing 6.77 ct. Examined under magnification with fiber-optic illumination, the stone displayed an unusual inclusion that consisted of a decorated dislocation string (figure 10). Copper exsolution platelets, which are common in Oregon sunstone, were also observed. In this example, the decorated dislocation followed a rectangular pattern, consistent with the crystal structure of the host feldspar. This unique light-scattering dislocation chain is the first that the author has encountered in Oregon sunstone.

Jessa Rizzo
GIA, Carlsbad

Tourmaline Inclusion in Russian Alexandrite

Alexandrite is the color-change variety of the mineral chrysoberyl. The most coveted alexandrite exhibits a luscious green to greenish blue color in daylight and a warm raspberry red in incandescent light. This phenomenal color change is caused by the presence of trace Cr^{3+} substituting for Al^{3+} in the chrysoberyl crystal structure. Alexandrite was originally found in the Ural Mountains of Russia in

Figure 10. This orangy red Oregon sunstone contained an interesting decorated dislocation that was visible using fiber-optic illumination. Photomicrograph by Jessa Rizzo; field of view 4.79 mm.

Figure 11. The longest inclusion in this photomicrograph of a Russian alexandrite was conclusively identified as tourmaline. This tourmaline inclusion exhibits a well-formed prismatic/rod-like crystal shape. Darkfield illumination. Photomicrograph by Jonathan Muyal; field of view 1.44 mm.

the early nineteenth century and was named in honor of Czar Alexander II.

GIA recently examined several Russian alexandrite rough specimens. These were reportedly from the Tokovaya mining area in the Ural Mountains, located a few kilometers away from the city of Yekaterinburg. Closer microscopic examination revealed a brown, transparent, well-formed prismatic crystal inclusion with triangular termination, indicating it might belong to the trigonal crystal system (figure 11).

The inclusion proved to be doubly refractive when viewed between crossed polarizers. Raman microspectrometry analysis conclusively identified the inclusion as tourmaline. In order to validate the Raman results and further identify the tourmaline species, laser ablation–inductively coupled plasma–mass spectrometry (LA-ICP-MS) was used to obtain the chemistry of the inclusion (Z. Sun et al., "A new method for determining gem tourmaline species by LA-ICP-MS," Spring 2019 *G&G*, pp. 2–17). It was classified as dravite, a sodium- and magnesium-rich tourmaline species. The trace element chemistry of the host alexandrite matched well with GIA's Russian alexandrite chemistry reference data.

Inclusions in alexandrite from various localities have been reported (E.J. Gübelin and J.I. Koivula, *Photoatlas of Inclusions in Gemstones*, Vol. 1, ABC Edition, Zurich, 1986, pp. 265–267; Vol. 3, Opinio Publishers, Basel, Switzerland, 2008, pp. 372–405). However, tourmaline in an alexandrite host is rare.

Alexandrite is traditionally popular for its beautiful color-change phenomenon rather than its inclusion scenes. The fine tourmaline crystal inclusion in this Russian alexandrite makes it an unusual collector's gem specimen.

Jonathan Muyal and Ziyin Sun
GIA, Carlsbad

Phenakite with Tourmaline Inclusion Containing Spiral Growth

A helix stands in high relief against the orangy pink of a well-defined tourmaline crystal—impressive screw dislocation growth is one of the main identifying characteristics detailing the inner world of a phenakite specimen from Ambohimanambola, Madagascar (figure 12).

Previously in the collection of longtime California mineral collector Kay Robertson, the unique inclusions in this gem were discovered during digitization for the Los Angeles Museum of Natural History's Gem and Mineral Lab. After spotting a series of parti-color tourmaline needles with vivid interference patterns under crossed polarizers, magnification was subsequently increased to investigate further. Soon it became clear that the needles scattered throughout the phenakite crystal exhibited strongly pleochroic colors as well as distinctive growth features.

In the absence of polarized light, the needles appeared in desaturated orange to red and green to blue hues. When magnification was increased once again, the eclectic world of this phenakite unveiled another surprise: The tourmaline inclusions were not alone. Alongside and extending from the base of the striated needles were colorless euhedral crystals exhibiting hexagonal form and inclusions of their own. One pair of primary inclusions, a needle anchored to another stubby crystal, were of particular interest. Raman spectroscopy confirmed the identity of the needle-like inclusions as tourmaline, though it was not possible to confirm the identity of the colorless crystal.

The pictured set of inclusions features an orangy pink tourmaline emerging from the body of a colorless crystal. The host specimen's high clarity highlights the growth fea-

Figure 12. A phenakite specimen from Ambohimanambola, Madagascar, contained a tourmaline with a spiral growth feature and a colorless crystal. Photomicrograph by Kimberly Abruzzo; field of view 0.88 mm.

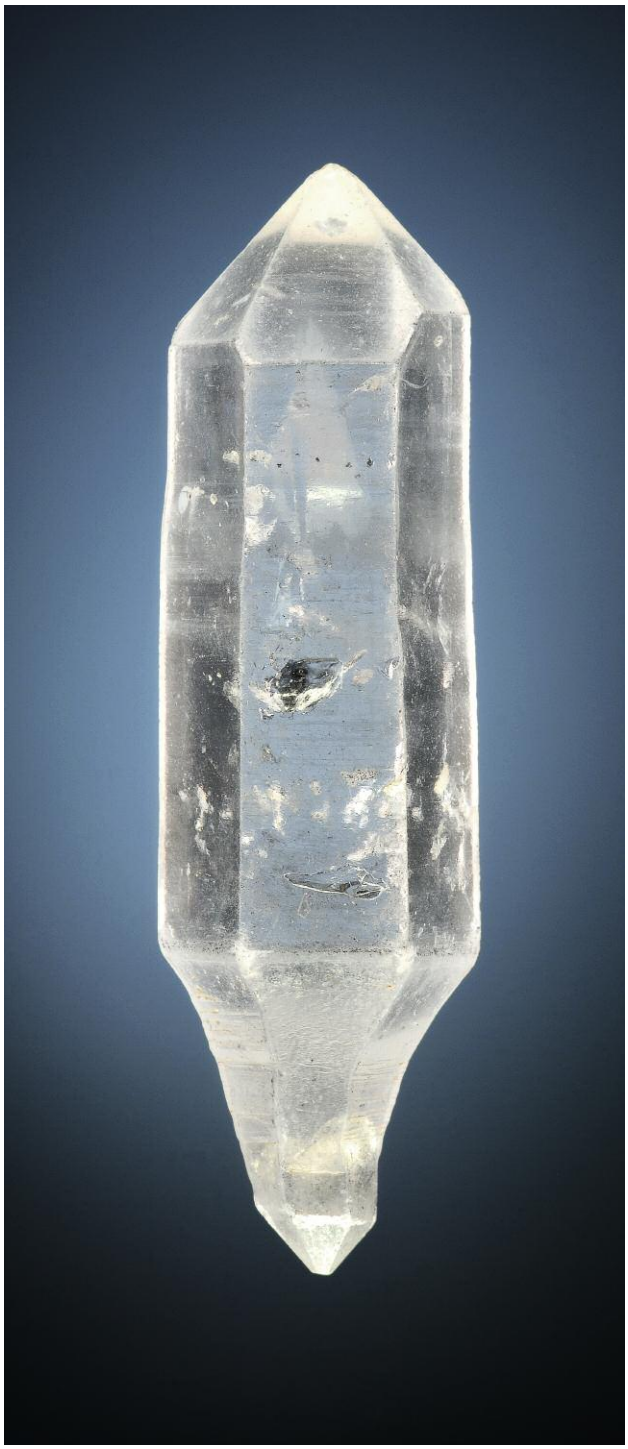

Figure 13. This doubly terminated scepter quartz crystal from Sichuan, China, weighs 200.28 ct and measures 75.03 mm in length. Photo by Diego Sanchez.

tures both inside and on the surface of its inclusions, not only showing striations parallel to the c-axis typical of tourmaline, but also more unusual "spiral" or screw dislocation growth. The entwined pair are crossed in the background by two larger dark greenish blue tourmaline needles that provide a striking geometric backdrop. Dislocation spirals like those seen here are formed when planes of atoms within a gemstone's crystal lattice are displaced during growth and rearrange themselves in a helical pattern corresponding to the direction of stress.

Perhaps best known for their intricate liddicoatite crystals, the Anjanabonoina pegmatites in Madagascar also produce a wide array of other gem minerals such as phenakite, beryl, spodumene, and danburite, among others. This particular stone presents an excellent example of the diverse mineralization that occurs at Anjanabonoina, showing off the habit, optical properties, and growth features of two important gem silicates from this gemologically important locality.

Kimberly Abruzzo
Natural History Museum of Los Angeles County

Quarterly Crystal: "Ball Bearing" in Quartz

Quartz crystals with three-phase fluid inclusions from the Jinkouhe mine in the Sichuan Province of China have been sold for many years at gem and mineral shows such as those held annually in Tucson, Arizona. Unfortunately, many of those crystals are damaged due to the mining methods used and the packing together of numerous crystals for transport. Good terminations on those crystals are few and far between, and the edges are generally chipped, while the broad flat crystal faces are often scratched and abraded.

So it was with high interest that we examined the relatively large doubly terminated scepter rock crystal quartz shown in figure 13. At 200.28 ct and measuring 75.03 × 21.76 × 17.98, this crystal was much larger than most others from the Jinkouhe mine. It was preserved in its own

Figure 14. Nomarski differential interference contrast revealed light etching on the prism faces of the quartz crystal. Photomicrograph by Nathan Renfro; field of view 0.72 mm.

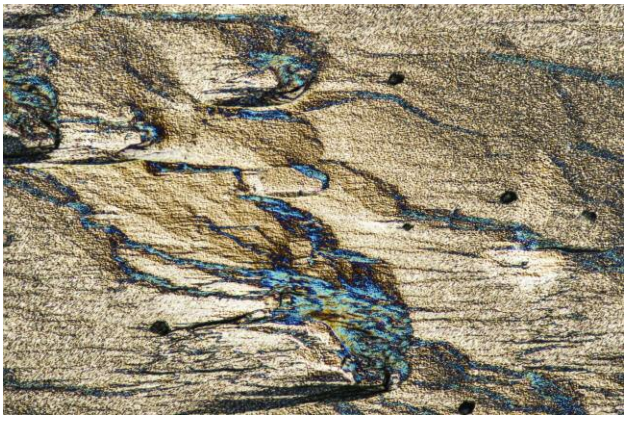

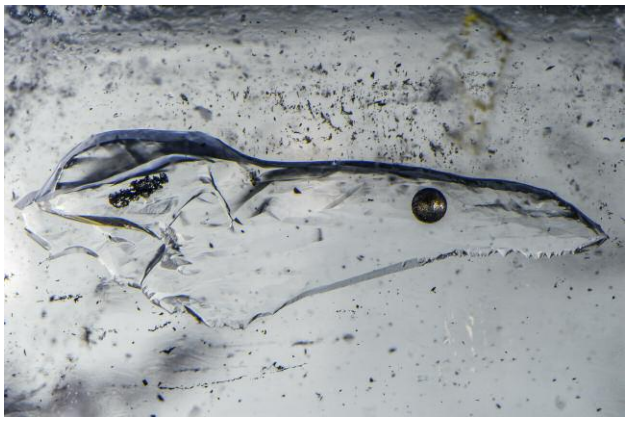

Figure 15. In this image, the silver-gray bubble can be seen at the right side of the liquid-filled void. The coating gives it the appearance of a small ball bearing. Photomicrograph by Nathan Renfro; field of view 7.42 mm.

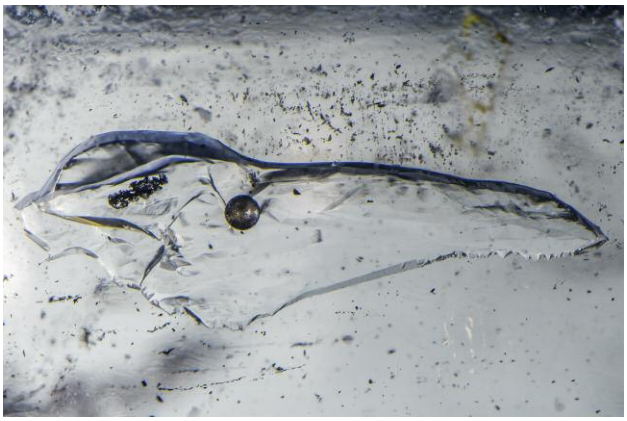

Figure 16. The metallic-looking bubble has floated toward the left end of the fluid inclusion chamber. Photomicrograph by Nathan Renfro; field of view 7.42 mm.

cotton-lined box, and as shown in figure 13, essentially undamaged.

Microscopic examination of the crystal revealed light etching on the prism faces (figure 14), which was highlighted using Nomarski differential interference contrast. Internally there were several primary fluid inclusions, with typical black organic compounds as the solid phase. One fluid inclusion in particular contained a gas bubble (figure 15) that moved freely across the entire length of the void (figure 16). The bubble was coated with a metallic-looking substance that gave it the appearance of a small stainless steel ball bearing. We could not identify the coating but suspect that it was an organic compound.

John I. Koivula and Nathan Renfro

Gem News International

Contributing Editors
Emmanuel Fritsch, *University of Nantes, CNRS, Team 6502, Institut des Matériaux Jean Rouxel (IMN), Nantes, France* (fritsch@cnrs-imn.fr)
Gagan Choudhary, *Gem Testing Laboratory, Jaipur, India* (gagan@gjepcindia.com)
Christopher M. Breeding, *GIA, Carlsbad* (christopher.breeding@gia.edu)

COLORED STONES AND ORGANIC MATERIALS

Blue gahnite from Nigeria. In recent years, Nigeria has gained considerable attention in the gem trade for the discovery of sapphires reportedly from the Mambilla Plateau in Taraba State. In addition to sapphires, spinels have been sporadically mined in Jemaa and recently in Kagoro, both in Kaduna State (figure 1). The spinel group of minerals, with a general chemical formula AB_2O_4, has a total of 22 different species. Four of these species have Al predominantly occupying the octahedral site: spinel ($MgAl_2O_4$), galaxite ($MnAl_2O_4$), hercynite ($FeAl_2O_4$), and gahnite ($ZnAl_2O_4$). The spinels from Kagoro have been identified as gahnite, the zinc end member. Gahnite is one of the rarer members of the spinel group of minerals, typically found at zinc deposits. Most crystals are very small, included, and translucent to opaque. Faceted gems are very collectible due to their rarity and color.

The geology of the Nigerian spinels has been previously studied (R. Jacobson and J.S. Webb, "The pegmatites of central Nigeria," *Geological Survey of Nigeria Bulletin*, No. 17, 1946, pp. 1–61), and the deposits can be subdivided into three groups based on their mineralogy: (1) microcline-quartz pegmatites, which commonly occur within the calc-alkaline granitoids and are rarely mineralized; (2) microcline-quartz-mica pegmatites, found within metasedimentary sequences; and (3) quartz-mica veins, which occur in schists and gneisses or marginal to group 2 pegmatites. Gahnite occurs in groups 2 and 3. Knowledge of the composition of zinc-rich spinels is useful in separating a wide variety of source environments. For example, Zn content is high in spinels occurring in rocks that have experienced low-grade metamorphism and high oxygen and sulfur fugacity (fO_2 and fS_2), whereas Zn content is lowest in high-grade metamorphic rocks (A. Heimann et al., "Zincian spinel associated with metamorphosed Proterozoic base-metal sulfide occurrences, Colorado: A re-evaluation of gahnite composition as a guide in exploration," *Canadian Mineralogist*, Vol. 43, No. 2, 2005, pp. 601–622).

Figure 1. Three single octahedra of natural gahnite, approximately 1.5 ct each, from Kaduna State, Nigeria. Photo by Robison McMurtry.

Standard gemological examination of three rough octahedra (figure 1) gave the following properties: color—blue; pleochroism—none; refractive index—1.791 to over the limit (flat reading from polished crystal face); hydrostatic specific gravity—4.180–4.294; fluorescence reaction—inert to both long- and short-wave UV; and color filter reaction—red. Internal characteristics observed with a gemological microscope were colorless unidentified crystals, fingerprints, and a red-brown crystal inclusion identified by Raman spectroscopy as sphalerite (figure 2).

Editors' note: Interested contributors should send information and illustrations to Stuart Overlin at soverlin@gia.edu or GIA, The Robert Mouawad Campus, 5345 Armada Drive, Carlsbad, CA 92008.

Gems & Gemology, Vol. 55, No. 3, pp. 434–455.

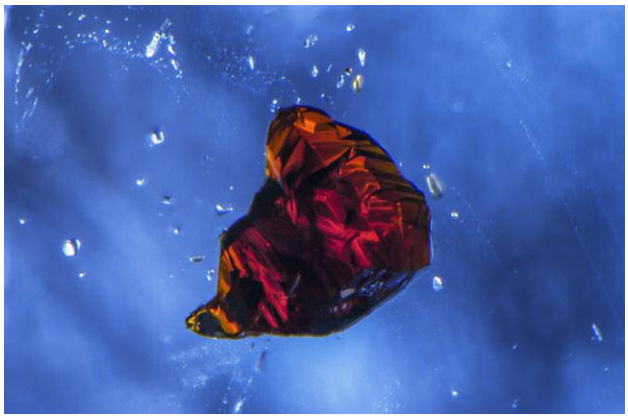

Figure 2. Raman identification of this inclusion was consistent with sphalerite. Photomicrograph by Nathan Renfro; field of view 0.91 mm.

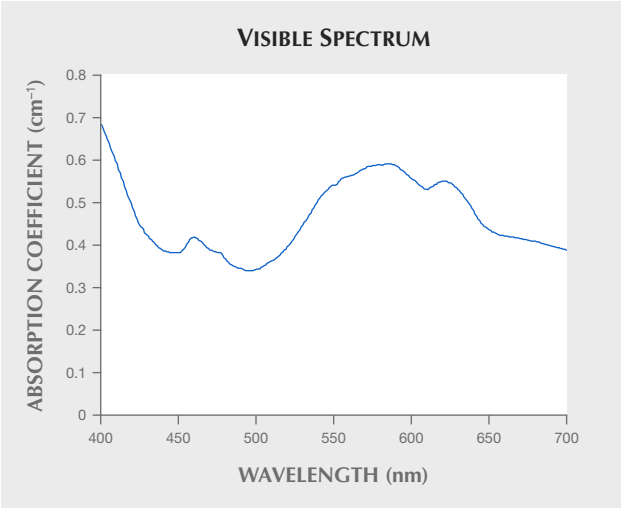

Figure 3. The visible spectrum of the Nigerian gahnite from Kagoro. The absorption bands from ~500 to 650 nm are largely due to Co^{2+}, but with modification from iron absorption bands. Absorption bands around 462 and 470 nm are related to iron chromophores.

Advanced spectroscopic testing was performed on the three samples. The Raman spectra were typical of gahnite, with peaks at 420, 510, and 661 nm. The visible spectrum showed significant cobalt absorption bands (figure 3) between 500 and 620 nm, with additional contribution from iron absorption bands modifying the cobalt absorption spectrum (e.g., A.C. Palke and Z. Sun, "What is cobalt spinel? Unraveling the causes of color in blue spinels," Fall 2018 *G&G*, pp. 262–263).

Figure 4. A vertical line 1 and a horizontal line 2, containing a total of 44 spots, were selected to apply LA-ICP-MS analyses across the whole section. Mol.% end member vs. position profiles revealed that the stone was predominantly composed of gahnite with minor hercynite, spinel, and galaxite. Detailed information on major element chemistry, site distribution, and species for each spot can be found in appendix 1 online. Spot spacing is 200 microns.

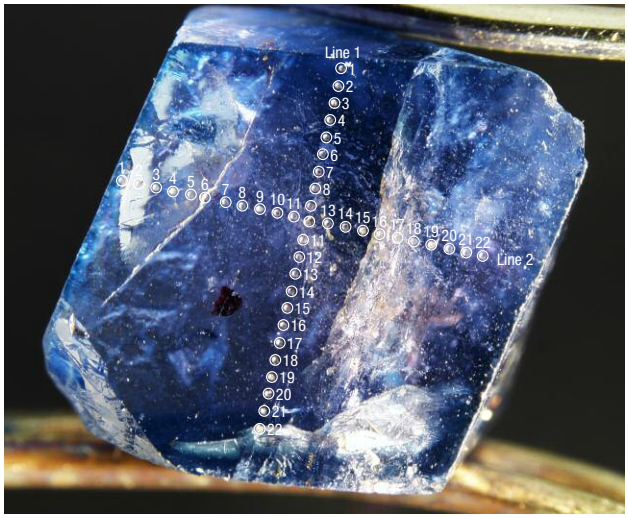

Laser ablation–inductively coupled plasma–mass spectrometry (LA-ICP-MS) analysis was used to obtain the accurate chemistry of the three stones. The chemical composition was acquired by a ThermoFisher iCAP Q ICP-MS coupled with an Elemental Scientific Laser NWR213 laser ablation system. NIST 610 and 612 were used as external standards, and ^{27}Al was used as an internal standard. LA-ICP-MS results (see appendix 1 at https://www.gia.edu/doc/FA19-GNI-Appendix1.xls) showed that the three stones were predominantly composed of more than 90 mol.% gahnite ($ZnAl_2O_4$), with minor other end members of Al-spinel species. They should thus be classified as gahnites.

To better understand the composition of this type of spinel, we prepared a cross-section cut from the middle of one octahedral crystal, sample NBS3 (figure 4). A vertical line of 22 spots (figure 4, line 1) and a horizontal line of 22 spots (figure 4, line 2) were selected to cross the whole section from outer rims to the opposite outer rims for LA-ICP-MS analyses. All the spots showed more than 90 mol.% gahnite with hercynite as the second most abundant species (figure 5). Spots near the outer rims contained more hercynite than spots on the inner rims and core. The mol.% end member distribution was very consistent throughout the whole section. Nine trace elements for each spot in lines 1 and 2 were plotted in figure 5. In general, the outer rims had higher concentrations of V and Co but lower concentration of Ni than the inner rims and core.

Maxwell Hain and Ziyin Sun
GIA, Carlsbad

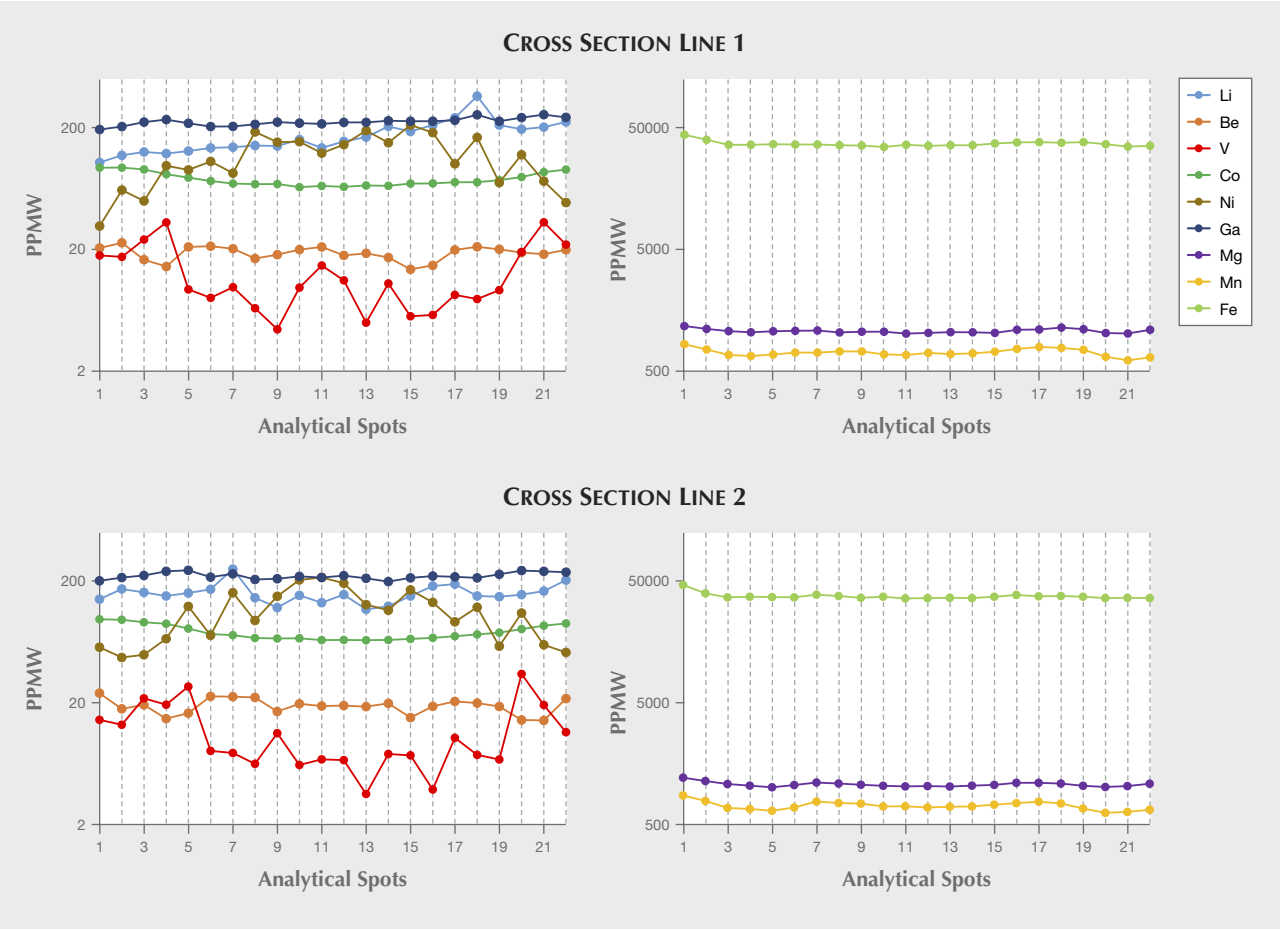

Figure 5. Trace element vs. position profiles revealed that the outer rims had higher concentrations of V and Co, but lower concentration of Ni than the inner rims and core. Detailed information on trace elements for each spot in lines 1 and 2 can be found in appendix 2 online (https://www.gia.edu/doc/FA19-GNI-Appendix2.xls).

Emerald update with Arthur Groom. At the 2019 AGTA GemFair in Tucson, Eternity Natural Emerald (Ridgewood, New Jersey) had emeralds up to 50 ct on display. Eternity's president, Arthur Groom, noted that the Afghanistan emerald melee sets (figure 6) had drawn the most interest. This rough melee is particularly attractive, he said, because of its higher brilliance than stones from other sources. "The Afghanistan melee is the brightest in its natural state when it's cut properly," he said. "Afghanistan emerald will rival Colombian any day of the week."

Figure 6. Melee goods from Eternity Natural Emerald. Photo by Kevin Schumacher.

Eternity has experimented with melee from different sources but finds Afghanistan melee the most plentiful and consistent. The company currently cuts Afghanistan emeralds in sizes from 1 mm to 70 ct, disproving the perception in the trade that the country produces only small emeralds. Groom pointed out that vibrant greens are not as easy to find in gems as other colors, and tsavorite is often used for green, but Eternity's emeralds offer the option to use one of the "Big Three" gemstones. Eternity also sources emerald rough from Ethiopia, Colombia, Brazil, and Zambia.

Cutting and mounting emerald melee has traditionally been challenging because of emerald's tendency for inclusions and fractures, and its typical enhancements. Most

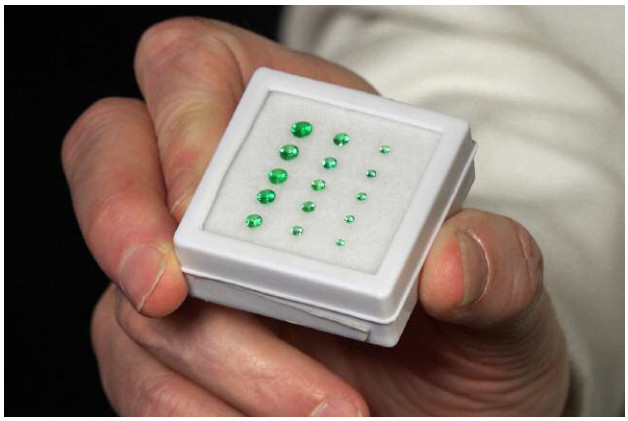

Figure 7. A set of 15 of Eternity Natural Emerald's calibrated emeralds ranging from 1 to 5 mm. Photo by Albert Salvato.

jewelry manufacturers do not like working with it, Groom said. Eternity has solved this problem after many years of effort, he said, producing "a finely made emerald that you can work with confidence and will never change." Eternity's enhancement process allows the stones to be cleaned in ultrasonic and steam cleaners with no adverse effects (traditional enhancement substances tend to alter over time).

Eternity has cut thousands of carats of rough and developed master sets of colors and clarities. They are able to fulfill orders for thousands of stones at a time. The emeralds are cut to exact proportions; the average weight retention is about 15 percent. "You can't be concerned with how much weight you'll lose," Groom said. In the past, manufacturers would buy a parcel of stones of different sizes, dimensions, and colors and find some stones unusable, but they can now buy stones of the same color, clarity, and size. Along with melee, the company offers cabochons and calibrated (figures 7 and 8) and faceted stones, in qualities from commercial-grade to very fine and at all price points. Groom showed us a set of calibrated emeralds (figure 8) ideal for a premium bracelet.

One of Eternity's aims is to promote Afghanistan emerald and country of origin. "The miner has to benefit from this," Groom said, "and this is one of our goals in Afghanistan." In our 2013 interview with Groom, he said Afghanistan's emerald resources are such that if the country were to see peace, acquire investors, and mechanize its mining operations, it would "outproduce the world."

Groom believes in promoting country of origin not because it adds value but because it adds identity to the stone. "We all know about Colombian emerald," he said. "But just because the emerald comes from Colombia doesn't make it more valuable. We just manufactured a 24 ct Tajik stone that sold for close to half a million dollars. You have to take the stone on its merit."

Duncan Pay and Erin Hogarth
GIA, Carlsbad

Figure 8. A set of calibrated emeralds (approximately 2 to 4 mm each) by Eternity Natural Emerald. Photo by Kevin Schumacher.

New find of deep blue aquamarine from Nasarawa State in Nigeria. The most unusual and exquisite things are often found in unexpected places. This has been seen in the explosion in gem discoveries in East Africa since the latter part of the twentieth century. However, West Africa has remained relatively underexplored, despite the development of some promising and productive gem deposits, including sapphire and Paraíba tourmaline in Nigeria. West Africa's gemological horizons expanded earlier this year with the find of a small batch of aquamarine with exceptionally deep and saturated color (figure 9). Reportedly found in Nasarawa State, the stones were recovered by small-scale artisanal miners whose workings reached only the near-surface exposure of a weathered pegmatite body. Mining was short-lived, starting likely in January and ending in May 2019, when the miners exhausted the surface deposit but lacked resources to continue with hard-rock mining once they hit bedrock. Through a local buyer in the Abuja market, author JH was able to obtain a large parcel that may account for the lion's share of the production from this deposit to date. This parcel amounted to 763 grams, of which 200 grams would cut stones over one carat.

Standard gemological testing showed properties consistent with aquamarine, with a uniaxial negative optic character, a refractive index of 1.582–1.590, a birefrin-

Figure 9. Nigerian aquamarine from a new find in Nasarawa State. The faceted stones range from 1.55 to 2.63 ct. Photo by Kevin Schumacher.

Figure 10. Two wafers of the new Nigerian aquamarine in unpolarized light (left), and with light polarized along the extraordinary ray (center) and along the ordinary ray (right). Photos by Aaron Palke.

gence of 0.008, and a specific gravity of 2.71–2.73. The stones were inert under short-wave and long-wave UV light. The most exceptional feature of this new find of aquamarine—besides its attractive, saturated blue color—is its unusually strong pleochroism, going from deep, saturated blue with light polarized parallel to the extraordinary ray to an unsaturated (almost colorless) greenish blue with light polarized parallel to the ordinary ray (figure 10). The origin of this extreme pleochroism is seen in the UV-Vis spectra (figure 11), in which the main feature is a highly polarizable broad absorption band at approximately 680 nm caused by Fe^{2+}-Fe^{3+} intervalence charge transfer (IVCT). This IVCT absorption is the cause of blue coloration in (non-Maxixe) aquamarine (e.g., I. Adamo et al., "Aquamarine, Maxixe-type beryl, and hydrothermal synthetic blue beryl: Analysis and identification," Fall 2008 *G&G*, pp. 214–226). Also seen are an absorption band at 835 nm related to octahedral Fe^{2+} and narrow absorption bands at 372 and 428 nm related to octahedral Fe^{3+}. The reason for the intense pleochroism is simply the increased intensity of the highly polarizable Fe^{2+}-Fe^{3+} IVCT chromophore relative to most other aquamarine. Note that the two wafers in figure 10 were cut from the same piece of rough and were used in a pilot heat treatment experiment. The larger one on the left was not heated, while the smaller piece on the right was heated at 400°C for two hours, with no apparent change in its color or appearance. It is not clear, however, if any of the material had been heated before it reached the market; further experiments may be warranted.

Microscopic observations showed an abundance of highly reflective, opaque, elongate needles and platelets that appeared light brown to black in darkfield and transmitted light (figure 12). Confocal Raman spectroscopy could not isolate the inclusions, but their dark color and reflective nature suggest they might be Fe oxides, which would be consistent with the iron-rich nature of these stones.

Figure 11. UV-Vis-NIR absorption spectra of a polished plate of Nigerian aquamarine showing both the ordinary (o-ray) and extraordinary (e-ray) ray absorption.

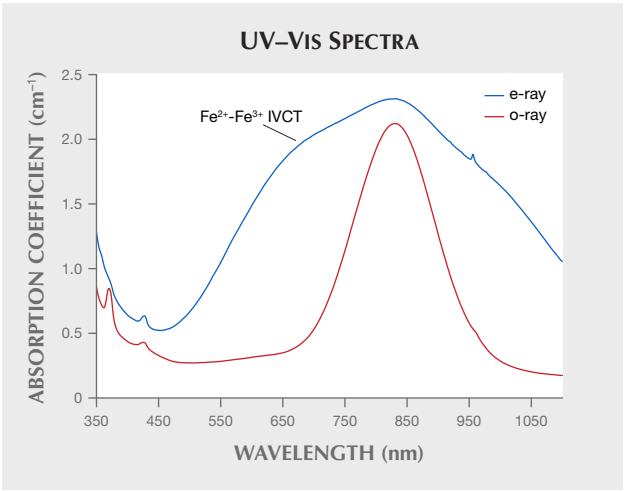

Figure 12. Needle and platelet inclusions are ubiquitous in this new find of Nigerian aquamarine, as seen with transmitted light polarized along the o-ray (top) and e-ray (bottom). Photomicrographs by Nathan Renfro; field of view 1.43 mm.

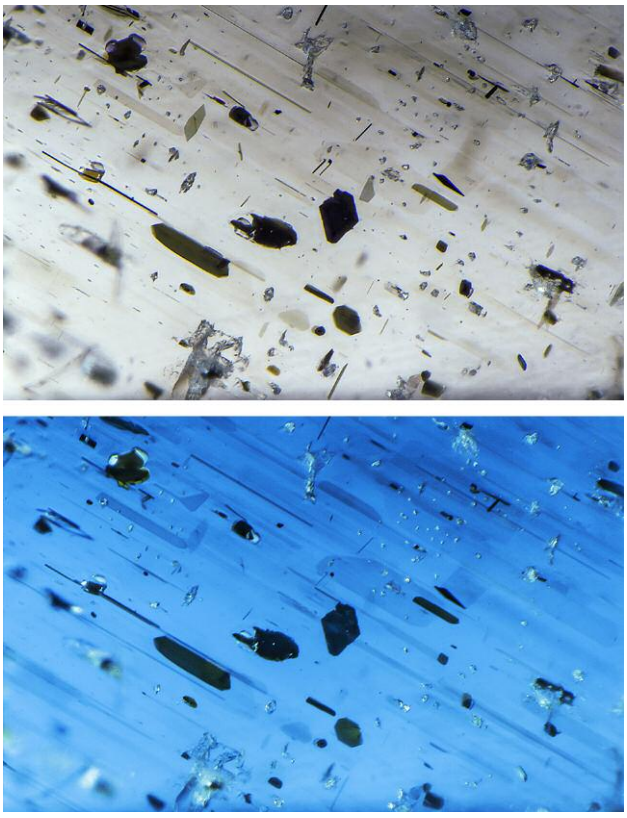

TABLE 1. Trace element chemistry (in ppmw) of Nigerian aquamarine from Nasarawa State.

	^{7}Li	^{23}Na	^{24}Mg	^{39}K	^{43}Ca	^{47}Ti	^{51}V	^{53}Cr	^{55}Mn	^{57}Fe	^{69}Ga	^{85}Rb	^{133}Cs
Average	434	8870	7900	1530	230	16	110	24	221	12000	32	183	905
Range	383–491	8530–9400	7620–8200	1440–1650	208–262	15–19	100–116	4–49	183–272	11000–12600	29–36	161–205	555–1450
Detection limits	0.02	1.1	0.09	0.2	4.3	0.1	0.01	0.1	0.02	0.6	0.004	0.003	0.01

Trace element content of the Nigerian aquamarines was measured by LA-ICP-MS (table 1). They were extremely enriched in alkali metals, especially Li, K, and Na (up to 9400 ppm). To the authors, these high concentrations of alkali metals seem unusual for gem-quality aquamarine among global deposits (including saturated material from Santa Maria in Minas Gerais, Brazil). The unique chemistry of this new material almost warrants the use of the term "alkali beryl," even though this term is nonstandard in the mineralogical community. Also notable is the relative enrichment of Cr from 4 to 49 ppm, compared to around 1 ppm Cr or less in aquamarine from most other deposits. The Cr enrichment was also indicated by the prominent Cr fluorescence measured by photoluminescence spectroscopy. Finally, the deep blue color of these stones was explained by their relative enrichment in Fe from 11,000 to 12,600 ppm. Such a high concentration of Fe increases the probability of having adjacent Fe^{2+} and Fe^{3+} cations, thereby facilitating and enhancing the Fe^{2+}-Fe^{3+} IVCT interaction. For now, this new deposit of fine Nigerian aquamarine lies dormant, but the world awaits the next important gem discovery in West Africa.

Aaron C. Palke
GIA, Carlsbad

Jeffrey Hapeman
Earth's Treasury, Westtown, Pennsylvania

A near-round natural pearl discovered in the edible oyster *Magallana bilineata*. Pakistan, which has a coastline stretching 1,046 km (650 miles) along the Arabian Sea, the Indian Ocean, and the Gulf of Oman, is blessed with numerous marine resources, including oysters that mainly inhabit estuaries and mangrove habitats. In Sindh Province, some oyster reefs at Hab River Delta have high ecological and economic value. Nine edible oyster species belonging to the genera *Crassostrea*, *Saccostrea,* and *Ostrea* have been recognized from different localities there. Pearl-forming mollusks belonging to the genera *Pinctada* have been reported from Daran Beach.

The Ostreidae family includes edible oysters and is most commonly known as a source of seafood (K. Scarratt et al., "A note on a pearl attached to the interior of *Crassostrea virginica* [Gmelin, 1791] (an edible oyster, common names, American or Eastern oyster)," *Journal of Gemmology*, Vol. 30, No. 1-2, 2006, pp. 43–50). Of these, *Magallana bilineata* has the widest distribution in the Indo-Pacific region, encompassing the coasts of northern Arabia, the Bay of Bengal, the Andaman Sea, the Java Sea, South China and Vietnam, the Philippines, and Okinawa.

Magallana bilineata is a euryhaline species that inhabits backwaters, creeks, estuary banks, coastal bays, and lagoons, forming oyster beds on a large scale. A large number of specimens of this species from Hab River Delta were examined to study the taxonomic characteristics of the genus *Magallana* as part of a joint project between Japan and Pakistan. Ten shells of each species were opened. Only one shell of *M. bilineata* (150 mm shell height) contained a pearl, attached to tissues near the adductor muscle. It was near-round, with a smooth surface and a purplish and off-white color very similar to the inner shell layer of *M. bilineata* (figure 13, left). The crystal structure of calcium carbonate was observed under high magnification. The non-nacreous, shiny pearl (figure 13, right) was 4.15 mm in diameter and weighed 0.02 g. The specimen is housed at the Centre of Excellence in Marine Biology, University of Karachi (part of the study collection of author SA).

Oysters living in tropical and warm regions have darker, more vivid, and more extensive coloration than

Figure 13. The inner and outer shell of M. bilineata *(left and center). A near-round pearl (right) was found inside the shell. Photos by Sadar Aslam.*

those in cooler climates. Our finding is very similar to that of Scarratt et al. (2006), which found a pearl inside *Crassostrea virginica* that was attached to an adductor scar. In our case, the pearl was attached to the tissues near an adductor scar. This finding demonstrates the very rare phenomenon of edible oysters producing natural pearls. However, further work will be needed to determine its chemical composition using highly accurate analytical methods.

Sadar Aslam, Malik Wajid Hussain Chan, Ghazala Siddiqui, and Syed Jamil Hasan Kazmi
University of Karachi, Pakistan

Noman Shabbir
PTV News, Karachi

Tomowo Ozawa
Nagoya Biodiversity and Biosystematics Laboratory, Nagoya, Japan

Natural sapphire with trapiche pattern inclusions. A blue gemstone pendant was recently submitted to Guild Gem Laboratories for identification. Standard gemological testing identified it as a sapphire, with a refractive index of 1.762–1.770 and birefringence of 0.008. Fourier-transform infrared (FTIR) spectroscopy combined with microscopic observation confirmed it was a natural sapphire. The UV-Vis spectrum indicated a basalt-related origin owing to relatively high iron content. The FTIR transmitted spectrum also revealed a 3309 series with peaks at 3366, 3309, 3232, and 3185 cm^{-1}, which are commonly seen in basalt-related sapphire.

Figure 14. The regular hexagonal inclusions consisted of six independent units, resembling a trapiche pattern. Photomicrograph and illustration by Yizhi Zhao; field of view 1.70 mm.

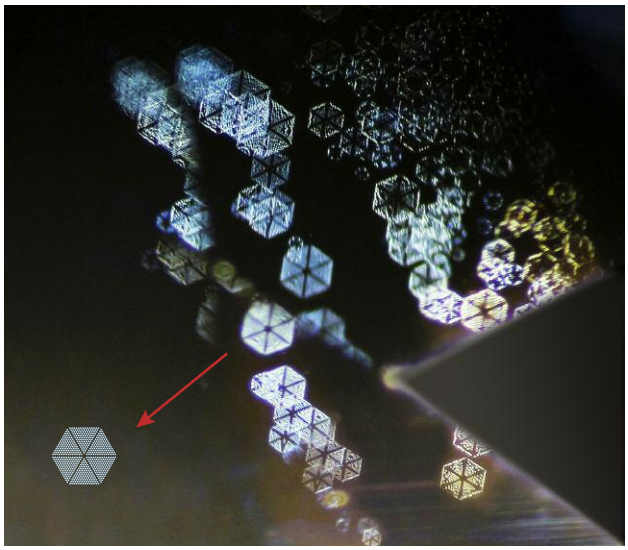

Microscopic observation showed several colorless crystals and fluid inclusions under reflective and transmitted light. Using a fiber-optic light, we also observed very interesting scenes of whitish clouds (figure 14) consisting of arrays of hexagonal particles. These particles seemed to be flat and parallel to each other. A distinct uniaxial interference pattern was observed when viewing perpendicular to these particles under the polariscope equipped with a conoscope, which proved that they were parallel to the basal plane (0001) crystalline face of corundum. Further observations revealed that each particle possessed six nearly identical triangular sectors, divided by six arms with hexagonal symmetry. Based on our microscopic observation and estimation, the diameters of the hexagons ranged from approximately 0.06 to 0.13 mm. This pattern was very similar to the trapiche structure seen in some sapphire, ruby, and emerald.

The depth of the inclusions prohibited Raman spectroscopy testing, but we will monitor this phenomenon in other samples for further study in the future.

Yujie Gao, Dan Ju (judan@guildgemlab.com), and Yizhi Zhao
Guild Gem Laboratories, Shenzhen, China

Opals revisited. In the 1980s, the author and his wife, Corky, acquired large quantities of Virgin Valley "wet" opal specimens displayed in glass domes with water and other specimens immersed in silicone oil. The domes had black rubber stoppers on the bottom. The mine representative had put them in water and silicone oil to enhance their beauty, since wetting the surface gives the illusion of a polished gem specimen.

Opal is a hydrated amorphous silica, and those with a high water content tend to craze and crack if left to dry. If a specimen is inclined to craze or crack, placing it in a liquid does not stabilize it or heal the cracks within, but it does delay the "day of reckoning" when the opal eventually deteriorates.

The specimens displayed in the domes with water began forming deposits, and within months the water became cloudy and the domes were crusted with precipitate from dissolved minerals. Those in silicone oil fared better, but eventually they too deteriorated, with the silicone oil taking on a yellow cast from the black rubber stoppers, which appeared to coat the opals with a yellow crust (figure 15).

After years of changing the water and silicone oil, the cleaning and repackaging eventually became very time-consuming. The author removed all the wet specimens from their domes, cleaned and wrapped them in paper towels, and put them in boxes. The boxes with the now-dry opal specimens were packed away and stored in the garage, where they remained for more than 27 years.

In July 2019, the author found the boxes containing these beautiful and long-forgotten opals. The results were astonishing. They had not fallen apart, and they looked more stable than they had when dried and put away. The cracks were

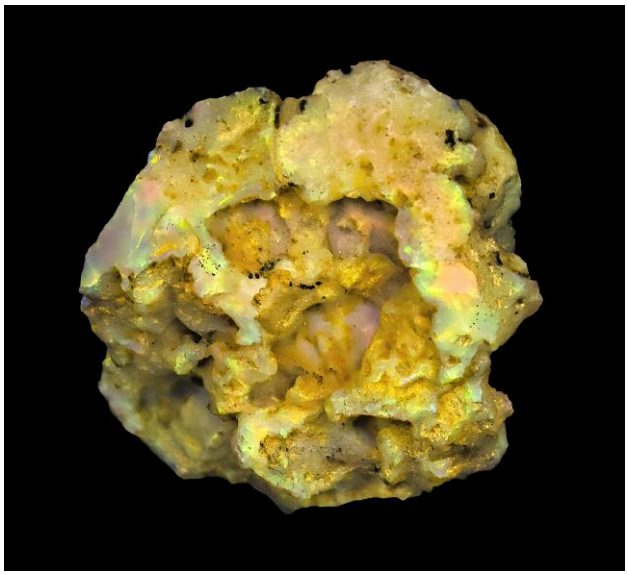

Figure 15. The untouched opal specimen displays the yellow coating caused by years of storage in silicone oil. Photo by Ted Grussing.

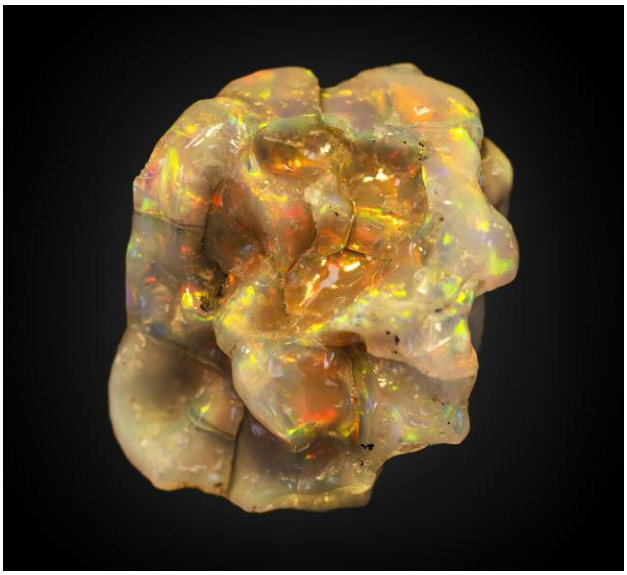

Figure 17. The finished piece, dry and ready for display. Photo by Ted Grussing.

still there, but the look was different. They looked like they could be worked—if not on the wheels, then with a flex shaft. The first opal that caught the author's eye (again, see figure 15) was cleaned and worked (figure 16). The completed piece, shown in figure 17, is named "Bonnie Jean." There are many more to finish, and they are dry and unlikely to craze or crack any further.

Ted Grussing
Sedona, Arizona

Trapiche emerald from Swat Valley, Pakistan. Trapiche emeralds are usually found in Colombia. Recently the authors received six emeralds reportedly from Swat Valley, Pakistan, polished as double-sided wafers, retaining their original hexagonal crystal habit and exhibiting a trapiche-like pattern (figure 18). These samples weighed from 0.38 to 0.83 ct, with a refractive index of 1.588–1.599 and a birefringence of 0.009–0.011.

Generally, these trapiche emeralds were composed of four parts from rim to core: a green rim, a light green area, six arms, and a colorless core, as illustrated in figure 19A. The rims had a highly saturated green color, and most were relatively clean except for several fractures and tiny fluid inclusions. The rims ranged from approximately 1 to 2 mm wide. Although the boundary between the green rim and

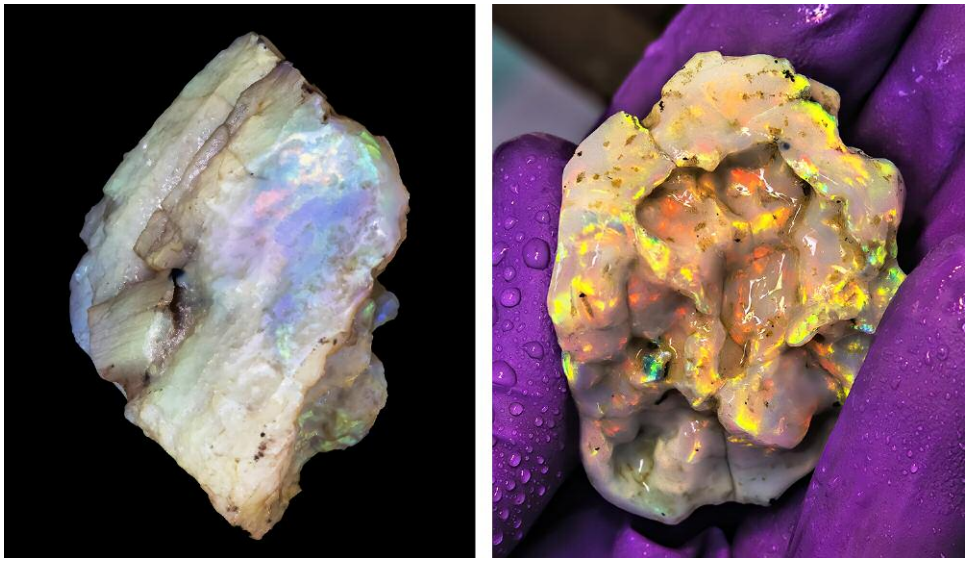

Figure 16. Left: The side of the specimen after cleaning and rubbing on a diamond wheel. Right: The nearly finished opal midway through the cleaning process. Photos by Ted Grussing.

Figure 18. Six emerald wafers reportedly from Swat Valley, Pakistan, showing a trapiche-like pattern. They range from 0.83 to 0.38 ct from left to right, with a thickness of about 1.51 to 2.08 mm. Photo by Kaiyin Deng.

the light area was not very sharp, a hexagonal boundary was visible. Six black arms spread in a hexagonal symmetric pattern, with each arm perpendicular to the hexagonal side. The colorless core usually had a hexagonal shape.

Microscopic observation revealed that every arm contained many minute black platy inclusions. These small particles appeared dark under transmitted light (figure 19B), while they showed bright metallic luster under reflected light (figure 19C). Micro-Raman analyses (figure 20) identified these inclusions as magnetite. Peaks at 662 and 545 cm^{-1} were consistent with two main peaks of magnetite, according to the RRUFF online database (rruff.info), while peaks at 683 and 400 cm^{-1} may be assigned to the emerald host. Chemical analysis by energy-dispersive X-ray fluorescence (EDXRF) on the sample shown in figure 19 revealed an iron content of 20,860 ppm (n = 3) in the light green area and 17,000 ppm (n = 3) in the rim. The difference in iron content may be due to the inclusions, since magnetite (Fe_3O_4) is mainly composed of iron and oxygen.

To our knowledge, there have not been many reports of trapiche emerald from localities other than Colombia.

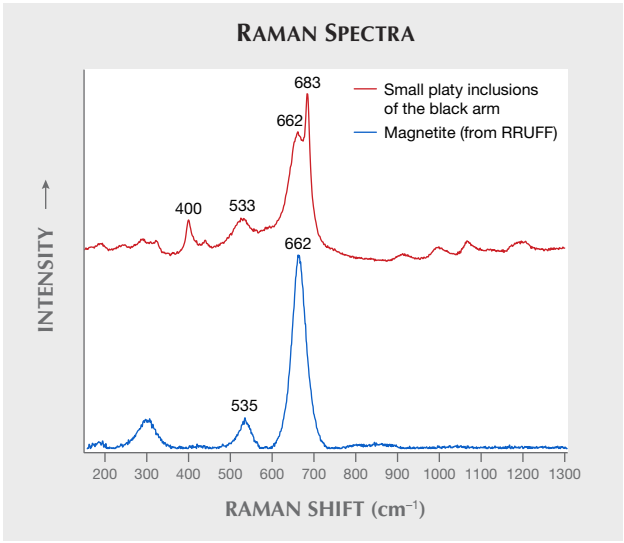

Figure 20. Raman analysis identified these inclusions as magnetite. Peaks at 662 and 545 cm^{-1} agree with the two main peaks of magnetite, according to the RRUFF database, while peaks at 683 and 400 cm^{-1} may be assigned to the emerald host.

The trapiche pattern caused by platy magnetite inclusions could help advance our understanding of trapiche.

Yujie Gao, Xueying Sun (shirley.sun@guildgemlab.com), and Mengjie Shan
Guild Gem Laboratories, Shenzhen, China

Uvarovite in prehnite from Pangasinan Province, Philippines. Uvarovite, $Ca_3Cr_2(SiO_4)_3$, is the rarest of the commonly encountered garnet species, and the only one that is consistently green. Although seldom faceted due to its tendency to be opaque, drusy coatings of tiny bright green uvarovite crystals on chromite matrix from Russia are used for jewelry. Recently, a new type of rock with lapidary po-

Figure 19. The trapiche emeralds from Pakistan were mainly composed of four parts: a green rim, a light green area, six arms, and a nearly colorless core as illustrated in figure A. These arms appear dark under transmitted light (B) and show bright metallic luster under reflected light (C); field of view 8.48 mm. Illustration and photos by Yujie Gao.

Figure 21. This new ornamental gem material from the Philippines consists of vibrant green uvarovite garnets in a white prehnite matrix. The polished freeform weighs 4.23 ct. Photo by Robison McMurtry.

tential was reportedly discovered in the Philippines, consisting of a white prehnite matrix with vibrant green crystals of uvarovite (figure 21).

This new material was brought to the authors' attention by Xavier A. Cortez, who operates Crystal Age, a gem shop in Quezon City. While attempting to source jade for his shop in early 2019, Xavier was offered unidentified white stones speckled with bright green crystals from local miners on the island of Luzon. Mr. Cortez was able to track down the source of this material to a rural portion of Pangasinan Province, in the Ilocos region of Luzon. Weathered calc-silicate rocks at this deposit yield small euhedral crystals of opaque bright green garnets as well as compact green masses in white matrix. The measured spot refractive index of 1.63 was consistent with prehnite. The identities of the green uvarovite and the white prehnite matrix were confirmed with Raman spectrometry.

While there is currently very little of this material on the market, it could be used as a jadeite simulant due to its mottled white and green appearance. Aside from its potential as a jadeite simulant, it is an interesting ornamental material that can be appreciated for its own unique beauty and vibrant green color.

Ian Nicastro
San Diego, California
Nathan Renfro
GIA, Carlsbad

DIAMONDS

The Rare Sun diamond. While manufacturers typically seek to minimize or remove inclusions in gem-quality diamonds, a few are specifically cut to highlight these features. Certain hydrogen-rich diamonds can yield fascinating inclusion forms when faceted. One such stone is the 5.24 ct Rare Sun diamond (figure 22), which GIA's New York laboratory recently had the opportunity to examine. Framed at the center of this Fancy Dark yellowish brown modified octahedron is an eye-visible cloud inclusion that scatters light to form the image of a star and its shining rays. The inclusion's orientation gives it an unusually distinct six-fold symmetry, which is very rare. The overall shape of the Rare Sun diamond has been precisely polished so that as light touches various parts of its surface, a different ray beams through. Achieving this effect required extremely precise fashioning—even the slightest error in cutting or polishing would have diminished the effect.

Very few diamonds have the potential to display this star-like pattern, and fewer still ever have this potential recognized and achieved. Diamonds with unusual inclusions, especially inclusions that suggest the shape of other objects, are also prized by gem collectors and seekers of the uncommon. The Rare Sun diamond is a large and noteworthy example and could be considered among those unique diamonds.

This diamond, with its particularly distinctive inclusion scene, also serves as a valuable research material. Gemologists welcome the opportunity to study gems with such unusual features.

Manoj Singhania and Apoorva Deshingkar
GIA, Mumbai

SYNTHETICS AND SIMULANTS

Artificial glass imitating blue amber. Artificial glass, a low-cost material, is capable of simulating any gemstone owing to its range of appearances (bodycolor, transparency, and

Figure 22. The Rare Sun diamond, a 5.24 ct Fancy Dark yellowish brown modified octahedron, has a centrally located, eye-visible inclusion resembling a star and its rays. Photo by Jian Xin (Jae) Liao.

Figure 23. This 139.34 ct piece of artificial glass bore a striking similarity to blue amber. Photo by Lai Tai-An Gem Lab.

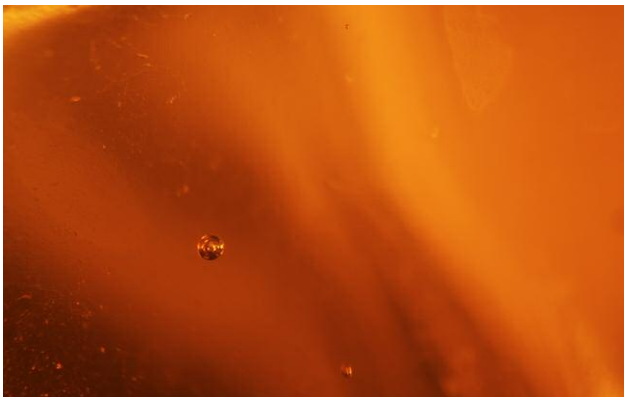

Figure 24. Examination with a gemological microscope revealed gas bubbles. Photomicrograph by Lai Tai-An Gem Lab; field of view 2.6 mm.

phenomena). While this material is usually straightforward to identify, in some cases it is visually similar to the gem material being imitated. The Lai Tai-An Gem Laboratory recently received an object for identification that the client claimed was blue amber, but was subsequently determined to be artificial glass (figure 23).

The transparent, irregularly shaped, brownish yellow object with a bluish surface-related effect and vitreous luster weighed 139.34 ct and measured 37.0 × 33.2 × 28.6 mm. While it closely resembled amber, its heft was completely at odds with that expected for an amber of its size, providing the first important clue about its identity. Standard gemological testing revealed a spot refractive index of 1.50, a specific gravity of approximately 2.50 (amber's is 1.08), a weak chalky blue reaction under short-wave ultraviolet radiation, and an inert response to long-wave UV. Inspection with a gemological microscope revealed gas bubbles (figure 24). Standard gemological testing confirmed that the item was not amber but artificial glass, though more advanced analysis was carried out. Fourier-transform infrared (FTIR) spectrometry was consistent with data we obtained on some samples of known glass (figure 25), confirming the identity. Energy-dispersive X-ray fluorescence (EDXRF) spectrometry also detected Si and Pb as the main chemical elements.

Blue amber's optical effect, produced by the extremely shallow blue fluorescence stimulated by UV light, is strictly confined to the surface. A strong blue fluorescence under long-wave UV radiation is also typical in such amber, so the inert reaction also indicated the material's artificial nature. The object exhibited a similar optical effect when viewed at different angles or when the direction of illumination changed.

In our experience, it is uncommon to see this type of artificial glass imitating blue amber. The gas bubble inclusions, while typical of glass, may also be encountered in amber, so additional gemological analysis may be neces-

Figure 25. Comparison of the infrared spectra for amber (red trace, collected by the author) and the artificial glass imitation (blue trace). The absorption at 1077 cm^{-1} is assigned to artificial glass.

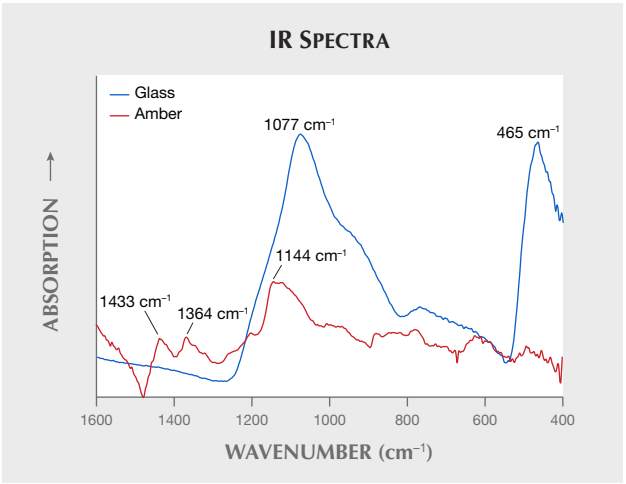

Figure 26. Two near-round beads cut from shell, 9.22 × 9.15 × 8.67 mm (left, 5.04 ct) and 9.51 × 9.44 × 8.69 mm (right, 5.45 ct). Photo by Hasan Abdulla.

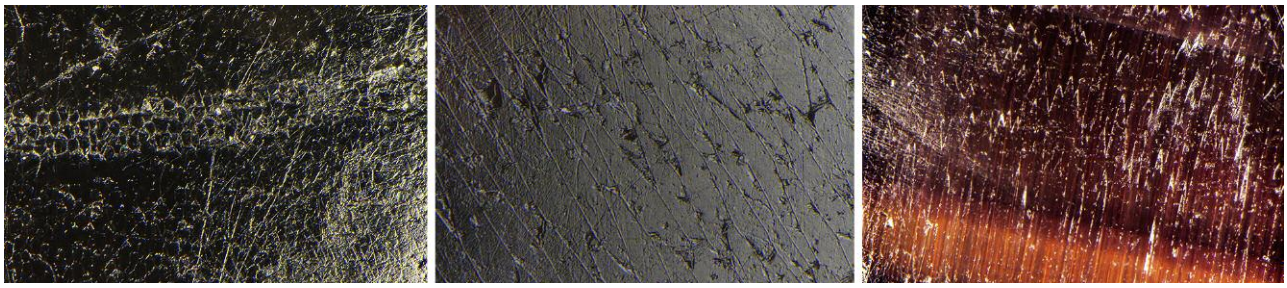

Figure 27. Columnar structures observed in the smaller bead made of calcite (left, reflected light) and elongated structures made of aragonite (center, reflected light) due to fibrous crystals of aragonite (right, reflected and transmitted light). Similar structures were also observed on the larger bead. Polish lines are observed in all images. Photomicrographs by Hasan Abdulla; fields of view 1.5 (left), 1.1 (center), and 2.4 mm (right).

sary to ensure the correct identification. This case clearly illustrates how artificial glass can imitate virtually every gemstone imaginable and mislead the unwary bargain hunter.

Larry Tai-An Lai (service@laitaian.com.tw)
Lai Tai-An Gem Laboratory, Taipei

Black non-nacreous pearl imitations made of beads cut from shell. DANAT (Bahrain Institute for Pearls & Gemstones) recently received a 5.04 ct bead (9.22 × 9.15 × 8.67 mm) and a 5.45 ct bead (9.51 × 9.44 × 8.69 mm), both of near-round shape (figure 26). Under the microscope, both beads presented columnar structures in some areas, similar to those observed in some non-nacreous pearls (N. Sturman et al., "Observations on pearls reportedly from the Pinnidae family (pen pearls)," Fall 2014 *G&G*, pp. 202–215), as well as elongated structures due to fibers reaching the surface (figure 27). Raman spectra with a 514 nm green laser were difficult to acquire, as they revealed high luminescence possibly linked to their high organic matter content; however, there was enough Raman signal to be able to identify calcite and aragonite. The calcium carbonate identification was confirmed by acquiring FTIR reflectance spectra. In the Raman spectra, weak bands linked to polyenic pigments were also observed.

Chemical analysis of the beads using energy-dispersive X-ray fluorescence (EDXRF) did not show any measurable manganese. Strontium was above 800 ppmw, and they remained inert under X-ray imaging, similar to saltwater pearls. Digital X-ray microradiographs and micro-CT did not show any internal structures.

Under long-wave and short-wave ultraviolet light, zoned/banded/layered fluorescence was observed (figure 28). Using transmitted fiber-optic illumination, banded structures and fibrous structures were visible with the unaided eye (figure 29). These characteristics were similar to those observed in imitation pearls made of non-nacreous shell material. Most of the imitation pearls described previously had a light color or were artificially dyed. The beads examined in this study, though, presented no evidence of any color treatment under the microscope or

Figure 28. Reaction of the beads under long-wave UV (top) and short-wave UV (bottom). Note the luminescence distribution in the different zones. Photos by Hasan Abdulla.

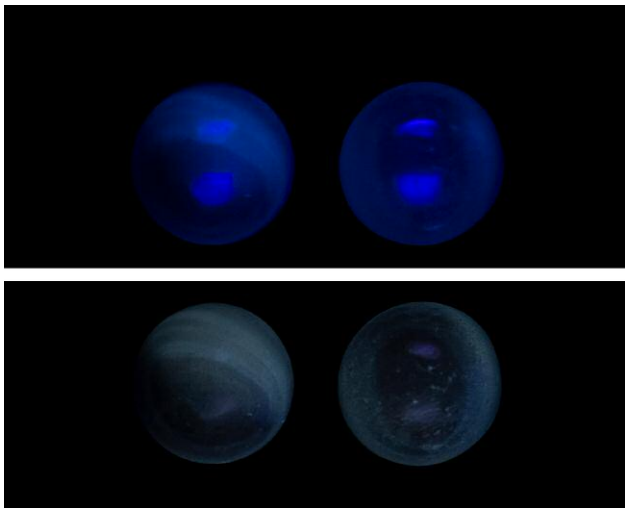

Figure 29. Under transmitted fiber-optic illumination, the 5.04 ct bead displayed a banded structure reminiscent of beads cut from the inner part of a shell. Photo by Hasan Abdulla.

Figure 30. This opal imitation shows a billowy play-of-color phenomenon. The largest block measures approximately 61.79 mm in length. Photo by Robison McMurtry and Diego Sanchez. Courtesy of Sanwa Pearl & Gems Ltd.

using EDXRF and Raman spectroscopy. The "zoned" fluorescence reaction under UV light was linked with different structures and not with the artificial colorants.

Large white beads with fibrous aragonite supposedly cut from bivalves from *Tridacna* species, which contain thick inner layers, have previously been used to imitate pearls (Summer 2004 GNI, p. 178; Summer 2006 Lab Notes, pp. 166–167; M. Krzemnicki and L. Cartier, "Fake pearls made from *Tridacna gigas* shells," *Journal of Gemmology*, Vol. 35, No. 5, 2017, pp. 434–429). These beads were sometimes dyed to alter their coloration. A salmon-colored bead of about 10 mm, supposedly cut from the inner part of *Lobatus gigas*, was used to imitate coral (E. Disner and F. Notari, "Gastropod shell beads disguised in a coral necklace," *Journal of Gemmology*, Vol. 34, No. 7, 2015, pp. 572–574). The beads we examined were of natural black color, and we are still looking for a mollusk that might have a non-nacreous inner shell layer where beads of that size could be cut.

Acknowledgments: The authors would like to extend their appreciation to Mr. Saud Bin Rajab (Manama, Bahrain) for allowing us to publish the study on these beads.

Stefanos Karampelas (Stefanos.Karampelas@danat.bh), Ali Al-Atawi, Hasan Abdulla, Bader Al-Shaybani, and Fatema Almahmood
DANAT (Bahrain Institute for Pearls & Gemstones)
Manama, Bahrain

Imitation opal with interesting play-of-color pattern. GIA's Carlsbad laboratory recently examined samples of a relatively new manufactured gem material sometimes known as a "hybrid opal product" (figure 30) (see Spring 2018 Lab Notes, pp. 60–62). This material showed a refractive index of 1.498–1.500, and the specific gravity ranged from 1.33 to 1.35. Both of these properties fall far outside the range for natural opal, making identification very straightforward for the gemologist. These anomalous gemological properties also mean that this material is best described as an opal imitation and not a synthetic opal. This material is reportedly composed of about 20% silica and about 80% resin, which is consistent with the gemological properties measured.

This new imitation opal showed a pronounced play-of-color phenomenon with a pattern unlike the kind one would expect to see in conventional synthetic opal. Instead of small cellular patches, it displayed broad swaths of ever changing play-of-color covering large areas of the surface (figure 31). The laboratory examined samples that showed

Figure 31. The imitation opal showed broad swaths of the play-of-color phenomenon when examined with a microscope. Photomicrograph by Nathan Renfro; field of view 18.80 mm.

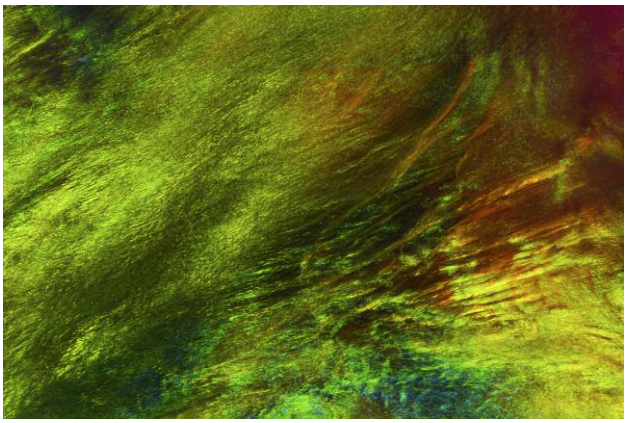

Figure 32. Thermal enhancement and unusual inclusions were detected in this 2.05 ct blue sapphire, measuring 7.07 × 6.55 × 4.99 mm. Photo by Kaiyin Deng.

either a black or white bodycolor and a variety of colors in the play-of-color areas. For those who love opal, this attractive material could offer a cost-effective alternative to natural material while retaining the allure of the play-of-color phenomenon.

Nathan Renfro

TREATMENTS

Dendritic inclusions of thorianite in heated blue sapphire. Recently, a 2.05 ct blue sapphire was sent to Guild Gem Laboratories for identification (figure 32). Standard gemological testing confirmed it was corundum, with a refractive index of 1.762–1.770 and specific gravity of 4.00. Under microscopic observation, cloudy particles and diffuse straight color zoning were seen, as well as fingerprint-like fluid inclusions as shown in figure 33, indicating that this stone had undergone thermal enhancement. This sapphire exhibited chalky greenish fluorescence around the girdle under short-wave (254 nm) ultraviolet fluorescence light. Further UV-Vis spectroscopic testing suggested a metamorphic origin, while FTIR spectra (figure 34) showed a distinct 3309 series at 3185, 3232, 3309, and 3367 cm^{-1}, confirming heat treatment. Energy-dispersive X-ray fluorescence (EDXRF) showed an Fe content around 300–500 ppm. Neither U nor Th was detected.

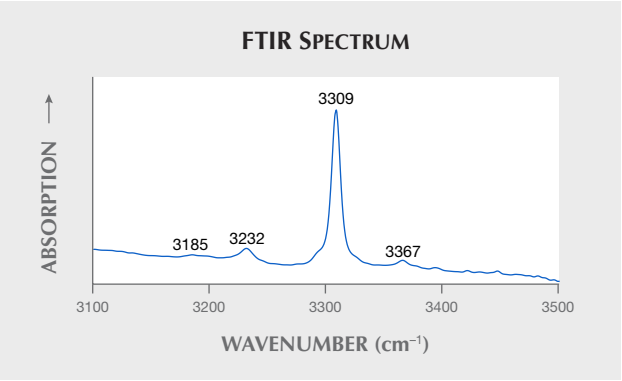

Figure 34. The sapphire's FTIR spectrum exhibited a distinct 3309 series at 3185, 3232, 3309, and 3367 cm^{-1}.

Also observed were interesting dendritic inclusions, which are not very common in sapphire. These inclusions showed relatively strong metallic luster under reflected light, and they appeared to be opaque under transmitted light. Lines of small dots were seen under higher magnification. These dot-like inclusions exhibited a blurred surface and a rounded shape. Raman analysis at the National Gemstone Testing Center (NGTC) using a 473 nm laser showed three distinct peaks at 466, 552, and 607 cm^{-1}, matched very well with thorianite, according to the RRUFF online database (rruff.info), as shown in figure 35. Thorianite (ThO_2) is an oxide mineral mainly composed of Th and O, first found in an alluvial deposit in Sri Lanka (D.

Figure 33. Left: Dendritic inclusions consisted of dot-like minerals showing a "melted and diffused" appearance. Photo by Yujie Gao; field of view 2.68 mm. Center: Resembling a tree root, these dendritic inclusions showed relatively strong metallic luster under reflected light. Photo by Yizhi Zhao; field of view 2.52 mm. Right: Dendritic inclusions coupled with blurred blue color zoning. Photo by Yujie Gao; field of view 9.73 mm.

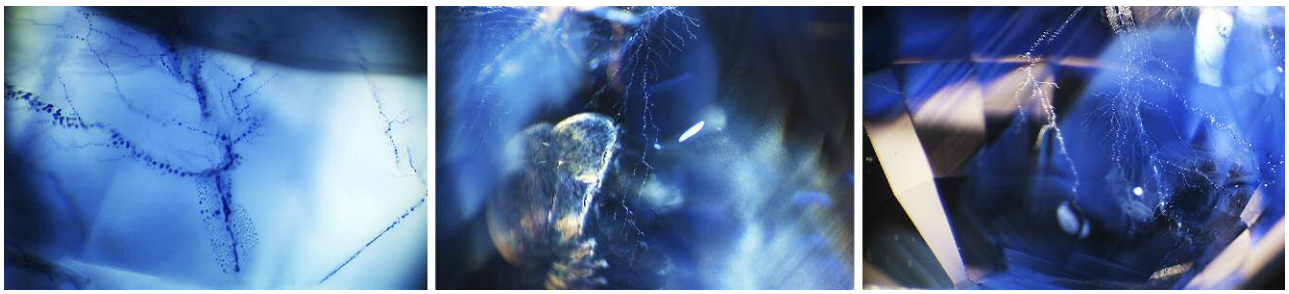

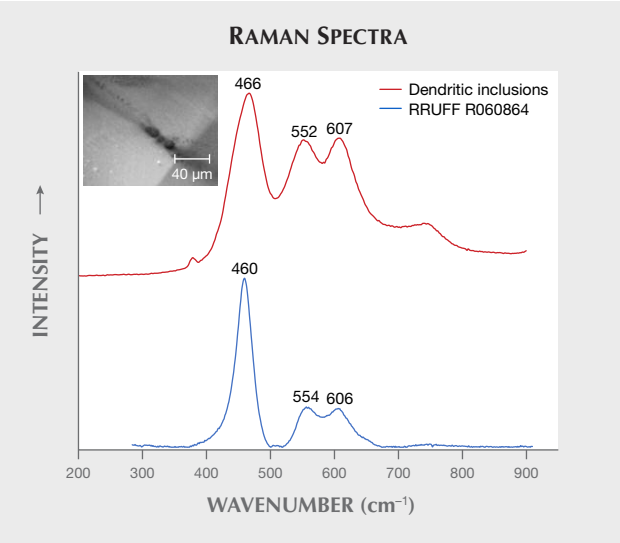

Figure 35. Raman spectra of the sapphire's dendritic inclusions matched with thorianite (ThO_2).

Wyndham, "The occurrence of thorium in Ceylon," *Nature*, Vol. 69, 1904, pp. 510–511). A melted appearance of a mineral inclusion and/or unnatural-looking discoid fractures around inclusions can be indicative of heat treatment in corundum. Such phenomena are normally attributed to the breakdown of mineral inclusions at high temperature. However, the thorianite inclusions here did not have the typical appearance of inclusions that have been altered by high-temperature heat treatment. The diffuse appearance of thorianite is unlikely to be an indicator of heat treatment. Further experiments and tests on thorianite in unheated sapphire would give us more clues in the future.

Yujie Gao (peter.gao@guildgemlab.com) and Xueying Sun
Guild Gem Laboratories, Shenzhen, China

Huihuang Li
National Gemstone Testing Center (NGTC)
Shenzhen, China

Recrystallization of baddeleyite as an indicator of PHT ("HPHT") treatment in sapphire. PHT ("HPHT") treatment in sapphire has been a controversial topic the last few years. Recently, Guild Gem Laboratories in Shenzhen received a 7.11 ct blue sapphire (figure 36) for identification. The refractive index of 1.762–1.770 and hydrostatic specific gravity of 4.00 confirmed the stone's identity. It was inert under long-wave and short-wave UV. Microscopic examination revealed several distinct features, such as diffuse color bands and melted white solid mineral inclusions surrounded by discoid fractures, indicating that this stone had undergone thermal enhancement (figure 37).

Further UV-Vis spectroscopic testing specified a metamorphic geological origin, while energy-dispersive X-ray fluorescence (EDXRF) analysis revealed low Fe content around 400–600 ppm. FTIR spectra (figure 38) showed a distinct 3309 cm^{-1} series at 3181 and 3373 cm^{-1}, consistent with heated metamorphic sapphire. We also noticed a broad band centered at 3042 cm^{-1}, accompanied by peaks at 2627, 2412, 2349, 2319, and 2096 cm^{-1}. According to previous reports (S.-K. Kim et al., "Gem Notes: HPHT-treated blue sapphire: An update," *Journal of Gemmology*, Vol. 35, No. 3, 2016, pp. 208–210; A. Peretti et al., "Identification and characteristics of PHT ('HPHT') - treated sapphires – An update of the GRS research progress," 2018, http://gemresearch.ch/hpht-update), the ~3042 cm^{-1} series band is diagnostic of sapphire treated by a high-pressure, high-temperature process.

Figure 36. This 7.11 ct oval blue sapphire, measuring 11.66 × 10.44 × 7.38 mm, exhibits eye-visible white mineral inclusions. Photo by Yizhi Zhao.

As shown in figure 39, the mineral inclusions melted and solidified within the surrounding discoid fractures, exhibiting a dendritic appearance. Micro-Raman spectra analysis on the white mineral and recrystallized dendritic

Figure 37. Blurred blue color zoning and melted white solid mineral inclusions surrounded by discoid fractures. Photomicrograph by Yujie Gao; field of view 5.26 mm.

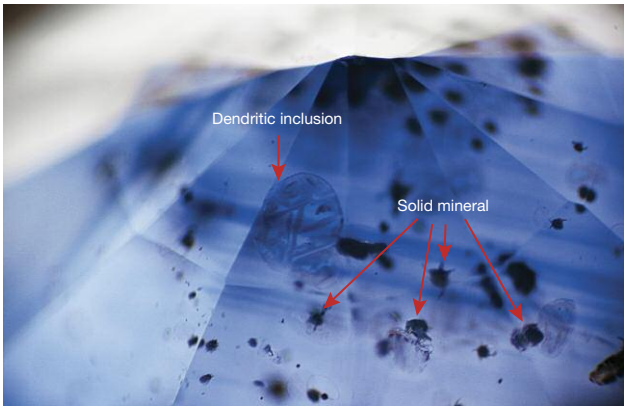

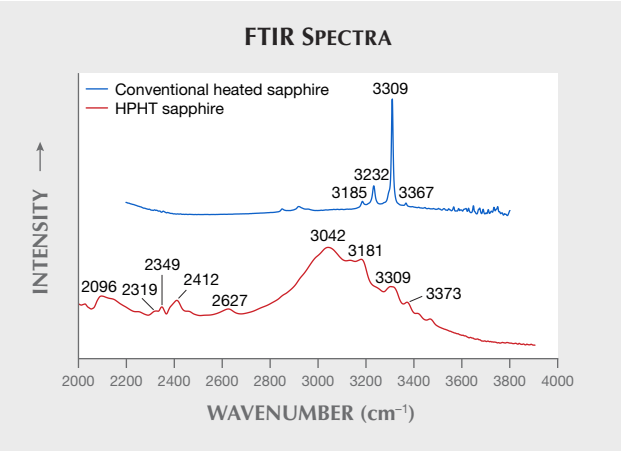

Figure 38. FTIR spectra of conventionally heated sapphire and the HPHT sapphire in figure 36. The latter showed distinct bands centered around 3042 cm^{-1}, accompanied by peaks at 2627, 2412, 2349, 2319, and 2096 cm^{-1}.

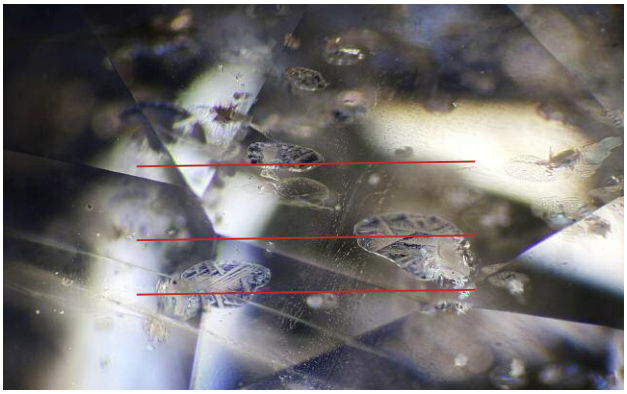

Figure 39. Discoid fractures were oriented in almost the same direction within the sapphire host. Photomicrograph by Yujie Gao; field of view 2.28 mm.

inclusions using 473 nm laser excitation produced some interesting results. The white melted minerals and the recrystallized inclusion showed almost the same peaks in the region of 1000–100 cm^{-1}, suggesting that they were the same mineral. Peaks at 641, 560, 541, 475, 334, and 221 cm^{-1} and a characteristic doublet at 188/178 cm^{-1} matched with the Raman spectrum for baddeleyite (a rare zirconium oxide mineral), according to the RRUFF database, as shown in figure 40.

Zircon ($ZrSiO_4$) is known as a common inclusion in sapphires, which may undergo solid state thermal dissociation to zirconia and silica at extreme conditions such as high temperature and/or high pressure as follows:

$$ZrSiO_4 \text{ (zircon)} \rightarrow ZrO_2 \text{ (baddeleyite)} + SiO_2$$

Baddeleyite, a monoclinic polymorph of zirconia, forms at relatively high pressure (up to about 7 GPa). W. Wang et al. ("The effects of heat treatment on zircon inclusions in Madagascar sapphires," Summer 2006 *G&G*, pp. 134–150)

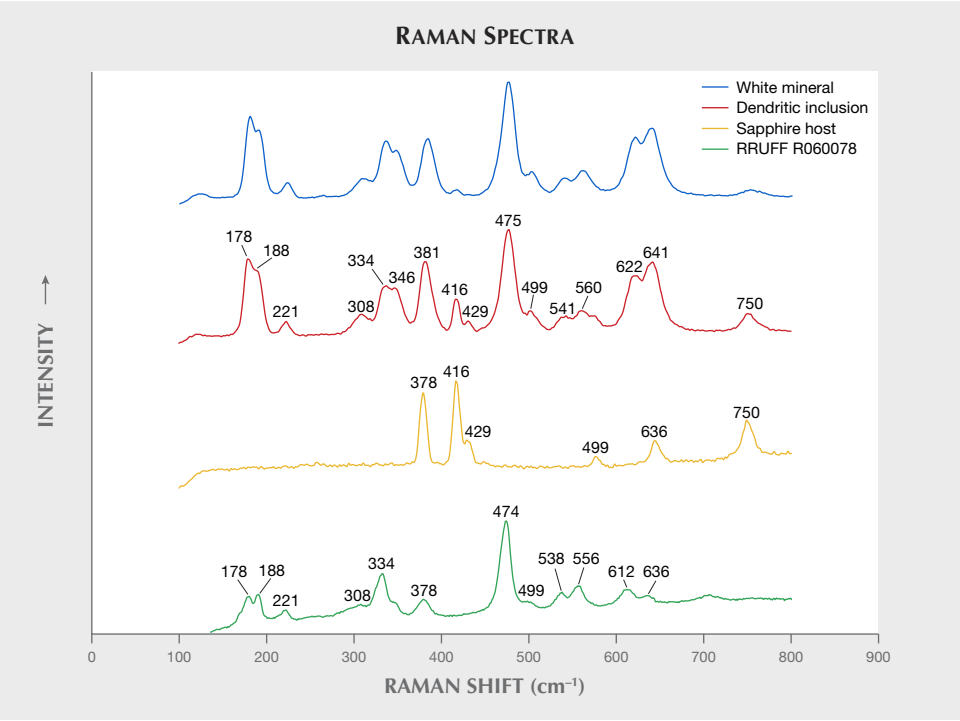

Figure 40. Raman spectra of the white mineral and dendritic inclusion both matched with baddeleyite (ZrO_2).

confirmed the existence of baddeleyite with zircon in heated blue sapphire by detecting a 188/178 cm^{-1} Raman doublet of baddeleyite in melted zircon after heating at around 1400–1700°C and normal pressure. The results of Wang et al. (2006) suggest that when using conventional heating techniques, only a small fraction of zircon transforms into baddeleyite, while most of the zircon inclusions keep their crystalline structure intact without any phase transformation. Based on our Raman testing, however, no zircon was found in this 7.11 ct sapphire, and spectra of both the white mineral at the center and the recrystallized minerals in the fracture were consistent with baddeleyite.

Additionally, we also noticed several fractures filled with baddeleyite in a uniform orientation (again, see figure 39). Using a polariscope and a conoscope under a microscope, we confirmed that these fractures occurred along the basal plane (0001) of the sapphire.

One question is whether these flat fractures already existed from parting before treatment (which is commonly encountered in sapphire) or formed during treatment. It is known that parting may occur along the basal plane of sapphire under certain situations, such as twinning or exsolution of inclusions. Neither distinct twinning nor exsolved inclusions were found, and almost all of the fractures were fully filled, leaving no empty space within them. Thus, we believe that these fractures could have been triggered by treatment. The proposed occurrence and healing process of these fractures are illustrated in figure 41.

In conclusion, we can appropriately speculate that PHT ("HPHT") treatment might cause flat fractures along the basal plane and facilitate the transformation from zircon to baddeleyite. The high baddeleyite content in heated sapphire may serve as a good indicator of PHT ("HPHT") treatment. Further experiments are needed to support this argument.

Xueying Sun and Yujie Gao
(peter.gao@guildgemlab.com)
Guild Gem Laboratories, Shenzhen, China

CONFERENCE REPORTS

2019 GSA annual meeting. The Geological Society of America (GSA) annual meeting took place in Phoenix, Arizona, September 22–25. GIA participated in the exhibition and hosted speaker and poster sessions that attracted great attention on gemology among the geoscience community (figure 42).

The talks started with research by **Dr. Tingting Gu** (formerly with GIA) on lower-mantle inclusions trapped in a type IaB diamond. The study identified inclusions of hydrous ringwoodite, ferropericlase, and enstatite (a back-transformation product of bridgmanite). This was the first evidence of them occurring together at this depth of the earth, which will help to unravel the pyrolytic nature of the 660 km discontinuity. The study was presented by co-author **Dr. Wuyi Wang** (GIA). **Dr. Sally Eaton-Magaña** (GIA) presented a detailed study of natural radiation stains in diamonds. Temperature-controlled experiments revealed that the stains' color changes from green to olive

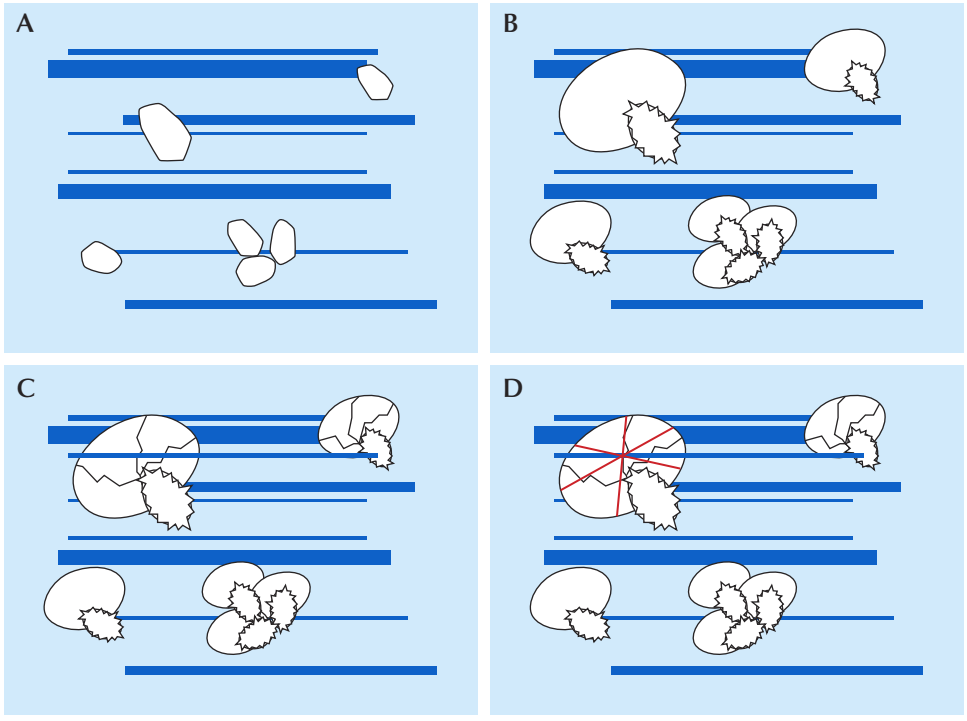

Figure 41. The occurrence and healing process of discoid fractures in the sapphire during treatment. A: Zircon inclusions and blue color bands in the sapphire. B: Under high pressure and high temperature, progressive decomposition of zircon results in the formation of baddeleyite and flat fractures. C: Baddeleyite penetrates into the discoid and fills the fracture with no space left. D: Baddeleyite recrystallizes in a dendritic pattern shown by the red line. Illustrations by Xueying Sun.

Figure 42. Presenters and session hosts from the gemology session at the 2019 GSA annual meeting. Front row, left to right: Sarah Steele, Dr. Christopher M. Breeding, Kyaw Soe Moe, and Rachelle Turnier. Back row: Dr. Evan Smith, William Aertker, Dr. Aaron Palke, Dr. Sally Eaton-Magaña, Roy Bassoo, Dr. Wuyi Wang, Samuel Martin, Dr. Jim Shigley, and Dr. John Valley. Photo by Tao Hsu.

green at about 400°C and then to brown at about 550–600°C. Color-changing rates of different related defects were then carefully calculated. This study provides needed information about the reliability of using radiation stain color to identify diamond color as either natural or treated. Graduate student **Roy Bassoo** (Baylor University) put forward a source study of Guyana diamonds mined from alluvial gravels in the Amazon rainforest. Several possible primary diamond sources were proposed, and multiple advanced analytical methods were used on rough diamond crystals. Detrital zircon dating ruled out West Africa as a potential source. Inclusion and isotopic data suggest that these diamonds are of upper-mantle peridotite paragenesis, with a subpopulation of eclogite paragenesis and an undiscovered kimberlite source that still needs to be identified. **Dr. Evan Smith** (GIA) shared the characteristics of the newly discovered nickel sulfide mineral crowningshieldite (α-NiS). This mineral was found as inclusions in a so-called CLIPPIR diamond (Cullinan-like, Large, Inclusion-Poor, Pure, Irregular, and Resorbed) that came from 350–750 km below the earth's surface. Crowningshieldite features one Ni atom connected to six sulfur atoms, while the known β-NiS features one connecting to five.

Dr. Christopher M. Breeding (GIA) discussed the rarity and color causes of orange diamonds. Orange diamonds account for only 2.4% of all colored diamonds, based on GIA's intake database. Single substitutional nitrogen and the 480 nm band are the two major mechanisms responsible for this rare color. Of the two, the 480 nm absorption band is not well understood and has been proposed to be composed of substitutional oxygen atoms in the diamond lattice. At low concentration this defect causes yellow color, while at high concentration the color shifts to orange. Diamonds with this defect can also be heated to temporarily change their color to orange. **Kyaw Soe Moe** (GIA) continued the discussion on the 480 nm band using the study results of a bicolor diamond. The 480 nm band was detected only in the brown-orange portion of this diamond. An interesting find was that the fluorescence image and optical image of this color zone do not match, which indicates that the 480 nm band caused color zoning that does not align with growth zones. This observation suggests that the defect causing the 480 nm absorption formed or penetrated the diamond after its growth. The authors proposed that the defect consists of localized vacancy clusters, in addition to other previously proposed possibilities.

Following a series of diamond presentations, the talks continued with colored gemstone discussions. Graduate student **Samuel Martin** (Brigham Young University) presented a geochemical comparison study of sapphires from Bingham Canyon in Utah and from Yogo Gulch, Montana.

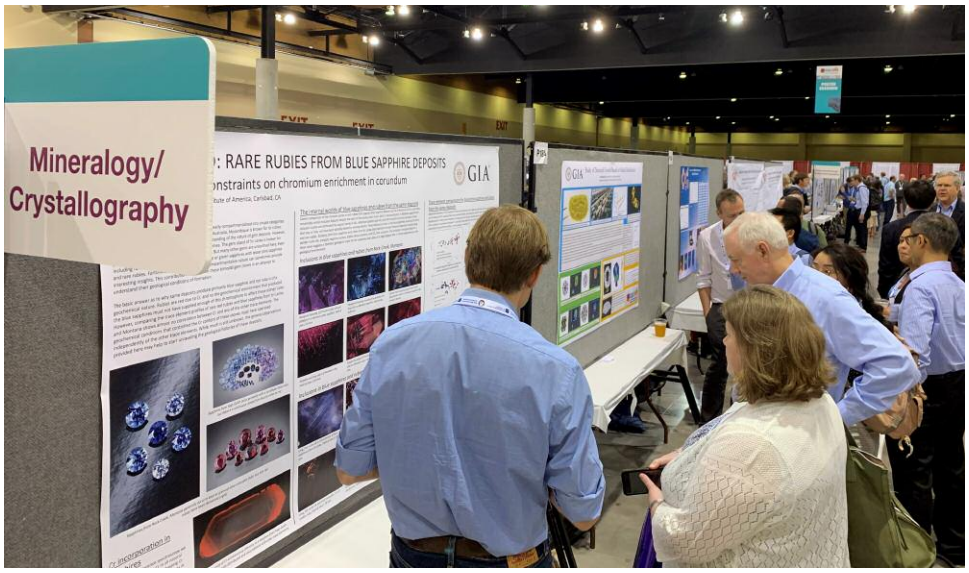

Figure 43. GSA poster presenters shared their latest research. Photo by Tao Hsu.

Although the two sapphire populations were formed 10 million years apart, they do broadly share the same trace element signatures, and both contain silica melt inclusions. Oxygen isotope study of both suggests that they have different protoliths, with Bingham Canyon sapphires as a mixture of multiple populations in the Bingham magma system. The study proposed that sapphires from both sources have been produced through partial melting of Al-rich rocks. Graduate student **Rachelle Turnier** (University of Wisconsin–Madison) shared her research on the genesis of basalt-related gem corundum with zircon inclusions in samples from nine different sources around the globe. Through a combination of element mapping, growth texture imaging, zircon geochronology, apparent pressure estimation, oxygen isotope study, and *in situ* geochemical analyses, variations were revealed among these deposits, which have generally been grouped in a single category. PhD candidate **William Aertker** (Colorado School of Mines) discussed the genesis of metasomatic sapphire from the Whitehorn stock metamorphic aureole in central Colorado. Sapphires occur within a ductile shear zone that experienced contact metamorphism. Extensive evidence suggests that desilication was not the only process involved in corundum formation. Element exchange must have happened at the same time, and ductile shearing facilitated fluid channeling to facilitate this exchange process, known as metasomatism. Retired geologist **Charles Breitsprecher** (California State University, Sacramento) presented a self-funded field investigation of sunstone from three mines in southeast Oregon. The occurrence and regional geology were discussed. Gemologist and professional lapidary **Sarah Steele** talked about her archaeogemological and chemistry study on gem-quality jet, including its use since the Upper Paleolithic and the market for it today. The author's analyses found 33 different hydrocarbons and biopolymers that are used as gems, which goes beyond the current commonly used definition for jet**. Dr. Aaron Palke** (GIA) closed the session with a presentation on the newly recognized mineral johnkoivulaite ($Cs[Be_2B]Mg_2Si_6O_{18}$), named in honor of renowned GIA researcher John Koivula. This new member of the beryl group was discovered in Mogok, an area full of opportunities to expand the mineral family. Due to its special structure, johnkoivulaite does not contain as much water as other members of the beryl group.

This year's poster session featured five presenters (figure 43). **Dr. Qishen Zhou** (China University of Geosciences, Wuhan) presented two posters, on the results of colored diamond and sapphire auctions, respectively. Dr. Zhou and his team collected more than 50,000 auction results over the past decade. These results are representative of the global auction sector, including the Chinese domestic auction sector, which is not well known to the rest of the industry. The colored diamond study poster focused on pink and blue diamonds. Both studies explored the relationship between auction results and the quality factors of the stones. The authors found that color largely determines colored diamonds' auction prices, while both color and carat weight have a high impact on sapphire. **Dr. Aaron Palke** (GIA) delivered research on rare rubies found in blue sapphire–dominant deposits. The study compared sapphires and rarely encountered rubies from four different sources. Geochemical results indicate that the trace element Cr, which causes the red color, behaves quite independently of the other trace elements. However, trace elements other than Cr share similarity between sapphires and rubies from the same deposit, which was also supported by inclusion scenes. **Paul Johnson** (GIA) displayed an interesting research project on melee-size HPHT lab-grown diamonds, which have a different crystal shape from large crystals made with the same method. The authors used element mapping of nickel to reveal the growth structure of these small diamonds. The results indicated multiple growth stages of the small lab-grown diamonds, which

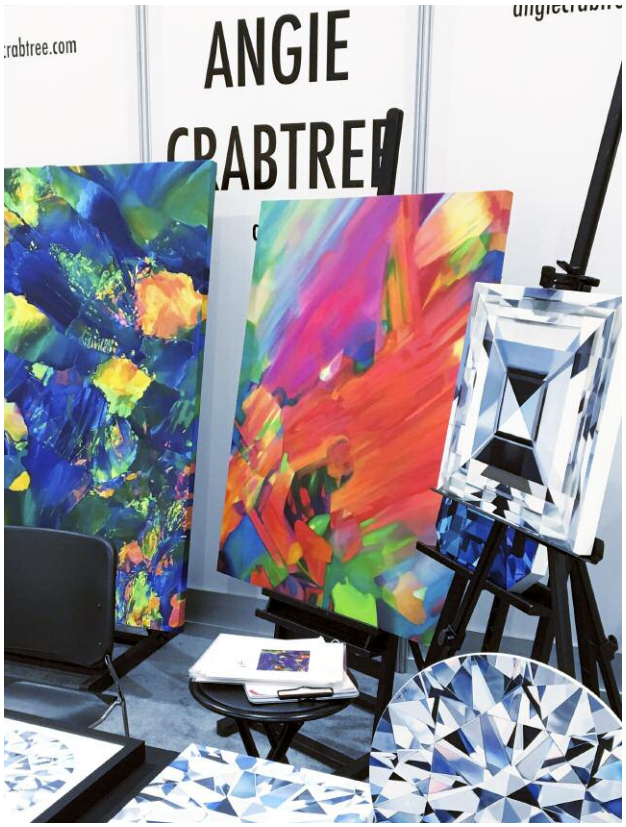

Figure 44. This selection of Angie Crabtree's paintings displayed at the AGTA GemFair showcases opal and cut diamond. Photo by GIA.

explained their elongated crystal shape. **Garrett McElhenny** (GIA) presented a study on type IIa pink diamonds. The author studied a suite of 30 samples with inclusions using Raman spectroscopy. The inclusions identified were mainly of sublithospheric origin. The existence of sublithospheric inclusions again proved that these diamonds came from the sublithospheric mantle.

The 2020 GSA annual meeting is scheduled for October 25–28 in Montreal.

Tao Hsu
GIA, Carlsbad

MISCELLANEOUS

Gemstone portrait artist Angie Crabtree. The 2019 AGTA show in Tucson featured the work of a gemstone portrait artist. On display in Angie Crabtree's booth were her oil paintings (figure 44) on canvas and panel. She also had a table with paints, palettes, and other supplies so people could see her at work (figure 45).

Crabtree's portraits range in size up to 64 × 48 inches. She said people are excited to see gemstones in great size and detail. One painting can take more than 300 hours to complete. She said because people outside the gem and jewelry industry don't always recognize the subjects as gemstones, the paintings can also be interpreted as abstract art.

The San Francisco–based artist said that all of her business, even from large corporate clients, comes from Instagram. "I've never paid to promote," Crabtree said. "I'm just very fortunate for that." Instagram also allows her to sell her own work instead of relying on galleries, which take a sizeable cut (typically around 50%). "That's hard for artists," she said. "Because of social media, artists have the opportunity to promote and market themselves."

Crabtree grew up on a ranch in Sonoma County, California, and was interested in nature and geology from a young age. Her grandfather used to go gold mining, and she would collect obsidian and other rocks along the way. She began painting and taking art classes at the age of five, and by 12 she was teaching painting. She attended an arts high school and college, studied abroad at Amsterdam's Gerrit Rietveld Academie, and graduated from the San Francisco Art Institute in 2009.

In 2012, while working as a high school art teacher, she did her first gemstone painting—a diamond portrait for an art gallery. She began painting different diamond cuts and posted them to Instagram. Soon people were asking for portraits of their engagement rings and other special stones. "That's when it really took off," she said.

Figure 45. Angie Crabtree at work at the AGTA show. Photo by Erin Hogarth.

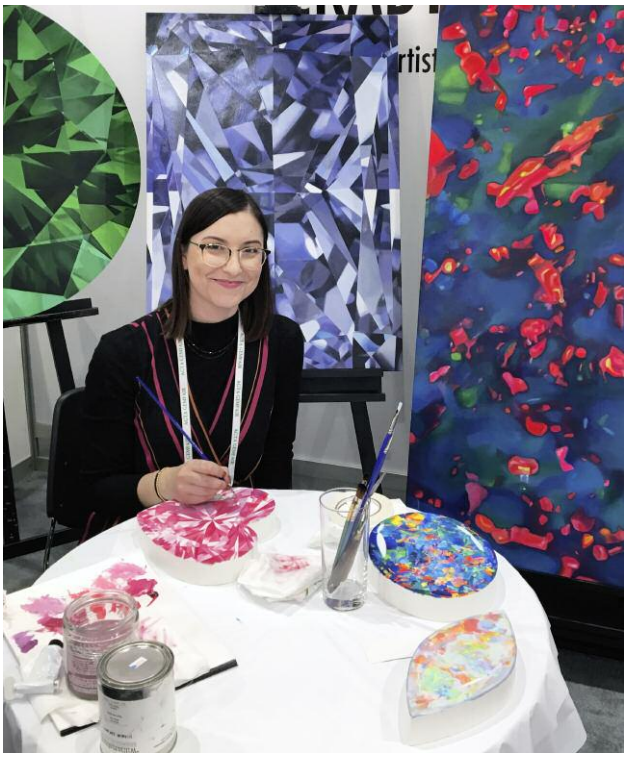

Figure 46. This 1.16 ct crystal of the new mineral johnkoivulaite was reportedly discovered in the legendary Mogok Valley of Myanmar in the Pein Pyit mining area. Photo by Robert Weldon/GIA.

One of the first people she met in the industry—via Instagram—was gemstone cutter Jean-Noel Soni of Top Notch Faceting. He told her about the gem industry and "completely opened my eyes," she said. "That's when I just fell in love with the whole thing."

In 2015, she established her business and quit her teaching job. "It was a pretty big leap," she said. "It's scary for any artist to do that." Within the first year, she was commissioned by Chopard and Forevermark to paint large series. Since then, business has grown to the point that she now has a studio manager who handles sales, accounting, and communication.

In 2018, Crabtree painted her first colored stone: an opal. "I wanted something a little bit more expressive and organic," she said. Then came a tsavorite and an alexandrite, and she has since moved into sapphires and other stones. She plans to eventually paint minerals and other natural objects.

Crabtree was trained in realism, but she said her biggest struggle has been understanding gemstone proportions and facet dimensions. She has consulted industry experts to learn how to use the correct dimensions and ratios for the stones in her paintings. She often does not see the actual stones—most clients send her photographs. Painting accurate colors can be challenging, she said, because of the way a gemstone's color changes with movement and light. Mixing color palettes is a laborious process: She will mix 30 or so colors and write down each color recipe for future use. "People think being an artist is painting all day every day, and it's not," she said. "It's numbers and talking to people, and it's sales and it's promotion. Even the cleanup and setup takes forever."

Crabtree has two autoimmune diseases. "There are certain days where I wake up and my hands are just stuck in fists. Sometimes I can't walk. Sometimes I can't open my paint," she said. "But I do what I love, and I get to create my own hours, and I get to travel. So I make it work and stay positive."

Erin Hogarth
GIA, Carlsbad

ANNOUNCEMENTS

Johnkoivulaite: A new gem mineral. A new mineral, johnkoivulaite, has been named in honor of John Koivula, a renowned microscopist and preeminent researcher at GIA for more than 40 years. In collaboration with scientists from the California Institute of Technology, Dr. Kyaw Thu of Macle Gem Trade Laboratory, and Nay Myo, a gem dealer from Mogok, GIA researchers described johnkoivulaite, which the International Mineralogical Association (IMA) formally accepted as a new mineral species on September 6, 2019.

The world's first specimen of johnkoivulaite was reportedly uncovered from the Pein Pyit mining area of Mogok in Myanmar. It subsequently passed through the hands of Nay Myo, a local gem dealer. When the 1.16 ct stone (figure 46) could not be identified, Nay Myo suspected he had encountered a new mineral and had the sample sent to GIA for identification. When the researchers

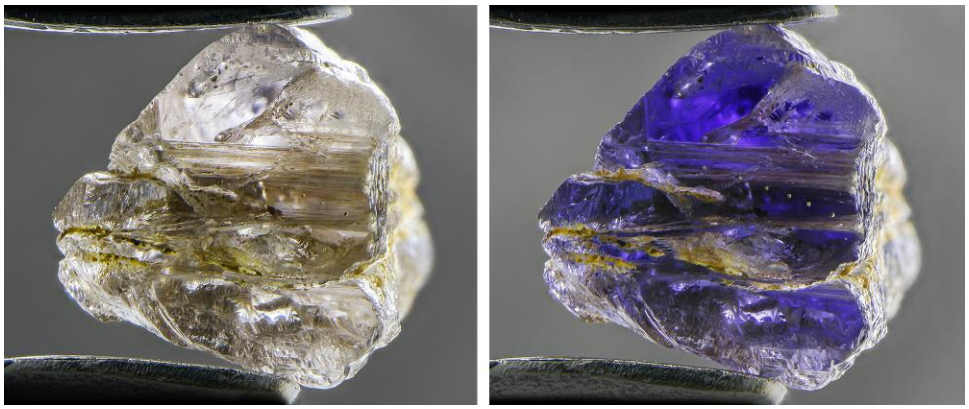

Figure 47. Johnkoivulaite shows strong pleochroism, going from near-colorless (left) to violet (right) when examined with polarized light. Photomicrographs by Nathan Renfro; field of view 10.05 mm.

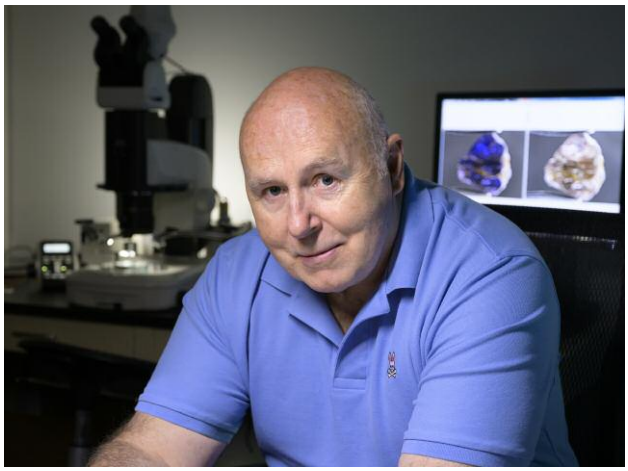

Figure 48. The new mineral johnkoivulaite is named after renowned gemologist John Koivula, best known for his contributions to inclusion research and photomicrography. Photo by Kevin Schumacher.

first examined the sample and realized its unique gemological properties, GIA made arrangements to purchase the unusual stone from Nay Myo so that additional advanced testing could be performed and the sample could be deposited in the GIA museum. Once the type specimen was housed in the museum (one of IMA's requirements for describing a new mineral), the team was able to submit a new mineral proposal. According to IMA guidelines, a new mineral can be named in recognition of a person's significant scientific contributions to the field of mineralogy. This one was named in honor of John Koivula's lifelong efforts to advance the sciences of mineralogy and gemology.

Single-crystal X-ray diffraction (XRD) analysis was performed in collaboration with researchers at the California Institute of Technology and indicated a hexagonal crystal structure that was very similar to beryl and other members of the beryl group such as pezzottaite. Chemical analysis by LA-ICP-MS and EPMA identified enrichment in cesium, boron, and magnesium and confirmed johnkoivulaite's membership in the beryl family, with its ideal end-member formula as $Cs(Be_2B)Mg_2Si_6O_{18}$. Standard gemological testing gave a refractive index of 1.608, with a birefringence too low to accurately measure, a specific gravity of 3.01, a hardness of 7 ½, a conchoidal fracture, vitreous luster, and no reaction to long-wave or short-wave UV. Especially notable is johnkoivulaite's strong pleochroism from deep violet to nearly colorless when observed with polarized light (figure 47).

John I. Koivula (figure 48) developed an interest in minerals and particularly their inclusions during childhood, when he found a quartz crystal with pyrite inclusions in North Bend, Washington. From there, Koivula earned degrees in geology and chemistry before working as an exploration geologist. In the 1970s, his career changed direction when a friend suggested the Graduate Gemologist program at GIA. He joined GIA in 1976 and began publishing gemological articles and short notes while refining his photomicrography techniques. In 1986, he co-authored with Edward J. Gübelin the immensely popular *Photoatlas of Inclusions in Gemstones*, which was followed by two additional volumes. Koivula also wrote *The Microworld of Diamonds* and co-authored *Geologica* with Robert Coenraads. Other highlights of his career include winning first place in Nikon's Small World Photomicrography competition in 1984, receiving the AGS's Robert M. Shipley Award in 1996, and being named one of *JCK* magazine's 64 Most Influential People in the Jewelry Industry in the 20th Century. In 2002, he was awarded the AGA's Antonio C. Bonanno Award for Excellence in Gemology. Mr. Koivula also received GIA's Richard T. Liddicoat Award for Distinguished Achievement in 2009 for his contributions to gemology.

After more than 40 years in the industry, Mr. Koivula still regularly contributes to gem and mineral research and is now a contributing editor for *G&G*'s Micro-World column.

The discovery of a new mineral is a rare and exciting occasion for the gemological community. It is a special honor for the authors to be able to name this mineral after such a prominent and well-deserving gemologist.

Aaron C. Palke, Ziyin Sun, and Nathan Renfro
GIA, Carlsbad

Lawrence M. Henling, Chi Ma, and George R. Rossman
California Institute of Technology, Pasadena

Kyaw Thu
Macle Gem Trade Laboratory, Yangon

Nay Myo
Greatland Gems and Jewelry, Mogok

Patcharee Wongrawang and Vararut Weeramonkhonlert
GIA, Bangkok

ERRATA

1. In the Spring 2019 GNI entry "Gray spinel: A new trend in colored stones" (p. 130), the figure 15 caption listed the incorrect carat weight and cutter. The gray spinel weighed 24.15 ct and was courtesy of 3090 Gems, LLC. We thank Bryan Lichtenstein for correcting this.

2. In the Summer 2019 article "A decade of ruby from Mozambique: A review" (pp. 162–183), the FTIR spectrum in figure 21D mislabeled the 3240 and 3161 cm^{-1} peaks. Also, the 2420 cm^{-1} peak should be disregarded, as it was caused by a fingerprint.